

THE ART OF FLEXURE MECHANISM DESIGN

**Florent Cosandier,
Simon Henein, Murielle Richard
and Lennart Rubbert**



EPFL Press
Distributed by CRC Press

THE ART OF FLEXURE MECHANISM DESIGN

Florent Cosandier, Simon Henein, Murielle Richard and Lennart Rubbert
Edited by Simon Henein and Lennart Rubbert

Flexure mechanism design is an art, and this book provides the theoretical and practical foundation for scientists and engineers to express their creativity in this field. Flexure mechanisms, also known as compliant mechanisms, rely on the elasticity of matter to provide motion to mechanism linkages. Flexure mechanisms eliminate the disadvantages of classical joints: friction, wear, lubrication and play, while permitting monolithic design. Flexure-based mechanisms have gained prominence in a wide variety of fields including robotics, surgical instrumentation, aerospace, astronomy, particle accelerators, metrology and horology.

This book establishes a conceptual framework for the design of flexure-based articulated structures. Topics featured deal with the theoretical foundations for the design of translational and rotational flexures, the simple kinematic analysis of flexure-based mechanisms, and advanced kinematic approaches to the design of complex flexure-based mechanisms using modules in parallel or serial arrangements. The book also features detailed examples of long stroke flexure mechanisms used in metrology applications, and a detailed example of planar flexure mechanisms having out of plane functionality and used in surgical applications. This book aims to provide scientists and engineers with a conceptual tool, an analytic methodology and the key references for their precision engineering needs.

Florent Cosandier, Ph.D., develops precision flexure mechanisms for watchmaking, aerospace and metrology applications at the Centre Suisse d'Electronique et Microtechnique (CSEM) in Neuchâtel, Switzerland.

Simon Henein, Ph.D., studied at the Ecole Polytechnique fédérale de Lausanne (EPFL) then worked at the Paul Scherrer Institute and the CSEM. He has been associate professor at EPFL since 2012.

Murielle Richard, Ph.D., works in a renowned Swiss horology group on product industrialization, assembly machines development and improvement of production lines.

Lennart Rubbert, Ph.D., studied at the Institut National des Sciences Appliquées (INSA), Strasbourg. He has been associate professor at INSA since 2015.

ISBN: 978-2-940222-56-8



9 782940 222568 >

EPFL Press

FLEXURE MECHANISM DESIGN

Cover illustration

Redundant flexure pivot with large angular deflection ($\pm 15^\circ$) and high radial stiffness thanks to the kinematic coupling of the intermediate block. This part with 16 circular arc notch hinges, each with a thickness of 30 microns, has been manufactured monolithically in carbon-steel by wire-electrodischarge machining (photography: Simon Henein).

FLEXURE MECHANISM DESIGN

**Florent Cosandier,
Simon Henein, Murielle Richard
and Lennart Rubbert**

**Edited by Simon Henein
and Lennart Rubbert**

EPFL Press
Distributed by CRC Press

The authors and publisher express their thanks to the CSEM (www.csem.ch) for its generous support towards the publication of this book.

EPFL Press is an imprint owned by Presses polytechniques et universitaires romandes, a Swiss academic publishing company whose main purpose is to publish the teaching and research works of the Ecole polytechnique fédérale de Lausanne (EPFL).

Presses polytechniques et universitaires romandes
EPFL – Rolex Learning Center
Station 20
CH-1015 Lausanne, Switzerland
E-mail: info@epflpress.org
Phone: +41 21 693 21 30

www.epflpress.org

First edition 2017, EPFL Press, Lausanne (Switzerland)
ISBN 978-2-940222-56-0 (print)
ISBN 978-2-8323-2331-1 (ebook, PDF), doi.org/10.55430/6219FMDHR

This text is under Creative Commons licence:



it requires you, if you use this writing, to cite the author, the source and the original publisher, without modifications to text or of the extract and without commercial use.

Preface

The marketplace is in continual search of new products having a large set of mechanical, electronic, computational, optical, chemical and even biological functionalities, and in continually decreasing physical size. The production facilities required to address this demand must therefore be cleaner, more flexible and more precise.

Mechanisms with flexible joints are as well suited to the needs of miniaturised products as they are to high precision production lines.

In the field of integrated products, flexure mechanisms are perfectly adapted to the realisation of force, pressure or acceleration sensors, as well as watch bearings or oscillators and medical biopsy forceps, micro-pumps or micro-valves. The restoring force intrinsic to these flexure bearings can introduce design difficulties but also brings a set of solutions. As shown in the present work, solutions allowing a reduction and even an elimination of this restoring force. The systems required for fabricating and assembling integrated products (ultra-high precision robots, grippers, specific bearings, compliant interfaces, etc.) will also benefit from flexures, particularly in regards to: zero play and zero friction, large bearing rigidity, perfect cleanliness and insensibility to vacuum and pollutants.

This reference work on the design of miniaturised products and fabrication systems highlights the huge potential of compliant mechanisms in a large number of fields and applications. Most notably, the reader will find:

- The theoretical foundation of structural mechanics and the mathematical formulas useful for sizing, as well as the characteristics of materials best lent to the realisation of flexure bearings.
- Original kinematic design methods illustrated by concrete and pertinent examples.
- A number of completely new systems having exceptional precision and mobility properties, in particular:
 - translational modules having 1, 2 or 3 degrees-of-freedom;
 - long stroke pivots;
 - two ultra-high precision linear bearings composed of flexible joints ingeniously arranged in space to ensure remarkable straightness precision (40 nanometers for 40 mm range of motion, in the best case); these bearings are based on the *Sarrus* and *13-hinge* rectilinear mechanisms;

- a toolbox composed of conceptual modules to aid in the design of 2 to 6 degrees-of-freedom ultra-high precision robots;
- spatial configuration microsystems bringing new solutions compatible with current fabrication technologies.

A veritable invitation to innovation as well as a source of inspiration, *The Art of Flexure Mechanism Design* proposes a rigorous and practical theoretical basis, varied new approaches, original and concrete solutions, as well as a view to new innovative concepts.

I would like to thank the authors for making this reference work available to professionals, and I wish the reader much pleasure in the discovery of this field as well as success in his/her future research and design endeavors.

Reymond Clavel
Emeritus Professor, EPFL
May 23, 2016

Foreword

This book edited by Simon Henein and Lennart Rubbert, combines the essential contributions of the four complementary Ph.D. theses of its four authors into a single reference. These Ph.D. theses were published in June 2000 (Simon Henein, EPFL), June 2012 (Murielle Richard, EPFL), December 2012 (Lennart Rubbert, University of Strasbourg) and March 2013 (Florent Cosandier, EPFL).

In 2001 Simon Henein published the book *Conception des guidages flexibles* (Presses polytechniques et universitaires romandes), based on his Ph.D. thesis. *The Art of Flexure Mechanisms Design* is a translation and update, as well as a significant extension of the original book, now out of print.

This book establishes a conceptual framework for the design of flexure-based articulated structures. Topics featured deal with the theoretical foundations for the design of translational and rotational flexures, the simple kinematic analysis of flexure-based mechanisms, and advanced kinematic approaches to the design of complex flexure-based mechanisms using modules in parallel or serial arrangements. The book also features detailed examples of long stroke flexure mechanisms used in metrology applications, and a detailed example of planar flexure mechanisms having out of plane functionality and used in surgical applications. This book aims to provide scientists and engineers with a conceptual tool, an analytic methodology and the key references for their precision engineering needs.

Acknowledgments

The authors are grateful to their thesis directors: Reymond Clavel, EPFL, and Jacques Gangloff and Pierre Renaud, University of Strasbourg, for having directed them to the blossoming field of flexure mechanisms. They also thank the members of their juries whose scrutiny and constructive feedback significantly contributed to the quality of their theses: Nicolas Andreff, Hannes Bleuler, Mohamed Bouri, Jean-Marc Breguet, Stéphane Caro, Ali Eichenberger, Pierre Genequand, Thomas Gmür, Ulrich Gengenbach, Jacques Giovanola, Patrick Helmer, Max-Olivier Hongler, Jean-Pierre Merlet, Max Odiet, Philippe Renaud and Roland Siegwart.

The authors thank Ilan Vardi for lending his rigorous hand to the proofing of key sections of the book, Damien Maillard for the editing numerous figures, Mitsuko Moser for addressing language issues, and the Presses polytechniques et universitaires romandes team for proofing and final editing of the manuscript.

The authors thank Jens Krauss and Mario El-Khoury of the Centre Suisse d'Electronique et Microtechnique (CSEM) for their generous practical and moral support which helped make this book possible.

The authors thank Stefano Bottinelli for supervising the manufacture of several flexure mechanisms presented in this book, which were cut by wire-electrodischarge machining by Mecartex SA, Muzzano.

The authors thank Philippe Fischer of the Fondation Suisse pour la Recherche en Microtechnique (FSRM) for disseminating the results presented in this book to industry by organising numerous training courses.

Contents

Preface	v
<i>Reymond Clavel</i>	
Foreword	vii
<i>Simon Henein</i>	
Contents	ix
1 Introduction	1
<i>Simon Henein</i>	
1.1 Flexure bearing importance	2
1.1.1 Plain and rolling bearing comparison	2
1.1.2 Contactless bearings comparison	5
1.2 Flexible element classification	6
1.3 Book goals and structure	7
1.4 Topic delimitation	8
I Basic flexures	11
2 Underlying theory	13
<i>Simon Henein</i>	
2.1 Basic assumptions	13
2.2 Allowable deflections	14
2.2.1 Yield criterion	15
2.2.2 Fatigue damage	16
2.2.3 Correction factor	17
2.2.4 Safety factor	19
2.2.5 Summary of allowable deflections	19
2.3 Stiffnesses	22
2.3.1 Definitions	22
2.3.2 Stiffnesses of flexure joints	23
2.3.3 Generalised stiffnesses	23

3 Flexure joint elements 25

Simon Henein

3.1	General considerations	25
3.1.1	Flexure joint classification	25
3.1.2	Definition of generalised stiffnesses and deflections . .	27
3.2	Leaf springs	28
3.2.1	Definition	28
3.2.2	Stiffnesses	29
3.2.3	Deflections	30
3.3	Rods	30
3.3.1	Definition	30
3.3.2	Stiffnesses	31
3.3.3	Deflections	32
3.4	Torsion bars	32
3.4.1	Clamping	33
3.4.2	Axis of torsion	35
3.5	Circular notch hinges	36
3.5.1	Definition	36
3.5.2	Angular stiffness	38
3.5.3	Angular deflection	39
3.5.4	Translational stiffness	39
3.5.5	Torsional stiffness	40
3.5.6	Transverse angular stiffness	41
3.5.7	Tensile/compressive stiffness	41
3.5.8	Other stiffnesses	42
3.5.9	Stiffness ratios	42
3.5.10	Truncated circular notch hinge	44

4 Translational flexures 45

Simon Henein

4.1	Two parallel leaf spring stage	45
4.1.1	Equilibrium of forces	45
4.1.2	Stiffness at zero load	47
4.1.3	Deflection at zero load	48
4.1.4	Path at zero load	49
4.1.5	Tensile/compressive loading: simplified model	49
4.1.6	Tensile/compressive loading: complete model	51
4.1.7	Summary	65
4.2	Overconstrained stage with four parallel leaf springs	65
4.2.1	Translational stiffness	66
4.2.2	Deflection	67

4.2.3	Main conclusions	69
4.3	Four prismatic notch hinge stage	70
4.3.1	Parameters	70
4.3.2	Stiffness at zero load	71
4.3.3	Deflection at zero load	72
4.3.4	Critical loading (buckling)	72
4.3.5	Tensile/compressive loading: simplified model	73
4.3.6	Tensile/compressive loading: complete model	75
4.3.7	Trade-off	79
4.4	Four circular notch hinge stage	84
4.5	Conclusion on linear translation bearings	88
5	Rotational flexures	89
	<i>Simon Henein</i>	
5.1	Separate cross spring pivot	89
5.2	Joined cross spring pivot	91
5.3	RCC pivot with two leaf springs	93
5.4	RCC pivot with four notch hinges	94
5.5	Cross pivot with four notch hinges	98
5.6	Comparison of the pivots	101
5.7	Radial loads	103
5.7.1	Variation in angular stiffness	103
5.7.2	Radial stiffnesses	104
5.7.3	Allowable loads	104
5.8	Overconstrained pivot with three leaf springs	105
II	Flexure mechanisms	107
6	Flexure structures	109
	<i>Simon Henein</i>	
6.1	Kinematics	109
6.1.1	Definitions	109
6.1.2	Statement of the method	110
6.1.3	Kinematic analysis	111
6.1.4	Kinematic synthesis	114
6.1.5	Parallel kinematics	115
6.2	Choice of materials	117
6.3	Working envelope	117
6.3.1	Serial arrangement of redundant DOFs	117
6.3.2	Mechanical stops	123

6.4	Stiffnesses	124
6.4.1	Minimisation of natural stiffnesses	124
6.4.2	Maximisation of natural stiffnesses (energy storage)	129
7	Modular design of flexure-based robots	133
	<i>Murielle Richard</i>	
7.1	Introduction	133
7.1.1	Preliminary definitions	135
7.2	Concept of modular kinematics	138
7.2.1	Modular parallel robot and building bricks	138
7.2.2	Exhaustive conceptual solution catalogue	146
7.2.3	Conclusion	147
7.3	Reduced solution catalogue for ultra-high precision	148
7.3.1	Hypotheses for ultra-high precision	148
7.3.2	Building bricks for ultra-high precision	149
7.3.3	Reduced conceptual solution catalogue	152
7.4	Mechanical design of the building bricks	154
7.4.1	Challenges in flexure-based brick design	154
7.4.2	Mechanical design of the active bricks for ultra-high precision	155
7.4.3	Mechanical design of the passive bricks for ultra-high precision	163
7.4.4	Discussion	167
7.5	Case study: 5-DOF ultra-high precision robot	168
7.5.1	Robot specifications	168
7.5.2	Kinematics synthesis	169
7.5.3	Mechanical design	174
7.5.4	$t_{ 1}t_{\perp}r_{ 1}r_{ 2}$ passive brick design	177
7.5.5	Design and assembly subtleties	178
7.5.6	Legolas 5 prototype	180
7.5.7	Discussion	183
7.6	Ultra-high precision parallel robot family	183
7.7	Conclusion	187
7.8	Final note	187
8	Rectilinear flexure mechanisms	191
	<i>Florent Cosandier</i>	
8.1	Introduction	191
8.1.1	Framework	191
8.1.2	Need for an ultrastraight bearing	191
8.1.3	Linear motion based on rotating joints	192

8.2	Rectilinear kinematics	192
8.2.1	Rectilinear and pseudorectilinear mechanisms based on rotation	192
8.2.2	Kinematic analysis of orthogyres and pseudo-orthogyres	198
8.2.3	Choice of two mechanisms	199
8.3	Sarrus guiding mechanism	200
8.3.1	Sarrus linkage kinematics	200
8.3.2	Realisation of a Sarrus prototype	205
8.3.3	Straightness measurement	206
8.4	13-hinge stage mechanism	207
8.4.1	13-hinge stage kinematics	207
8.4.2	Realisation of a 13-Hinge stage prototype	214
8.4.3	Straightness measurement	215
8.5	Analysis and comparison	217
8.5.1	Comparison criteria	217
8.5.2	Comparison chart	220
8.5.3	Performances table	220
8.6	Application to the watt balance	220
8.6.1	Description of the project	220
8.6.2	Problems related to the watt balance experiment	224
8.6.3	Context of the watt balance experiment	225
8.6.4	METAS watt balance mark II	227
8.7	Conclusions	228
8.7.1	General conclusions	228
8.7.2	Potential applications	228
9	Out-of-plane flexure mechanisms	229
	<i>Lennart Rubbert</i>	
9.1	Introduction	229
9.2	Example: design of an active cardiac stabiliser	232
9.3	In the vicinity of singularities	233
9.3.1	Modelling of the 3-RRR spherical parallel mechanism	235
9.3.2	Rotational stiffness of the 3-RRR flexure mechanism .	236
9.3.3	Analysis of the in-plane stiffness of the 3-RRR flexure mechanism	237
9.4	Optimisation of the spherical compliant joint	240
9.4.1	Formulation of the optimisation problem	240
9.4.2	Optimisation method and performance evaluation . . .	241
9.4.3	Results	244
9.5	Exploiting the singularities of parallel mechanisms	246
9.5.1	Singularities of parallel manipulators	246

9.5.2	Principle of the design approach	247
9.5.3	Design of a flexure mechanism for an active cardiac stabiliser	250
9.5.4	Step 1: selection of the 3-US parallel manipulator . . .	250
9.5.5	Step 2: singularity analysis for different actuation modes	252
9.5.6	Step 3: selection of an actuation mode	258
9.5.7	Step 4: design of the flexure mechanism	258
9.5.8	Performance of the flexure mechanism	260
9.6	Selection of an actuation mechanism	261
9.7	Integration of the three mechanisms in two planes	262
9.8	Conclusion	264
Afterword		267
<i>Simon Henein</i>		
Bibliography		269
Index		281

Introduction

Since the early 20th Century, miniaturisation has been one of the major themes of technological development. Miniaturisation is an efficient way to increase the performance of technological systems and microtechnology devices such as mobile phones, pacemakers and auditory prosthetics have rapidly decreased in size. The same is true for their components (integrated circuits, optoelectronic components, microsystems, etc.) requiring continually improving production methods for their manufacture.¹ This trend is accelerating, so it is essential to adapt instrumentation and tools allowing perception and intervention at the micrometre or even nanometre scale.² When the modification of existing tools no longer addresses the needs of miniaturisation, it becomes necessary to invent new ones.

High precision robotics is one class of tools allowing us to work on matter at the sub-micron scale.³ They allow us to carry out manipulation, machining and assembly tasks, generally in an automated fashion far surpassing human manual capacity, which, at present, cannot be realised by any other means. These robots have evolved from the first industrial robots where the mechanical structure, actuators, sensors and control of the robots was adapted for high precision tasks. In the case of mechanical structures, this adaptation led to improvement of plain and rolling bearings used in articulated robots. However, this progression has attained a practical limit of precision for physical reasons such as the presence of friction, the weak rigidity of small bearing components, as well as manufacturing tolerances. These limitations are intrinsic to bearings based on friction or rolling contact between solids. The only way to surpass such

¹ Although system miniaturisation usually implies a reduction in the number of components by maximising the functionality of a minimal number of components, systems necessarily maintain an interface with the macroscopic world, be it electrical, magnetic, optical or mechanical. Robotics is an indispensable tool for the realisation of these interfaces, often the Achilles heel of microsystems.

² The nanometre (10^{-9} metres) is a thousandth of a micrometre, equivalently, a millionth of a millimetre.

³ Silicon technology and biotechnology are examples of non-robotic methods applying at the sub-micron world.

limits is to radically change the physical principle underlying such bearings and use other types which are compatible with the increased precision of robotics, not by a few percent but by orders of magnitude. For example, this is the case for contactless bearings such as magnetic, air or hydrostatic bearings, as well as articulated flexure bearings (Fig. 1.1),⁴ the subject of this book. Flexure bearings are based on the physical principle of the elasticity of matter where precision is not limited as in contact between solids.

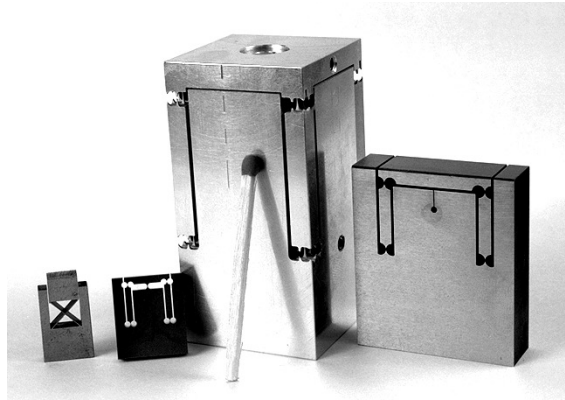


Figure 1.1 Example of monolithic electroeroded flexures.

1.1 Flexure bearing importance

In order to show their importance, flexure bearings will be compared to other bearings: plain, rolling, magnetic, hydrostatic, hydrodynamics and air.

1.1.1 Plain and rolling bearing comparison

Flexure bearing advantages

Absence of friction: Rolling or sliding contact between solids inevitably produces friction which is generally harmful to the linkage. It dissipates energy, producing heat and mechanical hysteresis. This friction depends in a highly non-linear way on the relative speed between the bodies resulting, at low speed, in a stick & slip motion which limits the movement resolution. Moreover, it is the reason for wear of contact parts. The use of rolling bearings for small amplitude displacements not producing complete rotations of the rolling com-

⁴ Unless otherwise indicated, the figures and photographs are the author's.

ponents leads to *fretting*⁵ which reduces bearing longevity by accelerating their wear and corrosion.

Flexible linkages, however, do not suffer from any solid or rolling friction. The only remaining friction is internal material friction⁶ produced elastically; it is virtually negligible.

Absence of wear: Wear of plain and rolling bearings reduces their precision by modifying their geometry and increasing play. Moreover, it is the principal factor limiting longevity.

Flexure bearing are immune from all wear. Their longevity is limited only by the material fatigue⁷ and its possible corrosion.

Absence of seizing: Seizing is a severe form of adhesive wear between frictional surfaces, binding or welding them, thereby blocking bearing function. The presence of dust or impurities can lead to seizing.

Flexure bearings eliminate the risk of seizing, conferring them great reliability, even in dirty environments.

Absence of lubrication: Plain and rolling bearings generally require lubrication in order to minimise friction and wear. Maintaining adequate lubrication during the entire lifespan of a mechanism requires regular maintenance. Moreover, lubricants can hardly be used in clean rooms and in partial vacuum (microscopes, satellites), as they are a source of pollution.

Flexure bearings do not require lubrication, do not release any polluting particles and do not require maintenance.

Large transverse rigidity: It is absolutely necessary to have a very rigid mechanical structure in order to produce precision displacements. Rolling bearings exhibit low rigidity unless they are pre-constrained (Hertzian pressure of a

⁵ Fretting is a type of wear produced by travel insufficient to remove friction waste products from the friction site. There is then a fine powder between the contact surfaces which accelerates wear by making it abrasive. Often, this powder reacts with air by oxidation exacerbating surface deterioration, one then speaks of *fretting-corrosion*.

⁶ Internal material friction is generally defined as the inverse of the quality factor $Q^{-1} = \tan \delta$ of a resonator made from this material (δ is the phase shift between the alternative constraint applied to the resonator and the observed deformation) (Schaller and Benoit, 1979). For steel, it is typically of order 10^{-4} to 10^{-3} (Moore, 1975), which is quite negligible compared to solid friction. The origin of interior friction are movement of dislocations, internal flaws, precipitates, motion of Bloch walls and the thermoelastic effect. Internal friction is therefore of a completely different nature than solid friction. Indeed, it is possible to use materials with high internal friction so as to improve the dynamic performance of flexible structures by dampening undesirable parasitic vibration.

⁷ As we show in the theoretical and experimental sections, careful dimensioning almost guarantees longevity with respect to fatigue.

rolling body on a rolling surface), and this increases as the rolling elements decrease in diameter.

Transverse rigidity of flexure bearings can be extremely high if the latter are well designed. The smaller the dimensions, the greater advantage to flexure bearings in terms of rigidity.

Absence of play: When plain and rolling bearings are not pre-constrained, mechanical play occurs, resulting in a number of inconveniences. Bearing play reduces mechanical structure precision in two ways. From the static point of view, it modifies the kinematics of articulated structures in a generally unpredictable way. From the dynamic point of view, it reduces the natural vibration frequencies of structures, making them less precise and susceptible to *float*⁸ which leads to harmful shock. When it is too bothersome, play can be checked by mechanical pre-constraint, but this complicates the mechanism. Flexure bearings do not have play, by design.

Monolithic components: Plain and rolling bearings are made of several mechanically assembled components. These assemblies generally increase congestion and fabrication tolerances decrease the precision of their construction. Flexure bearings can be made monolithically, rendering them very compact and precise while avoiding delicate and expensive assembly of small components.⁹ Flexure rigidity of beams being inversely proportional to the cube of span, compact construction yields a significant increase in structural rigidity.

Flexure bearing drawbacks

Limited range of motion: The range of motion of plain and rolling bearings is, in principle, limited only by the size of its component parts.

This is not the case for flexure bearings where range of motion is bounded by the elastic limit of matter. Overly large displacements of flexible parts produce constraints which can deform plastically or rupture articulations. This limits flexure bearings to small amplitude applications. For this reason, care has been taken to describe a number of conceptual principles which maximise range of motion.

Restoring force: Rigidity of flexure bearings along their degrees of freedom (natural rigidity) cannot generally be brought to zero, as should be the case for ideal linkages. During articulation deformation, a restoring force arises, which tends to bring the bearings back to their non-deformed state. In certain cases,

⁸ One says that a machine component experiences *float* when it loses contact with the component it is supposed to lead.

⁹ Let us mention that certain authors refer to this monolithic conception as *Design For No Assembly paradigm* (DFNA) (Ananthasuresh and Kota, 1995; Kota et al., 1999).

this restoring force varies with deformation amplitude and can be a hindrance: For example, a portion of actuator force is used to deform the elastic structure, which reduces the useful force. In other cases, it can be useful: restoring force can, for example, be used to pre-constrain a mechanism and eliminate play.

Geometrically complex models: The ideal elementary linkages (sliding connection, pivot, support plane, ball joint, etc.) have geometrical models with a simple mathematical description (translation along a straight line, rotation around a fixed point, etc.). Plain and rolling bearings reproduce these ideal motions relatively faithfully.

On the other hand, flexure bearings generally follow more complex motion (curvilinear translation, instantaneous rotation around a moving centre, etc.). This complicates the geometric modelling of flexible structures. Nevertheless, it should be noted that these trajectories are repeated with great precision. The problem is one of modelling, not of functionality.

Conclusion

Flexure bearings are advantageous when:

- There is a limited range of motion.
- Movement precision must be high.
- Friction, play and wear are troublesome.
- Lubrication is bothersome or impossible.
- Reliability must be very high.
- Restoring force is not a hindrance.
- Used in mechanisms for clean rooms or vacuum.
- Lifespan must be very long.
- No maintenance is expected.

1.1.2 Contactless bearings comparison

Magnetic bearings

Magnetic bearings support a rigid body through a magnetic field, which means there is no mechanical contact. This has a large number of advantages (no solid friction, wear, lubrication, etc.). On the other hand, there is the inconvenience of requiring electromagnets, sensors and an active regulatory loop. This explains their late appearance in the historical development of bearings. (Bleuler, 1984) and (Schweitzer et al., 1994) identify the introduction of the first magnetic bearing in the first half of the 20th Century (Kemper, 1937; Beams et al., 1946) and wider utilisation in the 1970s (Sabnis et al., 1975). Thus, it is the complexity of set-up and functioning of magnetic bearings which makes them unsuited for the realisation of articulated structures with several degrees of freedom, such as those used in high precision robotics.

Hydrostatic and hydrodynamic bearings

In hydrostatic and hydrodynamic bearings, a fluid lubrication film is used to separate bodies in relative friction. The film must be sufficiently thick so that surface asperities do not touch. Solid friction is thus replaced by a smaller liquid friction which, in addition, does not induce surface wear. In order for the film to sustain bearing load, it must be pressurised. In hydrodynamic bearings, the lubricating film is formed by relative movement of components via fluid viscosity. These bearings have the disadvantage of working through fluid friction only when speed is sufficiently high. They are therefore unsuited to articulate robotic structures. In order to address this issue, hydrostatic bearings use a pump injecting pressurised lubricant into pockets, allowing film formation even when stopped. However, this solution has the drawback of requiring a pump, recovery circuit and lubricant filtration. Moreover, it has a high energy consumption.

Although hydrostatic bearings have been known since the end of the 19th century (Girard, 1865; Thurston, 1885), they have only been used in machine-tools since the 1950s (Dowson, 1998). The complexity and cost of their set-up makes them unsuitable for articulated robot structures with many degrees of freedom, except in the particular cases where load is very high or where the coefficient of friction of start-up must be as low as possible.

Air bearings

Air bearings are based on the same principle as hydrostatic bearings, but use gas (air) as lubrication instead of liquid. This eliminates the need for a recovery circuit since air can be released into the atmosphere. Nevertheless, these bearings remain complex and costly since they require an air compressor and a supply circuit. Air bearings have been in existence since the 19th century (Willis, 1828; Hirn, 1854). The first applications date from the beginning of the 20th century but the most important advances were in World War II for military and nuclear applications.

Conclusion

By comparison with contactless bearings, flexure bearings are much easier and less costly to set-up: They do not require active control or an energy source.

1.2 Flexible element classification

We have chosen to classify flexible elements into three categories of increasing complexity:

Elementary flexible articulations: This category includes the most simple flexible elements such as beams, torsion bars and membranes. By themselves, elementary flexible articulations do not generally allow a one degree of liberty mechanical link. These articulations do not generally have a close equivalent among the standard mechanical links.¹⁰

Flexure bearings: The flexible elements in this category are composed of a combination of elementary articulations and of rigid segments linked between them. Flexure bearings are the homologue of plain or rolling bearings of classical articulated structures¹¹. They generally have close analogues among standard mechanical links.

Articulated structures with flexure bearings: The flexible elements of this last category, that we simply call *flexible structures*, are made up of a combination of flexure bearings and rigid segments. These structures are homologues of classical articulated structures. Relatively complex, they can have more degrees of freedom (generally more than 6). Certain rigid segments in these structures are designed to be moved by actuators. One of the segments is the structure's fixed base (*base block*) and the other the terminal mobile element (*mobile block*).

1.3 Book goals and structure

The principal objective of this book is to establish a conceptual framework for the design of flexure based high precision articulated structures. Its goal is to provide a *conceptual tool*, an *analysis instrument* and *key reference examples* to engineers and scientists working in precision engineering. The book is composed of three parts: Part I presents the *basic flexures* including a catalogue of flexure bearings, design principles, analysis as well as dimensional laws expressed in formula and scaling laws. This part provides the designer with the basic building blocs. Part II presents *Flexure mechanisms* with simple approaches for the kinematic analysis and synthesis of multi-degrees-of-freedom mechanisms, a well as principles for the minimisation of the natural stiffnesses and the maximisation of the transverse stiffnesses. It also provides more advanced kinematic approaches for the design of multi-degrees-of-freedom

¹⁰ We denote by *standard mechanical link* the *lower pairs* as defined by (Reuleaux, 1875) (see also (Hunt, 1978) or (Waldron and Kinzel, 1999)), that is, pivot joint, sliding connection, helical sliding connection, sliding pivot, support plane, ball joint, etc.).

¹¹ As opposed to *articulated structures with flexure bearings*, by *classical articulated structure* we denote traditional robot skeletons composed of rigid discrete segments linked together by plain or rolling bearings.

articulated structures based on a set of advanced modules which can be associated in parallel or serial kinematic arrangements. This second part of the book also presents two concrete examples. The first one consists of two architectures for a long stroke rectilinear flexure mechanism, which is a very common challenge. The second one is a planar flexure mechanism with out-of-plan functions, which is another typical issue for flexure mechanisms. This part of the book shows how the concepts presented in the first part are applied for advanced mechanism design.

This book aims for a technological leap in articulated structures which will release high precision engineering from some of the impasses in which it finds itself today and open the way to a very wide spectrum of applications presently out of reach.

This book is a tool principally addressing the design phase of high precision mechanisms and robots which goes from establishing specifications to the development of the chosen solution. It also constitutes a basic tool for the optimisation phase which, since it is tied to specific applications, is harder to generalise and requires the utilisation of other tools, for example, numerical modal analysis or vibration mechanics.

1.4 Topic delimitation

Modelling: This book is limited to the study of the *static* behaviour of flexure bearing structures. In particular, study is concentrated on the rigidity, admissible range of motion, admissible load as well as kinematics of these structures. Dynamic behaviour as well as vibratory phenomena (Del Pedro and Pahun, 1989) will not be considered.

The goal of this modelling is to obtain a conception and dimensioning tool which is quick and easy to use. This sometimes forces us to favour simplicity over exactitude¹². For this reason, we limit our study of flexible articulations to the *small deformation hypothesis*¹³.

Materials: We limit ourselves to *metal alloys* currently used in mechanics. Thus, we will not refer to the possibility of using polymers (Domininghaus, 1993), composites (Hull and Clyne, 1996), ceramics or shape memory alloys (Bellouard, 2000).

¹² When we appeal to numerous simplifications we will attempt to quantify the error induced by the simplifying hypotheses.

¹³ The small deformation hypothesis stipulates that structure deformation is sufficiently small when compared to structure dimension that its effect with respect to load can be neglected.

Fabrication methods: The study concentrates on *wire-cut electrical discharge machining* which today is one of the best suited fabrication method for flexible articulations. The possibility of manufacturing by electrical discharge, milling or turning are also mentioned. On the other hand, other machining methods such as laser, water jet cutting or injection moulding will not be addressed.

Type of elementary articulation: We primarily study flexure bearings composed of elementary articulations consisting of *beams under flexion or torsion*. Other elementary articulations such as flexible membranes or bellows will not be considered.

Part I

Basic flexures

Underlying theory

This chapter establishes the underlying theory used to calculate the stiffnesses and deflections of flexure joint elements (Chapter 3) and flexible bearings (Chapters 4 and 5). We use the fundamental propositions of *mechanics of structures* and regard flexure joint elements as beams subject to simple bending or torsion. To calculate allowable deflections, we use the maximum distortion strain energy as the yield criterion. We take into account the phenomenon of fatigue damage when determining the allowable stress in the material. A correction factor must be applied to the results obtained from standard fatigue tests if these are to be used for flexure joints. This correction factor can be determined by carrying out fatigue tests on special specimens taken directly from flexure joints.

2.1 Basic assumptions

The formulas and graphs presented in this work have been produced on the basis of the *mechanics of structures theory*¹. This theory is based on three assumptions regarding the composition of solid material: its continuity, homogeneity and isotropy; and two assumptions relating to the type of deflections: their proportionality with the stresses applied and their very low magnitude in relation to the dimensions of the solid object. To calculate the deflection of a beam subject to bending, we introduce an additional simplifying assumption: we consider that the curvature of the beam is equal to the second derivative of its deflection. This allows us to use the equation

$$y''(x) \simeq \frac{1}{\rho(x)} = \frac{-M(x)}{EI(x)} + \left\{ \frac{\eta}{GA(x)} \frac{dF(x)}{dx} \right\} \quad (2.1)$$

¹ *Mechanics of structures* can also be termed *strength of materials* or *mechanics of materials*, depending on the author. The following works have been consulted in preparing this chapter: (Del Pedro and Gmür, 2001; Del Pedro, 1985; Massonnet and Cescotto, 1994; Gere and Timoshenko, 1990).

where y'' is the second derivative of the beam's deflection, ρ its radius of curvature, M the bending moment, E the Young's modulus, I the moment of inertia of the beam cross section, F the shear force, η a shape factor², G the shear modulus and A the beam cross-sectional area. The term in braces represents the effect of the shear force, which we will disregard unless indicated otherwise.

The results presented here are only correct insofar as the foregoing assumptions hold true.

We shall consider that the first three assumptions do apply, provided that the dimensions of the flexible parts of the flexure joints remain greater than a few dozen microns³.

Tensile testing is used to verify that the assumption of proportionality is valid. This assumption generally holds true for the elastic alloys used to manufacture flexure joints.

The assumption about small deflections is the one with the greatest risk of not holding true for flexure joints. Given that we aim to maximize the travel of flexure joints, their deflections are often substantial. However, due to the complexity of the problem, we will not consider the effect of substantial deflections in this work.

The effect of shear force on deflection is often negligible, but we will take it into account in cases where this is not true (Sect. 3.5).

2.2 Allowable deflections

The travel of a flexure joint is the largest deflection (rotational or translational) that it can withstand without fracturing or yielding. First, the theoretical model used to calculate the travel applies a *criterion for plastic deformation* (Collins, 1993), enabling us to determine which critical stress state causes the joint to yield (Sect. 2.2.1). Second, the model introduces the phenomenon of *fatigue damage* (Pomey and Lieurade, 1982; Brand, 1984; Duprat, 1997; Spinnler, 1997a), since the magnitude of the stresses required to cause failure decreases as the number of load cycles increases (Sect. 2.2.2). Third, the model uses a *safety factor* to take uncertainty about the fatigue limit into account in addition to uncertainties arising from material imperfections and the simplifying

² This factor is the reciprocal of Timoshenko's shear coefficient. For rectangular cross sections $\eta = 6/5$.

³ If the dimensions of the flexible zones become too close to the grain size of the material, there is a risk that the assumptions of continuity, homogeneity and isotropy will no longer fully apply.

assumptions of the model used to calculate the stresses in the flexure joint (Sect. 2.2.4).

2.2.1 Yield criterion

To define the critical stress state that initiates plastic deformation of the flexure joint, we apply the *maximum distortion strain energy criterion*⁴, which stipulates that the energy supplied to increase or decrease the initial volume plays no part in disrupting the elastic equilibrium; only the energy supplied to deform the volume enters into the equation.

Bending

To calculate the deflections of some of the flexure joints we focus on in this work, we examine individual beams subject to bending. Generally, we neglect the effect of shear force. Therefore, the stress state in the material remains uniaxial, i.e., the elements of the material constituting the beam are subject to tensile-compressive loads. For this stress state, plastic deformation will occur when the tensile-compressive stress reaches a critical value σ_{lim} that can be determined by tensile testing.

In most of the cases dealt with in this work, we are concerned with prismatic beams with rectangular cross sections. Let h be the height of the beam and b its width. The normal stress sustained by an element of material located at a distance y from the beam's neutral axis, in a section of the beam where the bending moment is M , is given by the classical formula:

$$\sigma = \frac{My}{I} \quad \text{where} \quad I = \frac{bh^3}{12}. \quad (2.2)$$

The normal stresses are thus at a maximum in the outermost fibers of the beam, where $y = \pm h/2$. If the maximum allowable stress⁵ in the material is σ_{adm} , then the maximum allowable moment is:

$$M_{adm} = \frac{bh^2\sigma_{adm}}{6}. \quad (2.3)$$

This formula will be used throughout the following chapters.

⁴ The maximum distortion strain energy criterion is also known as the *Von Mises-Hencky yield criterion* or the *critical distortional energy criterion*.

⁵ The concept of *allowable stress* is defined in more detail in Section 2.2.4.

Torsion

To calculate the deflections of other flexure joints, we examine beams subject to pure torsion. In this case, the maximum distortion strain energy criterion shows that yielding occurs when shear stress reaches a critical value $\tau_{lim} = \sigma_{lim}/\sqrt{3}$.

NOTE: Another frequently used criterion for plastic deformation is the *maximum shear stress criterion*⁶. For beams subject to pure bending, this criterion states that yielding will occur when normal stress in the outermost fibers reaches its critical value σ_{lim} . This result is identical to the result obtained with the maximum distortion strain energy criterion. According to the maximum shear stress criterion, yielding will occur in beams subject to torsion when shear stress τ reaches a value $\tau_{lim} = \sigma_{lim}/2$. This result thus differs slightly from the value given by the energy criterion that we have chosen, where $\tau_{lim} = \sigma_{lim}/\sqrt{3}$. For steels, it would seem that the latter value is the most realistic value (Spinnler, 1997a).

2.2.2 Fatigue damage

We have just seen how the yield criterion is used to predict the occurrence of plastic deformation in a beam subject to bending or torsion if the critical stress σ_{lim} that has caused yielding in a tensile test specimen is known. It is now a question of determining the value of σ_{lim} more precisely, knowing that the fatigue damage phenomenon makes this value vary as a function of the number of load cycles. To do this, *fatigue tests* are frequently performed on standardised specimens. These tests apply cyclic stresses analogous to those that occur in the flexure joint to be dimensioned. Once the critical stress value for the specimens is known, a correction factor c , which takes the differences between the fatigue test conditions and the practical working conditions of the flexure joint into account, is used to determine the critical stress σ_{lim} below which the joint can operate. Materials suppliers often provide data on fatigue limits, which obviates the tedium of carrying out fatigue testing.

Fatigue testing

DEFINITIONS: The *fatigue limit* σ_D is the maximum stress value for which no failure is observed after an *infinite number of cycles*. The *endurance limit* $\sigma_D(N)$ is defined for our purposes as the maximum stress value for which 50% of failures is observed after a *finite number N of cycles*.

⁶ The maximum shear stress criterion is also known as the *Tresca criterion* or the *maximum tangential stress criterion*.

NOTE: For steels and titanium alloys, the fatigue limit σ_D is approximately equal to the endurance limit for 10^7 cycles $\sigma_D(10^7)$. Generally, this is not the case for other alloys, such as those of aluminium or copper, some of which have no fatigue limit at all.

LOADING METHODS: Fatigue tests are generally carried out using one of the following five loading methods: axial forces (tension or compression), plane bending, rotary bending, torsion or combined stresses. The loading methods are also differentiated by their stress ratio⁷ R . The typical values of this parameter that we are concerned with are: $R = 0$ for repeated stress and $R = -1$ for purely alternating stress.

To be able to determine σ_{lim} as precisely as possible based on the fatigue test results, it is in our interest that the type of loading used in the tests be as similar as possible to the loading sustained by the flexure joint in practice. For example, for a flexure joint with flexible parts that are subject to bending in both directions about its nominal position, we use the plane bending fatigue limit of the material subject to purely alternating stress. If the material supplier cannot provide this value, the fatigue limit for another type of loading may be used if an appropriate correction factor is applied. The following general rules apply when this correction factor is selected:

- The fatigue limit under bending is greater than the fatigue limit under tension, which in turn is greater than the fatigue limit under torsion.
- The fatigue limit under repeated stresses is greater than the fatigue limit under alternating stresses.

2.2.3 Correction factor

Several factors affect the fatigue resistance of the flexure joint material, which may deviate considerably from the fatigue resistance of standard test specimens. These are the main parameters:

- The condition of the surface resulting from manufacture and any treatment of the component: this includes surface roughness, the structural state of the material's surface layers (due to cold forming or thermal phenomena) and changes to the stress state (residual stresses).
- The size of the components: as size decreases, the probability of faults being present also decreases and the support of the layers increases (*scale*

⁷ If the stress varies over time between a minimum value σ_{min} and a maximum value σ_{max} , the stress ratio $R = \sigma_{min}/\sigma_{max}$. NOTE: Stresses are considered positive if the material is subject to tension, and negative if it is subject to compression.

effect)⁸. These two phenomena tend to reduce the fatigue limit for larger components.

- The mean stress: the level of static stress onto which the cyclic stress is superposed affects behaviour under fatigue.
- The temperature: the fatigue limit decreases as the temperature increases.
- The notch effect⁹: the cause of stress concentrations that reduce the fatigue limit.
- Corrosion: corrosion pits can act like small notches that help to initiate fatigue fissures.

When all these factors are taken into account, we arrive at the *corrected fatigue limit*

$$\sigma'_D = c \times \sigma_D, \quad (2.4)$$

where c is the correction factor covering the different phenomena stated above, and potentially the factor for switching from one type of loading to another (Sect. 2.2.2).

Uncertainties

Fatigue testing always involves a certain amount of randomness¹⁰. In a series of apparently identical tests, different results for the fatigue limit will be found, approximately following a Gaussian distribution about a mean value. There is therefore always some uncertainty about the values for σ_D .

Additionally, there is inevitably some uncertainty about the value of correction factor c , as it is impossible to accurately quantify the effects of the different phenomena at work. Therefore, the uncertainties about the values of the corrected fatigue limits σ'_D are always greater than the uncertainties about the original values of σ_D .

Determination of σ_{lim}

Critical stress σ_{lim} is simply the value of the corrected endurance limit $\sigma'_D(N)$ corresponding to the number N of cycles that the flexure joint must bear. The uncertainty about $\sigma'_D(N)$ is thus fully contained in σ_{lim} .

⁸ **Scale effect:** When a mechanical component is subject to bending or torsion, a stress gradient is produced in its surface layers. The smaller the component dimensions, the steeper the stress gradient for the same stress at the surface. For a given size of grain and faults in the material, this increased stress gradient means that the more lightly stressed layers are closer to the more heavily stressed layers, therefore better supporting them.

⁹ The term **notch** is used here to denote the presence of a discontinuity in the component geometry that tends to cause mechanical stress concentrations.

¹⁰ The scatter in fatigue test results cannot be reduced beyond a certain limit, due to the physical aspects of the phenomenon: inclusions in the material, heterogeneity of the metallurgical structure, etc.

Determining the value of critical stress σ_{lim} on the basis of standard fatigue test results inevitably creates a lot of uncertainty about this value.

2.2.4 Safety factor

Failure occurs when the actual stress within the material reaches the critical stress value $\sigma = \sigma_{lim}$. To prevent this from occurring, it is therefore necessary to guarantee that the stresses in the flexure joint remain below this critical value: $\sigma < \sigma_{lim}$. We have just seen that uncertainty about the value of σ_{lim} inevitably remains. In addition, there is uncertainty about the value of σ due to material imperfections and the simplifying assumptions of the model used to calculate the stresses in the flexure joint based on its deflection. These uncertainties about the terms on both sides of the inequality mean that a safety factor S must be introduced, which will guarantee that this inequality is always maintained. We therefore select an allowable stress σ_{adm} that is less than σ_{lim} :

$$\sigma_{adm} = \frac{\sigma_{lim}}{S}. \quad (2.5)$$

We typically choose a value of S between 1.5 and 3, in accordance with the desired *margin of safety*¹¹. This is a range between the greatest stress σ that could arise in the flexure joint (taking into account the uncertainties) and the lowest critical stress conceivable (taking into account the uncertainties) (Fig. 2.1, 2.2 and 2.3).

2.2.5 Summary of allowable deflections

For flexure joints with flexible elements that are subject to bending, deflection is the deformation that gives rise to the maximum tensile-compressive stresses σ equal to the allowable stress σ_{adm} for the material.

For flexure joints with flexible elements that are subject to torsion, deflection is the deformation that gives rise to the maximum shear stresses τ equal to $\sigma_{adm}/\sqrt{3}$.

Allowable stress σ_{adm} is determined on the basis of the corrected fatigue limit or endurance limit σ'_D for the number N of load cycles by applying a safety factor S .

The corrected fatigue limit σ'_D is determined on the basis of the fatigue limit σ_D by taking into account factors affecting the behaviour of the actual component subject to fatigue.

¹¹ In reality, the use of a generous margin of safety does not totally exclude the possibility of a flexure joint failing. If the statistical distributions of σ_{lim} and σ are Gaussian, the concepts of safety factor and margin of safety can only be interpreted via a probabilistic approach. Consequently, a margin of safety provides information about the *probability of flexure joint failure*, a probability that decreases as the margin increases, but which can never be reduced to 0. In the interests of simplicity, we will not take this probabilistic approach in this work.

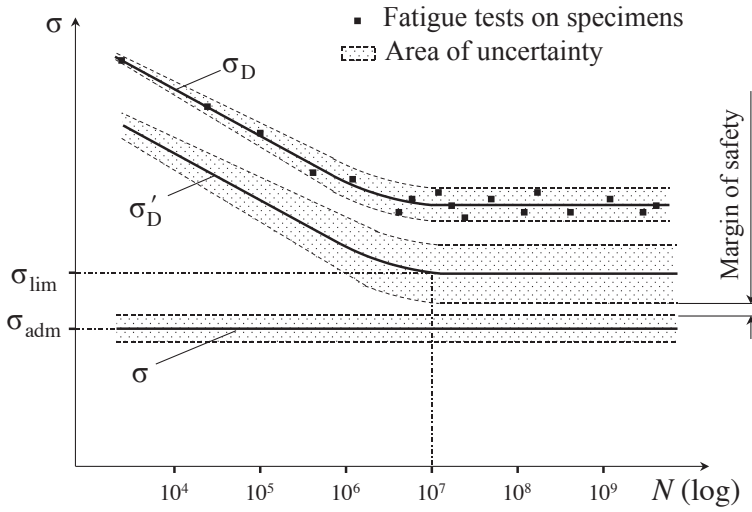


Figure 2.1 Determination of σ_{adm} on the basis of conventional fatigue tests (black squares). Example of a material that has a fatigue limit of $\sigma_D = \sigma_D(10^7)$ (like most steels and titanium alloys) and which is to be used to manufacture a flexure joint that will withstand an infinite number of load cycles. The random nature of fatigue failure gives rise to an area of uncertainty (dotted area) around the Wöhler curve (line σ_D). Correction factor c gives us the corrected Wöhler curve (line σ'_D) for the flexure joint: $\sigma'_D = c \times \sigma_D$. The uncertainty about c gives rise to another area of uncertainty about σ'_D (dotted area) that is greater than the uncertainty about σ_D . The stresses in the joint (line σ) are estimated by means of a model that can only be approximate and therefore have their own area of uncertainty (dotted area). The choice of safety factor $S = \sigma'_D / \sigma_{adm}$ is made such that there is still a margin of safety between the areas of uncertainty for σ'_D and σ when $\sigma = \sigma_{adm}$.

The fatigue limit σ_D is given by standard fatigue tests, the results of which may often be obtained from the material suppliers:

- In order for the flexure joint to withstand at least one to-and-fro movement over its full deflection, allowable stress must be lower than the ultimate tensile strength of the material: $\sigma_{adm} < R_m$.
- In order for the flexure joint to withstand several to-and-fro movements over its full deflection without undergoing plastic deformation, allowable stress must be lower than the elastic limit of the material: $\sigma_{adm} < R_e$.
- In order for the flexure joint to withstand N (several hundred, thousand or million) to-and-fro movements over its full deflection, allowable stress must be lower than the corrected endurance limit for the material for N cycles, taking into account the safety factor: $\sigma_{adm} < \sigma'_D(N)/S$ where $\sigma'_D(N) = c \times \sigma_D(N)$.

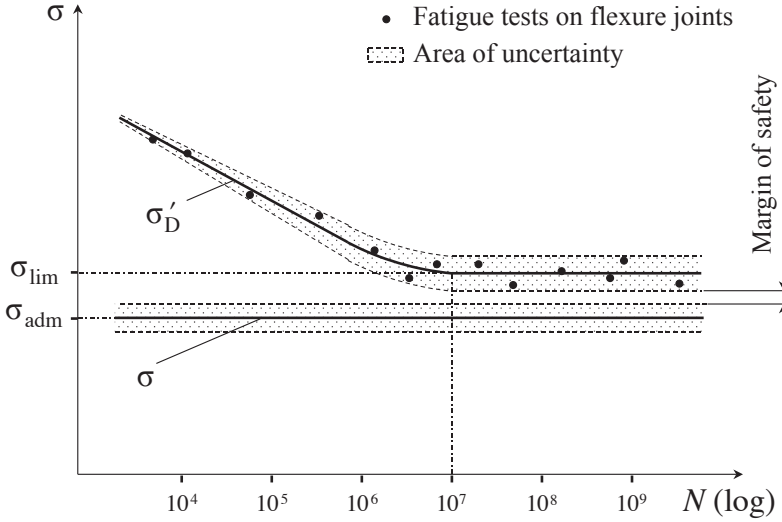


Figure 2.2 Determination of σ_{adm} on the basis of fatigue tests carried out directly on a series of flexure joints (black dots). The random nature of fatigue failure gives rise to an area of uncertainty (dotted area) around the Wöhler curve (line σ'_D). However, this uncertainty remains lower than the uncertainty for the curve for σ'_D in Figure 2.1, since here there is no need to apply a correction factor. This reduced uncertainty allows us to select a smaller safety factor without reducing the margin of safety. The value of σ_{adm} is therefore higher and gives a greater deflection without increasing the risk of failure.

- In order for the flexure joint to withstand an infinite number of to-and-fro movements without failure, allowable stress must be lower than the fatigue limit for the material, taking into account the safety factor: $\sigma_{adm} < \sigma'_D / S$ where $\sigma'_D = c \times \sigma_D$.

Through this theoretical approach to the deflections of flexure joints, we see that the main difficulty lies in determining the allowable stress σ_{adm} for the material. Among the steps that lead us from the fatigue limit σ_D provided by the material manufacturers to σ_{adm} , the step that causes the most uncertainty about the value of σ_{adm} is the consideration of correction factor c . For this reason, we have decided to determine this factor experimentally for the materials that we use most frequently. This is dealt with in (Henein, 2001), where we pay particular attention to the effect of the surface roughness resulting from the manufacturing process on correction factor c .

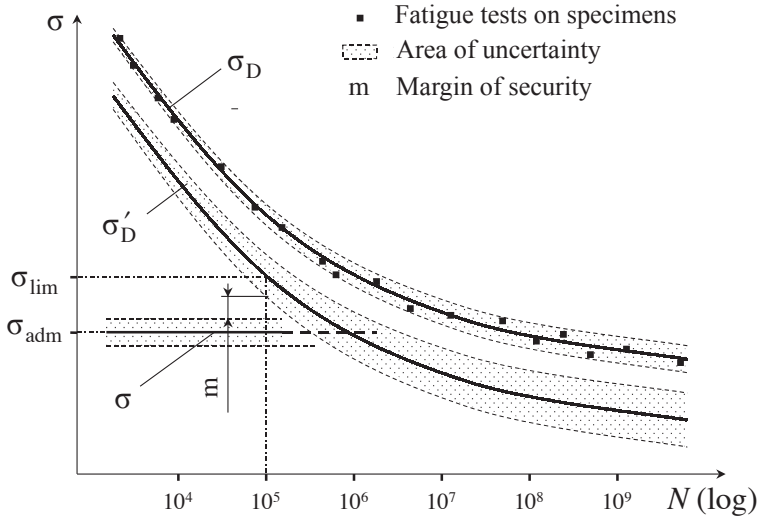


Figure 2.3 Determination of σ_{adm} on the basis of conventional fatigue tests (black squares). Example of a material that has no fatigue limit (like most aluminium and copper alloys) and which is to be used to manufacture a flexure joint that will withstand at least 10^5 load cycles.

2.3 Stiffnesses

2.3.1 Definitions

Consider an elastic body to which a force P is applied in such a way that the various geometric and load conditions cause the point of application of P to be displaced along its line of action. Let f be the length of this displacement. Force is related to displacement by the function $P = F(f)$, known as the *force-deformation characteristic*. **Translational stiffness**¹² is by definition $k = \frac{dF}{df}$. In practice, for most of the structures that we study, we make the assumption that the force-deformation characteristic is *linear*, so stiffness k is a constant that is independent of deformation f . We therefore denote this translational stiffness by K (capital letter K). The unit for translational stiffness is N/m.

Consider an elastic body to which a couple C is applied at the center of inertia of one of its sections, in such a way that the various geometric and load conditions cause a rotation of this section about an axis parallel to that of C . Let

¹² In the literature, the parameter that we term *translational stiffness* (N/m) is generally known simply as *stiffness*. We have chosen to add the adjective *translational* throughout in order to distinguish it from *angular stiffness* (Nm/rad).

α be the angle of rotation of this section. The moment is related to the rotation by the function $C = M(\alpha)$, known as the *moment-deformation characteristic*. **Angular stiffness** or *rotational stiffness* is by definition $k_\alpha = \frac{dM}{d\alpha}$. In practice, for most of the structures that we study, we make the assumption that the moment-deformation characteristic is *linear*, so stiffness k_α is a constant that is independent of rotation α . We denote rotational stiffness by K_α (capital letter K). The unit for rotational stiffness is Nm/rad.

2.3.2 Stiffnesses of flexure joints

A solid body, if not joined to anything, possesses 6 degrees of freedom (DOFs). Connecting this body to a fixed element by means of a mechanical bearing blocks some of these DOFs (constrained DOFs) while leaving others unconstrained (compliant DOFs) (Fig. 2.4).

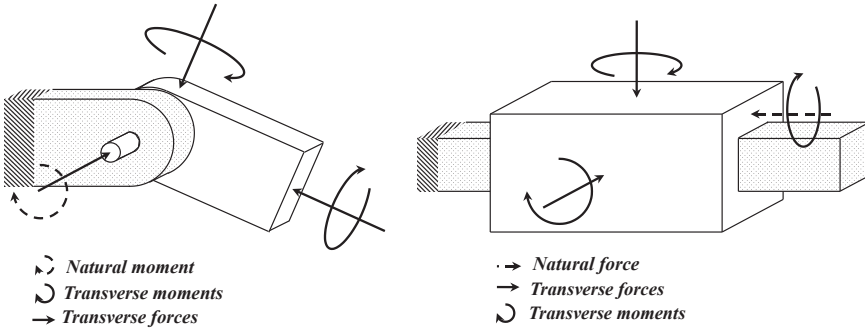


Figure 2.4 Natural and transverse stiffnesses of a pivot and a prismatic bearing.

Forces or moments that act on a bearing in accordance with one of its compliant DOFs are termed *natural* forces or moments. We term the stiffnesses associated with these natural forces and natural moments ***natural translational stiffness*** and ***natural angular stiffness*** respectively.

Forces or moments that act on a bearing in accordance with its constrained DOFs are termed *transverse* forces or moments. We term the stiffnesses associated with these transverse forces and transverse moments ***transverse translational stiffness*** and ***transverse angular stiffness*** respectively.

2.3.3 Generalised stiffnesses

Strictly speaking, translational stiffness is the force required to produce unit translational displacement (unit N/m) and angular stiffness the moment required to produce unit rotation (unit Nm/rad). When studying flexure joints, it is equally valuable to look at rotations caused by forces, as it is to consider translational displacements caused by moments. For this reason, we introduce

the concept of ***Generalised stiffness***, this being the *Generalised force* (i.e., a force or a moment) required to produce unit *Generalised displacement* (i.e., a translational displacement or a rotation). Generalised stiffnesses can therefore have four different units: N/m, N/rad, Nm/rad and N. The Generalised stiffnesses of flexure joint elements are defined in Chapter 3 (Sect. 3.1).

Flexure joint elements

This chapter discusses *flexure joint elements* – basic flexible components that are used to articulate the rigid bodies that make up flexible bearings and flexible structures. Of the conventional types of spring, only flexible arms, leaf springs and torsion bars have sufficiently high stiffness ratios to allow them to be used as flexure joints. Apart from springs, membranes and bellows can also be used as flexure joints; however, they are not discussed here.

The generalised stiffnesses and allowable deflections of the most common flexure joint elements (leaf spring, rod, torsion bar, circular notch hinge) are calculated. In the case of the circular notch hinge, the complexity of the calculations leads us to plot graphs (Henein, 2001) and devise simplified formulas. The detailed calculation of the stiffness ratios allows us to determine the number of degrees of freedom (DOF) for each type of flexure joint: three DOFs for the leaf spring and circular notch hinge, five DOFs for the rod and one DOF for the torsion bar.

3.1 General considerations

3.1.1 Flexure joint classification

Like springs, flexure joint elements can be classified according to their *state of stress* (Fig. 3.1). The states of stress that induce **normal stresses** are *simple tension* or *compression* (annular springs, Belleville washers) and bending (flexible arms or beams, leaf springs, coil springs, helical torsion springs). The states of stress that induce **tangential stresses** are *simple torsion* (torsion bars, helical tension or compression springs) and *simple shear* (as this state of stress can never occur in a complete solid, no spring makes exclusive use of this mode of loading).

But while the role of a spring is to store energy (barrel, etc.), exert forces (preloads, fasteners, etc.), dampen shocks or vibrations (suspensions, etc.) or measure forces (load cells, dynamometers, etc.), the role of flexure joints is to form a *kinematic joint*. This difference means that only springs with *transverse stiffnesses* much greater than *natural* stiffnesses can be used (mode of loading

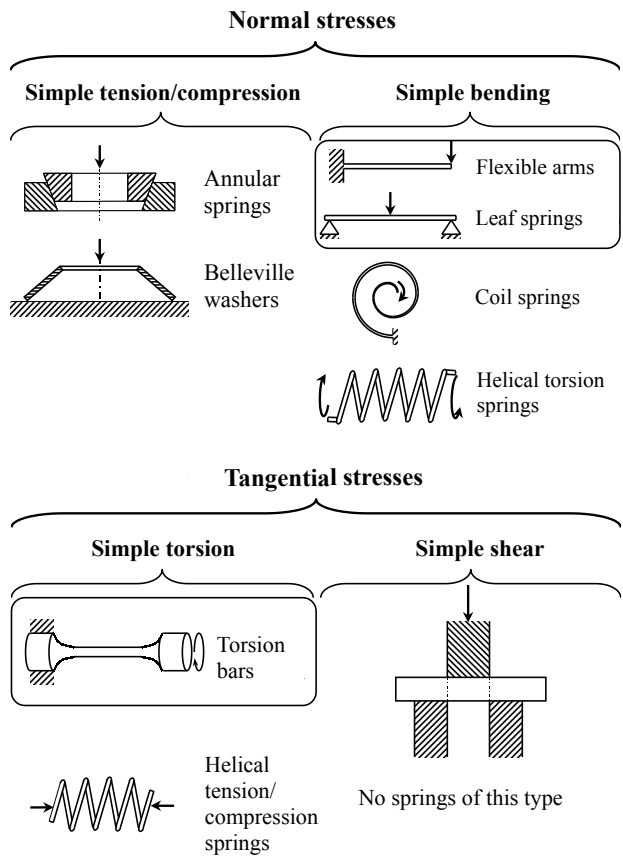


Figure 3.1 Classification of springs according to the stresses exerted on them. The springs in the boxes can serve as flexure joint elements since their transverse stiffnesses are much greater than the stiffnesses exhibited in their normal mode of loading. The other springs are not suitable for use as flexure joints due to their low stiffness ratios. (Based on (Duchemin, 1984)).

corresponding to the DOFs of the flexure joint). The practical result is that only flexible arms, leaf springs and torsion bars are the types of spring that can be used as flexure joints.

A high *stiffness ratio* is obtained, on the one hand, by exploiting the fact that, as is generally the case with any slender beam, the tensile and compressive stiffnesses are much higher than the bending and torsional stiffnesses, and, on the other, because the greater the slenderness of the cross sections of a beam (referring here to a leaf spring), the higher the stiffness ratio around the two principal axes of inertia of the cross section.

Apart from springs, the other elastic components that can serve as flexure joint elements are *membranes* and *bellows*. The state of stress in these components is generally triaxial, which makes their study complex. It is for this reason that they are discussed only briefly in this book. We classify flexure joint elements into the following categories:

- Leaf spring: joint with three DOFs (Sect. 3.2)
- Rod: joint with five DOFs (Sect. 3.3)
- Torsion bar: joint with one DOF (if designed to resist bending) (Sect. 3.4)
- Membrane: joint generally with three DOFs (not discussed in detail in this book)
- Bellows: joint with five DOFs (not discussed in detail in this book)

3.1.2 Definition of generalised stiffnesses and deflections

In this section, we define the various generalised stiffnesses¹ of the flexure joint elements calculated later in this book. For each of the modes of loading described above, we define an *allowable deflection* that corresponds to the displacement or rotation that creates normal or tangential stresses equal to the allowable stresses.

$K_{\alpha M}$ If a moment M applied to the end of a beam causes that beam to rotate through an angle α , we define $K_{\alpha M} = \frac{M}{\alpha} \left[\frac{\text{Nm}}{\text{rad}} \right]$. Allowable deflection: α_M (Fig. 3.2 a).

K_{fM} If a moment M applied to the end of a beam results in deflection f at that end, we define $K_{fM} = \frac{M}{f} \left[\text{N} \right]$. Allowable deflection: f_M (Fig. 3.2a).

$K_{\alpha P}$ If a force P applied to the end of a beam causes that beam to rotate through an angle α , we define $K_{\alpha P} = \frac{P}{\alpha} \left[\frac{\text{N}}{\text{rad}} \right]$. Allowable deflection: α_P (Fig. 3.2b).

K_{fP} If a force P applied to the end of a beam results in deflection f at that end, we define $K_{fP} = \frac{P}{f} \left[\frac{\text{N}}{\text{m}} \right]$. Allowable deflection: f_P (Fig. 3.2b).

K_{cis} Where a force P acts on a mobile block (that is infinitely stiff) attached to the end of a beam such that the rotation of that beam is zero (the block moves linearly) and if this force results in deflection f , we define² $K_{cis} = \frac{P}{f} \left[\frac{\text{N}}{\text{m}} \right]$. Allowable deflection: f_{cis} (Fig. 3.2c).

K_{trac} If a force P acts at the end of a beam, inducing tensile (or compressive) loading, and f is the resultant change in its length, we define the tensile stiffness as $K_{trac} = \frac{P}{f} \left[\frac{\text{N}}{\text{m}} \right]$. Allowable deflection: f_{trac} (Fig. 3.2d).

¹ The concept of *generalised stiffness* is defined in Section 2.3.

² We have chosen the concept K_{cis} (meaning K_{shear}), because, for this mode of loading, the central portion of the beam is loaded in simple shear.

K_{tors} If a moment M acts at the end of a beam, inducing torsional loading that rotates this end through an angle α , we define $K_{tors} = \frac{M}{\alpha} \left[\frac{\text{Nm}}{\text{rad}} \right]$. Allowable deflection: α_{tors} (Fig. 3.2e).

We can define similar terms for forces and moments acting on the beam in transverse bending and term the corresponding stiffnesses $K_{\alpha M}^t$, K_{fP}^t , $K_{\alpha P}^t$, K_{fP}^t and K_{cis}^t and the respective allowable deflections α_M^t , f_P^t , α_P^t , f_P^t and f_{cis}^t (Fig. 3.2f, g and h).

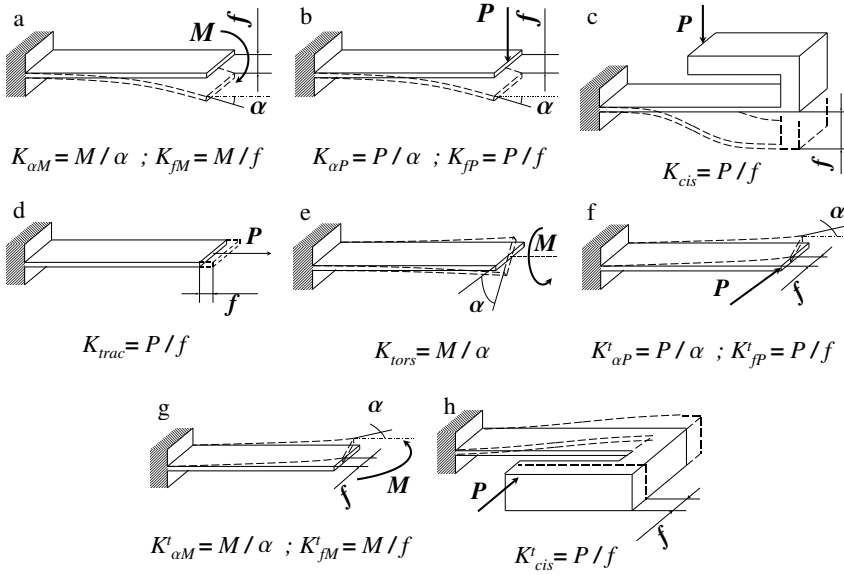


Figure 3.2 Definitions of the generalised stiffnesses of flexure joint elements.

3.2 Leaf springs

3.2.1 Definition

We define a *leaf spring* as any prismatic beam of rectangular cross section having a width b and a length l at least ten times greater than its thickness h : $b > 10h$ and $l > 10h$. The moments of inertia of the cross section are $I_x = hb^3/12$ and $I_y = bh^3/12$ and the polar moment of inertia is $I_p = (bh^3 + hb^3)/12$. We use the symbols E for the Young's modulus and G for the shear modulus of the spring material.

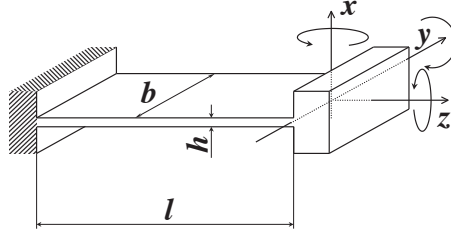


Figure 3.3 Leaf spring. Geometric parameters: l , length; b , width; h , thickness.

3.2.2 Stiffnesses

The classical formulas of theoretical structural mechanics give us (disregarding shear forces):

$$K_{\alpha M} = \frac{EI_y}{l}; K_{fM} = \frac{2EI_y}{l^2}; K_{\alpha P} = \frac{2EI_y}{l^2}; K_{fP} = \frac{3EI_y}{l^3}; K_{cis} = \frac{12EI_y}{l^3} \quad (3.1)$$

For bending in the transverse direction, we simply replace I_y by I_x in the formulas (3.1). The tensile and torsional stiffnesses³ are:

$$K_{trac} = \frac{bhE}{l}; K_{tors} = \frac{bh^3G}{3l} \quad (3.2)$$

STIFFNESS RATIOS

- Transverse angular stiffness to natural angular stiffness :
 $K_{\alpha M}^t / K_{\alpha M} = I_x / I_y = (b/h)^2$. If $b > 10h$ then $K_{\alpha M}^t / K_{\alpha M} > 100$. We can therefore consider the rotational DOF with respect to transverse bending to be totally constrained.
- Torsional stiffness to natural angular stiffness⁴:
 $K_{tors} / K_{\alpha M} = 4G/E \simeq 1.5$. As the torsional stiffness is of the same order of magnitude as the natural bending stiffness, we can consider the DOF with respect to torsion to be compliant.

³ This formula, which is valid only for very slender cross sections ($b \gg h$) is taken from (Massonnet and Cescotto, 1994).

⁴ The relationship between Young's modulus and shear modulus is given by $G = E/(2(1 + \mu))$. However, most of the materials we use to make flexure joints have a Poisson's ratio $\mu = 0.3$, therefore $G \simeq E/2.6$.

- Tensile/compressive stiffness to natural translational stiffness:
 $K_{trac}/K_{cis} = (l/h)^2$. If $l > 10h$ then $K_{trac}/K_{cis} > 100$. We can therefore consider the translational DOF with respect to tension/compression to be totally constrained.
- Transverse translational stiffness to natural translational stiffness:
 $K_{cis}^t/K_{cis} = I_x/I_y = (b/h)^2$. If $b > 10h$ then $K_{cis}^t/K_{cis} > 100$. We can therefore consider the translational DOF with respect to transverse bending to be totally constrained.

ASSESSMENT:

*A leaf spring constitutes a joint having **three DOFs** (two rotational displacements and one translational displacement), the stiffness ratios of which are higher the greater the b/h and l/h ratios.*

3.2.3 Deflections

For motions along the three natural DOFs, we obtain the following deflections⁵:

$$\alpha_M = \frac{2\sigma_{adm}l}{Eh}; \quad f_{cis} = \frac{\sigma_{adm}l^2}{3Eh}; \quad \alpha_{tors} = \frac{\tau_{adm}l}{hG} \text{ where } \tau_{adm} = \frac{\sigma_{adm}}{\sqrt{3}}$$

(3.3)

For motions along the three transverse DOFs, we obtain the following deflections :

$$\alpha_M^t = \frac{2\sigma_{adm}l}{Eb}; \quad f_{cis}^t = \frac{\sigma_{adm}l^2}{3Eb}; \quad f_{trac} = \frac{\sigma_{adm}l}{E}$$

(3.4)

3.3 Rods

3.3.1 Definition

We define a **rod** as any prismatic beam having two similar moments of inertia ($I_x \simeq I_y$) along its cross section and having a profile slenderness greater than 10 ($l/m > 10$, where m is the larger of the cross-sectional dimensions). We will limit our discussion here to the two most common special cases, i.e., rods of circular cross section (diameter d ; moments of inertia $I_x = I_y = \pi d^4/64$ and $I_p = \pi d^4/32$) and of square cross section (dimension $h = b$; moments of inertia $I_x = I_y = h^4/12$ and $I_p = h^4/6$).

⁵ COMMENT: We use the formula for tangential stress as a function of the torque $\tau = 3M/(bh^3G)$ to calculate the torsional angular deflection α_{tors} . This formula, given by (Massonnet and Cescotto, 1994, page 148) is valid only for very slender cross sections ($b \gg h$).

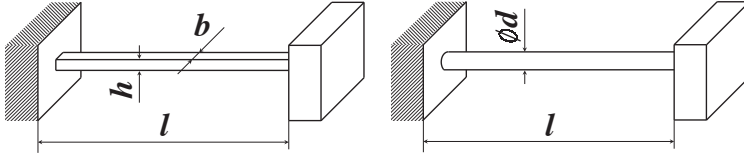


Figure 3.4 Rods of square and circular cross sections. Geometric parameters: l , length; h , thickness; b , width ($b = h$); d , diameter.

3.3.2 Stiffnesses

All the stiffnesses calculated for the leaf spring (3.1, 3.2) are also valid for rods of circular and square cross sections, except for their torsional stiffnesses⁶, which are respectively given by :

$$K_{tors}^{\circ} = \frac{GI_p}{l}; \quad K_{tors}^{\diamond} = 0.141 \frac{h^4 G}{l} \quad (3.5)$$

STIFFNESS RATIOS

- Transverse angular stiffness to natural angular stiffness :
As the two moments of inertia are similar ($I_x \simeq I_y$), we have $K_{\alpha M}^t \simeq K_{\alpha M}$ for both circular and square cross sections.
- Torsional stiffness to natural angular stiffness :
 $K_{tors}^{\circ}/K_{\alpha M} = 2G/E \simeq 0.77$; $K_{tors}^{\diamond}/K_{\alpha M} = 1.7G/E \simeq 0.65$. The torsional stiffnesses are of the same order of magnitude as the natural bending stiffness, which itself is similar to the transverse angular stiffness : we can therefore consider the three rotational DOFs to be compliant.
- Tensile/compressive stiffness to natural translational stiffness :
 $K_{trac}^{\circ}/K_{cis}^{\circ} = (4/3)(l/d)^2$. If $l > 10d$ then $K_{trac}^{\circ}/K_{cis}^{\circ} > 133$.
 $K_{trac}^{\diamond}/K_{cis}^{\diamond} = (l/h)^2$. If $l > 10h$ then $K_{trac}^{\diamond}/K_{cis}^{\diamond} > 100$.
We can therefore consider the translational DOF with respect to tension/compression to be totally constrained.
- Transverse translational stiffness to natural translational stiffness:
As the two moments of inertia are similar ($I_x \simeq I_y$), we have $K_{cis}^t \simeq K_{cis}$ for both circular and square cross sections. We can therefore consider the translational DOFs with respect to natural and transverse translational displacement to be compliant.

⁶ This formula is taken from (Massonnet and Cescotto, 1994).

ASSESSMENT:

*A rod constitutes a joint having **five DOFs** (only the translational displacement exerting tensile/compressive stress on the rod is constrained), the stiffness ratios of which are higher the greater the slenderness of the profile (l/h ratios for square cross sections and l/d for circular cross sections).*

3.3.3 Deflections**Rod of circular cross section**

For a rod of circular cross section and diameter d , we obtain the following angular deflections:

$$\alpha_M^\circ = \alpha_M^{t\circ} = \frac{2\sigma_{adm}l}{Ed}; \quad \alpha_{tors}^\circ = \frac{2\tau_{adm}l}{Gd} \quad \text{where} \quad \tau_{adm} = \frac{\sigma_{adm}}{\sqrt{3}} \quad (3.6)$$

and the following translational deflections:

$$f_{cis}^\circ = \frac{\sigma_{adm}l^2}{3Ed}; \quad f_{cis}^{t\circ} = \frac{\sigma_{adm}l^2}{3Ed}; \quad f_{trac}^\circ = \frac{\sigma_{adm}l}{E} \quad (3.7)$$

Rod of square cross section

For a rod of square cross section and dimension h , all the deflections calculated for the leaf spring (3.3, 3.4) are also valid (where $b = h$), except for the torsional deflection, which is given by⁷:

$$\alpha_{tors}^\diamond = \frac{1.48 \tau_{adm}l}{Gh} \quad \text{where} \quad \tau_{adm} = \frac{\sigma_{adm}}{\sqrt{3}} \quad (3.8)$$

3.4 Torsion bars

The torsional stiffness of beams with an open cross section formed by thin walls is mostly independent of the cross-sectional geometry (Fig. 3.5) (Massonnet and Cescotto, 1994, page 148). It can be considered with little error that the different rectangles (dimensions h and b where $b > 10h$) comprising the cross

⁷ For the calculation of the torsional deflection of a rod of square cross section, we calculate the shear stress using the formula $\tau = M/(0.208h^3)$ given by (Massonnet and Cescotto, 1994, page 148).

section resist torsion independently of one another. For a beam comprising n rectangles of dimensions h_i, b_i ($1 < i < n$), the torsional stiffness is thus given by

$$K_{tors} \simeq \frac{G}{3l} \sum_{i=1}^n h_i^3 b_i. \quad (3.9)$$

As for the bending stiffness, it is largely dependent on the arrangement of these rectangles. It is therefore possible, by choosing an appropriate profile, to obtain a high ratio between the bending stiffnesses and the torsional stiffness.

*If it is designed to resist bending, a torsion bar constitutes a joint having **one DOF** for rotation.*

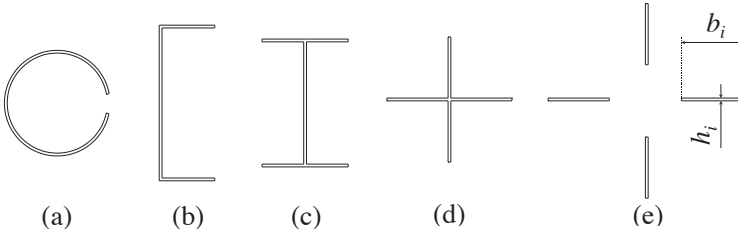


Figure 3.5 Thin-walled open cross sections. Torsion bars of such cross section resist bending more than torsion, making it possible to create joints with one rotational DOF.

3.4.1 Clamping

It is important to note that the formula (3.9) is valid only when torsion is uniform, i.e., when all the cross sections can warp freely. (Boresi et al., 1993) give the stiffness of a thin-walled prismatic beam with an open cross section that is clamped such that both ends of the beam cannot warp:

$$K_{tors}^{\square} \simeq \frac{JG}{l - 2\alpha \tanh \frac{l}{2\alpha}} \quad \text{where} \quad \alpha = \frac{h}{2} \sqrt{\frac{EI_p}{JG}} \quad \text{and} \quad J = \frac{1}{3} \sum_{i=1}^n h_i^3 b_i \quad (3.10)$$

I_p is the polar moment of inertia of the cross section⁸. It is worth comparing this formula to (3.9) by means of an example to illustrate the influence of clamping on angular stiffness. Let us consider two identical I-beams, one having both ends free to warp and the other having both ends clamped in rigid blocks that prevent them from warping (Fig. 3.6). We have plotted (Fig. 3.7) the angular

⁸ The formulas of the polar moments of inertia of I-shaped or U-shaped cross sections, for example, can be found in most works on structural mechanics (such as (Massonnet and Cescotto, 1994; Gere and Timoshenko, 1990)).

stiffness of these two beams as a function of their length. We can see that for stout beams (low l/b ratio), the beam whose ends are clamped is much more torsionally stiff than the beam whose ends are free to warp. The more slender the beam, the less this difference becomes. This is explained by the fact that clamping induces tensile/compressive stresses in the beam flanges (the horizontal elements of the I). These stresses reduce with increasing distance from the clamped region. Thus, if beams A and B (Fig. 3.6) are slender, their central portions are subjected to the same loading. This can be seen by plotting the rotation of the end of the beam as a function of the length (Fig. 3.7).

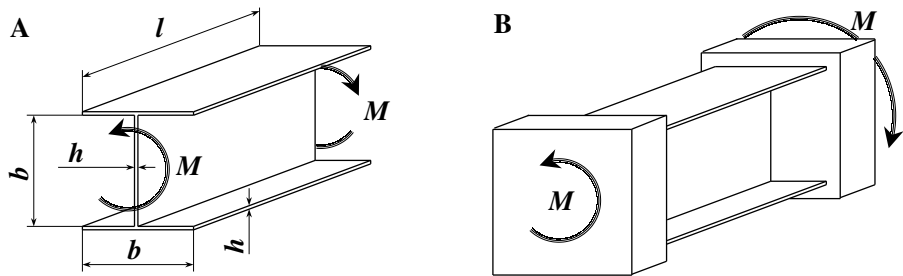


Figure 3.6 Torsion bars with ends that are free to warp (A) and clamped ends (B). The dimensions we have chosen for this example are: $h=0.5$ mm and $b=10$ mm. To plot the curves (Fig. 3.7) we varied l between 0 and 5 mm. The polar moment of inertia of this beam is $I_p = bh^3$.

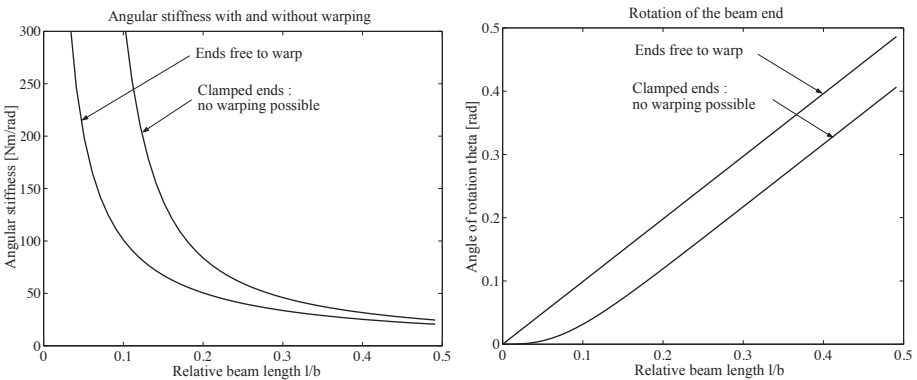


Figure 3.7 Effect of clamping the torsion bars on their angular stiffness: only the deformation of the ends of the beams is affected by clamping. We chose the following parameters to plot this example: $E=210$ GPa; $G=81$ GPa; $M=10$ Nm. The geometric parameters are those in Figure 3.6.

Thus, when making flexible bearings from torsion bars, care must be taken to ensure that securing the ends of the bars to the rigid blocks does not constrain their freedom to warp. This makes it possible to reduce their torsional stiffness without affecting their transverse stiffnesses, which results in increasing their stiffness ratios. This also has the effect of reducing the normal stresses exerted at the ends of the bars and thus increasing their allowable deflection. Actually making such joints is a very delicate operation and difficult to study analytically. The reader is referred to the work of (Boresi et al., 1993) for more details on this subject.

3.4.2 Axis of torsion

A force acting on a prismatic cantilever beam of any cross section bends the beam without twisting it only if it passes through the *axis of torsion*. This axis intersects the cross section of the beam at a point that we call the *shear center* C . For beams with two axes of symmetry, the shear center is located at the intersection of these axes, which coincides with the center of inertia G of the area of the cross section. For beams with only one axis of symmetry, the shear center is located along this axis but does not coincide with the center of inertia G of the cross section. In the latter case, the exact location of the shear center is complex and is beyond the scope of this book. The reader is referred to the work of (Boresi et al., 1993) which deals with this subject in detail. We simply give here the formulas for the position of the shear center of U-shaped cross sections and of those forming the arc of a circle. These exhibit the interesting property of pivoting about a point located outside the cross section. Figure 3.9 shows the location of the shear center of the most common cross sections.

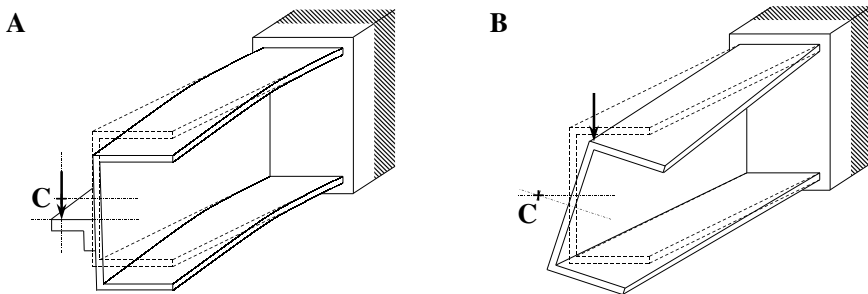


Figure 3.8 The axis of torsion of a U-shaped bar is located outside the profile: a force passing through this axis bends the bar without twisting it (A); a force that does not pass through this axis bends and twists the bar (B), causing its end to pivot approximately about the shear center C .

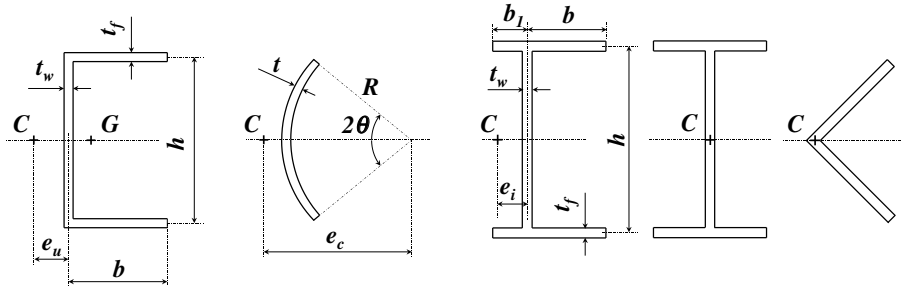


Figure 3.9 Position of the center of torsion C of various torsion bars.

$$e_u = \frac{b}{2 + \frac{1}{3} \frac{t_w h}{t_f b}}; \quad \frac{e_c}{R} = \frac{2(\sin \theta - \theta \cos \theta)}{\theta - \sin \theta \cos \theta}; \quad \frac{e_i}{b} = \frac{1 - \frac{b_1^2}{b^2}}{2 + \frac{2b_1}{b} + \frac{t_w h}{3t_f b}}, \quad b_1 < b. \quad (3.11)$$

3.5 Circular notch hinges

3.5.1 Definition

We define a **circular notch hinge**⁹ as any beam of rectangular cross section and variable thickness, having a profile that describes two concave semicircles (Fig. 3.10) whose radius r is at least more than five times the minimum thickness of the beam:

$$\frac{r}{e} > 5. \quad (3.12)$$

This condition ensures that the stress concentration factor is around 1, i.e., the variation in cross section is sufficiently mild to prevent any concentration of stress in the middle of the hinge (Pomey and Lieurade, 1982; Lu and Lieurade, 1998). The beam thickness is given by

$$h(x) = 2r + e - 2\sqrt{r^2 - (r-x)^2}. \quad (3.13)$$

Its moment of inertia is

$$I(x) = \frac{b(h(x))^3}{12}. \quad (3.14)$$

⁹ In the literature, this component is referred to as a ‘circular notch hinge’, a ‘circular necked down flexure’, and a ‘right circular flexure hinge’ (Kato et al., 1984).

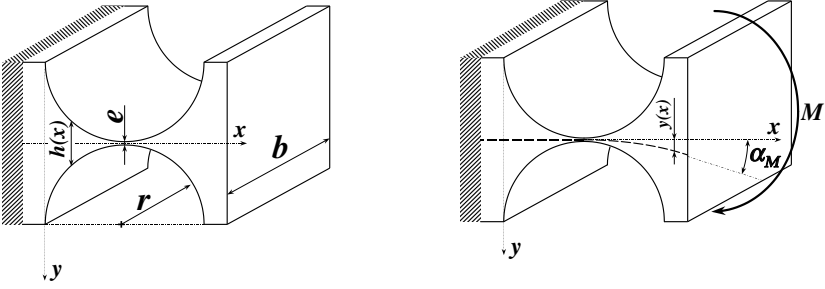


Figure 3.10 Circular notch hinge. Geometric parameters: e , thickness of the notch hinge at its narrowest point; r , radius of the notch; b , width. Angular stiffness : $K_{\alpha M} = M/\alpha$. Allowable angular deflection : α_M .

Let $y(x)$ be the equation for the deflection of the beam, $y'(x) = \frac{dy}{dx}$ its first derivative and $y''(x) = \frac{d^2y}{dx^2}$ its second derivative. According to equation (2.1), we have

$$y'(x) = \frac{-M_x(x)}{EI(x)}. \quad (3.15)$$

We can deduce that formulas of the following type exist for these stiffnesses:

$$K_{\alpha M} = C_1 E b e^{C_2} r^{C_3} \quad (3.16)$$

where C_1 , C_2 and C_3 are constants to be determined and which conform relatively well to the exact formulas. The constants can be determined numerically for a given point of the solution space (e, r) . We have therefore defined a *standard notch hinge*¹⁰ for which the simplified formulas have been optimised.

Standard notch hinge:

$$e = 50 \cdot 10^{-6} \text{ m} \quad \text{and} \quad r = 3 \cdot 10^{-3} \text{ m}. \quad (3.17)$$

We have also defined a subset of the solution space as the *domain of validity*¹¹ of the simplified formulas.

Domain of validity:

$$10^{-6} \text{ m} < e < 10^{-3} \text{ m} \quad , \quad 10^{-4} \text{ m} < r < 1 \text{ m} \quad \text{and} \quad \frac{r}{e} > 5. \quad (3.18)$$

¹⁰ We estimate that a notch hinge having a thickness of 50 μm and a radius of 3 mm is representative of the notch hinges used in microengineering and made by electrical discharge machining (EDM).

¹¹ We estimate that this domain covers most of the notch hinges encountered in microengineering. However, we note that for thicknesses of less than a dozen or so microns, it is necessary to verify experimentally whether the assumptions of continuum mechanics continue to apply.

We calculate the maximum deviation between the simplified formula and the exact formula, which appears in this domain for each of the stiffnesses and deflections we present.

3.5.2 Angular stiffness

EXACT FORMULA: If a pure bending moment M is applied to the notch hinge (Fig. 3.10), we have $M_x(x) = -M$ and the angular stiffness is, by definition:

$$K_{\alpha M} = \frac{M}{y'(2r)}. \quad (3.19)$$

SIMPLIFIED FORMULA¹²: For the standard notch hinge (3.17) we numerically determined the coefficients of formula (3.16): $C_1 = 0.071$, $C_2 = 2.5$ and $C_3 = -0.5$. (Paros and Weisbord, 1965) arrive at the same result using an analytical approach and give the following simplified formula for $K_{\alpha M_s} \simeq K_{\alpha M}$:

$$K_{\alpha M_s} = \frac{2Ebe^{2.5}}{9\pi\sqrt{r}}. \quad (3.20)$$

Within the domain of validity (3.18), the maximum deviation¹³ between the simplified formula (3.20) and the exact formula (3.19) ranges between 0% and 2.6% of the exact value.

SCALING LAWS¹⁴: $K_{\alpha M}^* = b^*E^*$; $K_{\alpha M}^* \simeq e^{*2.5}$; $K_{\alpha M}^* \simeq 1/\sqrt{r^*}$.

¹² It is occasionally necessary to make additional simplifying assumptions to establish formulas of a reasonable size for use. We use the \simeq sign to distinguish these *simplified* formulas, which are approximations, from the *exact* formulas.

¹³ This deviation represents the error resulting from simplification of the exact formula. We calculate this error as follows: $(K_{\alpha M} - K_{\alpha M_s})/K_{\alpha M}$. The errors of the following simplified formulas are calculated in exactly the same way.

¹⁴ The scaling laws are applied as follows: $K^* = x^*$ means that the stiffness K is *strictly proportional* to the physical quantity x according to classical mechanics of materials theory, without having to resort to simplifying assumptions other than those presented in Section 2.1. $K^* \simeq x^*$ means that the stiffness K is *approximately proportional* to quantity x ; the use of the \simeq sign indicates that additional simplifying assumptions had to be introduced in order to establish this relationship of proportionality. Some relationships of proportionality may be used *locally*. In other words, if for value x_1 we know the corresponding stiffness K_1 , then for a value x_2 similar to x_1 ($x_2 \simeq x_1$) we can deduce the corresponding value by applying the ‘rule of three’. Example of the scaling law and notation used: the angular stiffness of the circular notch hinge is approximately proportional to the thickness e of the notch hinge raised to the power of 2.5. In other words, if a given notch hinge having a thickness of e has an angular stiffness K , then an identical notch hinge having a thickness of e' similar to e will have a stiffness $K' \simeq K(e'/e)^{2.5}$. If the quotient of the equivalent magnitudes is indicated by an asterisk (*) we have $K^* = K'/K$ and $e^* = e'/e$. We can then write more simply: $K^* \simeq e^{*2.5}$. It is this notation that we have adopted to indicate application of the scaling law.

3.5.3 Angular deflection

SIMPLIFIED FORMULA: Once the maximum allowable moment as a function of the allowable stress (2.3) and the angular stiffness (3.20) is known, a simplified formula of the angular deflection of the circular notch hinge can be found:

$$\alpha_M \simeq \frac{3\pi\sigma_{adm}\sqrt{r}}{4E\sqrt{e}}. \quad (3.21)$$

Within the domain of validity (3.18), the maximum deviation between the simplified formula and the exact formula ranges between 0% and 2.6% of the exact value.

SCALING LAWS: $\alpha_M^* = \sigma_{adm}^*/E^*$; $\alpha_M^* \simeq \sqrt{1/e^*}$; $\alpha_M^* \simeq \sqrt{r^*}$; $\alpha_M^* = b^{*0}$ (α_M is independent of b).

3.5.4 Translational stiffness

EXACT FORMULA: For a force P acting at mid-length on the notch hinge (Fig. 3.11), we have $M_x(x) = Px - Pr$. Using (3.15), we obtain the translational stiffness:

$$K_{cis} = \frac{P}{y(2r)} \quad (3.22)$$

In this particular case, deformation due to shear is more significant than deformation due to bending¹⁵. We therefore took into account the term related to shear in equation (2.1) when calculating the simplified formula and the graph plot.

SIMPLIFIED FORMULA:

$$K_{cis} \simeq 0.218 \frac{Ebe^{1.5}}{r^{1.5}}. \quad (3.23)$$

Within the domain of validity (3.18), the maximum deviation between the simplified formula and the exact formula ranges between -9% and 9% of the exact value.

SCALING LAWS: $K_{cis}^* = E^*$; $K_{cis}^* \simeq b^*$; $K_{cis}^* \simeq e^{*1.5}$; $K_{cis}^* \simeq r^{*-1.5}$.

¹⁵ This is explained by the fact that with this particular distribution of the moment along the circular notch hinge, the bending moment is zero at the center of the notch hinge, where it is narrowest. Shear is thus the primary cause of deformation in this zone.

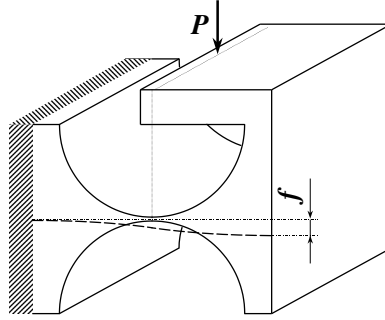


Figure 3.11 Translational stiffness: a force P applied to the mobile block of the pivot such that the direction of its vector passes through the central portion of the joint, inducing vertical translational displacement f of the mobile block. The translational stiffness of the pivot is: $K_{cis} = P/f$.

3.5.5 Torsional stiffness

Calculating the torsional stiffness of beams of non-circular cross section is highly complex due to warping effects of the cross sections. However, the literature (Massonnet and Cescotto, 1994) contains simplified formulas for rectangular cross sections with very high b/h ratios (3.2). If we consider the circular notch hinge as a series of thin slices of different thicknesses placed end to end (Fig. 3.12), we can deduce its angular stiffness:

$$K_{tors} = \frac{M}{\alpha} = \frac{bG}{3} \left(\int_0^{2r} \frac{1}{h^3(x)} dx \right)^{-1}. \quad (3.24)$$

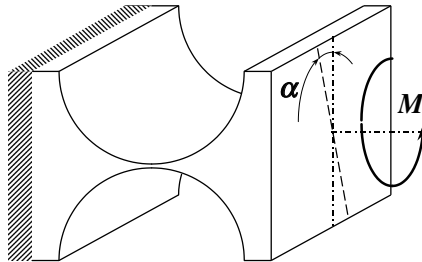


Figure 3.12 Torsional angular stiffness: for a pure moment M applying torsion to the joint and causing its end to rotate through an angle α , we obtain a torsional stiffness $K_{tors} = M/\alpha$.

SIMPLIFIED FORMULA: We have derived a simplified formula from it:

$$K_{tors} \simeq 0.284 \frac{Gbe^{2.5}}{\sqrt{r}}. \quad (3.25)$$

Within the domain of validity (3.18), the maximum deviation between the simplified formula and the exact formula ranges between -0.4% and 2.2% of the exact value.

SCALING LAWS: $K_{tors}^* = G^*$; $K_{tors}^* \simeq b^*$; $K_{tors}^* \simeq e^{*2.5}$; $K_{tors}^* \simeq 1/\sqrt{r^*}$.

3.5.6 Transverse angular stiffness

SIMPLIFIED FORMULA:

$$K_{\alpha M}^t \simeq 0.0295 \frac{Eb^3\sqrt{e}}{\sqrt{r}}. \quad (3.26)$$

Within the domain of validity (3.18), the maximum deviation between the simplified formula and the exact formula ranges between -11% and 22% of the exact value.

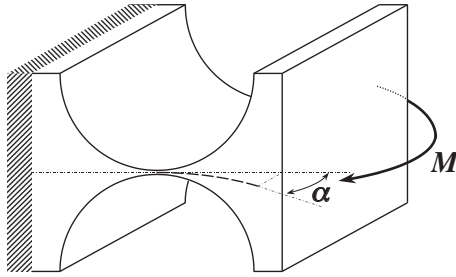


Figure 3.13 Transverse angular stiffness: for a pure bending moment M causing the notch hinge to bend about its transverse axis through an angle α we have an angular stiffness $K_{\alpha M}^t = M/\alpha$.

SCALING LAWS: $K_{\alpha M}^{t*} = E^*$; $K_{\alpha M}^{t*} = b^{*3}$; $K_{\alpha M}^{t*} \simeq \sqrt{e^*}$; $K_{\alpha M}^{t*} \simeq \sqrt{r^*}$.

3.5.7 Tensile/compressive stiffness

SIMPLIFIED FORMULA:

$$K_{trac} \simeq 0.353 \frac{Eb\sqrt{e}}{\sqrt{r}} \quad (3.27)$$

Within the domain of validity (3.18), the maximum deviation between the simplified formula and the exact formula ranges between -11% and 22% of the exact value.

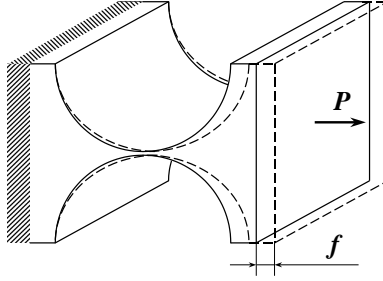


Figure 3.14 Tensile/compressive stiffness: for a tensile force P that elongates the notch hinge by a length f , we have a tensile/compressive stiffness $K_{trac} = P/f$.

SCALING LAWS: $K_{trac}^* = E^*$; $K_{trac}^* = b^*$; $K_{trac}^* \simeq \sqrt{e^*}$; $K_{trac}^* \simeq 1/\sqrt{r^*}$.

3.5.8 Other stiffnesses

Transverse translational stiffness

Given that, for a transverse translational loading, the shear force cannot be disregarded, the stiffness K_{cis}^t is evidently proportional to neither h nor b . We therefore cannot find a simplified formula of the same type as (3.16).

‘Generalised stiffnesses’ K_{fM} , K_{fP} and $K_{\alpha P}$

We calculate here some other ‘generalised stiffnesses’ without providing simplified formulas. These terms are used further on in this book (Sect. 4.4).

The first of these terms is the ratio between the moment M (Fig. 3.10) and the deflection f it induces at the end of the notch hinge:

$$K_{fM} = \frac{M}{f} = \frac{M}{y(2r)} \quad (3.28)$$

The following two terms are related to the angle and the deflection induced by a bending force P acting at the end of the notch hinge (Fig. 3.15). In this case we have $M_x(x) = -P(2r - x)$ and the two terms are given by:

$$K_{fP} = \frac{P}{f} = \frac{P}{y(2r)} \quad \text{and} \quad K_{\alpha P} = \frac{P}{\alpha} = \frac{P}{y'(2r)} \quad (3.29)$$

3.5.9 Stiffness ratios

- Natural angular stiffness to transverse angular stiffness:

$K_{\alpha M}^t / K_{\alpha M} = 0.417(b/e)^2$. If $b > 10e$, then $K_{\alpha M}^t / K_{\alpha M} > 41$. Since the

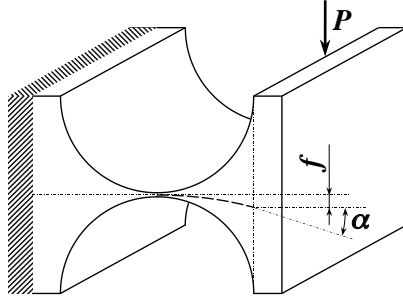


Figure 3.15 Generalised stiffnesses $K_{fP} = \frac{P}{f}$ and $K_{\alpha P} = \frac{P}{\alpha}$.

transverse angular stiffness is greater by one order of magnitude than the natural angular stiffness, the DOF under transverse bending is considered to be totally constrained.

- Torsional stiffness to natural angular stiffness:
 $K_{tors}/K_{\alpha M} = 4G/E \simeq 1.5$. As the torsional stiffness is of the same order of magnitude as the natural bending stiffness, the DOF with respect to torsion is considered to be compliant.
- Tensile-compressive stiffness to natural translational stiffness:
 $K_{trac}/K_{cis} = 1.62r/e$. If $r > 5e$, then $K_{trac}/K_{cis} > 8$. As the tensile-compressive stiffness is nearly one order of magnitude greater than the translational stiffness, the DOF with respect to tension-compression can be considered to be totally constrained.
- Transverse translational stiffness to natural translational stiffness:
 As we do not provide a simplified formula for transverse translational stiffness, we cannot calculate this stiffness ratio. Nevertheless, we can predict that, as in the case of the leaf spring (Sect. 3.2) this ratio will be high and all the more since the profile cross section is slender (high b/e ratio). The DOF with respect to the transverse translational displacement is considered to be totally constrained.

ASSESSMENT:

*A circular notch hinge constitutes a joint having **three DOFs** (two rotational displacements and one translational displacement), the stiffness ratios of which are higher the greater the b/e and r/e ratios. A circular notch hinge has the same degrees of freedom as a leaf spring¹⁶.*

¹⁶ Compared to a leaf spring, a circular notch hinge possesses the advantage of not having any sharp corners that could act as stress concentrators close to its ends.

3.5.10 Truncated circular notch hinge

A circular notch hinge can be reduced in size by truncating it beyond a thickness equal to approximately 4 times the minimum thickness e . This virtually changes neither the allowable deflection nor the stiffness (Fig. 3.16). Indeed, the deformation amplitude of a bending leaf spring is inversely proportional to the cube of its thickness (thus most of the bending occurs in the central portion of the notch hinge) and the intensity of the stresses is inversely proportional to the square of its thickness. Thus, at the position along the notch hinge where the thickness is $4e$, the stress is 16 times weaker than in the central portion (under pure bending stress). It is therefore tolerable, at this location, to have a stress concentration effect at the small fillet radius between the circular arc and the end of the arm to which it is joined. An elliptical profile (Fig. 4.29d) fulfills the same function as the truncated circular arcs and possesses the additional advantage of having a minimum curvature in the most heavily loaded portion of the notch hinge.

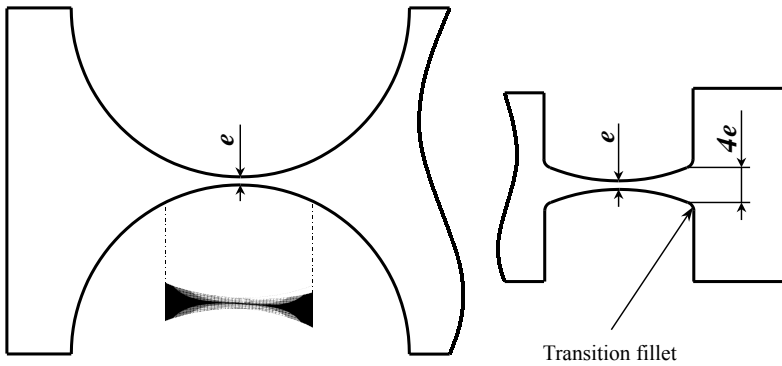


Figure 3.16 A circular notch hinge and a truncated circular notch hinge that is virtually equivalent and less bulky. Finite element simulation shows that the stresses are localised in the central portion of the neck (the shades of gray represent the intensity of the stresses (absolute value): black = 53 MPa; white = 475 MPa).

Translational flexures

This chapter discusses the simplest and most common flexible linear translation bearings – the *two parallel leaf spring stage*, the *overconstrained stage with four parallel leaf springs*, the *four prismatic notch hinge stage* and the *four circular notch hinge stage*. We will calculate the stiffnesses, deflections and allowable loads for each linear translation bearing. We will show that, for a given form factor and deflection, the stage with four prismatic (or circular) notch hinges, which has minimal notch hinge thicknesses h (or e) and length l_c (or radius r) is the best linear translation bearing in terms of stiffness ratios. Compared with prismatic notch hinges, circular notch hinges also possess the advantage of not having sharp corners that could act as stress concentrators. We therefore recommend using, when allowed by the manufacturing process, tables with four circular notch hinges with a minimal notch radius as linear translation bearings.

Compared with the other linear translation bearings presented, the overconstrained stage with four parallel leaf springs possesses the advantage of constituting a *rectilinear* translation bearing. However, for an identical form factor, its deflection is less, its force-deformation characteristic is progressive and it induces significant stresses in the base and mobile blocks.

4.1 Two parallel leaf spring stage

4.1.1 Equilibrium of forces

A table with two parallel leaf springs comprises a fixed base block and a mobile block connected to each other by two identical, parallel, flexible leaf springs. A force¹ \bar{P} acting on the mobile block deforms the two leaf springs in a virtually identical manner, resulting in a translational displacement of the mobile block.

¹ Notation: Symbols with an overbar are the parameters relating to the mobile block of the parallel leaf spring stage. As we will see in the calculations, it is often preferable to isolate one of the two leaf springs to study its behaviour. We have reserved symbols without an overbar for parameters relating to only one of the two leaf springs.

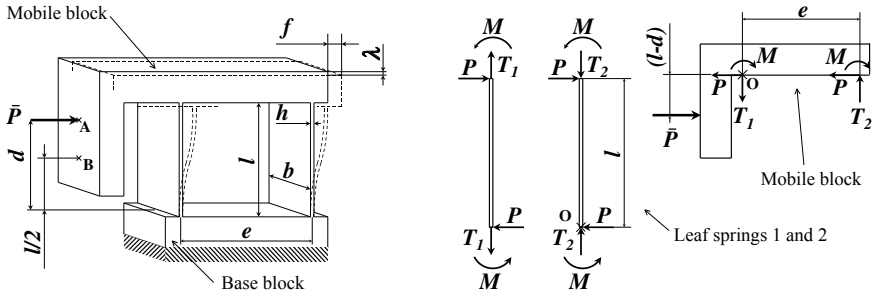


Figure 4.1 Parallel leaf spring stage and equilibrium of forces: h , thickness of the leaf springs; b , width of the leaf springs; l , length of the leaf springs; e , pitch of the leaf springs; d , distance between the base block and the point of application of the driving force \bar{P} ; f , horizontal displacement; λ , vertical displacement.

Let us isolate one of the two leaf springs. We can break down the forces acting on each of its ends into a horizontal force P , a vertical force T and a moment M . Let us make the assumption that the deformation amplitude of the leaf spring under the effect of these forces is sufficiently weak to allow us to disregard its influence on the equilibrium of the leaf spring. The equilibrium of horizontal (respectively vertical) forces indicates that the forces P (respectively T) acting at each end are of the same magnitude and in the opposite direction. The equilibrium of moments allows us to deduce that

$$M = \frac{Pl}{2}. \quad (4.1)$$

Now let us isolate the movable platform. It is subjected to the reactions of the forces and the moments acting on the leaf springs, and the force \bar{P} acting at point A located at a distance d from the base block. In this case, the equilibrium of forces along the horizontal axis shows us that $P = \bar{P}/2$. The equilibrium of forces along the vertical axis shows us that the tensile force T_1 in one of the leaf springs is equal to the compressive force in the other $T_1 = T_2 = T$. By using equation (4.1), the equilibrium of moments at point O yields:

$$T = \frac{\bar{P}}{e} \left(d - \frac{l}{2} \right) \quad (4.2)$$

The result is that the tensile/compressive forces T_1 and T_2 of the leaf springs cancel each other out if the force \bar{P} acts at a distance $d = l/2$ (point B) from the base block. Another result is that the further the point of application of \bar{P} moves from B and the smaller the pitch e of the leaf springs, the more the tensile and compressive forces increase.

Since the stiffness of the leaf springs is not infinite under tensile/compressive loading, the presence of the non-zero forces T_1 and T_2 elongates leaf spring 1 and shortens leaf spring 2. The result is that the output block pivots. *Strictly speaking, the table with parallel leaf springs is a purely translational bearing only if the driving force \bar{P} acts on the mobile block at a distance $l/2$ from the base block.*

Since the leaf springs are much more rigid under tensile/compressive loading than under bending, it is possible at a first approximation to disregard the influence of forces T_1 and T_2 on their deflection. In this case, the table with two parallel leaf springs may be regarded as a purely linear translational bearing even when the driving force \bar{P} does not act at a distance $l/2$ from the base block. Nevertheless, one should bear in mind that this is an approximation that becomes less precise as the magnitude of the forces increases. It is therefore important to minimise T through careful design. This can be achieved primarily in two ways:

- By bringing the point of application of the force \bar{P} as close as possible to point B located at a distance $l/2$ from the base block.
- By maximising the pitch e of the leaf springs.

Section 4.1.5 discusses the effect of tensile and compressive forces on the leaf springs in more detail.

4.1.2 Stiffness at zero load

Let us consider the specific case where the force \bar{P} acts at point B, cancelling out the tensile/compressive forces: $T_1 = T_2 = 0$. Now let us isolate one of the two leaf springs. A force P and a moment $M = Pl/2$ act at each of its ends. Let us draw the axes as shown in Figure 4.2. A cross section of the leaf spring located at a distance x from the origin is subjected to a moment:

$$M_x(x) = M - P(l - x) = Px - \frac{Pl}{2}. \quad (4.3)$$

From equation (2.1) we can deduce the second derivative of the deflection of the leaf spring:

$$y''(x) = \frac{-M_x(x)}{EI} = \frac{Pl/2 - Px}{EI}. \quad (4.4)$$

By integration, and knowing that $y'(0) = 0$ and $y(0) = 0$, the first derivative can be deduced:

$$y'(x) = \frac{P}{2EI}(lx - x^2), \quad (4.5)$$

as well as the deflection equation:

$$y(x) = \frac{P}{2EI} \left(\frac{lx^2}{2} - \frac{x^3}{3} \right). \quad (4.6)$$

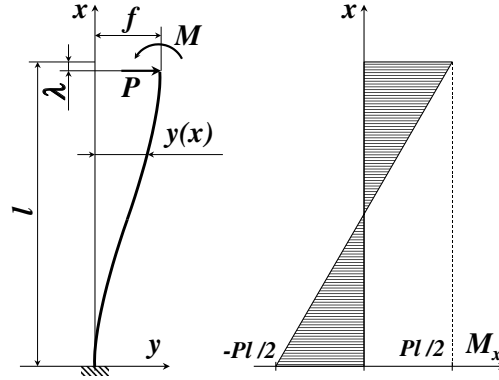


Figure 4.2 Deflection and bending moment of one of the leaf springs in the table with two parallel leaf springs.

The beam end deflection is therefore:

$$y(l) = \frac{Pl^3}{12EI}. \quad (4.7)$$

The translational stiffness of a leaf spring $K_o = P/f$ is thus:

$$K_o = \frac{12EI}{l^3}. \quad (4.8)$$

Knowing that $P = \bar{P}/2$, we can also deduce from (4.7) the translational stiffness of the table with two parallel leaf springs $\bar{K}_o = \bar{P}/f = \bar{P}/y(l)$:

$$\bar{K}_o = \frac{24EI}{l^3} \quad (4.9)$$

which is twice that of just one leaf spring. Thus the two leaf springs function as two springs fitted in parallel.

4.1.3 Deflection at zero load

Equation (4.3) shows us that the bending moment is zero at the middle of the leaf spring (at $x = l/2$) and that its magnitude² is highest where the leaf spring is restrained in the base and mobile blocks (at $x = 0$ and $x = l$), where it becomes $M_{max} = Pl/2$. But we know that the maximum moment allowed for

² We call the *magnitude* of the moment its absolute value $|M_x(x)|$.

the leaf spring is $M_{adm} = \sigma_{adm}bh^2/6$ according to equation (2.3). Therefore, the maximum force allowable on a leaf spring is $P_{adm} = 2M_{adm}/l$ and the maximum force allowable on the mobile block is $\bar{P}_{adm} = 2P_{adm}$. The deflection at zero load is thus $f_{adm_o} = \bar{P}_{adm}/\bar{K}_o$:

$$f_{adm_o} = \frac{\sigma_{adm}l^2}{3Eh}. \quad (4.10)$$

4.1.4 Path at zero load

The path along which the mobile block moves is not a straight line but a parabola. Its demonstration requires calculation of the vertical displacement λ of the ends of the leaf springs. This is the difference between the length of the leaf springs before deformation and the length of the deformed leaf springs as projected onto the x-axis (Fig. 4.2). The classical formula is found in the literature (Gere and Timoshenko, 1990):

$$\lambda \simeq \frac{1}{2} \int_0^l (y'(x))^2 dx \quad (4.11)$$

It involves a limited series expansion that is valid only for small angles of deflection of the leaf springs. Using (4.11) and (4.5) yields

$$\lambda \simeq \frac{P^2 l^5}{240E^2 I^2} \quad (4.12)$$

which becomes simplified if (4.8) is used to give the vertical displacement λ as a function of the translational displacement f :

$$\lambda \simeq \frac{3f^2}{5l}. \quad (4.13)$$

We thereof deduce that the mobile block follows a parabolic path and that the lateral displacement is inversely proportional to the length of the leaf springs.

4.1.5 Tensile/compressive loading: simplified model

Let us continue to consider the specific case where the force \bar{P} acts at point B, cancelling out the tensile/compressive forces ($T_1 = T_2 = 0$). This time, however, let us add a vertical force \bar{N} that acts at the center of the mobile block³. We

³ In practice, this force \bar{N} may be created by a weight placed on the mobile block or by another external force.

consider that the sign of this force is positive when it exerts a compressive load on the leaf springs, and negative when it exerts a tensile load on them. Let us isolate one of the two leaf springs. As well as the aforementioned forces M , P and T , the leaf spring is subjected to an additional load $N = \bar{N}/2$. If we disregard once again the effect of the tensile/compressive forces on the deflection of the leaf spring, the presence of the load \bar{N} in no way changes the path followed by the mobile block (4.13). Now let us attempt to determine the translational stiffness of the table thus loaded.

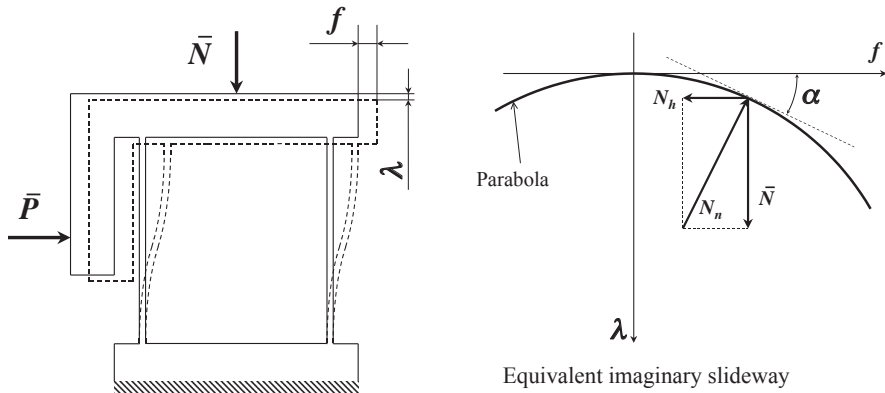


Figure 4.3 Two parallel leaf springs stage subjected to tensile/compressive load and simplified model.

First let us make the assumption that the translational stiffness (4.9) is zero: $\bar{K}_o = 0$. The translation bearing thus acts like an imaginary parabola-shaped ‘slideway’ whose path equation is $\lambda(f) = -3f^2/(5l)$. If it is positive, the load \bar{N} tends to move the ‘slide’ from its middle position. The slideway exerts a reaction N_n on the slide that is normal to its path. A horizontal opposing force N_h must be exerted to maintain the slide in position. Let α be the slope of the parabola. This yields:

$$N_h = \bar{N} \tan \alpha = \bar{N} \frac{d\lambda}{df} = \frac{-6\bar{N}}{5l} f.$$

The translation bearing thus acts as if it had a constant negative stiffness

$$\bar{K}_n = \frac{-6\bar{N}}{5l}. \quad (4.14)$$

This is the consequence of the specific property of the parabola having a linear derivative – the more the slide moves away from its equilibrium position, the

more \bar{N} tends to move it away even more to an extent proportional to the horizontal displacement f .

In the case where the load \bar{N} is negative (tensile load), formula (4.14) remains valid and the translation bearing acts as if it had a constant positive stiffness.

If we now reconsider the stiffness \bar{K}_o of the translation bearing with leaf springs, the total stiffness of the table becomes $\bar{K}_{tot} = \bar{K}_o + \bar{K}_n$. We can conclude from this that the translational stiffness of the table with two parallel leaf springs depends on the load \bar{N} applied to it, and that it is constant along the entire deflection for a given load \bar{N} :

$$\bar{K}_{tot} = \frac{24EI}{l^3} - \frac{6\bar{N}}{5l}. \quad (4.15)$$

This allows us to see that there is a load \bar{N}_o that cancels out the stiffness \bar{K}_{tot} of the table with two parallel leaf springs:

$$\bar{N}_o = \frac{20EI}{l^2}. \quad (4.16)$$

The simplified model that we have just described makes it possible to explain in a relatively intuitive manner why the translational stiffness of the table with two parallel leaf springs depends on the load applied to it, why it is constant for a given load and how it is that there is a load that makes it tend to zero. The complete model that we describe below leads us to the same conclusions through a more rigorous approach. Furthermore, it allows us to show phenomena not observable with the simplified model: buckling of the leaf springs, compressive stiffness of the table, load-dependent deflection.

4.1.6 Tensile/compressive loading: complete model

Thus far, we have routinely disregarded the effect of tensile/compressive forces on the deflection of the leaf springs. Doing so was correct at first approximation, particularly for small deformation amplitudes. Now the aim is to take into account the effect of these forces to ascertain the behaviour of the table with two parallel leaf springs under load conditions more accurately. Given that these forces act in the plane of the leaf springs, it is crucial to take into account their deformation amplitude when calculating the loading induced by these forces in the leaf springs.

This model, which reflects reality better than the previous one, makes it possible to explain the *buckling* of the leaf springs when the compressive loads exceed a certain threshold. Indeed, beyond a certain load referred to as the *critical load*, a phenomenon of elastic instability occurs, causing the amplitude of the deformations to rise sharply and destroy the system.

This model also makes it possible to calculate – with more rigor than in Section 4.1.5 and for loads below the critical levels, i.e., when the system is elastically stable – the translational stiffness of the table with two parallel leaf springs under load conditions as well as its transverse stiffness in vertical translational displacement.

Buckling: critical load and elastic instability

Let us consider that only a vertical compressive force \bar{N} is acting at the center of the mobile block. This force divides itself equally between the two leaf springs, compressing each of them with a force $N = \bar{N}/2$. Let us constrain the horizontal movement of the mobile block but leave it free to move vertically. When the vertical force exceeds the critical load \bar{N}_c the two leaf springs buckle, taking the shape illustrated in Figure 4.4. This buckling mode is just one variant of the well-known mode that is also depicted in the figure and whose critical load is given by Euler's formula⁴:

$$N_{Euler} = \frac{\pi^2 EI}{l_o^2}. \quad (4.17)$$

In our case, we have $l_o = l/2$ which allows us to find the critical load for a leaf spring

$$N_c = \frac{4\pi^2 EI}{l^2}, \quad (4.18)$$

as well as the critical load on the table, since $\bar{N} = 2N$:

$$\bar{N}_c = \frac{8\pi^2 EI}{l^2}. \quad (4.19)$$

It is important to note that the critical load does not depend on the stress allowable in the material σ_{adm} . It is futile, for example, to hope to increase the critical load of a table with parallel steel leaf springs by subjecting the leaf springs to heat treatment to increase their elastic limit.

It should also be noted that the critical load is independent of the initial deflection f of the stage⁵.

⁴ The derivation of Euler's formula can be found in most works on strength of materials theory, such as (Massonnet and Cescotto, 1994) (Gere and Timoshenko, 1990). We will therefore not present it here.

⁵ This is contrary to common intuition, which would generally expect the critical load to decrease when the table moves away from its nominal position.

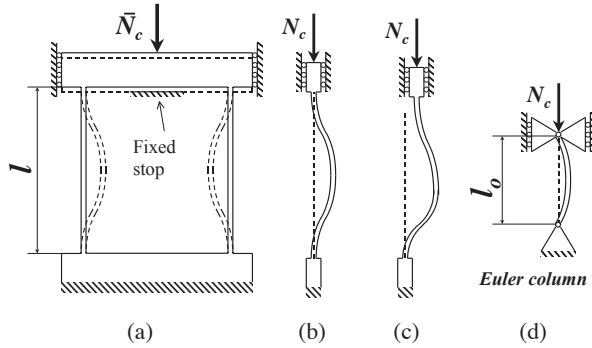


Figure 4.4 Buckling of the two parallel leaf spring stage. When the compressive load exerted on the table reaches the critical load, the leaf springs buckle, taking the shape illustrated in (a). The leaf springs may buckle inward or outward at random. When the leaf springs buckle, the system becomes unstable. To be able to observe it in this state, a fixed stop must be added. The critical load is independent of the deflection f of the leaf spring: the critical load of leaf springs (b) and (c) is the same. The Euler column equivalent to load case (b) is represented by (d).

It is vital to remember here that the buckling model that we use makes the assumption that the beam remains within the elastic deformation range for all loads ranging up to the critical load $0 \leq \bar{N} < \bar{N}_c$. Thus, the critical load that we have just calculated forms a threshold beyond which the system is inevitably destroyed by a phenomenon of elastic instability regardless of the elastic limit of the material used. In actual fact, the material used has a finite elastic limit. As a result, depending on the case, the system could be destroyed by the onset of stresses in the leaf springs that exceed the stress allowed by them, for loads below the critical load, i.e., before elastic instability occurs. At this stage of our development, we can draw just one conclusion – the allowable load of a table with parallel leaf springs is always less than its critical load.

$$\bar{N}_{adm} \leq \frac{8\pi^2 EI}{l^2} \quad (4.20)$$

At the end of this section we will prove that for small deflections in relation to the maximum deflection allowed by the two parallel leaf spring stage, the allowable load is well and truly equal to the critical load. However, for larger deflections (close to f_{adm}), the elastic limit is exceeded at loads below \bar{N}_c .

Tensile/compressive behaviour in the elastically stable domain

Let us consider once again that the force \bar{P} is applied to point B and that it thus does not induce any tensile/compressive forces in the leaf springs: $T_1 = T_2 = 0$. This force causes the mobile block to move through a distance f , which this

time we will take into account in the calculation of the leaf spring equilibrium⁶. Since the load \bar{N} is applied at the center of the mobile block, it will distribute itself equally between the two leaf springs, producing on each a force $N = \bar{N}/2$. Let us isolate one of the two leaf springs. The forces acting on its end are: $P = \bar{P}/2$, M and N (Fig. 4.5).

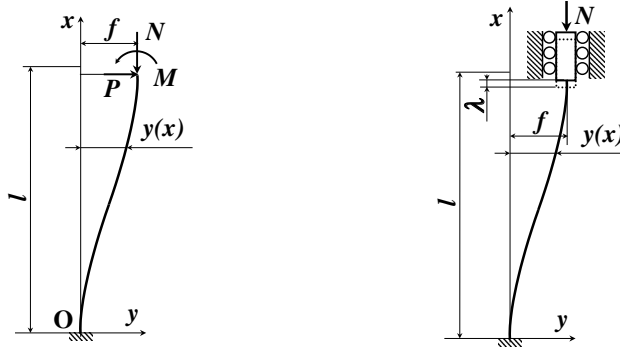


Figure 4.5 Deflection of one of the leaf springs of the table with two parallel leaf springs subjected to tensile/compressive load.

Since the leaf spring is in equilibrium, these three forces are not independent. The sum of the moments at O makes it possible to find the relationship between them: $2M - Nf - Pl = 0$. This gives

$$M = \frac{Nf + Pl}{2}. \quad (4.21)$$

A cross section of the leaf spring located at distance x from the base block is subjected to a moment:

$$M_x(x) = M - N(f - y(x)) - P(l - x) \quad (4.22)$$

Equation (2.1) gives us the second derivative of the deflection $y''(x) = -M_x(x)/(EI)$ and results in the following differential equation:

$$y''(x) + \frac{N}{EI}y(x) = \frac{-P}{EI}x + \frac{Pl + Nf - M}{EI}. \quad (4.23)$$

This is a second-order linear equation with constant coefficients of the following type:

$$y'' + k^2 y = k_a x + k_b \quad (4.24)$$

⁶ At the start of Section 4.1 we performed the same calculation but disregarded the effect of the deformation of the leaf spring on the equilibrium of forces acting on it.

where

$$k = \sqrt{\frac{N}{EI}}; k_a = \frac{-P}{EI}; k_b = \frac{Pl + Nf - M}{EI}. \quad (4.25)$$

The general solution of the equation without the right-hand side is of the type:

$$y_g = C_1 \cos kx + C_2 \sin kx. \quad (4.26)$$

It is easy to find a particular solution of the equation with the right-hand side

$$y_p = ax + b, \quad (4.27)$$

where

$$a = \frac{-P}{N} \quad \text{and} \quad b = \frac{Pl - M}{N} + f. \quad (4.28)$$

The general solution of the equation with the right-hand side is the sum of y_p and y_g :

$$y(x) = C_1 \cos kx + C_2 \sin kx + ax + b. \quad (4.29)$$

Its derivative is

$$y'(x) = -kC_1 \sin kx + kC_2 \cos kx + a. \quad (4.30)$$

The conditions at the ends of the leaf spring are known:

$$y(0) = 0; y'(0) = 0; y(l) = f.$$

The first condition makes it possible to find C_1 and the second C_2 :

$$C_1 = \frac{M - Pl}{N} - f \quad \text{and} \quad C_2 = \frac{P}{kN}. \quad (4.31)$$

The third condition gives

$$\left(\frac{M - Pl}{N} - f \right) \cos kl + \frac{P}{kN} \sin kl - \frac{Pl}{N} + \frac{Pl - M}{N} + f = f.$$

Equation (4.21) allows us to eliminate the unknown M and to find P as a function of f :

$$P = f \frac{N(1 + \cos kl)}{-l(1 + \cos kl) + \frac{2 \sin kl}{k}}. \quad (4.32)$$

This formula can be written more simply⁷:

$$P = \frac{Nf}{\frac{2}{k} \tan \frac{kl}{2} - l}. \quad (4.33)$$

Now that we have completely solved the differential equation (4.23), we can calculate the deflection (4.29) of the leaf spring, or its derivative (4.30), knowing the force P and the load⁸ N applied to it as well as dimensions h , b , l and its Young's modulus E . To do so, the above figures in boxes must be used: (4.21), (4.28), (4.31) and (4.32). Figure 4.9 shows the characteristics of the deflection $y(x)$.

The last equation (4.33) gives us the translational stiffness of a leaf spring $K = P/f$:

$$K = \frac{N}{\frac{2}{k} \tan \frac{kl}{2} - l} \quad \text{where} \quad k = \sqrt{\frac{N}{EI}}. \quad (4.34)$$

This allows us to see that there is a load N_o that induces zero stiffness:

$$N_o = \frac{\pi^2 EI}{l^2}. \quad (4.35)$$

It is worth writing equation (4.34) as a function of K_o and N/N_o . To do so, let us write

$$\gamma = N/N_o.$$

This gives us

$$N = \gamma N_o = \frac{\gamma \pi^2 EI}{l^2} \quad (4.36)$$

and

$$k = \sqrt{\frac{N}{EI}} = \frac{\pi}{l} \sqrt{\gamma}. \quad (4.37)$$

Let us replace terms N and k of equation (4.34) by (4.36) and (4.37). We also know from equation (4.8) that $K_o = 12EI/l^3$, so that substituting for EI/l^3

⁷ To achieve this simplification we use the goniometric relationships $\sin 2a = 2 \sin a \cos a$ and $\cos 2a = 2(\cos a)^2 - 1$.

⁸ If the load exerts a tensile stress on the leaf spring, N is negative. The term k (4.25) and the constant C_2 (4.31) become complex imaginary numbers, but all the formulas presented in this section remain valid. To use them, one merely has to use Euler's formulas: $\cos \varphi = \frac{e^{i\varphi} + e^{-i\varphi}}{2}$ and $\sin \varphi = \frac{e^{i\varphi} - e^{-i\varphi}}{2i}$. Given that most calculation programs do this automatically, the formulas presented here can generally be used 'as is' for tensile as well as compressive loads.

gives us:

$$K = K_o Z(\gamma) \quad \text{where} \quad Z(\gamma) = \frac{\gamma \pi^2}{12 \left(\frac{2}{\pi \sqrt{\gamma}} \tan \frac{\pi \sqrt{\gamma}}{2} - 1 \right)}. \quad (4.38)$$

This equation makes it possible to calculate the translational stiffness of a leaf spring in a two parallel leaf spring stage subjected to tensile/compressive loading if we know the leaf spring stiffness under no load K_o , the load N_o that induces zero stiffness and the applied load N . (The reader is reminded that $\gamma = N/N_o$).

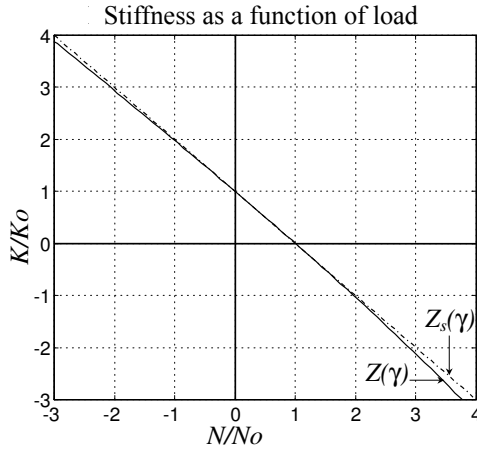


Figure 4.6 Plot of the function $Z(\gamma)$ and the simplified function $Z_s(\gamma)$. This graph shows that the translational stiffness of one of the leaf springs of a two parallel leaf spring stage varies virtually linearly as a function of the applied load N .

The plot of the function $Z(\gamma)$ (Fig. 4.6) shows that it is a curve with a negative slope, with $Z(0) = 1$ and $Z(1) = 0$. The curve is virtually a straight line between these two points. It is thus possible to approximate the exact function $Z(\gamma)$ by a straight line passing through these two points, the equation of which is $Z_s(\gamma) = 1 - \gamma$. Figure 4.7 shows the relative error E_r between the exact and simplified functions: $E_r = (Z - Z_s)/Z$. We see that this error is less than 1.5% when $-1 < \gamma < 1$, i.e., when $-N_o < N < N_o$, and less than 9% when $-4 < \gamma < 4$, i.e., when $-4N_o < N < 4N_o$. It is therefore possible in practice to use the simplified function Z_s without making significant errors. We therefore have:

$$K = K_o Z(\gamma) \simeq K_o Z_s(\gamma) = K_o(1 - \gamma) = K_o \left(1 - \frac{N}{N_o} \right) = K_o - \frac{K_o}{N_o} N.$$

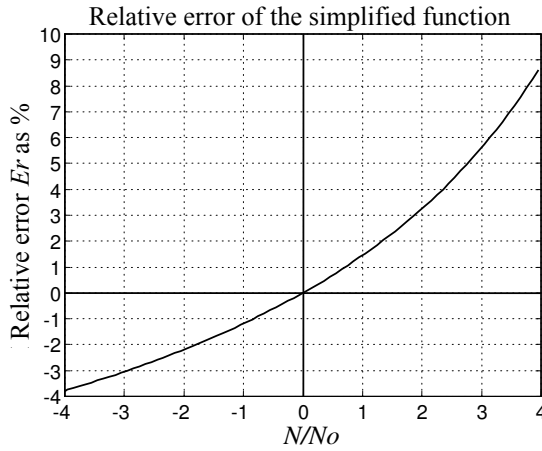


Figure 4.7 Relative error of the simplified function $Z_s(\gamma)$.

This gives us an extremely simple formula for calculating the translational stiffness of a leaf spring under load:

$$K \simeq K_o - \frac{K_o}{N_o} N \quad \text{where} \quad K_o = \frac{12EI}{l^3} \quad \text{and} \quad N_o = \frac{\pi^2 EI}{l^2} \quad (4.39)$$

Results for the complete stage (with its two leaf springs)

Now let us consider the two parallel leaf spring stage in its entirety. We know that $P = \bar{P}/2$ and $N = \bar{N}/2$. The load \bar{N}_o that effectively makes the stage stiffness zero is thus, according to (4.35):

$$\bar{N}_o = \frac{2\pi^2 EI}{l^2}. \quad (4.40)$$

We see that the critical load \bar{N}_c (4.19) that causes the leaf springs to buckle is four times greater than the load that induces zero stiffness:

$$\bar{N}_c = 4\bar{N}_o. \quad (4.41)$$

If we compare formula (4.40) with that obtained from the approximate model (4.16), which does not take into account the effect of the compressive forces on the deflection of the leaf springs, we see that the only difference lies in the coefficients 20 and $2\pi^2 \simeq 19.7$, which are numerically very similar. For the rest of these analyses, we will adhere to formula (4.40), which is more rigorous.

Knowing that $\bar{\gamma} = \bar{N}/\bar{N}_o = 2N/(2N_o) = \gamma$, that $\bar{K}_o = 2K_o$ and that $\bar{K} = 2K$, equation (4.38) for a two parallel leaf spring stage becomes:

$$\bar{K} = \bar{K}_o Z(\gamma) \quad \text{where} \quad Z(\gamma) = \frac{\gamma \pi^2}{12 \left(\frac{2}{\pi \sqrt{\gamma}} \tan \frac{\pi \sqrt{\gamma}}{2} - 1 \right)}. \quad (4.42)$$

As the function $Z(\gamma)$ is identical to that of equation (4.38), it is possible to use the simplified function $Z_s(\gamma) = 1 - \gamma$, which thus gives, as we have seen, an excellent approximation. We obtain:

$$\bar{K} \simeq \bar{K}_o - \frac{\bar{K}_o}{\bar{N}_o} \bar{N} \quad \text{where} \quad \bar{K}_o = \frac{24EI}{l^3} \quad \text{and} \quad \bar{N}_o = \frac{2\pi^2 EI}{l^2}. \quad (4.43)$$

Vertical displacement as a function of load

Now that we know the equation for the deflection of the leaf spring under load conditions $y(x)$, let us calculate its vertical displacement $\lambda(f, N)$ (Fig. 4.5) as a function of both the load and the horizontal displacement of the mobile block. This displacement can be broken down into two parts: a displacement λ_1 resulting from the variation in the deflection induced by the load N (effect of the bending moment) and a displacement λ_2 resulting from the shortening induced by N (effect of the compressive forces). From the classical formula (Gere and Timoshenko, 1990), we have:

$$\lambda_1 \simeq \frac{1}{2} \int_0^l (y'(x))^2 dx.$$

As for the shortening, it is calculated very simply (Hooke's law):

$$\lambda_2 = \frac{Nl}{hbE}.$$

The total displacement is the sum of these two components:

$$\lambda = \lambda_1 + \lambda_2.$$

Given the complexity of the function $y(x)$, we do not calculate $\lambda(f, N)$ algebraically here. However, it is easy to perform this calculation numerically by computer to observe the shape of the curve for this function for some specific cases. This is what is shown in Figure 4.8. We see first that the transverse stiffness in vertical translational displacement $K_c = N/\lambda$ of the stage decreases as the stage is moved away from its equilibrium position. We also see that this stiffness is not linear but degressive: for a given displacement f , the greater the compressive load, the lower the stiffness.

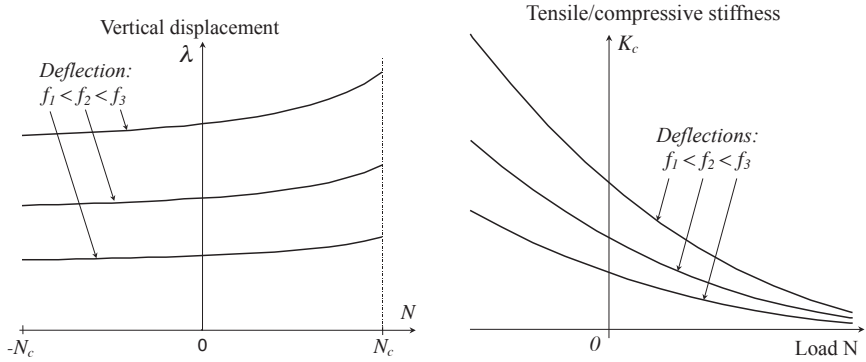


Figure 4.8 Vertical displacement λ and transverse stiffness in vertical translational displacement \bar{K}_c as a function of load N .

Allowable deflection as a function of load

Deflection f_{adm} is the displacement that produces a stress in the leaf springs equal to the allowable stress σ_{adm} . This stress is proportional to the moment in the leaf spring (2.3). However, the moment is not evenly distributed along the leaf spring. The part of the leaf spring that is subjected to the most intense bending moment must thus be located⁹. Equation (4.22) gives us the magnitude of the moment along the leaf spring. This formula brings into play the leaf spring deflection equation $y(x)$, which is relatively complex. It is therefore not easy to calculate the point x along the leaf spring at which the magnitude of the moment is highest. However, it is easy for us to understand the shape of the curve for the function $M_x(x)$ as shown in Figure 4.10.

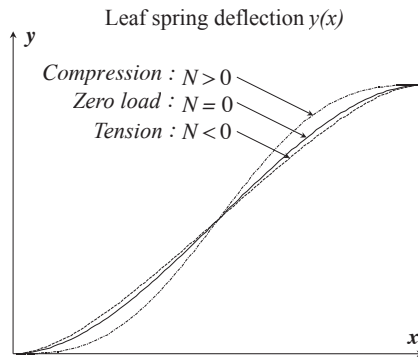


Figure 4.9 Curves of leaf spring deflection $y(x)$ for different tensile/compressive loads below the critical level (elastically stable range).

⁹ The *magnitude* of the moment is its absolute value $|M_x(x)|$.

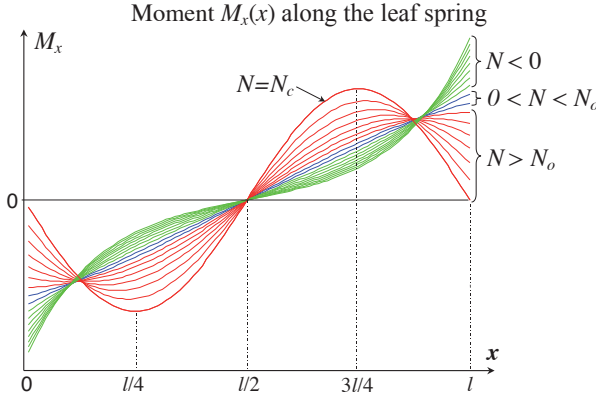


Figure 4.10 Curves of moment $M_x(x)$ along the leaf spring for different loads N . For tensile or compressive loads less than N_o , the extreme values of the moment always occur where the leaf springs are clamped (at $x = 0$ and at $x = l$). For greater loads ($N_o < N < N_c$), these extreme values no longer occur at these points. At the critical load $N = N_c$, it is possible to show that its extreme values occur at $x = l/4$ and $x = 3l/4$.

We see that, for compressive loads ranging between 0 and N_o , the magnitude of the moment is always highest where the leaf spring is clamped in the mobile and base blocks¹⁰:

$$\text{when } 0 \leq N \leq N_o \quad \text{then} \quad M_{\max}(N) = |M_x(0)| = |M_x(l)| = \frac{Nf + Pl}{2} \quad (4.44)$$

$$\text{and} \quad M_{\max}(N) \leq M_{\max}(0).$$

It is worth noting that over this range the maximum moment in the leaf spring decreases as the compressive load N increases; it is thus always less than the moment under zero load ($N = 0$).

For some tensile loads (negative N), we also see that the moment is highest where the leaf springs are clamped in the mobile and base blocks:

$$\text{when } N < 0 \quad \text{then} \quad M_{\max}(N) = |M_x(0)| = |M_x(l)| = \frac{Nf + Pl}{2} \quad (4.45)$$

$$\text{and} \quad M_{\max}(N) > M_{\max}(0).$$

Over this range, the maximum moment increases with the magnitude of the tensile force ($|N|$); it is thus always greater than the moment under zero load ($N = 0$).

¹⁰ M_{\max} is a function of the load N . M_x is a function of x (position along the leaf spring).

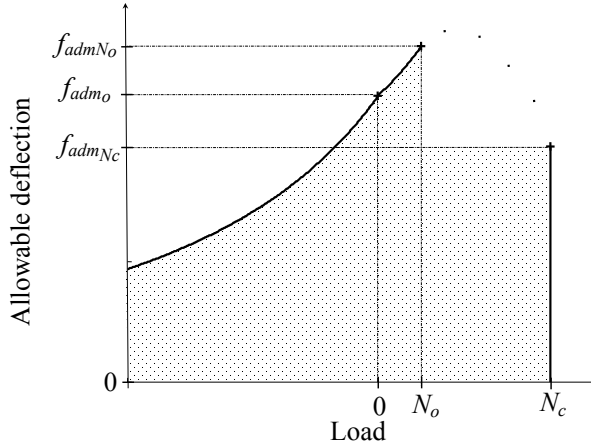


Figure 4.11 Allowable deflection as a function of load. This function comprises four sections. The first, for $N < 0$, is defined by (4.51). The second, for $0 \leq N < N_o$, is defined by (4.52). The third, for $N_o < N < N_c$, has not been calculated. All that we know about it is that it is located above $f_{adm}(N_c)$. The fourth section, for $N = N_c$, is a vertical straight line defined by (4.58). This figure corresponds to a case for which condition (4.55) is fulfilled. This graph may also be construed as a plot of the allowable load as a function of deflection. We have shown that all the load and deflection combinations corresponding to the shaded area do not produce stresses greater than the allowable stress.

From (4.33) and (4.39) we know that

$$P = Kf = \left(K_o - \frac{K_o}{N_o}N\right)f,$$

which allows us to eliminate P from equation (4.45) and find the moment at the beam's clamped ends as a function of the deflection f and the load N :

$$M = f \left(\frac{N}{2} + \frac{K_o l}{2} - \frac{K_o N l}{2N_o} \right). \quad (4.46)$$

According to (2.3), this moment, in applying a bending load on the leaf spring, induces a stress

$$\sigma_{flex} = \frac{6M}{bh^2}. \quad (4.47)$$

The force N also applies a compressive load on the leaf spring and induces a stress

$$\sigma_{comp} = \frac{N}{bh}. \quad (4.48)$$

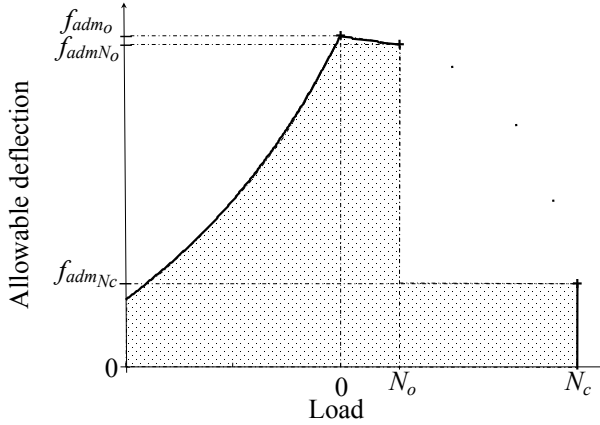


Figure 4.12 Like Figure 4.11, this figure presents the allowable deflection as a function of load. But, unlike the case in the previous figure, the condition (4.55) has here not been fulfilled. The consequence is that the allowable deflection decreases as the load increases between 0 and N_o .

The maximum stress that occurs in the leaf spring is the sum¹¹ of the stresses due to the bending moment and the compressive force

$$\sigma = \sigma_{flex} + |\sigma_{comp}|. \quad (4.49)$$

By combining (4.46), (4.47), (4.48) and (4.49), we obtain the stress as a function of load and deflection:

$$\sigma = 3f \left(\frac{Eh}{l^2} + \frac{N(\pi^2 - 12)}{bh^2\pi^2} \right) + \left| \frac{N}{bh} \right|. \quad (4.50)$$

By isolating f in this equation, we can deduce the formula for the allowable deflection as a function of the allowable stress (Fig. 4.11 and 4.12):

$$f_{adm} = \frac{hl^2\pi^2(N + bh\sigma_{adm})}{3bEh^3\pi^2 + 3l^2N(\pi^2 - 12)} \quad \text{valid for } N < 0 \quad (4.51)$$

$$f_{adm} = \frac{hl^2\pi^2(-N + bh\sigma_{adm})}{3bEh^3\pi^2 + 3l^2N(\pi^2 - 12)} \quad \text{valid for } 0 \leq N < N_o \quad (4.52)$$

¹¹ The term σ_{flex} is always positive regardless of the sign of N . As for the stress σ_{comp} , it is negative when the load exerts a tensile stress on the leaf springs (negative N). This is why the absolute value is used in (4.49).

Using this last formula, let us calculate the allowable deflection for $N = N_o$

$$f_{adm}(N_o) = \frac{4l^2 \sigma_{adm}}{Eh\pi^2} - \frac{h}{3}. \quad (4.53)$$

It is worth knowing whether the allowable deflection for the load N_o is greater or less than the deflection at zero load. We have

$$\frac{f_{adm}(N_o)}{f_{adm_o}} = \frac{12}{\pi^2} - \frac{Eh^2}{\sigma_{adm}l^2}. \quad (4.54)$$

from which we can deduce a condition for the slenderness of the leaf spring profile that will guarantee that the deflection for a load N_o will be greater than the deflection at zero load (the ratio (4.54) must be greater than 1).

$$\boxed{\frac{l}{h} > \left(\frac{(12 - \pi^2)\sigma_{adm}}{E\pi^2} \right)^{-\frac{1}{2}}}. \quad (4.55)$$

If this condition is fulfilled, then the allowable deflection increases as the compressive load N increases between 0 and N_o . If this condition is not fulfilled, then the allowable deflection decreases as the load increases over this same range.

According to Figure 4.10, we see that for loads ranging between N_o and N_c , the maximum moment no longer occurs where the leaf spring is clamped, but elsewhere, at two points symmetrically located on either side of the leaf spring midpoint. Let us use x_{max_1} to denote the position of the point that is nearest the base block and x_{max_2} to denote the position of the point nearest the mobile block. To find their positions, we need to solve the equation

$$\frac{d}{dx}M_x(x) = 0. \quad (4.56)$$

The function $M_x(x)$ (4.22) brings into play the deflection equation $y(x)$, which is relatively complex. We will therefore not explain the solution to this equation here¹². We will merely give its result for the special case where the load is at its critical level:

$$\text{when } N = N_c \quad \text{then} \quad x_{max_1} = \frac{l}{4} \quad \text{and} \quad x_{max_2} = \frac{3l}{4}. \quad (4.57)$$

¹² Equation (4.56) is difficult to solve for the general case. However, it becomes simplified in the special case where the load is at its critical level $N = N_c$. It can then be easily solved by an algebraic computation program, such as Mathematica.

The maximum moment is thus

$$M_{max} = |M_x(x_{max_1})| = |M_x(x_{max_2})| = \frac{bEfh^3\pi}{6l^2}.$$

By considering, as we have done above, the stress due to the bending moment M_{max} and the compressive stress due to the force N_c , we can calculate the allowable deflection:

$$f_{adm} = \frac{l^2 \sigma_{adm}}{Eh\pi} - \frac{h\pi}{3} \quad \text{valid for } N = N_c \quad (4.58)$$

Although we have not calculated the allowable deflection for loads ranging between N_o and N_c , we know that it is greater than $f_{adm_{N_c}}$. To construct stages with two parallel leaf springs, we can thus use all the deflection and load combinations corresponding to the shaded areas in Figure 4.11 and 4.12 without the risk of exceeding the allowable stress.

4.1.7 Summary

We have shown that the translational stiffness \bar{K} of a two parallel leaf spring stage depends on the load \bar{N} applied to it. At zero load, the stage has stiffness \bar{K}_o . This stiffness increases if the stage is subjected to a tensile load and decreases if the stage is subjected to a compressive load. For a compressive load equal to \bar{N}_o , the stiffness cancels itself out. For even higher loads, it becomes negative. If the compressive load reaches the critical level $\bar{N}_c = 4\bar{N}_o$, the system becomes unstable and the leaf springs fail by buckling. We have shown that, for tensile or compressive loads of a magnitude less than N_o , the simplified formula (4.43) makes it possible to calculate the stage stiffness with a relative error of less than 1.5% compared with the exact formula (4.38). For higher loads ranging up to the critical level \bar{N}_c , this formula remains usable even though the relative error increases (it remains less than 9%).

We have also shown that, under zero load, the deflection allowed for a two parallel leaf spring stage f_{adm_o} is given by formula (4.10). Subjecting the stage to a tensile load decreases the allowable deflection (4.51). Subjecting the stage to a compressive load increases (or decreases) the allowable deflection if condition (4.55) is fulfilled (or not fulfilled) ((4.51) and (4.52)).

4.2 Overconstrained stage with four parallel leaf springs

An overconstrained stage with four parallel leaf springs comprises two stages, each with two parallel leaf springs (Sect. 4.1) having the same mobile block

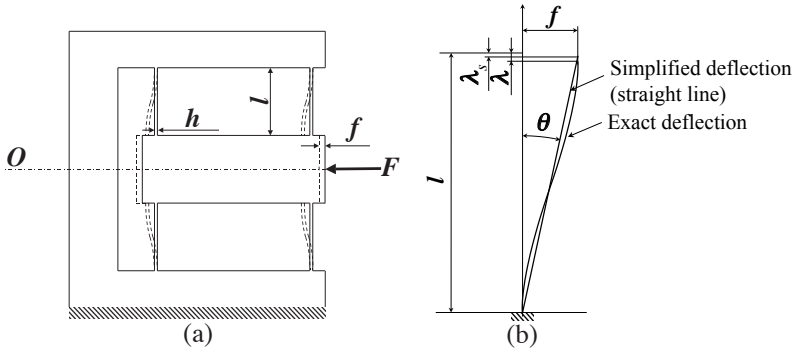


Figure 4.13 (a) Overconstrained stage with four parallel leaf springs: h , thickness of the leaf springs; b , width of the leaf springs; l , length of the leaf springs from one clamped end to the other. (b) Deflection of one of the leaf springs in the stage if no tensile force were produced. To calculate the vertical displacement λ , we use a simplified model that uses the assumption that the deflection is a straight line. According to this model, the tensile force N produced at the ends of the leaf spring is such that it elongates the leaf spring under pure tensile loading by a length λ_s .

(Fig. 4.13). The base and mobile blocks are assumed to be infinitely stiff. Since the system is symmetrical about axis O , the mobile block is subjected to a *rectilinear* translational displacement when force F is applied to it. As a result, this structure is commonly used when the *parabolic* (or *circular*) path¹³ of a two parallel leaf spring stage (or stage with four notch hinges) poses problems for the intended application.

4.2.1 Translational stiffness

When the mobile block moves away from its equilibrium position, a tensile force is created in the leaf springs, elongating them and exactly compensating for the longitudinal displacement the springs would undergo without tension (4.13). However, in Section 4.1.6 we saw that the translational stiffness of a stage with two leaf springs depends on the tensile or compressive load applied to it. In the present case, we are dealing with a tensile force that increases as the mobile block moves away from its middle position. The consequence of this is that the stiffness of the overconstrained stage with four parallel leaf springs is progressive.

The tensile force N created in the leaf springs is such that it cancels out the vertical displacement λ they would have if N were equal to 0. We saw in Section 4.1.6 that the transverse stiffness in vertical translational displacement is complex to calculate. To determine N , we will thus use the simplified model

¹³ When the length of the notch hinges in a stage with four notch hinges is very short, the path of the mobile block is approximately circular.

shown in Figure 4.13: we make the assumption that the leaf spring deflection is a straight line when $N = 0$. Now the vertical displacement is easily calculated:

$$\lambda_s = l(1 - \cos(\theta)) \simeq \frac{l\theta^2}{2}. \quad (4.59)$$

For small angles θ , we have

$$\theta = \arctg \frac{f}{l} \simeq \frac{f}{l}. \quad (4.60)$$

According to this model, the force N is such that it elongates the leaf spring under pure tensile loading by a length λ . Let us call K_{trac} the tensile/compressive stiffness of the leaf spring:

$$K_{trac} = \frac{bhE}{l}. \quad (4.61)$$

This gives us

$$N \simeq \frac{-bhEf^2}{2l^2}. \quad (4.62)$$

Replacing the N in equation (4.33) with (4.62) gives the equation of the force-deformation characteristic curve for the overconstrained stage with four¹⁴ parallel leaf springs:

$$F \simeq \frac{6bhEf^4}{3fl^3 - \sqrt{6}hl^3 \text{th} \frac{\sqrt{3}f}{h}}. \quad (4.63)$$

The stiffness of the overconstrained stage with four parallel leaf springs is the slope of this characteristic curve. Figure 4.14 shows the shape of this curve for a typical case.

4.2.2 Deflection

The tensile force N applies a bending moment and a tensile force to the leaf springs. Let σ_{trac} be the stresses caused by the tension and σ_{flex} be the stresses caused by the bending. σ_{trac} is constant along the entire length of the leaf spring

$$\sigma_{trac} = \frac{N}{bh}. \quad (4.64)$$

¹⁴ The four leaf springs in the stage behave, in terms of stiffness, like springs fitted in parallel. The stage stiffness is thus four times the stiffness of just one leaf spring. Several intermediate calculation steps that result in formula (4.63) are not detailed here.

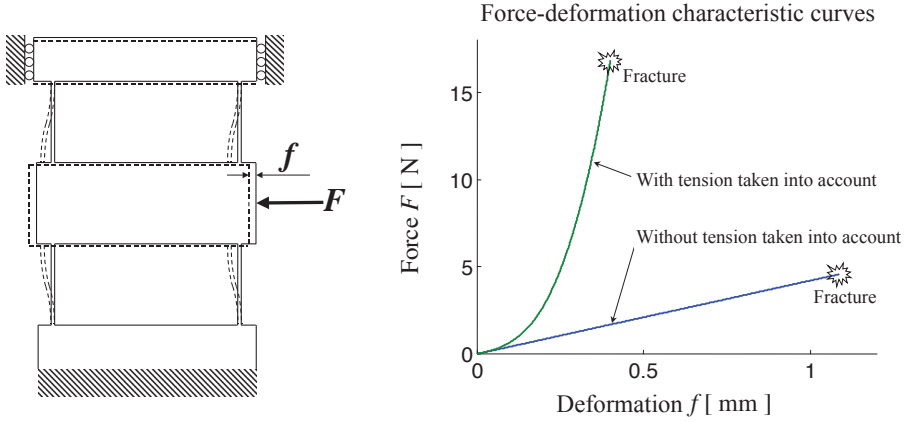


Figure 4.14 Force-deformation characteristic curves for an overconstrained stage with four parallel leaf springs. The following parameters were used to plot these curves: $h = 0.1$ mm; $l = 10$ mm; $b = 5$ mm; $\sigma_{adm} = 685$ MPa; $E = 210$ GPa. The top curve is the characteristic of the stage as described in Figure 4.13. This characteristic is progressive. The allowable deflection is 0.4 mm. The bottom curve is the characteristic of the stage without taking account of the tension in the leaf springs, which corresponds to an arrangement as illustrated in the left-hand diagram. The allowable deflection is 1.1 mm. The two curves are tangential at the origin.

σ_{flex} is directly proportional to the bending moment (2.3)

$$\sigma_{flex} = \frac{6M}{bh^2}.$$

For a tensile load, the bending moment M is highest where the leaf spring is clamped, just as we saw in Figure 4.10. Equation (4.21) gives us

$$M = \frac{Nf + Pl}{2}.$$

By replacing P with (4.33) and simplifying, we obtain

$$\sigma_{flex} = \frac{3Ef^3}{l^2 \left(\sqrt{6} f \coth \frac{\sqrt{\frac{3}{2}} f}{h} - 2h \right)}. \quad (4.65)$$

The sum of the stresses is $\sigma = \sigma_{trac} + \sigma_{flex}$:

$$\sigma = \frac{3Ef^3}{l^2 \left(\sqrt{6} f \coth \frac{\sqrt{\frac{3}{2}} f}{h} - 2h \right)} + \frac{Ef^2}{2l^2}. \quad (4.66)$$

This expression may be rearranged as follows:

$$\frac{\sigma}{E} = \frac{3(f/l)^3}{\sqrt{6}(f/l) \coth \frac{\sqrt{3/2}(f/l)}{h/l} - 2(h/l)} + \frac{(f/l)^2}{2}, \quad (4.67)$$

where σ/E , f/l and h/l are dimensionless parameters.

Figure 4.15 shows an example of how this stress varies as a function of deflection f and thickness h . As shown by (4.66), stress is directly proportional to E/l^2 .

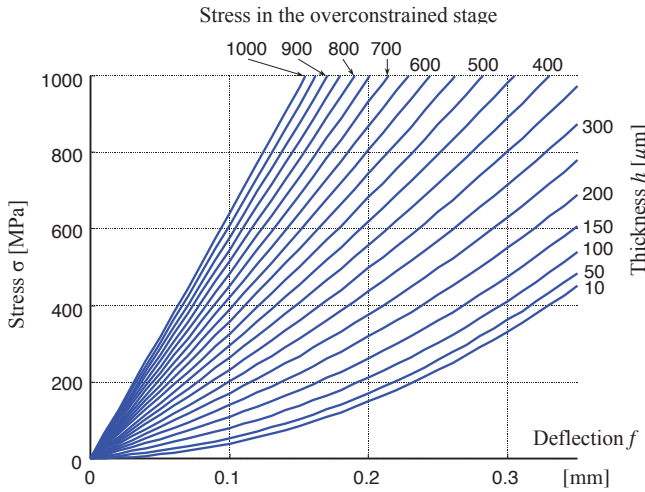


Figure 4.15 Maximum stress in the leaf springs in an overconstrained stage with four parallel leaf springs as a function of deflection f and the thickness h of the leaf springs. For this example, we chose $l = 10$ mm and $E = 210$ GPa.

4.2.3 Main conclusions

The force-deformation characteristic curve of the overconstrained stage with four parallel leaf springs is given by formula (4.63). Although we were unable to establish an explicit formula for the allowable deflection, we provide a formula that gives stress as a function of deflection (4.66) and makes it possible to calculate deflection iteratively. The deflection is much lower than that allowed in a two parallel leaf spring stage constructed with the same leaf springs. This is due to this structure being statically indeterminate, which induces tensile stresses in the leaf springs.

This structure is difficult to study due to its being statically indeterminate, which is why we had to resort to a wide range of simplifying assumptions. As a

result, the formulas presented in this section may, depending on the case, contain significant errors in relation to reality¹⁵. When designing this type of structure, it is crucial to take these uncertainties into account, especially by applying a large safety factor when calculating the allowable deflection. Nevertheless, the analysis presented in this section provides qualitative information that is extremely useful for designing an overconstrained stage with four parallel leaf springs:

- Its translational path is rectilinear (this is probably the only advantage this structure has over a conventional two parallel leaf spring stage).
- Its force-deformation characteristic curve is highly progressive.
- Its deflection is significantly lower than that of a two parallel leaf spring stage made with the same leaf springs.
- As this structure is statically indeterminate, it induces significant stresses (force N) in the base and mobile blocks. If these bodies are not designed to be very stiff, the model presented is no longer applicable.

4.3 Four prismatic notch hinge stage

4.3.1 Parameters

A four prismatic notch hinge stage comprises a fixed base block and a mobile block connected to each other by two identical parallel arms (Fig. 4.16). Each arm comprises a rigid segment deemed to be infinitely stiff and two identical, small, flexible leaf springs that we call *prismatic notch hinges*, located at each end of the stiff segment. To study this structure, we introduce a parameter ξ that depends on the ratio between the lengths of the flexible portions and the stiff portions of the arms:

$$\xi = \frac{2l_c}{l} \quad \text{where} \quad 0 < \xi \leq 1. \quad (4.68)$$

The length of the stiff segment is therefore given by $l_r = l - 2l_c = l(1 - \xi)$. Thus, by varying parameter ξ between 0 and 1, we go from a stiff segment that runs the entire length of the arm to a stiff segment of zero length, i.e., a continuous leaf spring. A two parallel leaf spring stage is therefore the special case of a four prismatic notch hinge stage where $\xi = 1$.

¹⁵ The consequence of the simplifying assumption that we used to calculate the tensile force N in the leaf springs, which assumes that the deflection of the leaf springs for $N = 0$ is a straight line (Fig. 4.13), is that we underestimate N . The real stress is therefore greater than the stress given by (4.66).

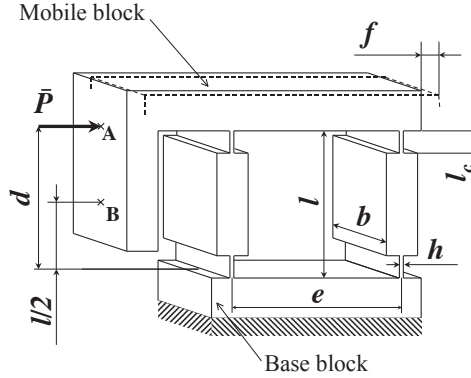


Figure 4.16 Four prismatic notch hinge stage: h , thickness of the prismatic notch hinges (small flexible leaf springs); l_c , length of the prismatic notch hinges; b , width of the arms; l , length of the arms; e , pitch of the arms; d , distance between the base block and the point of application of the driving force \bar{P} ; f , horizontal displacement; λ , vertical displacement.

4.3.2 Stiffness at zero load

A horizontal force \bar{P} acting on the mobile block deforms the two arms in a virtually identical manner, resulting in a translational displacement of the mobile block through a distance f .

Let us isolate one of the two arms. Just as we demonstrated in Section 4.1 for a two parallel leaf spring stage, it is easy to show that when the force \bar{P} acts on the mobile block at point B, located at a distance $l/2$ from the base block, it does not induce any tensile or compressive force in the arms. We consider that this is the case in the entire subsequent analysis. The equilibrium of moments acting on an arm allows us to show, just as in Section 4.1, that a horizontal force $P = \bar{P}/2$ and a moment $M = Pl/2$ both act at each of the ends of the arm, and thus that the distribution of the bending moment along the arm, described by equation (4.22), applies here as well. We can thus deduce that the bending moment is zero at the middle of the arm, at $x = l/2$.

Now let us isolate the bottom half of one of the arms. Only one force P acts at its end, located at $x = l/2$. As the arm and the distribution of the moment are symmetrical about the point located at $x = l/2$, we can thus deduce that the deflection of this point is half the total deflection of the arm. The deflection of the half-arm is thus $f_b = f/2$.

Lastly, let us isolate the bottom prismatic notch hinge with force P and a moment $M_c = Pl(1 - \xi)/2$ acting at its end. Let us call the deflection and the angle of rotation f_c and α_c , respectively. This gives us, for small angles:

$$f_b = f_c + \sin \alpha_c l(1 - \xi)/2 \simeq f_c + \alpha_c l(1 - \xi)/2.$$

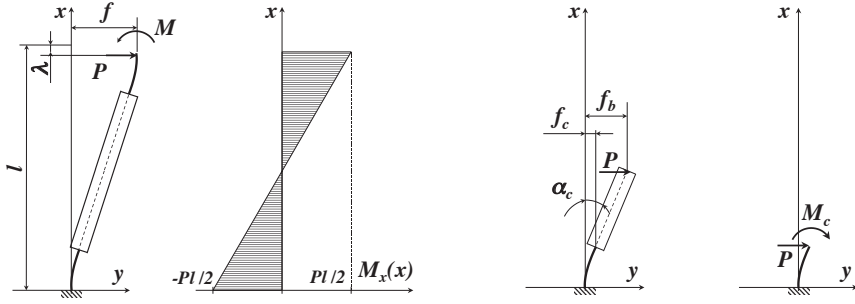


Figure 4.17 Model used to calculate the translational stiffness (at zero load) of a four prismatic notch hinge stage.

Using the parameters defined in Section 3.1.2 and applying the superposition principle, let us calculate f_c and α_c .

$$f_c = \frac{P}{K_{fP}} + \frac{Pl(1-\xi)}{2K_{fM}} \quad \text{and} \quad \alpha_c = \frac{P}{K_{\alpha P}} + \frac{Pl(1-\xi)}{2K_{\alpha M}}.$$

If we use formulas (3.1) and replace l by the length of the prismatic notch hinge $l_c = \xi l/2$, we can thus deduce the translational stiffness of the arm $K_o = P/f = P/(2f_b)$

$$K_o = \frac{bh^3E}{\xi(3-3\xi+\xi^2)l^3}. \quad (4.69)$$

Knowing that $\bar{P} = 2P$, we can thus deduce the translational stiffness of a four prismatic notch hinge stage

$$\bar{K}_o = \frac{2bh^3E}{\xi(3-3\xi+\xi^2)l^3}. \quad (4.70)$$

4.3.3 Deflection at zero load

The moment allowed for the prismatic notch hinge is, according to formula (2.3), $M_{adm} = bh^2\sigma_{adm}/6$. The maximum allowable force is thus $P_{adm} = 2M_{adm}/l$ and the allowable deflection is $f_{adm} = P_{adm}/K$. We thus obtain:

$$f_{adm} = \frac{\xi(3-3\xi+\xi^2)l^2\sigma_{adm}}{3Eh}. \quad (4.71)$$

4.3.4 Critical loading (buckling)

Let us consider that only a vertical compressive force \bar{N} is acting at the center of the mobile block. This force distributes itself equally onto the two arms,

compressing each with a force $N = \bar{N}/2$. Let us constrain the horizontal displacement of the mobile block but leave it free to move vertically. When the vertical force exceeds the critical load \bar{N}_c , the two arms buckle, taking the shape illustrated in Figure 4.18. For this deformation mode, Euler's formula (4.17), where $l_o = \xi l/2$, allows us to find the critical load for an arm:

$$N_c = \frac{4\pi^2 EI}{\xi^2 l^2}. \quad (4.72)$$

Knowing that $\bar{N} = 2N$, we can thus deduce the critical load for a four prismatic notch hinge stage:

$$\bar{N}_c = \frac{8\pi^2 EI}{\xi^2 l^2}. \quad (4.73)$$

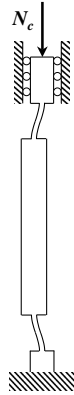


Figure 4.18 Buckling of one of the arms in a four circular notch hinge stage.

4.3.5 Tensile/compressive loading: simplified model

In this section, we study the behaviour of a four prismatic notch hinge stage subjected to a load \bar{N} below the critical level \bar{N}_c .

Simplifying assumptions

The model we use here makes significant simplifying assumptions:

- The first assumption is that the compressive load does not modify the deflection of the arms.
- The second assumption is that parameter ξ is nearly 0, i.e., the prismatic notch hinges are very short (small l_c) and the length of the stiff segment is nearly l .

- The third assumption follows from the first two and considers the prismatic notch hinges to be imaginary pivot points having an angular stiffness that is not zero. This assumption allows us to consider that the translational path taken by the mobile block is a circular arc of radius l .

Parabola that closely approximates to a circle

First let us make a fourth assumption, where we consider the translational stiffness (4.70) of a four prismatic notch hinge stage to be zero: $\bar{K}_o = 0$. The translation bearing thus acts like an imaginary circular-arc-shaped slideway whose path equation relates to the coordinates visible in Figure 4.19:

$$\lambda_{circle}(f) = -l + \sqrt{(l^2 - f^2)}. \quad (4.74)$$

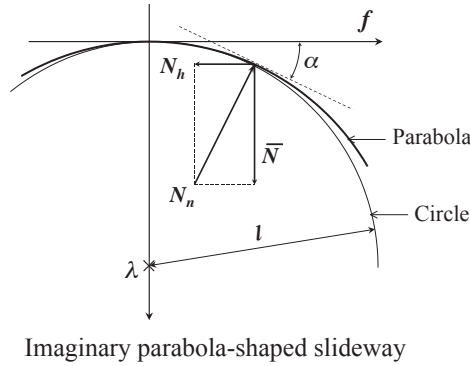


Figure 4.19 Simplified model for calculating the stiffness under tensile and compressive loads of a four prismatic notch hinge stage. In the case of low-amplitude displacements, the arcs of the circle and the parabola effectively merge.

If it is positive, the load \bar{N} thus tends to move the ‘slide’ from its middle position. The slide thus acts as if it had a negative translational stiffness \bar{K}_n . In Section 4.1.5 we saw that if the path taken by the mobile block is a parabola, then \bar{K}_n is constant along the entire path. In the present case, the path is circular, not parabolic, so \bar{K}_n varies depending on the position along the path. For small angular displacements of the arms, it is quite possible to use a parabolic arc to approximate, with a very small error, to the circular arc. The parabola of equation

$$\lambda_{parabole}(f) = \frac{-f^2}{2l} \quad (4.75)$$

has the same first and second derivatives as the circular arc at $f = 0$. It therefore virtually coincides with the curvilinear slideway. We can now make our fifth and final assumption, which is that the mobile block follows the parabolic path

described by (4.75). The slideway exerts a reaction N_n on the slide that is normal to its path. A horizontal opposing force N_h must be exerted to maintain the slide in position. Let α be the slope of the parabola. This yields:

$$N_h = \bar{N} \tan \alpha = \bar{N} \frac{d}{df} \lambda_{parabole} = \frac{-\bar{N}}{l} f = \bar{K}_n f.$$

The translation bearing thus acts as if it had a constant negative stiffness:

$$\bar{K}_n = \frac{-\bar{N}}{l}. \quad (4.76)$$

In the case where the load \bar{N} is negative (tensile load), formula (4.76) remains valid and the translation bearing acts as if it had a constant positive stiffness.

If we reconsider the stiffness \bar{K}_o that we had assumed to be zero (fourth simplifying assumption), the total stiffness of the stage then becomes $\bar{K}_{tot} = \bar{K}_o + \bar{K}_n$. We can thus conclude from this that the translational stiffness of a four prismatic notch hinge stage depends on the compressive load \bar{N} applied to it, and that it is approximately constant along the entire deflection for a given load \bar{N} :

$$\bar{K}_{tot} \simeq \bar{K}_o - \frac{\bar{N}}{l}. \quad (4.77)$$

This allows us to see that there is a load \bar{N}_o that effectively makes the stiffness \bar{K}_{tot} zero:

$$\bar{N}_o \simeq l \bar{K}_o. \quad (4.78)$$

4.3.6 Tensile/compressive loading: complete model

As in the previous section, here we study the behaviour of a four prismatic notch hinge stage subjected to a load \bar{N} below the critical level \bar{N}_c . But in the analysis that follows, we will not use the many simplifying assumptions we used previously.

Let us consider once again that the force \bar{P} is applied to point B and that it thus does not induce any tensile/compressive forces in the leaf springs. This force causes the mobile block to move through a distance f . Since the load \bar{N} is applied at the center of the mobile block, it will distribute itself equally between the two arms, producing on each a compressive force $N = \bar{N}/2$. Let us isolate one of the two arms. The forces and moments acting on its ends are $P = \bar{P}/2$, $M = Pl/2$ and N . Since the leaf spring is in equilibrium, these three parameters are not independent. Equilibrium of moments gives

$$M = \frac{Nf + Pl}{2}. \quad (4.79)$$

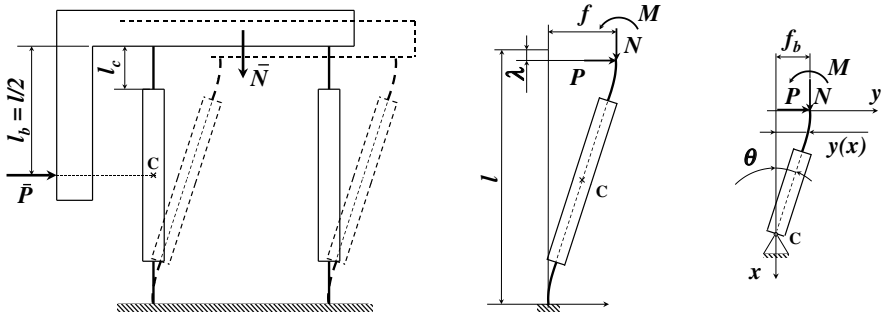


Figure 4.20 Model used to calculate the behaviour, under tensile and compressive loads, of a four prismatic notch hinge stage.

Since both the distribution of the moment and the arm geometry are symmetrical about point C, located at the middle of the arm, we can thus deduce that the arm deflection will also be symmetrical about C. Now, if we isolate the upper half of the arm, we obtain the system shown in Figure 4.20. The deflection of the half-arm is $f_b = f/2$. The length of the half-arm is $l_b = l/2$. When the axes are drawn as in the figure, the distribution of the bending moment along the beam is given by:

$$M_x(x) = M - N(f_b - y(x)) - Px. \quad (4.80)$$

We can thus deduce the differential equation for the deflection:

$$y''(x) + \frac{N}{EI}y(x) = \frac{P}{EI}x - \frac{M}{EI} + \frac{Nf_b}{EI}, \quad (4.81)$$

This is a second-order linear differential equation with constant coefficients of the following type:

$$y'' + k^2y = k_ax + k_b \quad (4.82)$$

where

$$k = \sqrt{\frac{N}{EI}}; k_a = \frac{P}{EI}; k_b = \frac{Nf_b - M}{EI}.$$

The general solution of the equation without the right-hand side is of the type:

$$y_g = C_1 \cos kx + C_2 \sin kx. \quad (4.83)$$

It is easy to find a particular solution of the equation with the right-hand side

$$y_p = ax + b \text{ where } a = \frac{P}{N} \text{ and } b = \frac{-Pl_b}{N}. \quad (4.84)$$

The general solution of the equation with the right-hand side is the sum of y_p and y_g :

$$y(x) = C_1 \cos kx + C_2 \sin kx + ax + b. \quad (4.85)$$

Its derivative is:

$$y'(x) = -kC_1 \sin kx + kC_2 \cos kx + a. \quad (4.86)$$

The conditions at the ends of the leaf spring are known:

$$y(0) = f_b ; y'(0) = 0 ; y'(\xi l_b) = -\theta = \frac{-y(\xi l_b)}{(1 - \xi)l_b}.$$

The first two conditions make it possible to find

$$C_1 = f_b + \frac{Pl_b}{N} \quad \text{and} \quad C_2 = \frac{-P}{kN}. \quad (4.87)$$

To simplify the way the third condition is written, let

$$c = \cos k\xi l_b, \quad s = \sin k\xi l_b \quad \text{and} \quad t = (1 - \xi)l_b.$$

We thus obtain the equation

$$-kf_b s - \frac{kPl_b}{N} - \frac{Pc}{N} + \frac{P}{N} = \frac{1}{t} \left(-f_b c - \frac{Pl_b c}{N} + \frac{Ps}{kN} - \frac{P\xi l_b}{N} + \frac{Pl_b}{N} \right).$$

Rearranging this equation to obtain an expression for P gives us:

$$P = f_b \frac{N(ks - c)}{-ktsl_b - ct + t + lc - \frac{s}{k} + \xi l_b - l_b}, \quad (4.88)$$

which allows us to find the translational stiffness of a half-arm in a four prismatic notch hinge stage subjected to a compressive load $K_b = P/f_b$.

However, knowing that $f = 2f_b$, the translational stiffness of an arm is given by $K = P/f = P/(2f_b) = K_b/2$, and knowing that $\bar{P} = 2P$, we can thus deduce that the translational stiffness of a four prismatic notch hinge stage \bar{K} is equal to the stiffness \bar{K}_b of a half-arm: $\bar{K} = \bar{P}/f = 2P/f = 2K = K_b$. From (4.88) we obtain:

$$\bar{K} = \frac{N(ks - c)}{-ktsl_b - ct + t + lc - \frac{s}{k} + \xi l_b - l_b}. \quad (4.89)$$

Transverse stiffness in vertical translational displacement

Let us calculate the displacement λ under the effect of the load N on the half-arm studied above. The load causes bending and tensile/compressive stress in the arm. Let λ_{flex} be the displacement induced by the bending moment and λ_{comp} be the displacement induced by the tensile/compressive stress. According

to (4.11), and knowing that $l_c = \xi l_b$, the bending moment changes the deflection of the prismatic notch hinge, resulting in a shortening

$$\lambda_{flex1} = \int_0^{\xi l_b} (y'(x))^2 dx \quad (4.90)$$

of its length as projected onto a vertical axis. The change in deflection induces a change in the angle of the stiff segment, producing an additional vertical displacement

$$\lambda_{flex2} = l_b(1 - \xi)(1 - \cos(\arctg y'(\xi l_b))). \quad (4.91)$$

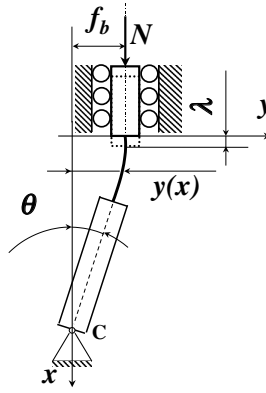


Figure 4.21 Transverse stiffness in vertical translational displacement of a half-arm: $K_{cb} = N/\lambda$.

The tensile/compressive stresses lead to a shortening of the prismatic notch hinge

$$\lambda_{comp} = \frac{N l_c}{h b E}. \quad (4.92)$$

The total displacement is thus

$$\lambda = \lambda_{flex1} + \lambda_{flex2} + \lambda_{comp}. \quad (4.93)$$

The transverse stiffness of the half-arm is $K_{cb} = N/\lambda$. The transverse stiffness of a whole arm is $K_c = N/(2\lambda)$, and the transverse stiffness of the stage is $\bar{K}_c = 2K_c = K_{cb}$. Thus, the transverse stiffness of a four prismatic notch hinge stage is equal to the transverse stiffness of a half-arm:

$$\boxed{\bar{K}_c = \frac{N}{\lambda}.} \quad (4.94)$$

Algebraic calculation of this stiffness is tedious. However, it is easy to perform this calculation numerically by computer for typical magnitudes. Such a calculation makes it possible to ascertain the behaviour of a four prismatic notch hinge stage under a compressive load qualitatively. Figure 4.22 shows the shape of the force-deformation characteristic curves together with those of the stiffness \bar{K}_c . We see that the transverse stiffness decreases as the deflection increases and that it is degressive (the stiffness decreases as the load increases).

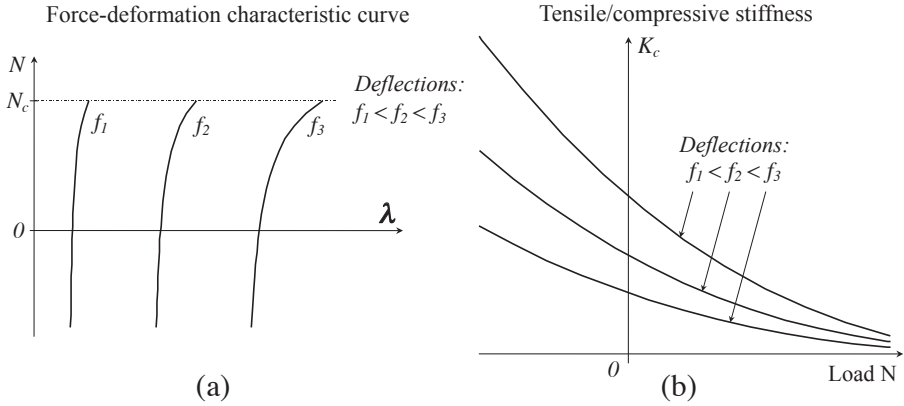


Figure 4.22 (a) Force-deformation characteristic curves in vertical translational displacement. (b) The transverse stiffness in vertical translational displacement is the derivative of the force-deformation characteristic curve.

4.3.7 Trade-off

Let us imagine that we have to design a four prismatic notch hinge stage according to a set of specifications requiring a specific form factor (length l and thickness b), a given deflection (f) and a certain material (E and σ_{adm}). These specifications can be met by an infinite number of combinations of parameters ξ and h . We look for the combinations that

- A) Maximise the thickness of the prismatic notch hinges to facilitate their manufacture and reduce their tolerance sensitivity.
- B) Maximise the critical load.
- C) Minimise the slenderness of the prismatic notch hinges as well as facilitate their manufacture.
- D) Maximise the transverse stiffness in vertical translational displacement.
- E) Minimise the translational stiffness.

The aims of all these criteria are either to facilitate the manufacture of the translation bearing or improve its mechanical properties. However, they do not all lead to the same optimum combination of parameters ξ and h . In the

following sections (A to E), we will determine each optimum combination and discuss the compromises.

A Maximisation of the thickness h

For a given value of ξ , formula (4.71) gives us the maximum thickness compatible with the set of specifications:

$$h = \frac{\xi(3 - 3\xi + \xi^2)l^2\sigma_{adm}}{3Ef}. \quad (4.95)$$

Meeting criterion A thus amounts to examining the relationship between parameters ξ and h (Fig. 4.23).

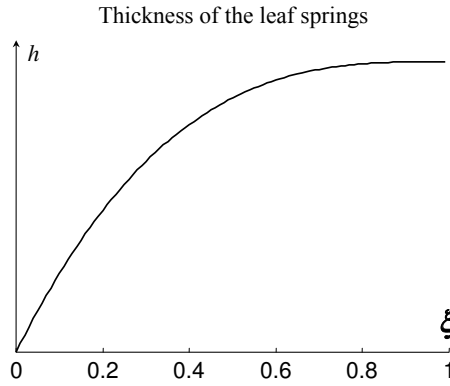


Figure 4.23 Maximum thickness h compatible with the required specifications as a function of the parameter ξ (4.95).

B Maximisation of the critical load \bar{N}_c

For a given value of ξ , the value of h that maximises the critical load is its maximum value as given by (4.95). This equation allows us to eliminate¹⁶ h from (4.72) and obtain the critical load as a function of parameter ξ :

$$N_c(\xi) = \frac{\xi(3 - 3\xi + \xi^2)^3 bl^4 \pi^2 \sigma_{adm}^3}{81E^2 f^3}. \quad (4.96)$$

¹⁶ The reader is reminded that $I = bh^3/12$.

The function $N_c(\xi)$ is a bell curve whose shape is shown in Figure 4.24. To find the maximum of this function, let us differentiate it:

$$\frac{d}{d\xi} N_c(\xi) = \frac{(3 - 3\xi + \xi^2)^2 (3 - 12\xi + 7\xi^2) b l^4 \pi^2 \sigma_{adm}^3}{81 E^2 f^3}. \quad (4.97)$$

Several values of ξ make this derivative zero. The solution that interests us lies between 0 and 1:

$$\xi_{optimal} = \frac{6 - \sqrt{15}}{7} \simeq 0.3. \quad (4.98)$$

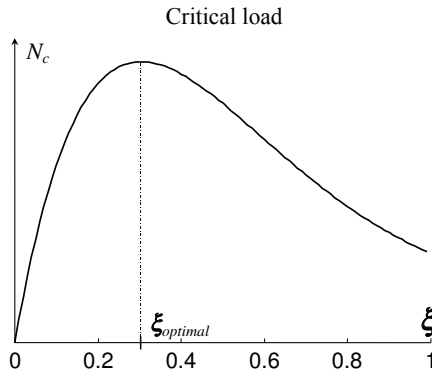


Figure 4.24 Critical load as a function of parameter ξ . There is a value of ξ that maximises the critical load: $\xi_{optimal} \simeq 0.3$.

Equation (4.95) gives us the thickness $h_{optimal}$ corresponding to $\xi_{optimal}$. We thus know the parameter combination that maximises the critical load.

Now let us look for the length of the prismatic notch hinges corresponding to $\xi_{optimal}$. Equation (4.68) gives us:

$$l_{c optimal} = \frac{6 - \sqrt{15}}{7} \times \frac{l}{2} \simeq \frac{l}{6.58}. \quad (4.99)$$

Hence, the stage offering the highest critical load is one where the length of the prismatic notch hinges l_c is equal to approximately one-seventh of the total length of the arms.

C Minimisation of the slenderness of the notch hinge profile ε

We define the slenderness of prismatic notch hinges as being the ratio between their length and their thickness:

$$\varepsilon = \frac{l_c}{h}. \quad (4.100)$$

Thus, for a given value of ξ , the value of h that minimises the slenderness is its maximum value as given by (4.95). If, in (4.100), we replace h by (4.95) and l_c by $\xi l/2$, we obtain the slenderness as a function of ξ :

$$\epsilon(\xi) = \frac{3Ef}{2(3 - 3\xi + \xi^2)l\sigma_{adm}}. \quad (4.101)$$

Over the range $0 < \xi \ll 1$, this function increases continuously (Fig. 4.25), i.e., the slenderness of the flexible notch hinges increases as the parameter ξ increases. In practice, it is therefore worthwhile to decrease ξ to minimise the slenderness.

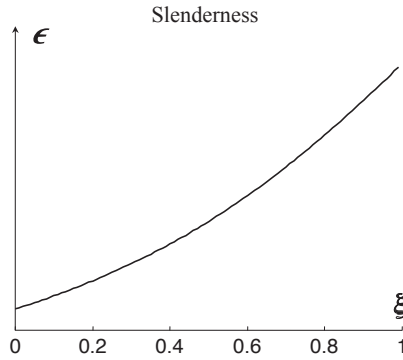


Figure 4.25 Slenderness of prismatic notch hinges as a function of parameter ξ .

D Maximisation of the transverse stiffness in vertical translational displacement \bar{K}_c

For a given value of ξ , the value of h that maximises the critical load is its maximum value as given by (4.95). In Figure 4.8, we plotted the shape of the curve of transverse stiffness in vertical translational displacement K_c (Sect. 4.3.6) of the stage as a function of load N . Using relationship (4.95), we can, in the same way, plot the shape of the transverse stiffness curve as a function of parameter ξ for various loads N (Fig. 4.26). We see that this criterion dictates choosing a parameter ξ that is as small as possible.

E Minimisation of the translational stiffness

Formula (4.70) indicates that, to minimise the translational stiffness, ξ must be maximised and h must be minimised.

This last constraint on h is contrary to that obtained with the four previous criteria (A to D). If we opt not to meet it, and instead of minimising h , we

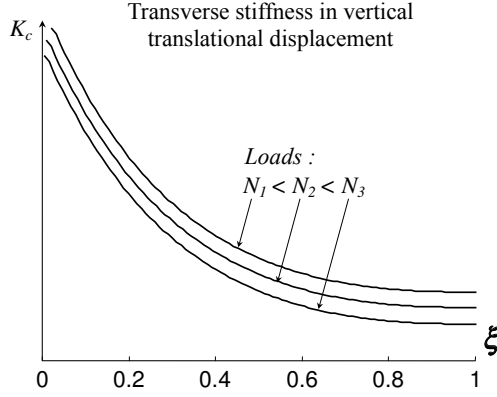


Figure 4.26 Curves of transverse stiffness in vertical translational displacement K_c as a function of parameter ξ . We see that the smaller ξ is, the greater the stiffness.

maximise it according to (4.95), we thus obtain the translational stiffness as a function of ξ :

$$\bar{K}_o = \frac{2\xi^2(3 - 3\xi + \xi^2)^2 bl^3 \sigma_{adm}^3}{27E^2 f^3}. \quad (4.102)$$

This function is plotted in Figure 4.27. We see that the smaller ξ is, the lower the translational stiffness.

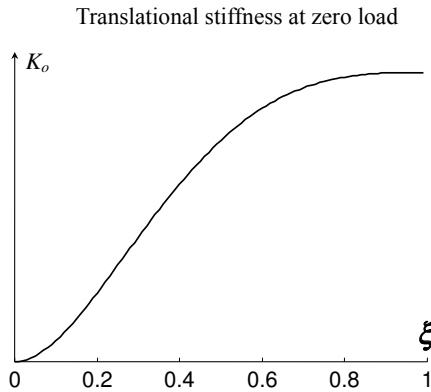


Figure 4.27 Translational stiffness at zero load N as a function of parameter ξ (4.102). The smaller ξ is, the lower the translational stiffness.

Discussion of the trade-offs

The first four criteria dictate that parameter h be maximised. We have shown that meeting this requirement amounts to examining the relationship between parameters ξ and h (4.95). Thus, searching for the optimum combination of the two parameters boils down to searching for one optimum parameter $\xi_{optimal}$.

Criteria C, D and E all dictate that ξ be maximised. But, as criterion A shows, the smaller ξ is, the more the thickness h of the notch hinges decreases. However, a technological limit makes it impossible to manufacture flexible notch hinges having a thickness below a certain threshold. It is this technological limit that determines the value of $\xi_{optimal}$ for these three criteria.

Criterion B dictates choosing $\xi_{optimal} \simeq 0.3$. If the corresponding thickness h can be manufactured, then it is this value of ξ that must be chosen. If the corresponding thickness h is too thin to be manufactured, this practical limit again determines the value of ξ and the optimum coincides with that of criteria C, D and E.

In practice, priority is usually given to criteria A, C, D and E rather than to B. Parameters ξ and h are therefore chosen in the following manner:

- The smallest thickness h practicable with the technology used is determined¹⁷ (also taking the tolerances into account).
- The corresponding parameter ξ is calculated using formula (4.95).
- The length of the notch hinge is calculated using formula (4.68).

4.4 Four circular notch hinge stage

In the previous section, we showed that stiffening the central portion of the leaf springs in a two parallel leaf spring stage in order to convert it into a four prismatic notch hinge stage makes it possible to improve the stage's properties in terms of allowable load and stiffness ratio. However, prismatic notch hinges have a major drawback in that they have sharp corners that act as stress concentrators. Notch hinges of different profiles can be used to alleviate this disadvantage. A first solution consists in using transition fillets where the prismatic notch hinges join the stiff bodies (Fig. 4.29c). A second, and very common, solution consists of using circular notch hinges (Fig. 4.29a). This geometry has the advantage of being simple to describe: three parameters – e , r and b – suffice to describe it in full. It is very easy to program in the numerical control system of machine tools or can be achieved simply by drilling. Other relatively simple geometries, such as elliptical (Fig. 4.29d) or hyperbolic profiles (Letonje and Janezic, 1999) may also be used. However, they are not discussed here.

¹⁷ The smallest thicknesses that may be manufactured by wire EDM usually range between

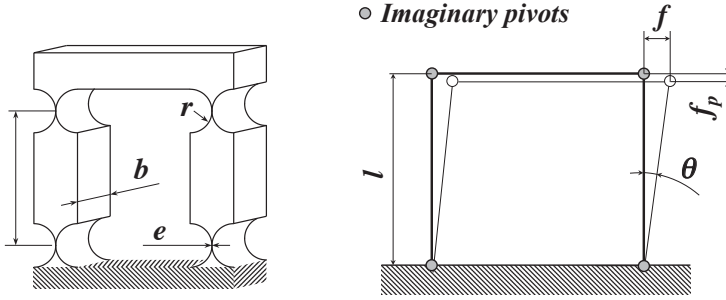


Figure 4.28 Four circular notch hinge stage and simplified geometrical model: e , thickness of the notch hinge at its narrowest point; r , radius of the notches; b , width; l , length of the arms between the centers of the notch hinges.

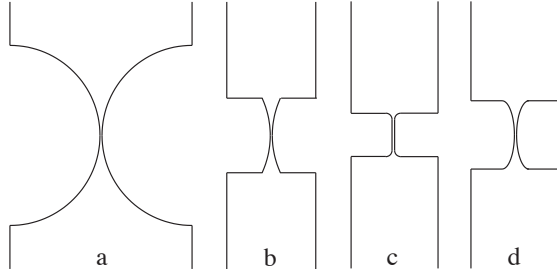


Figure 4.29 Different notch hinge profiles that mitigate the stress concentration effects: (a) circular notch hinge; (b) truncated circular notch hinge; (c) prismatic notch hinge with transition fillets; (d) elliptical notch hinge.

Translational stiffness

SIMPLIFIED FORMULA: To model this structure simply, we make the following assumptions:

- The circular notch hinges behave like imaginary pivot points whose angular stiffness is $K_{\alpha M}$ and whose other stiffnesses are infinite (Fig. 4.28).
- The angles of rotation of the pivots are small enough to be approximately equal to their sines: $\sin \theta \simeq \theta$.

By adopting this simplified model, the translational stiffness can be very easily calculated using the energy method. For a displacement of length f of the mobile block, the four pivots deflect through an angle $\theta \simeq f/l$. Knowing that the mechanical work provided by the force F to induce the displacement f is equal to the elastic energy stored in the four pivots, we can write:

$$\frac{1}{2} K f^2 \simeq 4 \times \frac{1}{2} K_{\theta} \theta^2 \quad (4.103)$$

from which we obtain the linear stiffness of the stage as a function of the angular stiffness of the pivots:

$$K \simeq \frac{4K_\theta}{l^2}. \quad (4.104)$$

By replacing K_θ by (3.20) we obtain:

$$K \simeq \frac{8Ebe^{2.5}}{9\pi l^2 \sqrt{r}}. \quad (4.105)$$

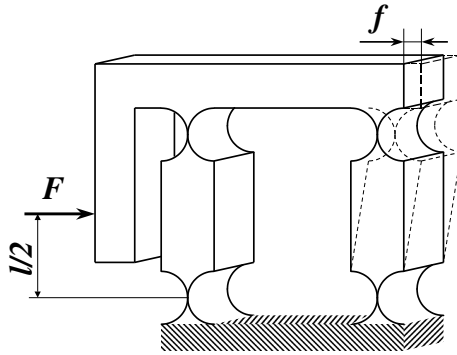


Figure 4.30 Translational stiffness and deflection of a four circular notch hinge stage: for a horizontal force F , applied to the movable platform, inducing a displacement f , we obtain a translational stiffness $K = F/f$. The linear deflection f_{adm} is the displacement that induces stresses in the notch hinges equal to σ_{adm} .

SCALING LAWS: $K^* = E^*$, $K^* = b^*$, $K^* \simeq 1/l^{*2}$, $K^* \simeq e^{*2.5}$, $K^* \simeq 1/\sqrt{r^*}$.

EXACT FORMULA: In reality, the circular notch hinges do not behave like pivot points, but rather like beams of variable cross section subjected to bending. Just as we calculated the translational stiffness of a four prismatic notch hinge stage (Sect. 4.3.2 and Fig. 4.17), we can determine the translational stiffness of a stage with four notch hinges of any profile:

$$K = \frac{2}{\frac{l^2}{2K_{\theta M}} - \frac{l}{K_{\theta P}} - \frac{l}{K_{fM}} + \frac{2}{K_{fP}}}. \quad (4.106)$$

The terms K_{fP} , $K_{\alpha P}$, K_{fM} and $K_{\alpha M}$ characterise the notch hinges (Sect. 3.1.2). We have calculated these terms for the case of circular notch hinges (Sect. 3.5).

Translational deflection

SIMPLIFIED FORMULA: Knowing the angular deflection of a circular notch hinge (3.21), the simplified model allows us to calculate the translational deflection:

$$f \simeq \frac{3\pi l \sigma_{adm} r^{0.5}}{4E e^{0.5}}. \quad (4.107)$$

SCALING LAWS: $f^* = \sigma_{adm}^*$; $f^* = 1/E^*$; $f^* \simeq l^*$; $f^* \simeq 1/\sqrt{e^*}$; $f^* \simeq \sqrt{r^*}$.

Vertical displacement

According to the simplified geometrical model, the mobile block moves along a circular path. A horizontal displacement f of the mobile block is accompanied by a vertical displacement:

$$f_v = l - \sqrt{l^2 - f^2} = l(1 - \cos \theta) \simeq \frac{l\theta^2}{2}. \quad (4.108)$$

Transverse translational stiffness

SIMPLIFIED FORMULA: Using the same simplified geometrical model as that for the translational stiffness of a four circular notch hinge stage, we can determine its transverse translational stiffness:

$$K^t \simeq \frac{4K_{\alpha M}^t}{l^2}, \quad (4.109)$$

where $K_{\alpha M}$ is the transverse angular stiffness of a notch hinge (3.26). We make the assumption here that the solid portion of the arms is infinitely stiff when compared to the stiffness of the notch hinges. This assumption is reasonable in the case where the notch hinges bend in the natural direction. However, in the direction at right angles to this, the stiffness of the notch hinges is much higher and it would be negligent to disregard the bending of the solid portion of the arms. The stiffnesses obtained may exceed those exhibited in reality. To obtain a better approximation of the total deflection f , it is necessary to add the deflection and angle made by the solid portion of the arms, which is none other than a prismatic beam subjected to bending.

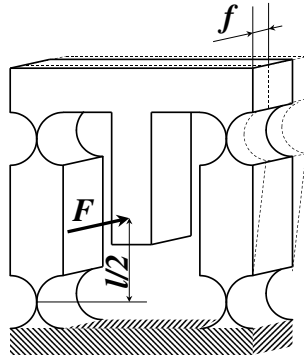


Figure 4.31 Transverse translational stiffness of a four circular notch hinge stage: a horizontal force F is applied to the movable platform at mid-height of the arms, the direction of which is at right angles to the natural displacement of the stage. This force induces a translational displacement of the platform through a distance f . We define the transverse translational stiffness of the stage as $K^t = F/f$.

4.5 Conclusion on linear translation bearings

In this analysis of the most common types of linear translation bearings, we have shown that stiffening the central portion of the leaf springs of a two parallel leaf spring stage, and reducing their thickness so that the allowable deflection remains unchanged, makes it possible to increase the stiffness ratios of this type of translation bearing. Compared with prismatic notch hinges, circular notch hinges also possess the advantage of not having sharp corners that could act as stress concentrators. We therefore recommend using stages with four circular notch hinges whenever the manufacturing process permits this.

Rotational flexures

This chapter discusses the simplest and most common types of rotational bearings – the *separate cross spring pivot*, the *joined cross spring pivot*, the *RCC (Remote Center Compliance) pivot with leaf springs*, the *RCC pivot with four notch hinges* and the *cross pivot with four notch hinges*. For each of these structures, we calculate the angular stiffness and deflection as well as the parasitic translation that accompanies rotation, and we discuss the effect of radial loads on the angular stiffness and the respective allowable loads. The comparison of these various pivots leads us to the following conclusions: for the same form factor and deflection, pivots with notch hinges offer a higher radial stiffness than pivots with leaf springs. We therefore recommend the use of pivots with notch hinges. Among these, the *cross pivot with four notch hinges* has the highest angular deflection (it is nearly twice that of its constituent notch hinges). However, in its usual configuration, the cross pivot has the drawback of having two kinematic joints that cross over and do not allow it to be made in a single plane, thus complicating its manufacture. As for the *RCC pivot with four notch hinges*, it can be made in a single plane. However, it has the drawback of having an angular deflection that, at best, is only half that of the cross pivot. The parasitic translation and the displacement of the instantaneous center of rotation of the RCC pivot and the cross pivot are similar.

5.1 Separate cross spring pivot

This type of bearing is commonly used to make flexure pivots from separate parts (assemblies of stiff blocks and leaf springs). It comprises two orthogonally arranged leaf springs that connect the mobile block to the base block. This structure forms a pivot with an axis of rotation O that approximately coincides with the line of intersection between the two planes defined by the unloaded (undeflected) leaf springs.

Simplified geometrical model

The reader is referred to the vast amount of literature on the rigorous study of the path followed by the mobile block as well as the exact deflection of the leaf springs. Here we will merely remind the reader that a cross spring pivot does not exactly pivot about the axis O. The rotation of the mobile block through an angle θ is accompanied by a parasitic translation (shift vector \vec{PP}' , Fig. 5.2). According to (Wittrick, 1951) we have¹

$$PP' = \frac{\sqrt{2}}{12} l \theta^2 \simeq 0.118 l \theta^2. \quad (5.1)$$

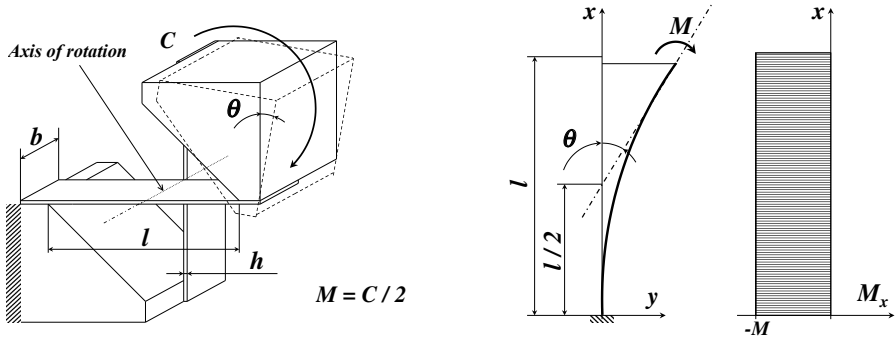


Figure 5.1 Separate cross spring pivot: h , thickness of the leaf springs; b , width of the leaf springs; l , length of the leaf springs from one clamped end to the other. For small angles of rotation, we can make the assumption that the leaf springs deform into circular arcs and are thus subjected to pure bending.

Angular stiffness

For small pivot angles, we can make the assumption that the leaf springs deform into circular arcs, in which case the angular stiffness $K_\theta = C/\theta$ of the cross spring pivot is twice that of a single leaf spring subjected to pure bending (Fig. 5.1) because the two leaf springs work in parallel.

$$K_\theta = \frac{2EI}{l} \quad \text{where} \quad I = \frac{bh^3}{12} \quad (5.2)$$

¹ (Haringx, 1949) and (Mesnager, 1903) give the formulas $PP' = 0.112 l \theta^2$ and $PP' = 0.125 l \theta^2$ respectively. These correspond within 6% to (5.1).

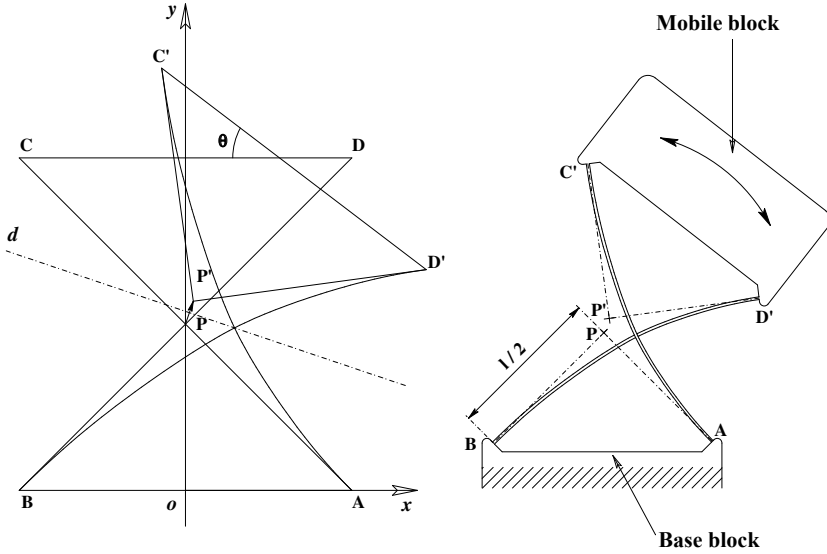


Figure 5.2 Parasitic translation of a separate cross spring pivot: vector $\vec{PP'}$.

For large pivot angles, the fact that the leaf springs do not deform exactly into circular arcs results in increased stiffness. According to (Haringx, 1949), for a pivotal movement of 45° , the angular stiffness is 10% greater than the value given by (5.2).

Angular deflection

If we make the assumption that the leaf springs deform into circular arcs, then the angular deflection of a cross spring pivot is the same as that of a single leaf spring subjected to a pure bending moment (2.3):

$$\theta_{adm} = \frac{2\sigma_{adm}l}{Eh}. \quad (5.3)$$

For large pivot angles, the fact that the leaf springs do not deform exactly into circular arcs results in increased stresses in the leaf springs. According to (Haringx, 1949), for a pivotal movement of 45° , the stresses are 30% greater than the value given by (5.3).

5.2 Joined cross spring pivot

This pivot is the monolithic equivalent of the separate cross spring pivot. This structure forms a pivot with an axis of rotation that approximately coincides

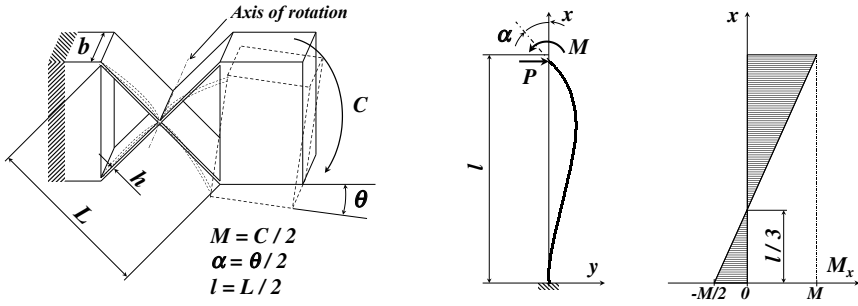


Figure 5.3 Jointed cross spring pivot: h , thickness of the leaf springs; b , width of the leaf springs; L , length of the leaf springs from one clamped end to the other; l , half-length of the leaf springs.

with the line of intersection between the two planes defined by the unloaded (undeflected) leaf springs.

Angular stiffness

From the study of the loading of a half-leaf spring² (Fig. 5.3), we deduce that the stiffness $K_\theta = C/\theta$ is:

$$K_\theta = \frac{8EI}{L} \quad \text{where} \quad I = \frac{bh^3}{12}. \quad (5.4)$$

We note that this stiffness is four times that of a separate cross spring pivot of the same dimensions.

Angular deflection

From the study of the loading of a half-leaf spring (Fig. 5.3), we deduce that the allowable deflection is:

$$\theta_{adm} = \frac{\sigma_{adm}L}{2Eh}. \quad (5.5)$$

We note that this deflection is one-quarter of the deflection of a separate cross spring pivot of the same dimensions.

² For small angles of rotation, we can make the assumption that the axis of rotation remains perfectly constant. This leads to the case of a beam loaded under simple bending where the deflection is zero and the rotational displacement of the end is equal to α .

5.3 RCC pivot with two leaf springs

An RCC pivot³ is a bearing with an axis of rotation that approximately coincides with the line of intersection between the two planes defined by the unloaded (undeflected) leaf springs. The difference between this structure and the separate and joined spring pivots lies in the relative position of the axis of rotation of the leaf springs. In the case of an RCC pivot, the axis of rotation is outside the physical structure, while in the case of the two other pivots it passes through the leaf springs.

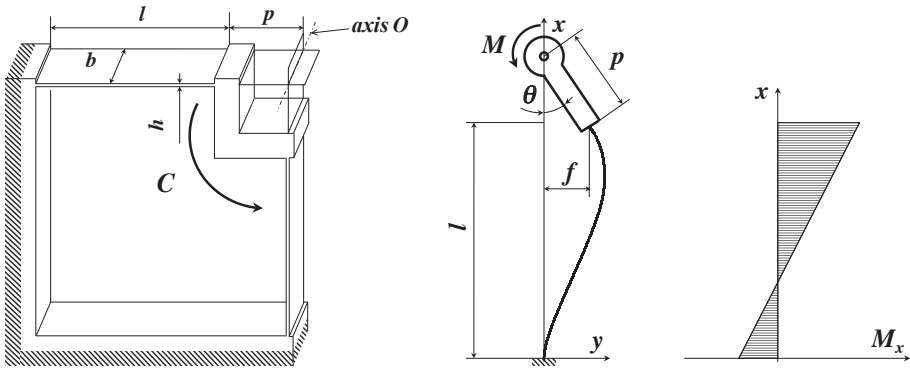


Figure 5.4 RCC pivot with two leaf springs: h , thickness of the leaf springs; b , width of the leaf springs; l , length of the leaf springs from one clamped end to the other; p , distance between the axis of rotation O (line of intersection between the two planes defined by the leaf springs) and the end of the leaf springs

Angular stiffness

From the study of the loading of one of the leaf springs⁴ (Fig. 5.3), we deduce that the stiffness $K_\theta = C/\theta$ is:

$$K_\theta = \frac{8EI}{l} \left(1 + \frac{3p}{l} + \frac{3p^2}{l^2} \right) \quad \text{where} \quad I = \frac{bh^3}{12}. \quad (5.6)$$

³ RCC stands for Remote Center Compliance. This term indicates that the center of pivotal movement of the flexure joint is located outside the structure, at a point where it is possible to be free of any material.

⁴ For small angles of rotation, we can make the assumption that the axis of rotation remains perfectly constant. This leads to the case of a beam loaded under simple bending where the deflection and the rotational displacement of the end are related: $f = p \sin \theta \simeq p\theta$.

Angular deflection

The angular deflection of the RCC pivot with two leaf springs is:

$$\theta_{adm} = \frac{\sigma_{adm} l^2}{E(2hl + 3hp)} \quad (5.7)$$

COMMENTS

- The angular stiffness of the RCC pivot with two leaf springs is *greater* than that of the separate or joined cross spring pivots made with the same leaf springs, and all the more so the greater the p/l ratio.
- The angular deflection of the RCC pivot with two leaf springs is *less* than that of the separate or joined cross spring pivots made with the same leaf springs, and all the more so the greater the p/l ratio.

5.4 RCC pivot with four notch hinges

An RCC pivot with four circular notch hinges is a pivot whose axis of rotation P approximately coincides with the line of intersection between the two planes defined, for each arm, by the axes of rotation of their notch hinges. l and $\eta \times l$ are the two main parameters that define the geometry of the pivot. If we set the length l at 1, the angles remain unchanged and the lengths are divided by l . We thus have just the one parameter that defines the pivot geometry:

$$0 < \eta < 1. \quad (5.8)$$

Simplified geometrical model

To model this structure simply, we make the following assumptions (Fig. 5.5):

- The circular notch hinges behave like identical imaginary pivot points whose angular stiffness is $K_{\alpha M}$ and whose other stiffnesses are infinite.
- The angles of rotation of the notch hinges and the mobile block of the RCC pivot are small enough to assume that:
 - The mobile block pivots exactly about axis P .
 - The base block pivots (and the mobile block pivots) turn through the same angles: $\alpha \simeq \beta$ and $\delta \simeq \gamma$.
 - The angles are approximately equal to their sines: $\sin \alpha \simeq \alpha$; $\sin \delta \simeq \delta$; $\sin \theta \simeq \theta$.

This gives us, for a rotation of the mobile block through an angle θ , a rotation of pivots A and B through an angle α , and a rotation of pivots C and D

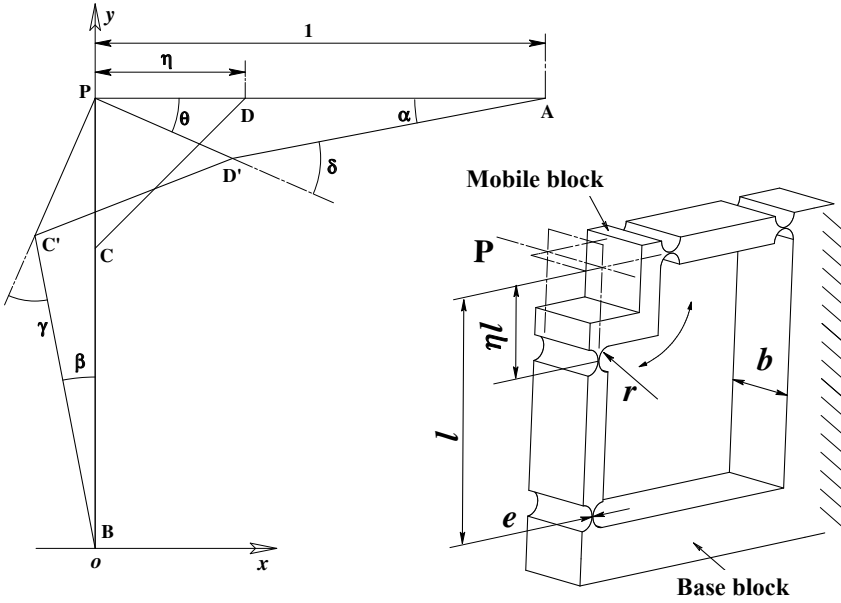


Figure 5.5 RCC pivot with four circular notch hinges and simplified geometrical model (unitary length: $l = 1$): e , thickness of the notch hinges at their narrowest point; r , radius of the notches; b , width; l , distance between the center of rotation P and pivots A and B; $\eta \times l$, distance between P and pivots C and D.

through an angle δ where

$$\alpha = \frac{\eta}{1-\eta} \theta \quad \text{and} \quad \delta = \left(1 + \frac{\eta}{1-\eta}\right) \theta. \quad (5.9)$$

Angular stiffness

The simplified geometrical model makes it possible to calculate the angular stiffness $K_{\theta}^{\text{RCC}} = M/\theta$ using the energy method: the mechanical work performed to make the mobile block pivot through an angle θ is equal to the elastic energy stored in the four imaginary pivots

$$\frac{1}{2} K_{\alpha M}^{\text{RCC}} \theta^2 = 2 \left(\frac{1}{2} K_{\alpha M} \alpha^2 \right) + 2 \left(\frac{1}{2} K_{\alpha M} \delta^2 \right). \quad (5.10)$$

By substituting from (5.9), we obtain

$$K_{\theta}^{\text{RCC}} = K_{\alpha M} \left(4 \frac{\eta^2}{(1-\eta)^2} + 4 \frac{\eta}{(1-\eta)} + 2 \right) \quad (5.11)$$

where $K_{\alpha M}$ is the angular stiffness of one of the circular notch pivots (3.20).

Angular deflection

From equations (5.9) we see that $\delta \geq \alpha$. Pivots C and D are therefore loaded the most during the rotation of the mobile block and it is their angular deflection that limits the angular deflection θ_{adm} of the complete RCC pivot.

$$\theta_{adm} = \frac{\alpha_M}{\frac{\eta}{1-\eta} + 1} \quad (5.12)$$

where α_M is the angular deflection of pivots C and D (3.21).

COMMENT: The angular deflection of the RCC pivot is always less than the deflection of its constituent pivots and all the more so the closer η is to 1. When η tends to 0, the deflection of the RCC pivot tends to the deflection of its constituent pivots (C and D).

Exact geometrical model

In actual fact, the RCC pivot does not pivot exactly about axis P . Its rotation through an angle θ is accompanied by a parasitic translation (vector $\vec{PP'}$) that becomes greater the more the pivot moves away from its nominal position. Likewise, the instantaneous center of rotation, which ideally would stay at P , moves (vector $\vec{PI'}$).

We use the geometrical model shown in Figure 5.6. to find the amplitude of the parasitic displacements. We again make the assumption that the notch hinges behave like imaginary pivot points. However, we no longer use the small-angle approximations used in the simplified model. The angles of rotation of the four pivots are all different, but related as follows:

$$\gamma = \beta + \theta \quad \text{and} \quad \delta = \alpha + \theta. \quad (5.13)$$

The instantaneous center of rotation I' is at the intersection of the straight lines (AD') and (BC').

We have plotted the angles of rotation of the four pivots as a function of the angle of rotation θ of the mobile block (Fig. 5.7). This graph also shows the norm of vectors $\vec{PP'}$ and $\vec{PI'}$ as a percentage of l . For this plot, we took⁵ $\eta = 1/4$. For example, for a rotation of the mobile block through a 15° , pivots A, B, C and D rotate through the following angles respectively: $\alpha = 6^\circ$, $\beta = 4^\circ$, $\gamma = 19^\circ$ and $\delta = 21^\circ$. Point P moves through a distance equal to 1.6% of l ($PP' = 1.6 \times l/100$). The instantaneous center of rotation moves through a distance equal to 12% of l ($PI' = 12 \times l/100$).

⁵ We have seen that it is wise to choose parameter η as near to 0 as possible to minimise the angular displacement of the pivots. Practical reasons of manufacture and mechanical interferences limit the value of this parameter. We used the reasonable value of $1/4$ to plot the graph in Figure 5.7.

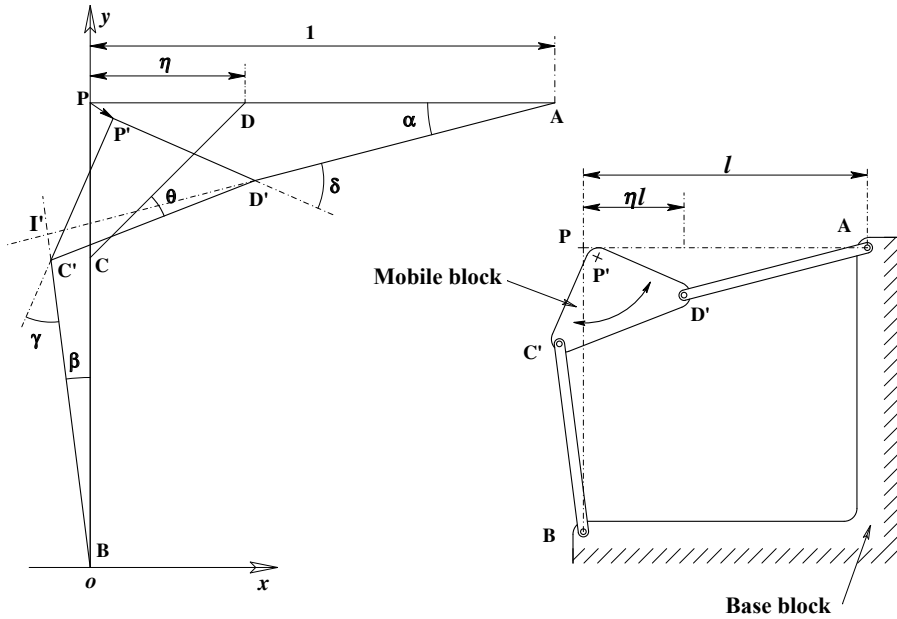


Figure 5.6 Exact geometry of the RCC pivot (with the assumption that the pivots are infinitesimal points). Nominal positions: A B C D P. Positions after rotation through an angle θ : A B C' D' P'.

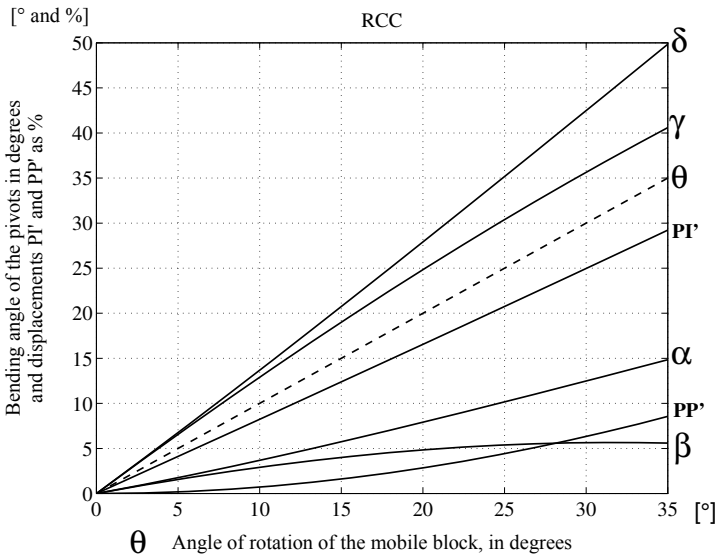


Figure 5.7 Angular displacements of the four pivots as a function of the angle of rotation θ of the mobile block and the norms of vectors $\vec{PP'}$ and $\vec{PI'}$ as a percentage of l (for $l = 1$, and $\eta = 1/4$).

5.5 Cross pivot with four notch hinges

A cross pivot with four circular notch hinges is a pivot whose axis of rotation P approximately coincides with the line of intersection between the two planes defined, for each arm, by the axes of rotation of the notch hinges. l is the main parameter that defines the pivot geometry. If we set the length l at 1, the angles remain unchanged and the lengths are divided by l .

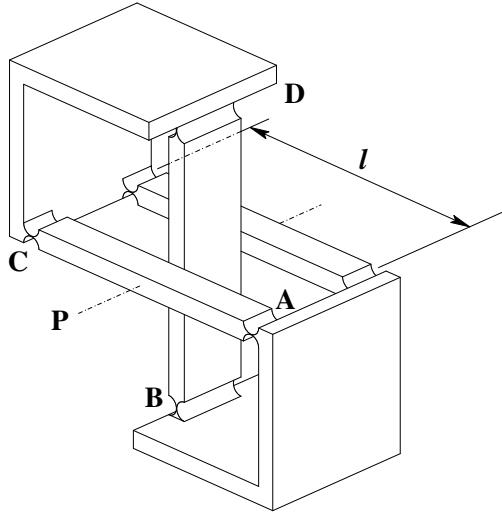


Figure 5.8 Cross pivot with four notch hinges.

Geometrical model

At the nominal position, the position of the mobile block is defined by $C D P$ (Fig. 5.9). After one rotation through an angle θ , the position becomes $C' D' P'$. The quadrilateral $A B C' D'$ is a trapezoid with one axis of symmetry: d . We thus obtain $I'A = I'D'$ and $I'B = I'C'$, hence $I'B + I'A = I'B + I'D' = 1$. We can thus deduce that the locus of the instantaneous center of rotation I' is an ellipse (e) whose equation on the coordinates oxy is

$$4x^2 + 8y^2 = 1. \quad (5.14)$$

The trapezoid symmetry also allows us to show that pivots A and D (or B and C) rotate through the same angle α (or β) and that both of these angles are related to the angle of rotation of the mobile block by the simple equation

$$\alpha + \beta = \theta. \quad (5.15)$$

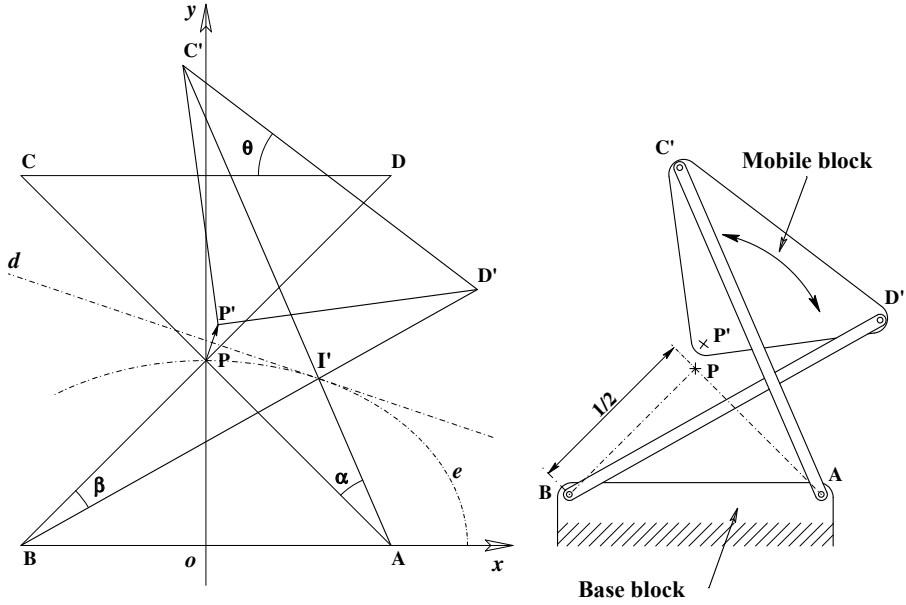


Figure 5.9 Geometrical model of the cross pivot with four notch hinges. Nominal position: A B C D P. Position after rotation of the mobile block through an angle θ : A' B' C' D' P'. Vector of parasitic translation: $\vec{PP'}$. Vector of displacement of the instantaneous center of rotation: $\vec{PI'}$.

The rotation of the mobile block is accompanied by a parasitic translation denoted by the vector $\vec{PP'}$. Let $X_{I'}$ and $Y_{I'}$ be the coordinates of point I' . We obtain

$$\frac{X_{I'}}{l} = \frac{\tan(\theta/2)}{\sqrt{2 + 4(\tan(\theta/2))^2}} = S \quad \text{and} \quad \frac{Y_{I'}}{l} = \frac{\sqrt{1 - 4S^2}}{2\sqrt{2}}. \quad (5.16)$$

Let $X_{PP'}$ and $Y_{PP'}$ be the coordinates of $\vec{PP'}$. We obtain

$$\frac{X_{PP'}}{l} = \frac{S(-1 + \sqrt{1 - 4S^2})}{-1 + 2S^2} \quad \text{and} \quad \frac{Y_{PP'}}{l} = \frac{-1 + 4S^2 + \sqrt{1 - 4S^2}}{\sqrt{2}(1 - 2S^2)}. \quad (5.17)$$

The norm of $\vec{PP'}$ is

$$\frac{PP'}{l} = \sqrt{1 + \frac{\sqrt{1 - 4S^2}}{-1 + 2S^2}}. \quad (5.18)$$

The angle of displacement β of pivots B and C as a function of the angle of rotation θ of the mobile block is given by

$$\beta = \frac{\pi}{4} - \text{arccotg} \frac{1 + 2\sqrt{2}S}{\sqrt{1 - 4S^2}}. \quad (5.19)$$

The angle of displacement α of pivots A and D as a function of the angle of rotation θ of the mobile block and of β is simply

$$\alpha = \theta - \beta. \quad (5.20)$$

We have plotted the angles of the four pivots as a function of the angle of rotation θ of the mobile block (Fig. 5.10). This figure also shows the norm of vectors $\vec{PP'}$ and $\vec{PI'}$ as a percentage of l . For small angles of rotation of the mobile block, the pivots bend through around one-half of this angle:

$$\alpha \simeq \beta \simeq \frac{\theta}{2}. \quad (5.21)$$

For example, for an angle of rotation of the mobile block $\theta = 15^\circ$, pivots A and D turn through angle $\alpha = 8^\circ$ and pivots B and C turn through an angle $\beta = 7^\circ$. Point P moves through a distance equal to 1.2% of l ($PP' = 1.2l/100$). The instantaneous center of rotation moves through a distance equal to 9% of l ($PI' = 9l/100$).

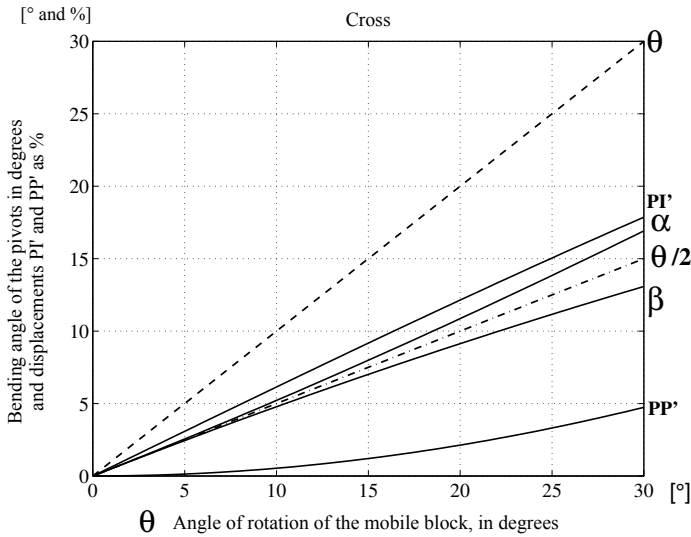


Figure 5.10 Angular displacements of the four pivots as a function of the angle of rotation θ of the mobile block and the norms of vectors $\vec{PP'}$ and $\vec{PI'}$ as a percentage (for $l = 1$).

Angular stiffness

We can calculate the angular stiffness $K_\theta^{\text{croise}} = M/\theta$ using the energy method: the mechanical work performed to make the mobile block pivot through an

angle θ is equal to the elastic energy stored in the four pivots

$$\frac{1}{2}K_{\theta}^{\text{croise}}\theta^2 = 2\left(\frac{1}{2}K_{\alpha M}\alpha^2\right) + 2\left(\frac{1}{2}K_{\alpha M}\beta^2\right) = K_{\alpha M}(\alpha^2 + \beta^2). \quad (5.22)$$

Substituting for θ from (5.15), we obtain

$$K_{\theta}^{\text{croise}} = \frac{K_{\alpha M}}{\frac{1}{2} + \frac{\alpha\beta}{\alpha^2 + \beta^2}}. \quad (5.23)$$

where $K_{\alpha M}$ is the angular stiffness (3.20) of each of the circular notch pivots (e.g., the pivot marked C, Fig. 5.8). For small angles of rotation, (5.21) can be used to simplify the last expression to

$$K_{\theta}^{\text{croise}} \simeq K_{\alpha M}. \quad (5.24)$$

The angular stiffness of the cross pivot with four circular notch hinges is thus approximately equal to the angular stiffness of each of its constituent notch hinges.

5.6 Comparison of the pivots

Let us consider a cross spring pivot, an RCC pivot with four notch hinges and a cross pivot with four notch hinges that, in their nominal positions, fit inside identical squares with sides one unit long (Fig. 5.11). We plotted the angle of displacement of the most loaded pivot of each structure as well as the norms of the vectors of parasitic translation \vec{PP}' and of the displacement of the instantaneous center of rotation \vec{PI}' on the same graph (Fig. 5.12).

The conclusions that we may draw from comparing the cross spring, RCC (with $\eta = 1/4$) and cross pivots are as follows:

- The RCC and cross pivots produce a parasitic translation and a displacement of the instantaneous center of rotation that are very similar and are approximately 1.5 times greater than those of the cross spring pivot.
- For the same rotation of the mobile block, the most-loaded pivot of the RCC bends through an angle more than twice that of the most-loaded pivot of the cross system. Therein lies the main advantage of the cross pivot.
- However, cross pivots cannot be manufactured in the same plane, complicating their production. The advantage of the RCC pivot is that it is a flat structure without any crossing components.

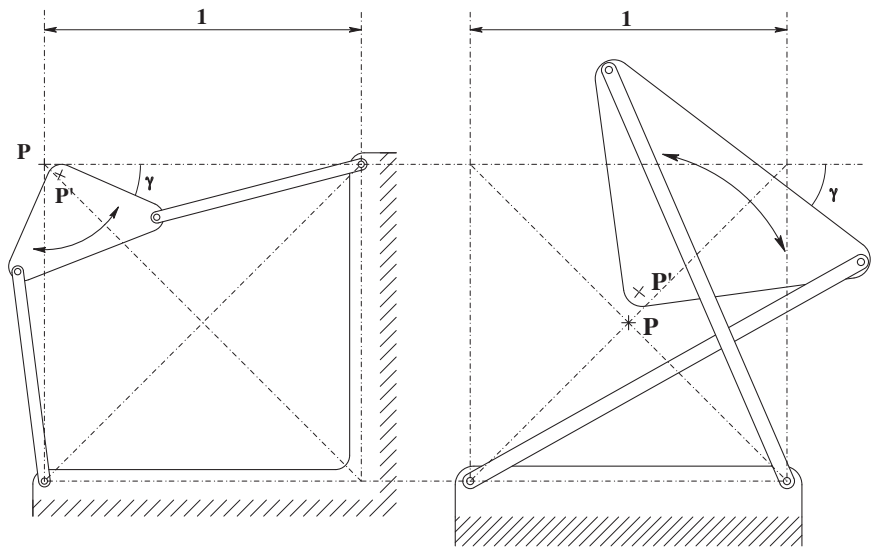


Figure 5.11 RCC and cross pivots inside identical squares with sides equal to 1 (the cross spring pivot is not shown).

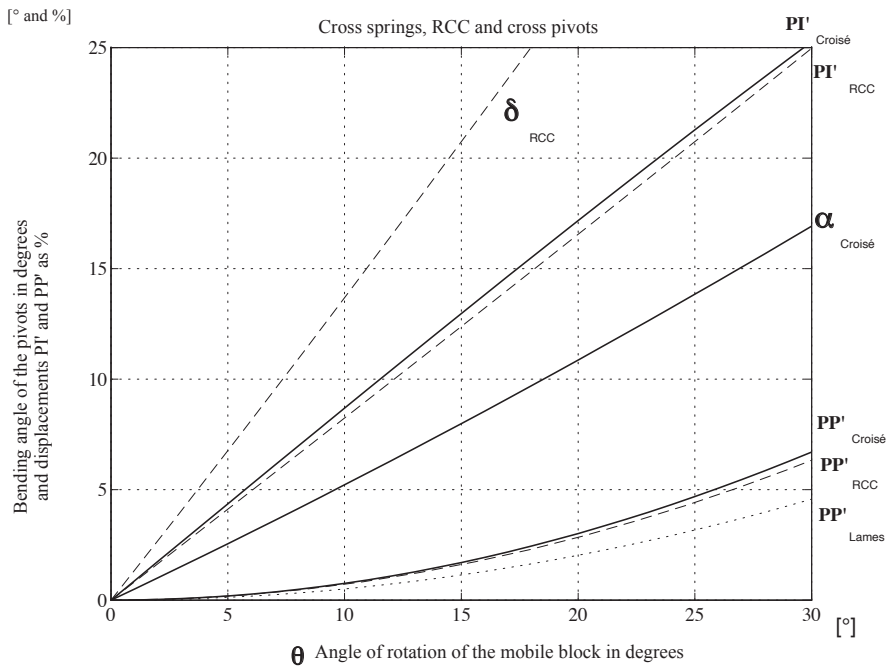


Figure 5.12 Comparison of cross spring (dotted lines), RCC ($\eta = 1/4$) (broken lines) and cross pivots (solid lines) of the same dimensions.

5.7 Radial loads

5.7.1 Variation in angular stiffness

Let us consider a radial force F applied to the mobile block on one of the pivots studied. Let us assume that this force is applied at the point that coincides with the axis of rotation at the nominal position (point P in the various figures). Will the presence of this force affect the angular stiffness of the pivots? If so, how? Given the complexity of the problem, providing an exact (quantitative) answer to this question is beyond the scope of this book. However, it is easy to provide a qualitative answer: there is a very simple way to find out whether the force F increases, decreases or has virtually no effect on the angular stiffness.

For a pivot on which no radial force is acting, we know that the energy to be provided to make it pivot through a certain angle is equal to the energy stored elastically in its flexible parts (leaf springs or notch hinges). The presence of a radial force alters this energy equilibrium only if it itself provides or requires mechanical work due to its displacement. Thus, if during a rotation that shifts the pivot away from its nominal position, the point of application of F moves such that this force provides mechanical work, then this force decreases the angular stiffness of the pivot: the work of F constitutes as much released potential energy as is no longer required to make the structure rotate. On the other hand, if the point of application of F shifts such that this force requires energy in order to be moved, then this force increases the angular stiffness of the pivot (Fig. 5.13).

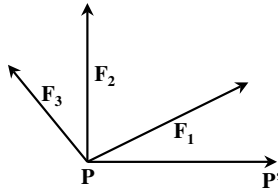


Figure 5.13 The effect of radial forces on the stiffness of the pivots depends on their direction in relation to the parasitic translation vector $\vec{PP'}$ of the pivot. The force $\vec{F_1}$ decreases the angular stiffness because its work is positive during the displacement (release of its potential energy). $\vec{F_2}$, which is at right angles to $\vec{PP'}$, has no effect on the angular stiffness because its work during the displacement is zero. $\vec{F_3}$ increases the angular stiffness because its work is negative during the displacement (requiring potential energy).

This approach allows us to predict that a radial force that puts a compressive load on the leaf springs (or notch hinges) of the pivots studied:

- Increases the angular stiffness of cross spring pivots and cross pivots with four notch hinges.

- Decreases the angular stiffness of joined cross spring pivots, RCC pivots with leaf springs and RCC pivots with four notch hinges.

A radial force that puts a tensile load on the leaf springs or notch hinges of these same pivots has the opposite effect.

In the case of a radial force that puts a compressive load on one of the leaf springs (or one of the arms) and a tensile load on the other, more accurate observation of the respective directions and senses of the parasitic translation vector \vec{PP}' and the force vector \vec{F} is necessary to understand its effect on stiffness.

5.7.2 Radial stiffnesses

In Chapter 4 we show that, for a given form factor and deflection, a stage with four prismatic (or circular) notch hinges that has minimal length l_c (or radius r) is the best linear translation bearing in terms of stiffness ratios. However, just as with a stage with four notch hinges, pivots with four notch hinges are constructed with conrods⁶ subjected to tensile/compressive loading. We can therefore extrapolate, without formally demonstrating it, that for the same form-factor and the same angular deflection:

- Pivots with notch hinges have greater radial stiffnesses than pivots with leaf springs.
- The shorter the length (or radius) of the notch hinges, the higher the radial stiffnesses.

Compared with prismatic notch hinges, circular notch hinges also possess the advantage of not having sharp corners that could act as stress concentrators. We therefore recommend using, when the manufacturing process permits it, pivots with circular notch hinges with a minimal notch radius as rotational bearings.

5.7.3 Allowable loads

Exact calculation of the radial loads allowed for the various pivots studied as a function of their direction and the pivot angle θ is beyond the scope of this book. That said, we note that the critical loads calculated for one of the leaf springs in a two parallel leaf spring stage (4.18) (or one of the arms in a four prismatic notch hinge stage (4.72)) also apply to the pivots with leaf springs (or notch hinges) analyzed here. To use them, one simply has to resolve the radial force into its components parallel to the constituent leaf springs (or arms) of the pivot.

⁶ These conrods each have a stiff segment in the central portion with flexible notches at each end.

5.8 Overconstrained pivot with three leaf springs

An overconstrained pivot with three leaf springs (Fig. 5.14), which is an equivalent⁷ of the overconstrained stage with four parallel leaf springs (Sect. 4.2), has the same properties qualitatively:

- It constitutes a purely rotational bearing: the movable ring rotates about point O without any parasitic translation.
- Its force-deformation characteristic curve is highly progressive.
- Its deflection is significantly lower than that of a pivot with two cross leaf springs made with the same leaf springs.
- This statically indeterminate structure induces significant stresses in the base and mobile blocks.

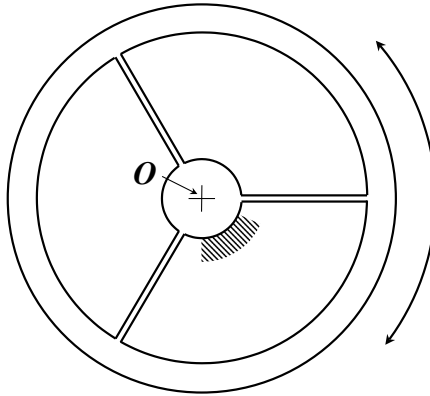


Figure 5.14 Overconstrained pivot with three leaf springs.

⁷ The concept of *equivalence* is defined in Section 6.1.1.

Part II

Flexure mechanisms

Flexure structures

The *kinematic analogy* between structures with flexible bearings and those with ideal bearings makes it possible to apply conventional kinematic design methods to synthesise or analyse flexible structures. Some examples of analyses that use Grübler's criterion to determine the number of DOFs of a structure are described here. They reveal the possible presence of internal DOFs or statically indeterminate systems in the structures. The use of parallel kinematics is encouraged by the fact that its advantages are of great interest for high precision robotics with flexible structures and that its drawbacks are generally less problematic than in conventional robotics.

A summary of the results of the first and second parts of this book shows the limits of flexible bearings in terms of deflection. Isolated bearings can achieve deflections nearing one half of their dimensions, while complex structures rarely exceed one tenth of their dimensions (form factor). Angular deflections seldom exceed some fifteen degrees. Some design principles – such as the redundant use of two identical bearings mounted in series – make it possible to increase the deflection of bearings. Other design principles that make it possible to minimise or maximise the natural stiffnesses of bearings are described. Protecting bearings from excess loads and excess deflection requires careful placement of mechanical stops.

6.1 Kinematics

6.1.1 Definitions

Articulated structure: an articulated structure forms the skeleton of a robot¹ or mechanism, i.e., the mechanical portion that withstands forces and transmits motion. It is made up of stiff bodies that are joined to one another by bearings. It comprises a fixed segment, referred to as the *base*, and a segment, referred to as the *end effector*, that holds the tool or whose motion is utilised. Some other

¹ In robotics, an articulated structure is often referred to as an arm (André et al., 1983) (Coiffet, 1992).

segments, referred to as *motoric segments*, are subjected to the forces produced by actuators to move the end effector within its degrees of freedom.

Kinematics of articulated structures: kinematics is the study of the motion of articulated structures, independently of any forces present (Hunt, 1978). This motion may be described by the position, speed and acceleration of the various parts of the structure.

Kinematic geometry: this subdivision of kinematics only concerns the motions of articulated structures independently of the time variable (Hunt, 1978). We will limit our discussion in this section to this subdivision, which is the simplest.

Kinematic analogy principle: two articulated structures are referred to as *kinematically analogous* if their motions are identical independently of their constituent physical elements and the forces present. Thus, an articulated structure with rolling bearings and another structure with flexible bearings may share the same kinematics if their motions are identical. We call this equivalence between the essential functions of these two structures with different constituent elements *kinematic analogy*².

Analogous bearings: two bearings are referred to as *analogous* if they have the same kinematics, independent of their physical construction. Cross spring pivots, ball bearings and plain journal bearings are three analogous bearings.

Homologous bearings: two bearings are referred to as *homologous*³ if their physical construction is similar, independent of their kinematics. Cross spring pivots and two parallel leaf spring stages are homologous bearings because both are made up of two flexible leaf springs connecting two rigid blocks.

6.1.2 Statement of the method

The *analogy* between articulated structures with ideal bearings and those with flexible bearings makes it possible to use conventional kinematic design methods to synthesise or analyse flexible structures.

Synthesis consists in translating a structure with ideal bearings designed using conventional methods into an analogous structure with flexible bearings.

² The *kinematic analogy principle* introduced by the author is drawn from anatomy, which describes as *analogous* those organs that are similar in function and sometimes similar in shape, but which are entirely different in origin (Lender et al., 1992). The wing of a bird and the wing of an insect are an example.

³ The concept of *homology* between bearings introduced by the author is drawn from embryology, which describes as *homologous* organs which may be used in different ways but which derive from the same embryonic primordium in two related zoological groups (Lender et al., 1992). The front leg of a mammal and the wing of a bird are an example.

Analysis consists in translating the structure with flexible bearings into an analogous structure with ideal bearings and studying its kinematics with the use of conventional methods.

Translation of a structure with ideal bearings into a structure with flexible bearings (or vice versa) consists in replacing the ideal bearings by analogous flexible bearings (or vice versa).

The iterative exercise of synthetic and analytical translations is of great help in the design of flexible structures. Just as with translating from one language to another, translating a structure with ideal bearings into a flexible structure (or vice versa) is not an automatic process because it is not unequivocal. It requires experience and an ability for interpretation. Thus, this design method is not systematic, but rather *heuristic*⁴.

6.1.3 Kinematic analysis

Our approach to designing flexible structures allows us to make use of the many methods of design and kinematic analysis found in the literature for articulated structures with ideal bearings. This book is not the place to describe or even list these methods; they are described in abundant detail in the literature (Reuleaux, 1875) (Artobolevski, 1975) (Hunt, 1978) (Erdman, 1993) (Flückiger, 1998) (Waldron and Kinzel, 1999).

Here we will describe only Grübler's kinematic analysis criterion (Grübler, 1917)⁵, which makes it possible to determine the number of degrees of freedom M of an articulated structure comprising n bearings with d_i ($1 \leq i \leq n$) degrees of freedom and having b loops

$$M = \sum_{i=1}^n d_i - 6b. \quad (6.1)$$

For plane structures, this formula becomes

$$M = \sum_{i=1}^n d_i - 3b. \quad (6.2)$$

Examples of analyses

Using this method, let us analyse the kinematics of the flexible arm in Figure 6.1. It is a serial structure (no loop: $b = 0$) comprising two flexure joints ($n = 2$), each with three DOFs, connecting three rigid segments: the fixed block **o**, the

⁴ Heuristic is defined as 'Proceeding to a solution by trial and error or by rules that are only loosely defined' (The New Oxford Dictionary of English).

⁵ This method is generally credited to (Grübler, 1917) (Schoenflies and Grübler, 1908), but it is sometimes attributed to (Kutzbach, 1929) as well. Expression (6.1) is not the original formula but a practical way of writing it, as proposed by (Hunt, 1978).

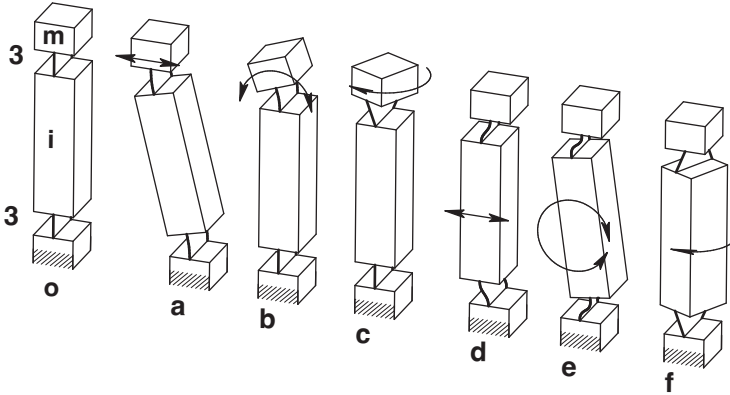


Figure 6.1 The six DOFs of a flexible arm.

mobile block **m** and the intermediate block **i**. From criterion (6.1), the number of degrees of this arm is $M = 3 + 3 - 0 = 6$. As shown by the figure, the three DOFs **a**, **b** and **c** correspond to the motions of the mobile block, while DOFs **d**, **e** and **f** correspond to the motions of the intermediate block and barely move the mobile block. We can therefore interpret the result of criterion (6.1) by saying that, from the functional perspective, this arm has only three DOFs and that DOFs **c**, **d** and **e** are *internal*⁶ degrees of freedom of the structure. This enables us to translate this arm into the structure with ideal bearings in Figure 6.2d, which has three DOFs that are identical to the three *external* DOFs of the flexible arm (**a**, **b** and **c**).

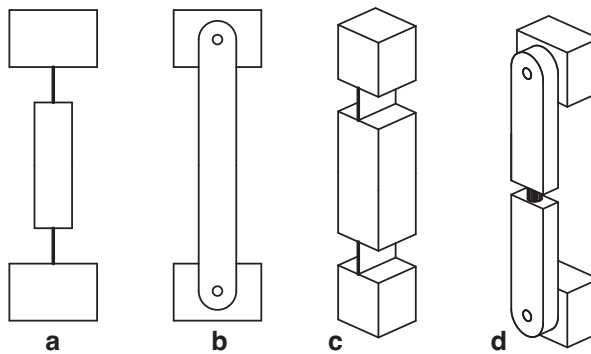


Figure 6.2 Translation of a flexible arm into a structure with ideal bearings in a plane (**a** → **b**) and in space (**c** → **d**) (**d**: the arm is articulated at mid-span by a revolute joint having an axis of rotation that is coincident with the axis of the arm).

⁶ A definition of the concept of *internal* degree of freedom is found in (Waldron and Kinzel, 1999), for example.

If this arm is to be used to construct a flat articulated structure, DOFs f and c must be disregarded, as their axis of rotation is not normal to the plane of the structure. Construed as a plane structure, the flexible arm has four DOFs, two of which are external (a and b) and two internal (d and e). It can therefore be translated into the structure with ideal bearings shown in Figure 6.2b.

In the light of these results, let us now analyse the stage with four notch hinges by considering it as a plane structure. We can translate it into the structure with ideal bearings shown in Figure 6.3b. Let us apply criterion (6.2) to this structure. It has four flexure joints with one DOF ($n = 4$) and one loop ($b = 1$). The number of its DOFs is therefore $M = 4 - 3 = 1$. The stage with four notch hinges is well and truly a translation bearing with one DOF.

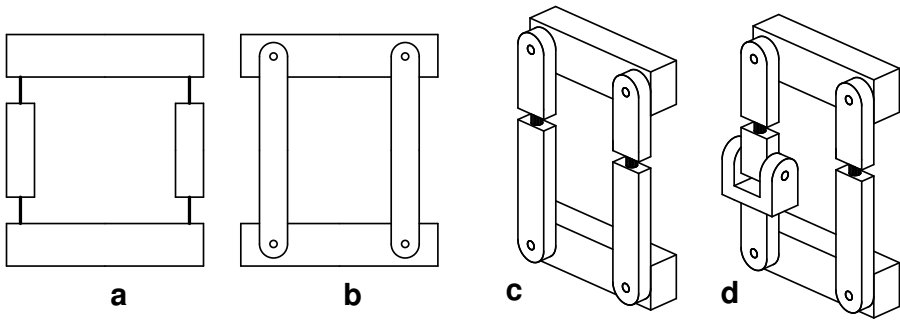


Figure 6.3 Analysis of a stage with four notch hinges as a plane structure ($a \rightarrow b$), then as a spatial structure ($a \rightarrow c$). The kinematic system c is statically indeterminate. The analogous kinematic system d is statically determinate.

Now let us analyse the stage with four notch hinges as a spatial articulated structure. We can translate it into the structure with ideal bearings shown in Figure 6.3c. Let us apply criterion (6.1) to this structure. It has six flexure joints, each with one DOF ($n = 6$) and one loop ($b = 1$). The number of its DOFs is therefore $M = 6 - 6 = 0$. However, experience shows that the stage with four notch hinges has one DOF. The lesson to be drawn from the result of the applied criterion is that this structure is statically indeterminate⁷. Indeed, this structure has one DOF only if its two arms are along the same plane. If this structure is manufactured monolithically by wire EDM, it is easy to guarantee that the coplanarity of the motion of the two arms and the statically indeterminate system is not problematic. Note that adding a flexure joint to one

⁷ The identification of statically indeterminate structures is very important because such structures can, in a basically unforeseeable manner, cause significant variations in the stiffnesses of flexible structures as well as in the stresses acting on their flexure joints. It is therefore essential to avoid statically indeterminate systems in the design phase.

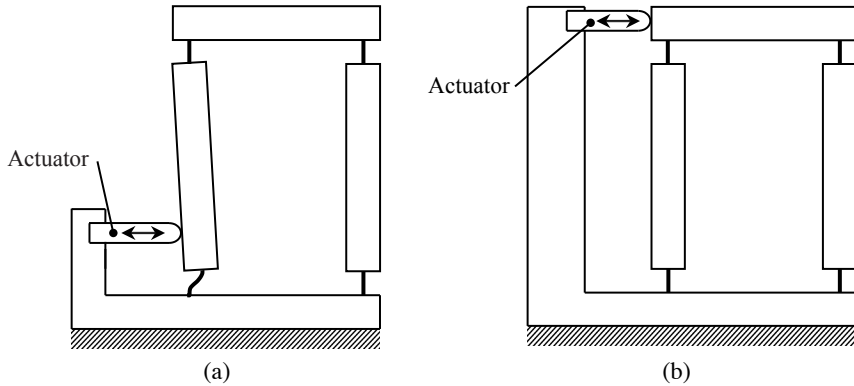


Figure 6.4 Some external forces, such as those produced by actuators, may act on the internal DOFs of the structures and disrupt their correct operation ((a) wrong, (b) right).

of the arms (Fig. 6.3d) could be a way to eliminate this statically indeterminate situation.

Now let us consider the internal degrees of freedom of a stage with four notch hinges. From Figure 6.1, we know that each of the two arms can move within DOFs d, e and f. The stage thus has six internal DOFs. If none of these DOFs is acted on by a force, their presence will have no effect on the functioning of the linear translation bearing. However, if forces related to the acceleration⁸ of the mass of the intermediate block, or to external loads applied to either the mobile block or the intermediate block, move the latter within one of the internal DOFs, the functioning of the linear translation bearing can be affected. For example, using an actuator that acts directly on the intermediate block is not recommended⁹ (Fig. 6.4a). It is better to drive the mobile block directly (Fig. 6.4b).

These examples illustrate how design tools and principles routinely used to study the kinematic behaviour of structures with ideal bearings may be used to analyse the behaviour of flexible structures.

6.1.4 Kinematic synthesis

In this book we use several examples showing how a flexible structure can be synthesised from an analogous structure with ideal bearings.

⁸ It is important to know the internal degrees of freedom of a structure in order to carry out a dynamic analysis of them. This is because they may be a source of significant vibrations.

⁹ This solution has occasionally been used to amplify the displacement produced by piezo-electric actuators.

6.1.5 Parallel kinematics

Benefits and drawbacks

Let us consider the benefits and drawbacks of parallel robots¹⁰ as listed by (Clavel, 1994) in terms of ultra-high precision robots with flexible structures. The benefits of parallel robots are:

- High mechanical stiffness.
- High natural frequency, thus little error in reproducibility of the movements from uncontrolled oscillation of the mobile structure.
- Possibility of highly dynamic motion (high accelerations).
- Possibility of positioning the actuators directly on the fixed base.
- High load capacity.

These advantages are of very great interest for high precision robotics. The drawbacks of parallel robots are:

- Limited working envelope.
- Geometric models that are sometimes hard to determine.
- Presence of singularities that result in loss of control of the mobile structure.
- Highly variable coupling between kinematic chains.

The kinematic geometry of flexible bearings is generally different from that of the simplest ideal bearings for which the paths are often simple straight lines or circles, constituting an additional challenge in determining geometric models. Incidentally, exteroceptive position measurement¹¹ is often used in high precision robotics applications. In these cases, inaccuracies in the geometric models have little effect on movement precision. As a result, it is possible to approximate flexible bearings by using analogous ideal bearings when determining geometric models.

In the case of high precision robots with flexible structures, the small deflection of the bearings results in a lower risk of encountering the kinematic singularities. In addition, the coupling between kinematic chains varies little throughout the working envelope, and the reduced envelope is less significant since there are fewer risks of mechanical interference between the kinematic chains. The drawbacks of parallel architectures are therefore less of a

¹⁰ A parallel manipulator is made up of an end effector with n DOFs and a fixed base connected to one another by at least two independent kinematic chains driven by n simple actuators (Merlet, 1997).

¹¹ Exteroceptive position measurement makes it possible to locate the position of the end effector immediately without working from the individual positions of the flexure joints in the mechanical structure. Observations of end effectors via an artificial vision system, such as a camera, are a common example.

disadvantage in the case of high precision robots with flexible structures than in the case of conventional industrial robots.

To conclude, parallel kinematics are all the more well suited to high precision robots with flexible structures.

Functions of parallel kinematic articulated structures

Schematically, a typical parallel structure (Fig. 6.5) comprises a fixed base block, a mobile block with M DOFs and M motoric segments that are acted on by the forces of actuators. Without the actuators, the mobile block can move freely within its M DOFs. If the M motoric segments are constrained, the mobile block is constrained as well (0 DOF). The motion of each of the motoric segments controls the motion of each of the DOFs of the mobile block.

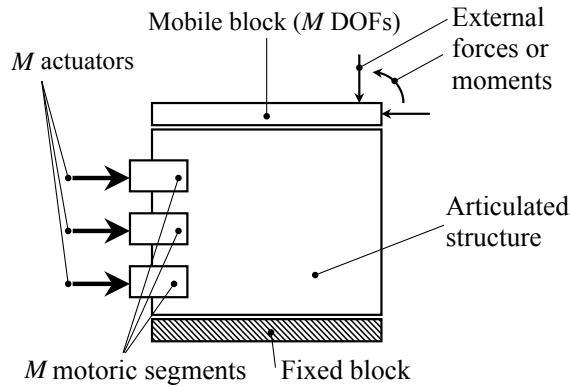


Figure 6.5 Diagram of a parallel structure.

The essential functions of articulated structures are thus:

- To constrain the movement of the mobile block within the transverse DOFs by providing stiff resistance to loads.
- To impose the position of the mobile block within its DOFs by transmitting the force of the actuators to the mobile block through rigid kinematic chains.

Optimisation criteria

When designing articulated structures, the aim is:

- To minimise the influence of external forces on the position of the mobile block. This is accomplished by maximising the stiffness of the structure within its transverse DOFs in order to withstand transverse forces and moments, and by maximising the stiffness of the kinematic chains leading

from the motoric segments to the mobile block in order to withstand natural forces and moments.

- To maximise allowable loads.
- To minimise the opposing forces resulting from the elasticity of the flexible bearings.
- To maximise the working envelope and minimise the footprint. These two constraints are contradictory because the scaling laws show that translational displacements increase proportionally to the form factor of the structures¹². In the case of flexible structures, the envelope is usually limited by the deflections of the bearings, not the mechanical interferences between the segments, as is generally the case with conventional structures. The aim therefore is to optimise the arrangement of the kinematic chains so as to minimise the displacements of the bearings loaded the most.

6.2 Choice of materials

As with any other mechanism, the constituent materials of flexible bearings are chosen based on a wide range of conventional criteria, such as density, corrosion resistance, machinability and price. We will not discuss these criteria here.

The distinguishing feature of flexible bearings is that they require materials that can tolerate high relative elongation, i.e., strain ε , without plastic deformation. According to Hooke's law, however, strain is proportional to the stress in the material: $\varepsilon = \sigma/E$. Choosing a material that will result in bearings with the highest possible deflection thus amounts to choosing a material with the highest ratio:

$$\sigma_{adm}/E.$$

6.3 Working envelope

6.3.1 Serial arrangement of redundant DOFs

Serial arrangement of two identical DOFs makes it possible:

- To double the allowable deflection for a form factor that is virtually unchanged.
- Potentially to compensate for parasitic translations of the bearings (out-of-straightness of linear translation bearings and parasitic translation of rotational bearings).

¹² Note: on the other hand, the scaling laws show that the angular deflections are independent of the dimensions of the bearings.

However, one of the two redundant DOFs is a structurally internal DOF that can be acted on either by forces related to acceleration of the masses during dynamic motions or by static transverse loads. Thus, the presence of this internal DOF can:

- Reduce transverse stiffnesses.
- Make the bearing motion difficult to reproduce.
- Reduce the allowable deflection.
- Create vibrations.

These drawbacks can be overcome if the internal DOF is coupled to the external DOF by a suitable kinematic chain (which amounts to suppressing the internal DOF). This is illustrated by one example each of redundant translational and rotational bearings.

Redundant translational bearing

The most common examples are the compensated stage with four parallel leaf springs (Fig. 6.6) and the compensated stage with eight notch hinges (Fig. 6.7). They comprise two stages with two parallel leaf springs (or four notch hinges) mounted in series such that their vertical parasitic displacements f_p offset each other. If the deformations of the two tables are identical, the translational displacement of the mobile block is rectilinear and the deflection of the compensated stage is twice the deflection of each of its constituent stages.

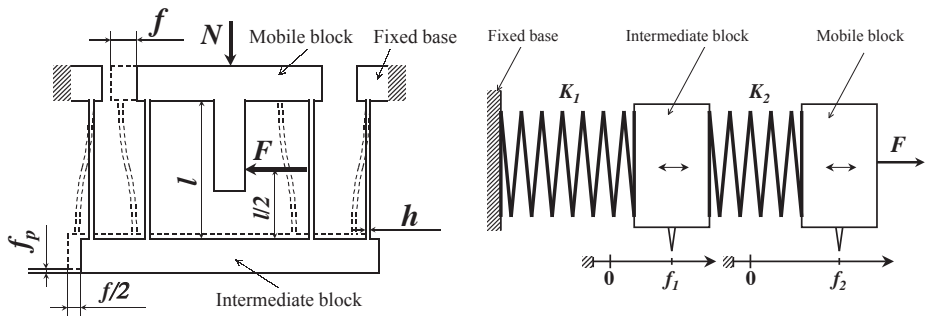


Figure 6.6 Compensated stage with four parallel leaf springs and equilibrium of stiffnesses.

To analyse this structure, let us translate it into an analogous structure with ideal bearings (Fig. 6.8). From criterion (6.2), this structure with eight pivots and two loops has two DOFs. One of these DOFs is the horizontal translational displacement of the mobile block; it is the external DOF. The second DOF may be construed as being either the horizontal translation of the intermediate

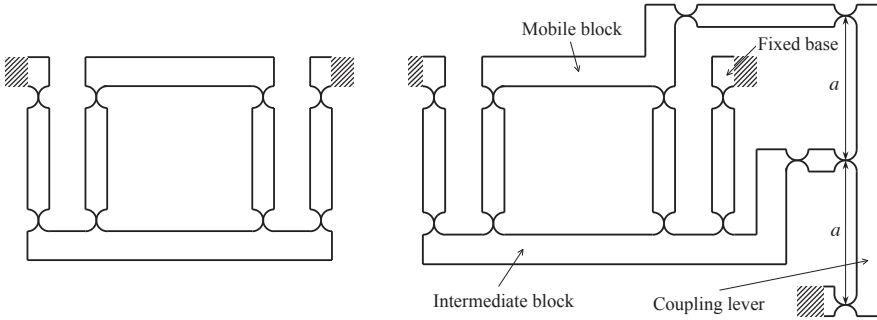


Figure 6.7 Compensated stage with eight notch hinges. The internal degree of freedom is suppressed by a coupling lever. Chapter 8 provides an in-depth study of this architecture.

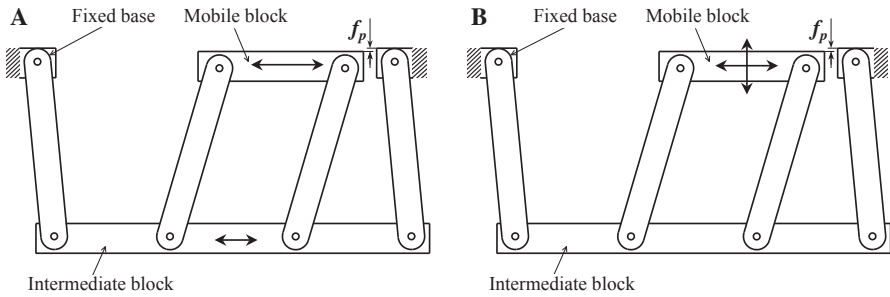


Figure 6.8 Translation of a compensated stage into a structure with ideal bearings for analysis. This structure has two DOFs.

block (Fig. 6.8A) (internal DOF) or the vertical translational displacement of the mobile block¹³ (Fig. 6.8B) (second external DOF).

For the rest of this analysis, we will consider this second DOF as an internal DOF (A) that produces a parasitic translation f_p of the mobile block. This internal DOF may be acted on either by forces related to the acceleration of its mass during dynamic motion (Genequand, 1996) or by static transverse loads. Let us consider, for example, load N in Figure 6.6. As we have seen (Sect. 4.1.6) the stiffness K_1 of the stage formed by the two internal leaf springs subjected to compressive stress decreases under the action of N , while that (K_2) of the stage formed by the two external leaf springs subjected to tensile stress increases. However, in the absence of dynamic effects, the position of

¹³ The nominal position of this structure corresponds to a kinematic singularity in which the vertical translational displacement DOF disappears. However, for any other position the mobile block has two DOFs.

the intermediate block depends on the balance between these two stiffnesses. If they are identical ($K_1 = K_2$) then $f_1 = f_2/2$ and the translational displacement of the mobile block is rectilinear. If they are different ($K_1 \neq K_2$), which is the case under the action of N , then $f_1 \neq f_2/2$ and the translational displacement of the mobile block deviates from a straight line. In addition, the allowable deflection decreases since one of the parallel leaf spring stages is loaded more than the other. Lastly, the transverse stiffness under the action of N is low, since it corresponds to one of the DOFs of the structure.

To summarise, the internal DOF of compensated stages can be acted on either statically under the action of transverse loads or dynamically under the action of accelerations. Its motion is usually detrimental since it results in an error in straightness, a decrease in the transverse stiffness of the bearing, a reduction of the allowable deflection and, potentially, vibrations.

This drawback can be overcome by suppressing the internal DOF of the intermediate block by coupling its displacement with that of the mobile block such that the motion of the former is always half that of the latter. The best-known solution is that presented in Figure 6.7, which uses a lever with a $1/2$ ratio. Criterion (6.2) applied to this structure after its translation into a plane structure with ideal bearings (a structure comprising 13 pivots and 4 loops) shows that it has only one DOF: $M = 13 - 3 \times 4 = 1$ DDL.

COMMENT: There are other rectilinear translation bearings that do not have the drawback of an internal DOF. An example is shown in Figure 6.9.

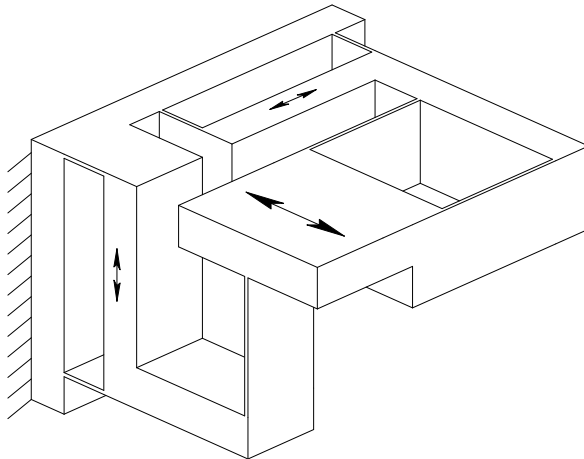


Figure 6.9 Linear translation bearing with leaf springs: two bearings in the XY planes perpendicular to each other define a straight line at the intersection of the two planes, along which the mobile block moves.

Redundant rotational bearing

A serial arrangement of two RCC pivots with four notch hinges having coincident centers of rotation (point O Fig. 6.11A) results in a structure with an angular deflection that is twice that of each constituent RCC pivot. Criterion (6.2) indicates that this structure has two DOFs. The external DOF corresponds to the rotation of the mobile block BM about O , while the internal DOF corresponds to the rotation of the intermediate block BI about O . Just as with that of the compensated stage, the internal DOF of the compensated pivot can be acted on either statically under the action of transverse loads or dynamically under the action of accelerations. Its motion is usually detrimental since it results in poor reproducibility of the path of the mobile block, low radial stiffness, a decrease in the allowable deflection and, potentially, vibrations.

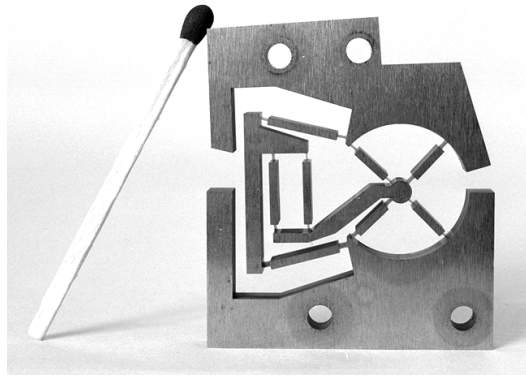


Figure 6.10 Redundant rotational bearing with high angular deflection ($\pm 15^\circ$) and high radial stiffness with coupling of the intermediate block.

This drawback can be overcome by suppressing the internal DOF of the intermediate block by coupling its angular displacement with that of the mobile block such that the rotational displacement of the former is always half that of the latter. We have invented a kinematic system that achieves this coupling function (Fig. 6.11B). The conditions required for the design to constitute a¹⁴ $1/2$ ratio coupling are as follows:

¹⁴ An elegant way to show that such kinematics imposes on the intermediate block a rotational displacement that is half that of the mobile block is to change the frame of reference by considering the intermediate block BI as fixed and the base block BB and mobile block BM as free to move. In this frame of reference, the $1/2$ ratio coupling is indicated by a symmetrical movement of BB and BM in relation to d . This symmetrical motion results in a translational displacement of the double pivot P_d along d . A rectilinear translation bearing for P_d along d thus guarantees the $1/2$ ratio coupling. To achieve the bearing for P_d , we use the segment S_5 , which compels P_d to follow a circular arc tangential to d . For small angles of rotation, this circular arc may be coincident with d and this kinematic system constitutes a coupling ratio that is very

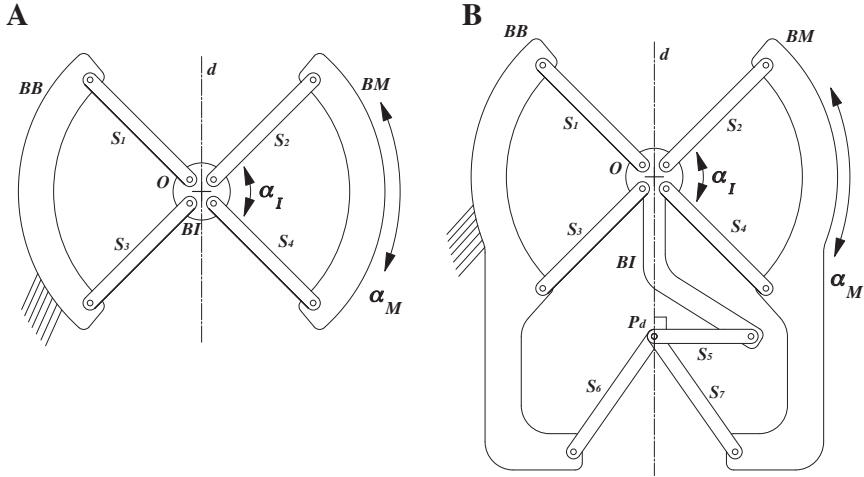


Figure 6.11 A: RCC pivots in series. B: The kinematics of the coupling suppresses the internal DOF.

- Segments S_6 and S_7 are symmetrical with respect to the straight line d passing through the center of rotation O of the compensated pivot and through the double pivot P_d .
- Segment S_5 is perpendicular to d .

The kinematic system in Figure 6.11B incorporates a double pivot P_d , which does not allow it to be fabricated monolithically from a plate by wire EDM. The kinematic system in Figure 6.12 fulfills the same function and has the advantage of having only simple pivots. It could therefore be translated into a structure with flexible bearings that can be manufactured from a single plate of material (Fig. 6.12 and 6.10) (Henein et al., 1998). This flexible structure with one DOF has 16 circular arc notch hinges, each with a thickness of $30\ \mu\text{m}$, a radius of $6.5\ \text{mm}$ and an angular deflection of $\pm 10^\circ$. The angular deflection of the mobile block is $\pm 15^\circ$. Radial stiffness measurements have shown that the stiffness of the system without the kinematic coupling is $0.6\ \text{N}/\mu\text{m}$ and $5.3\ \text{N}/\mu\text{m}$ with the coupling chain. Suppressing the internal DOF thus increased the radial stiffness by a factor of approximately 9.

close to $1/2$. For greater angles of rotation, the coupling ratio deviates from $1/2$. As a result, the two constituent RCC pivots of the compensated pivot no longer rotate through the same angle, reducing the allowable deflection. However, this variation in the coupling ratio during the rotational displacement is perfectly reproducible. In other words, the path followed by the mobile block BM is repeatable, the pivot is radially stiff, and the vibration mode corresponding to the rotation of the intermediate block BI is less likely to be induced. With criterion (6.2) it is easy to verify that this structure has just one DOF.

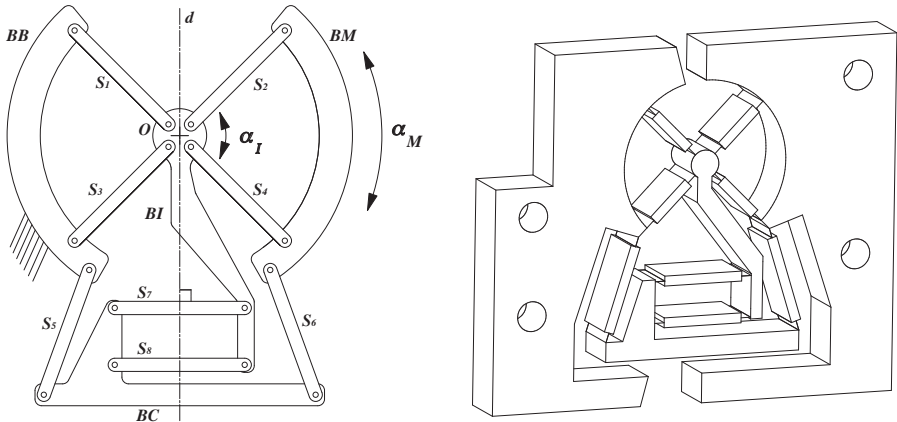


Figure 6.12 Alternative kinematic coupling without double pivot and physical realisation into a plate to produce a monolithic prototype.

Arranging the two RCC pivots in Figure 6.11A in series caused the parasitic translations to be cumulative. As a result, the parasitic translation of the mobile block is approximately twice that of the individual RCC pivots. In other arrangements, the parasitic translations of the RCC pivots may partially offset one another, thus decreasing the parasitic translation of the mobile block.

6.3.2 Mechanical stops

Mechanical stops that limit deflections are generally used to protect flexible structures from excess loads and excess deflection. Where possible, these stops are integrated in the monolithic structure, enabling them to be positioned with great precision. In the case of flexible bearings with one or two DOFs, these stops are usually easy to design. With more complex structures, however, determining the positions of these stops can be more of a challenge. There are two approaches:

- Stops that limit the deflections of motoric segments (Fig. 6.13A), thus protecting the structure from any actuator control signal errors. Such stops are highly useful during the setting phase for robots and their controls. If an excess load is applied to the mobile block of a structure with reversible actuators¹⁵, these stops prevent the allowable deflections from being exceeded but do not protect against excess loads.
- Stops that limit deflections of the mobile block (Fig. 6.13B) protect the structure from any excess loads if the actuators are reversible. If the

¹⁵ If the actuators are irreversible, this type of stop is ineffective against excess loads applied to the mobile block.

actuators are irreversible, preloaded segments that are advanced or retracted when the loads exceed a certain threshold must be used. These stops then arrest the travel of the mobile block. In the event of actuator control signal errors, these stops prevent the allowable deflections from being exceeded but do not protect the structure against the forces generated by the actuators.

For reasons of static indetermination, it is not possible to combine the two approaches.

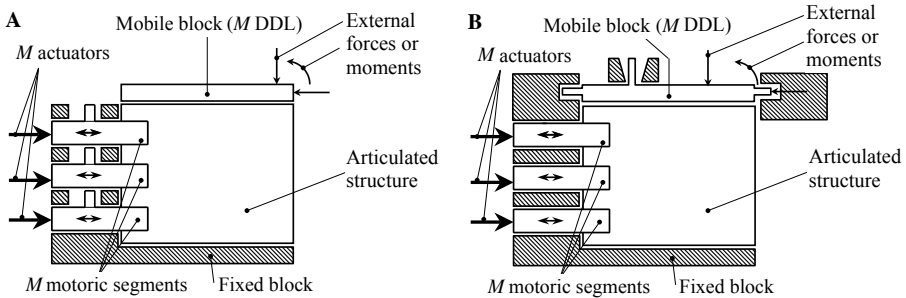


Figure 6.13 Mechanical stops limiting the deflections of the motoric segments (A) or the mobile block (B).

6.4 Stiffnesses

6.4.1 Minimisation of natural stiffnesses

In some cases, the elastic restoring force in flexible bearings can be an issue. To reduce it, we looked for principles that would make it possible to minimise the natural stiffness of the bearings. For example, we show in Section 4.3.6 that the use of stages with four notch hinges, with a parameter ξ tending to 0, makes it possible to minimise the natural translational stiffness. There are other principles that make it possible to reduce this stiffness even further.

In Section 4.1.5 and Section 4.1.6 we show that the natural stiffness of a two parallel leaf spring stage depends on the load \bar{N} applied to it. It is possible to exploit this property to construct bearings with an adjustable natural stiffness that can be reduced to zero or made negative. Achieving this requires applying to the mobile block of a parallel leaf spring stage a force \bar{N} similar to the load \bar{N}_o (4.40) that induces zero natural stiffness. The intensity and direction of this force must remain constant during the motion of the stage.

A simple way to produce it is to place a mass with a weight equal to \bar{N}_o on the mobile block of the stage. This solution has significant drawbacks in that

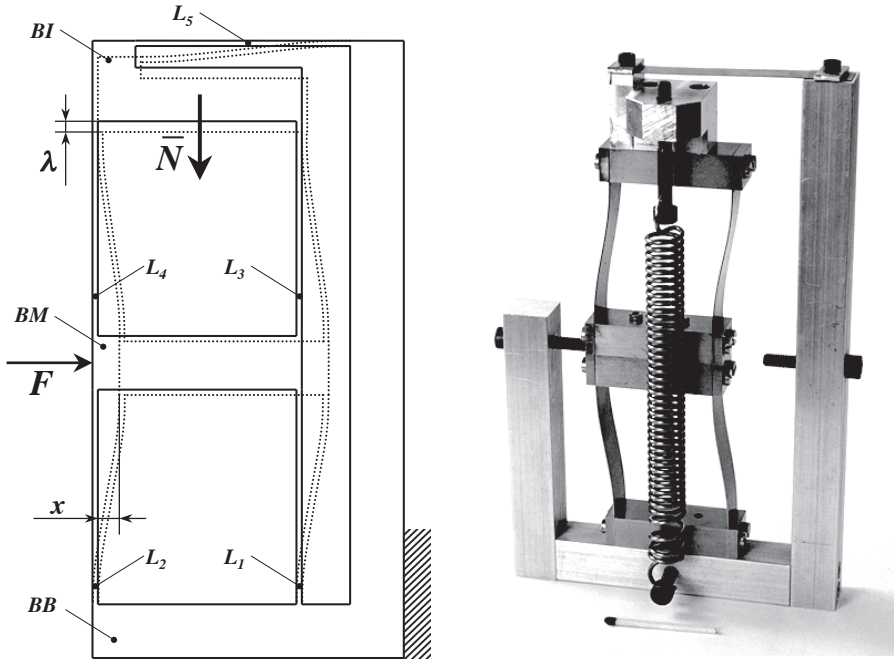


Figure 6.14 Principle of a translational bearing with adjustable stiffness: principle and demonstration device.

it requires having a significant movable mass and can be used only if the leaf springs are in a vertical position.

Another way to produce it is to use the structure shown in Figure 6.14 and to apply the force not to the mobile block *BM*, but to the intermediate block *BI*, whose motions are much lower in amplitude. This force can be, for example, a dead weight, the opposing force of a spring, or the force of an electromechanical actuator.

Let us consider the case where force \bar{N} is produced by a spring with stiffness K_r , as in the photo (Fig. 6.14). Let us disregard the horizontal displacement of *BI* and take as zero the natural stiffness K_{cis} (Sect. 3.1.2) of the leaf spring L_5 . The direction of the force \bar{N} remains constant during the displacement of *BI* but the vertical displacement λ of *BI* causes a decrease in the preload of the spring when *BM* moves away from its nominal position. The stiffness of this structure is thus not constant but progressive. From (4.13) we obtain

$$\lambda(x) = \frac{6}{5l}x^2.$$

Let us use λ_0 to denote the elongation of the preload spring in the nominal position. This gives us

$$\bar{N}(x) = K_r(\lambda_0 - \lambda(x)).$$

Let us use \bar{K}_t to denote the stiffness of the two parallel leaf spring stages (4.9) fitted in parallel

$$K_t = \frac{48EI}{l^3}$$

and \bar{N}_0 to denote the load inducing zero stiffness (4.40). From (4.43), the secant stiffness¹⁶ is given by

$$K_s(x) = K_t - \frac{K_t}{\bar{N}_0} \bar{N}(x).$$

This is a second-order polynomial. The force to be produced to move BM through a distance x is

$$F(x) = K_s x.$$

The force-deformation characteristic curve is thus a third-order polynomial that passes through the origin:

$$F(x) = \left(\bar{K}_t - \frac{K_t K_r \lambda_0}{\bar{N}_0} \right) x + \frac{6K_t K_r}{5l\bar{N}_0} x^3. \quad (6.3)$$

The tangent stiffness is the derivative of the force-deformation characteristic equation:

$$K(x) = \bar{K}_t - \frac{K_t K_r \lambda_0}{\bar{N}_0} + \frac{18K_t K_r}{5l\bar{N}_0} x^2. \quad (6.4)$$

We manufactured this bearing with adjustable stiffness monolithically using the leaf spring L_5 not only as a guide for BI , but also as a preload spring (Fig. 6.15 and 6.16). This principle of stiffness compensation makes it possible to reduce stiffness considerably and obtain completely novel force-deformation characteristic curves with, for example, points where the tangent stiffness is zero and the force is non-zero (Fig. 6.17 and Fig. 6.18).

¹⁶ The *secant* stiffness of a structure with a non-linear force-deformation characteristic curve is the ratio between the applied force and the resulting deformation: $K_s = F/x$. It corresponds to the stiffness of a spring with a linear force-deformation characteristic curve (constant stiffness) that, under the same force, would be subjected to the same deformation as said structure. The secant stiffness should not be confused with *tangent* stiffness, which is the slope of the force-deformation characteristic curve $K = dF/dx$ (Spinnler, 1997b).

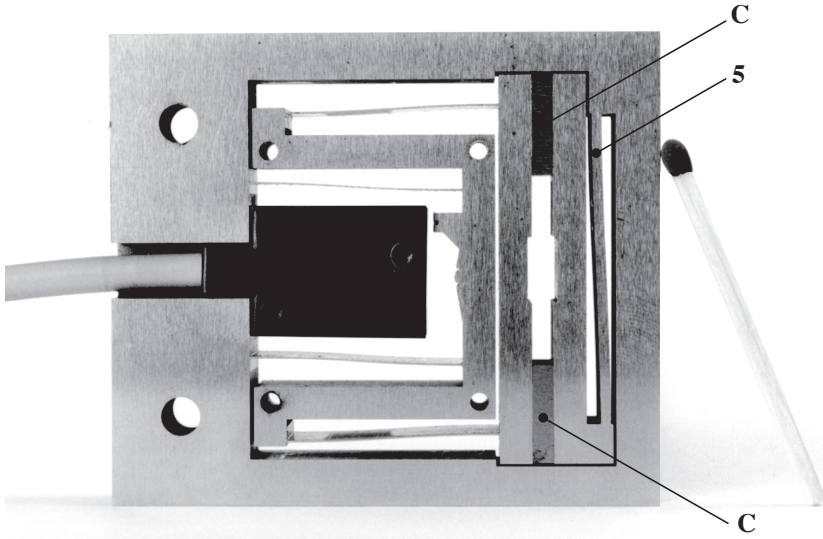


Figure 6.15 Photo of a monolithic bearing with adjustable stiffness. The shims C make it possible to adjust the preload force of the leaf spring 5.

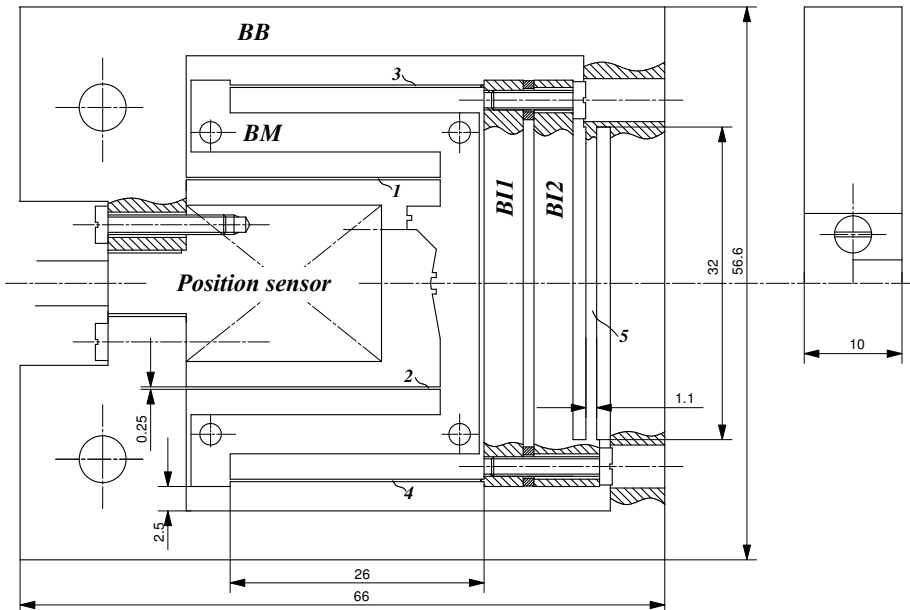


Figure 6.16 Monolithic bearing with adjustable stiffness. Material: X220CrVM013-4 tempered steel; $E = 196$ GPa.

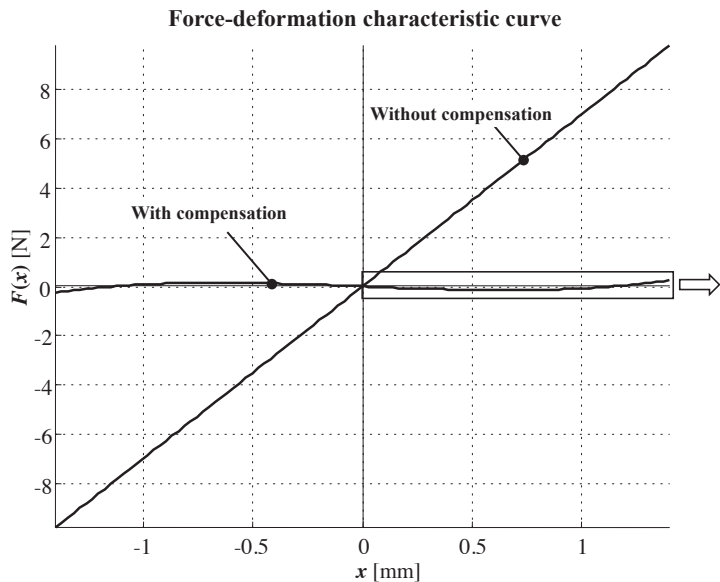


Figure 6.17 Theoretical force-deformation characteristic curve of the monolithic structure in Figure 6.16 preloaded such that its stiffness in the nominal position is slightly negative ($\bar{N} = 1.05 \times \bar{N}_0$).

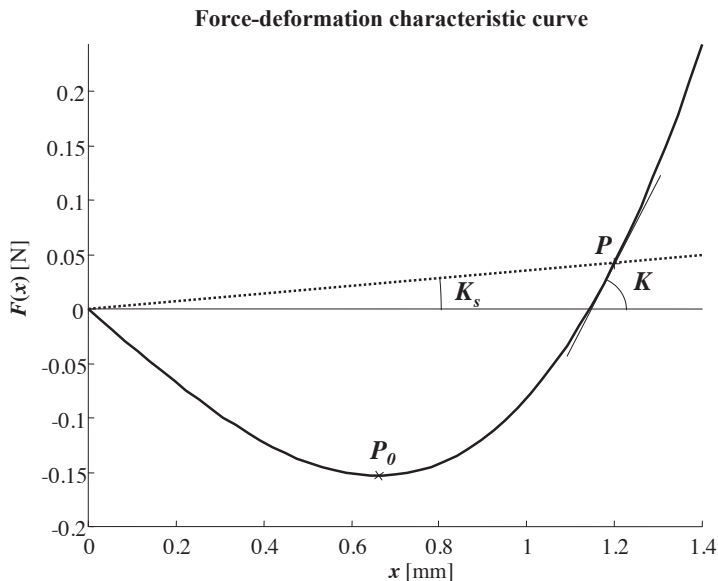


Figure 6.18 Close-up view of the interesting part of the characteristic curve (box in Fig. 6.17) with the secant stiffness K_s and tangent stiffness K at one of its points (P). At point P_0 , the tangent stiffness is zero and the force is non-zero.

The low stiffness and progressiveness of the characteristic curves make this structure an ideal load cell for creating a high precision force sensor. To achieve this, we placed an optical position sensor with a resolution of $1\text{ }\mu\text{m}$ in the structure to measure the displacement of the mobile block.

This same approach may be used to achieve rotational bearings with adjustable stiffness and even structures with more than one DOF.

6.4.2 Maximisation of natural stiffnesses (energy storage)

In some cases, it is necessary to maximise the natural stiffnesses of bearings while still maintaining their allowable deflection, such as when the elastic restoring force on bearings is used as a preload or when a bearing is used to store mechanical energy. This issue boils down to a classic case of maximising the *utilisation coefficient*¹⁷ of springs. In the case of bearings that use beams subjected to bending as flexure joint elements, profiles of *uniform bending strength*¹⁸ must be used. In common cases where the bending moment varies linearly along the beam, profiles of uniform bending strength are parabolic.

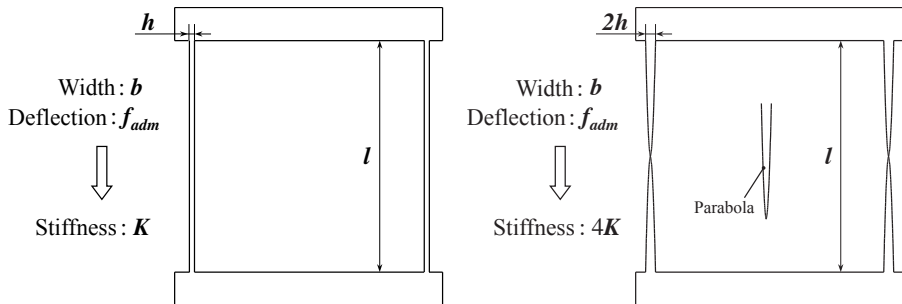


Figure 6.19 The use of leaf springs of uniform bending strength (parabolic leaf springs in this case) makes it possible to increase the natural stiffness without reducing the allowable deflection.

¹⁷ The *utilisation coefficient* of a spring is the ratio between the energy stored in the spring and the energy stored in a tensile spring of the same volume subjected to the same maximum stress (Duchemin, 1984). The amount of energy that can be stored in an elastic element is proportional to the ratio σ_{adm}^2/E . Hence, the material selection criterion differs depending on whether the aim is to maximise the allowable deflection (maximise σ_{adm}/E (Sect. 6.2)) or the energy that can be stored elastically (maximise σ_{adm}^2/E).

¹⁸ A beam profile is said to be of *uniform bending strength* if the My/I ratio (2.2) is constant along the entire beam (where M is the bending moment; y is the distance of the most heavily loaded fiber from the neutral fiber; I is the moment of inertia of the beam cross section).

Let us take the example of a two parallel leaf spring stage. If we replace the leaf springs of constant thickness h with parabolic-profile leaf springs of thickness $2h$ at the ‘clamped’ ends, the allowable deflection of the stage remains the same but its stiffness is multiplied by four (6.19). The shear force must also be taken into consideration in the dimensioning of the central portion of the leaf spring.

EXAMPLE: To manufacture the load cell of a bicycle torque sensor fitted between the bottom bracket axle and the chainwheels, we designed a rotational bearing that withstands the maximum torque that may be applied by the cyclist (100 Nm) without exceeding the allowable stress but producing the greatest possible rotational displacement (Fig. 6.20) (Boillat, 1997; Henein et al., 2000). The five beams with a virtually parabolic profile were optimised by finite element simulations (particularly the central ‘wasp waist’ and the transition fillets at the ends of the beams).

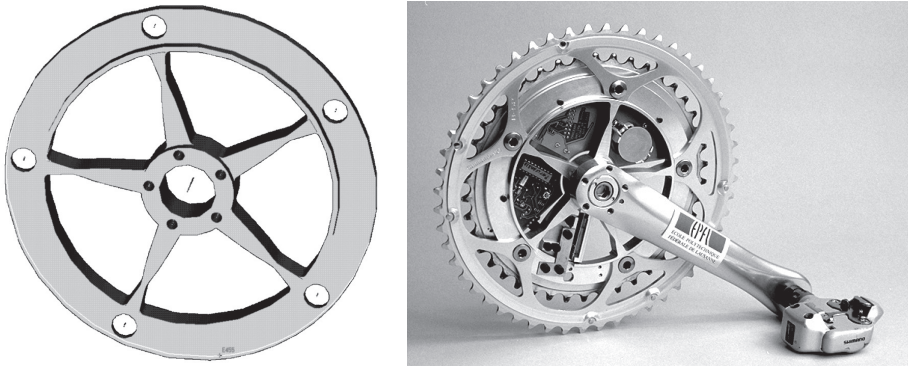


Figure 6.20 Rotational bearing with virtually parabolic leaf springs of uniform bending strength used as a load cell for a bicycle torque sensor.

Figure taken from (Genoud, 2000), author's photos.

Another solution for increasing the stiffness of bearings without reducing their deflection is to fit several flexure joints in parallel. Figure 6.21 shows an overconstrained pivot with 21 leaf springs. This approach has the drawback of producing many statically indeterminate systems that can make the behaviour hard to predict.

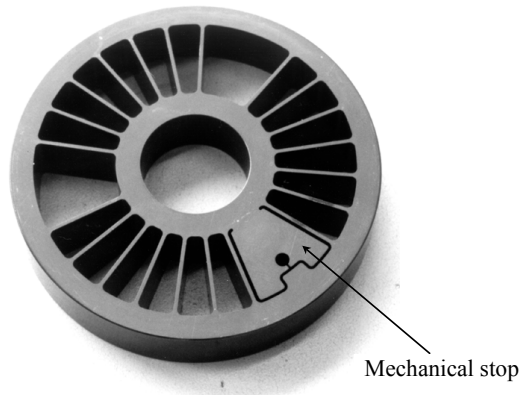


Figure 6.21 Overconstrained pivot with 21 leaf springs.

Modular design of flexure-based robots

7.1 Introduction

Miniaturisation will be the key challenge of the next decade in numerous industrial domains, such as microelectronics, optics and biomedical engineering. Although most of their products already achieve footprints of some square millimetres, the trend towards the integration of a maximum number of components in a minimal volume still demands more compact devices. Subsequently, *current manufacturing processes and machines will soon be overtaken by this decrease in the size of the products: this tendency thus creates an urgent need for new production methods*. Two possible directions to solve this issue are currently investigated: the bottom-up and the top-down approaches. Bottom-up manufacturing is based on atomic and molecular manipulation: techniques such as self-assembly, chemical synthesis and positional assembly, which consists in building devices atom by atom, are the main investigation fields of this avenue. On the other hand, the top-down approach consists in removing and shaping material using ultra-high precision techniques. Usual cleanroom processes (lithography, etching) and classical material removal manufacturing methods (turning, milling, grinding, laser beam machining, electro-discharge machining), are included in this approach (Tolfree, 2006). Furthermore, both philosophies notably share the objective of miniaturising the whole production line, thus using down-scaled pick-and-place machines, conveyers, and miniaturised specific operation robots, intended for tasks such as manipulation, packaging or dispensing. Consequently, new production plant concepts emerge, such as microfactories: they consist in tabletop production lines, often combined with mini-cleanroom modular production cells, and have already been investigated for several years (Kobel and Clavel, 2011; Verettas, 2006).

The main implication of both new manufacturing approaches for small devices is *the creation of a need for robots able to perform micromanipulation and microassembly tasks with a submicrometric precision*. Typical requirements of such machines are performing more than 3 Degrees of Freedom (DOF), with

strokes of some millimetres in translation and of more than 5° in rotation. The aimed precision order of magnitude is 10 to 100 nanometres and $1 \mu\text{rad}$. Furthermore, the total volume of the robot should be minimised to permit the miniaturisation of the production line.

Nonetheless, *the design of such machines is nowadays costly, both in time and money*, mostly because of the twofold complexity of their development: first, from a kinematic standpoint, the *use of a parallel structure* consists of a particularly interesting approach for building ultra-high precision robots. However, *the synthesis of such a kinematics proves especially challenging for machines presenting more than 3 degrees of freedom*. Numerous design methodologies have been developed, such as those described in (Danescu, 1995; Helmer, 2006; Gogu, 2010). However, these share the common drawback that *the resulting machines are barely flexible*: if the industrial specifications change, requiring, for example, a degree of freedom to be added or the position of a rotation centre to be changed, the synthesis process has to be restarted, often from the very beginning.

The second challenge consists in the *mechanical design of flexure-based mechanisms*. As seen throughout this whole book, the synthesis of planar and low-degree-of-freedom structures is now widely investigated; nonetheless, the development of a whole tridimensional flexure-based robot is still infrequent, especially in the industrial context.

The aim of this chapter is thus to introduce a *modular design methodology*, which drastically decreases the time-to-market of ultra-high precision robots. This procedure can be compared to a *robotic Lego*, where a *finite number of conceptual building bricks* allows parallel robots to be easily designed and modified. Furthermore, this work has proved that the machines resulting from this approach present *similar or even improved performances* compared to more traditionally developed robots.

The chapter is organised as follows:

- Section 7.2 presents the *concept of modular kinematics*: the bases and notations of the methodology, as well as the exhaustive conceptual solution catalogue, are introduced.
- Section 7.3 presents the *reduced solution catalogue for ultra-high precision applications*, as well as the selection criteria linked with the design and machining of flexure-based mechanisms which have allowed its establishment.
- Section 7.4 details the *mechanical design of the building bricks*: original flexure-based designs, as well as common and innovative uses of well-known mechanisms, are proposed as mechanical solutions for each building brick.

- Section 7.5 illustrates the practical use of the methodology thanks to the *case study of a 5-DOF ultra-high precision robot, Legolas 5*. The selection of an adapted kinematics in the solution catalogue and the development of the Legolas 5 prototype are presented.
- Section 7.6 introduces the *Legolas family, a new family of ultra-high precision parallel robots* which has been generated by this case study.
- Section 7.7 finally concludes this Section by highlighting the potentialities of this modular design methodology.

7.1.1 Preliminary definitions

First of all, the key concepts of this work need to be properly defined, namely ultra-high precision, parallel robots and modularity.

Resolution, precision, repeatability and accuracy

The positioning capability of a robot is usually described in terms of resolution, precision, repeatability and accuracy. These concepts, as well as their use in this chapter, need to be clearly defined.

- **Resolution** refers to the *minimal motion a robot or a mechanism can perform*. This denomination is also used for sensors, where it represents the *smallest change in the quantity which can be measured*. The overall resolution of a closed-loop system, for example a robot, depends on the performances of its sensors, actuators, mechanical design and controller.
- **Precision** and **repeatability** are used as synonyms and represent the *statistical measure of how much a robot actual motions differ from each other when the robot is commanded to repeat a single desired motion* (Ackerson and Harry, 1985; Lubrano, 2011). Note that this quantity is usually evaluated with a measuring device which is external to the robot. Moreover, the repeatability of a robot cannot be smaller than its resolution.
- **Accuracy** refers to the difference between the desired position which a robot is commanded to achieve, and the actual position it actually reaches; this quantity cannot be smaller than the robot repeatability.

Figure 7.1 illustrates the difference between repeatability and accuracy by analogy with a shooter. Moreover, precision and repeatability differ from accuracy in one key aspect: the first concepts are characteristics which are intrinsic to the robot design and assembly, whereas the second is strictly linked to the mathematical model of the robot. Consequently, precision and repeatability cannot be improved once the robot has been built: the mechanical design of the robot must thus be meticulously handled. Conversely, accuracy can be drastically improved by a calibration process, which aims at optimising the model of the robot by taking into account the error sources acting on it. A

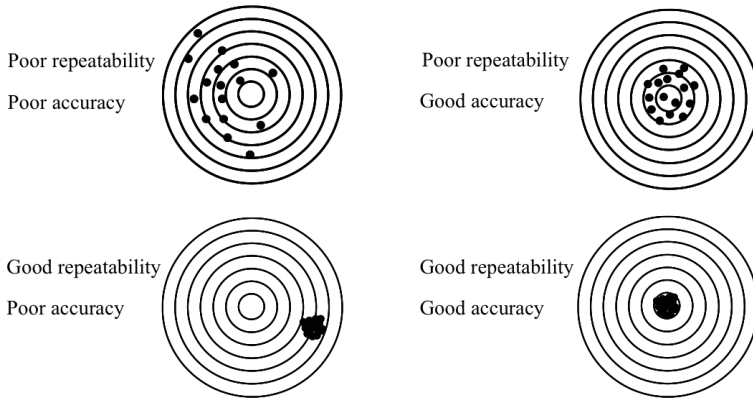


Figure 7.1 Illustration of the repeatability and accuracy concepts with the analogy of a shooter (Fazenda, 2007).

powerful calibration procedure dedicated to high precision applications, which compensates for temperature effects and deformations due to forces generated by the task the robot has to accomplish, has been developed in (Lubrano, 2011).

Finally, the distinction between high precision and ultra-high precision, often used in this work to qualify robots and mechanisms, needs to be clearly specified:

- **High precision** refers to robots and mechanisms which present precisions between 0.1 and $10\ \mu\text{m}$.
- **Ultra-high precision** refers to robots and mechanisms which present precisions better than $0.1\ \mu\text{m}$ ($100\ \text{nm}$).

Parallel robots

A **parallel robot** is a robot composed of at least two bodies which are linked together by more than one kinematic chain (Clavel, 1991). A well-known example is the Delta robot, which is illustrated in Figure 7.2. When the tasks that have to be accomplished by the machine require a submicrometric precision, the use of parallel kinematics presents crucial advantages over serial arrangements:

- **Lower inertia** thanks to the actuators which are fixed to the robot frame. Moreover, as the mass which has to be set in motion is lower the dynamical behaviour of parallel robots surpasses the performances of serial manipulators by achieving higher accelerations.
- **Higher stiffness**: as more than one kinematic chain link the robot end-effector to the fixed part, the stiffness is increased, exactly as several springs arranged in parallel are stiffer than one single spring. Consequently, parallel robots also present higher eigenfrequencies than serial manipulators.

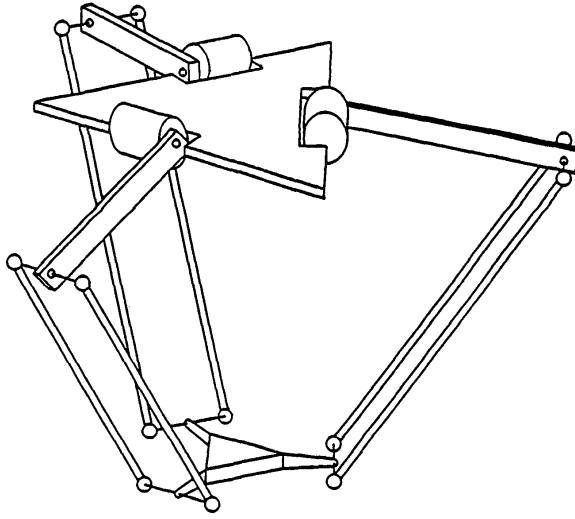


Figure 7.2 Sketch of the classical Delta kinematics, presenting 3 kinematic chains which link the end-effector (lower triangle) to the fixed frame of the robot, to which the 3 motors are attached (upper triangle) (Clavel, 1991).

- **Higher precision**, because the kinematic loops average the machining and assembly errors instead of adding them, which is the case in serial manipulators.

In addition, the location of the motors, which are fixed to the robot frame, presents another crucial advantage for high and ultra-high precision applications: indeed, the actuators consist of the main heat source acting on the machine. Consequently, their thermal isolation allows heat conduction to be limited throughout the robot structure, and thus its thermal expansion. For instance, (Niaritsiry, 2006) proposes a system that covers the robot actuators, thus limiting both convection and conduction to the mechanical parts: the robot is thus isolated from the temperature variations of both its environment (ambient air) and its actuators.

As for the drawbacks of parallel robots, namely their limited workspace, the presence of singularities resulting in uncontrolled degrees of freedom and the complex geometric models, they can be easily overcome by a smart design and an appropriate control strategy.

Modularity of industrial robots

Although *modularity* or *reconfigurability* of industrial robots is being widely explored, no strict and unique definition of this notion can be highlighted. Nonetheless, the extensive review of the topic literature performed in (Pozna,

2007) has allowed commonly shared features of modular robots to be underlined, such as the use of standard modules to build different products and the notion of interface, which relates to the possibility of connecting the modules to the assembly. Moreover, modularity in industrial robotics mostly refers to the possibility of increasing the dynamic performances of the manipulators by modifying their structures (Pozna, 2007).

In this work, *modularity of parallel industrial robots* specifically refers to the following characteristics:

- *Simplified synthesis of the robot kinematics*, thanks to the use of standardised conceptual building bricks and solution catalogues
- *Straightforward modification of the robot degrees of freedom*, at any step of the design process
- *Possibility of increasing the performances of the robot*, particularly by adjusting the location of the rotation centres

Lastly, the study conducted in (Pozna, 2007) notably highlights the limited impact of modularisation in the industrial field, which is explained by the complexity of the reconfiguration steps. Consequently, design methodologies which allow to easy and rapid modifications of parallel manipulators are crucial to enable the breakthrough of modularity in industrial robotics.

7.2 Concept of modular kinematics

This section introduces the fundamentals of the design methodology, which consist in the conceptual aspects leading to the kinematic synthesis of modular parallel robots. As the aspects presented in this section are purely conceptual, i.e., totally independent from any mechanical design, this part of the methodology can be applied to design the kinematics of a large variety of robots, from machine-tools to microscale robots.

7.2.1 Modular parallel robot and building bricks

This methodology consists in designing a modular parallel robot composed of one to three kinematic chains, which are orthogonally arranged. This robot is symbolised by a cube: each kinematic chain is disposed along a different face, whereas the end-effector is located on one of its corners (Fig. 7.3, left). Its kinematic synthesis makes use of a finite number of conceptual building bricks, which can be either active or passive (Fig. 7.3, right). Each kinematic chain of the modular robot consists in the serial arrangement of an active brick with a passive one.

The modular methodology takes as an input the desired robot mobility: only the presence or absence of the 6 possible end-effector degrees of freedom

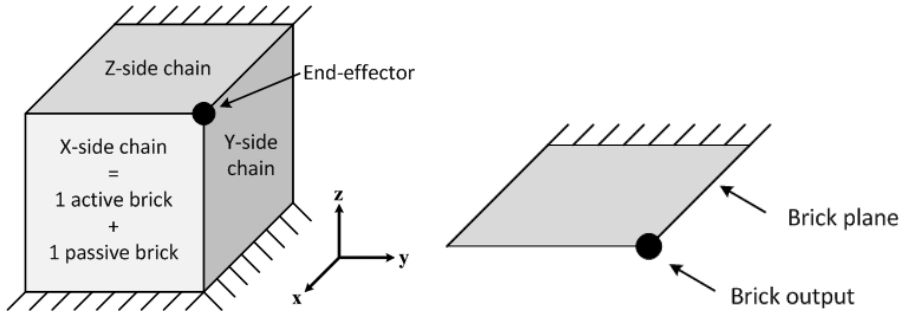


Figure 7.3 Symbolism of the parallel robot designed with the modular concept (left) and of the building bricks (right)

is considered at this step of the procedure. This global requirement is then transformed into a thorough list of all possible combinations of active and passive bricks fulfilling it, thanks to the exhaustive conceptual solution catalogue, which will be presented in Section 7.2.2. Finally, a kinematics is selected depending on the robot specific requirements, as well as on mechanical design considerations.

The ability of this concept to respond to changes in the industrial specifications during the design process lies in its modularity: only a minimal number of bricks, in most cases just one, needs to be modified to add or remove a degree of freedom. Moreover, the active bricks composing a robot are kinematically uncoupled, even its geometric model and its control algorithm require only minor changes to fulfill the new specifications.

Conceptual building bricks

The modular methodology makes thus use of a finite number of conceptual building bricks, which can be either active or passive:

- The role of the **active bricks** is to actuate from one to three degrees of freedom; the other motions are blocked.
- The **passive bricks** link the output of the active bricks to the end-effector of the robot, thus performing a transmission of the actuated motions. Their degrees of freedom are either passive, i.e. free to move but not actuated, or blocked.

A generic notation uniformly represents the conceptual building bricks by symbolising their two main features:

- **The free degrees of freedom of the brick, i.e. the active or passive motions, are represented by letters**, namely T for translations and R for rotations. Uppercase letters (T, R) stand for actuated motions, whereas lowercase letters (t, r) symbolise passive degrees of freedom, which allows both types of building bricks to be identified.

- *The subscripts indicate the direction of the motions relative to the face of the cube on which the brick is positioned.* Regarding the orthogonal coordinate system presented in Figure 7.3, three directions are possible: \perp indicates that the considered motion is along an axis which is orthogonal to the face plane, whereas \parallel stands for a degree of freedom which is along one of the two directions that belong to that plane (Fig. 7.4). Moreover, the additional subscripts 1 and 2 explicitly express the directions of several degrees of freedom along both possible axes of the plane. Figure 7.5 illustrates an example where this discrimination is mandatory.
- The order of the motions in the brick notation has arbitrarily been set to the following: T_{\parallel} , T_{\perp} , R_{\parallel} , and R_{\perp} for the active bricks, and the corresponding t_{\parallel} , t_{\perp} , r_{\parallel} , and r_{\perp} for the passive bricks.

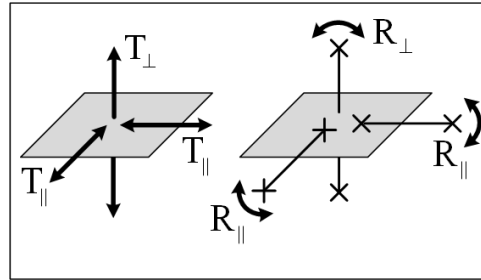


Figure 7.4 Possible directions of the brick degrees of freedom relative to the face plane.

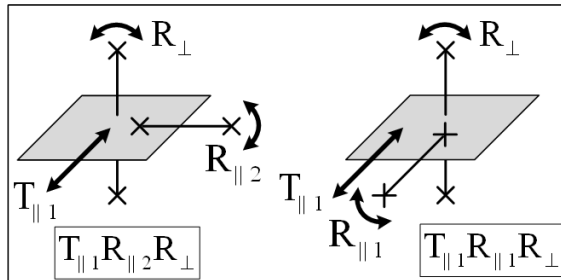


Figure 7.5 Example of two active bricks to illustrate the use of the additional 1 and 2 subscripts.

Following these guidelines, the exhaustive set of conceptual building bricks is established. The active bricks, which actuate from one to three motions, perform the 12 possible output mobilities: their total number is 25, as several bricks can present the same degrees of freedom with different orientations relative to the face of the cube on which they are located. The choice to limit

the number of actuated degrees of freedom to three is related to the aim of the design methodology, which consists in simplifying the kinematic synthesis of parallel robots: designing bricks which actuate a higher mobility than three is as complex as directly building an equivalent robot. Thus, their inclusion in the concept does not help decreasing the intricacy of the synthesis.

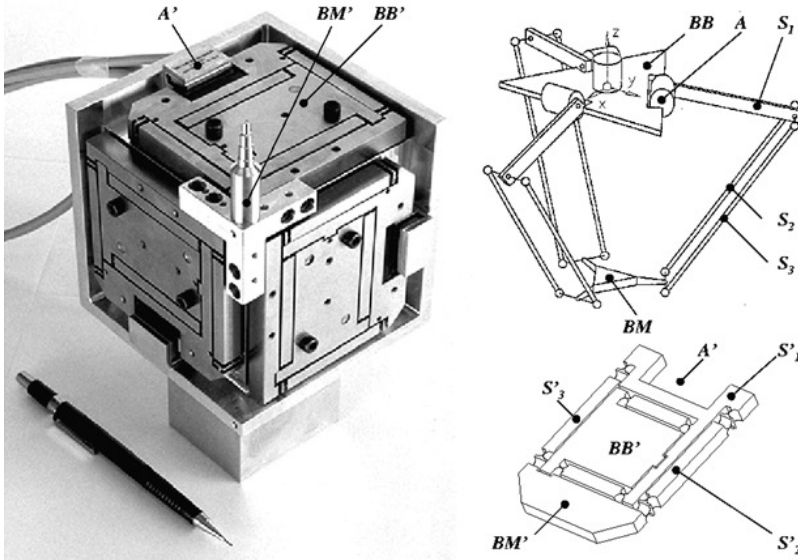


Figure 7.6 Flexure-based Delta robot (Delta³) (Henein, 2001).

Furthermore, 38 passive bricks are featured in the methodology, including the passive version of the 25 active bricks and the 13 bricks performing the 4- and 5-DOF motions. Note that the 6-DOF passive brick has been discarded as it cannot perform the transmission of any motion, all its degrees of freedom being free. Moreover, the 0-DOF brick, whose motions are all blocked, has also been relinquished for its uselessness. All other mobilities have been included in the concept, as the design of 4- or 5-DOF passive bricks is easier to achieve than the corresponding actuated mechanisms. Both the 4-DOF space parallelogram which is included in the flexure-based Delta kinematics (Fig. 7.6), and the Sigma 6 robot arms (see Fig. 7.37) epitomise this observation.

The exhaustive list of the conceptual building bricks, including their notation and their graphical representation, is illustrated in Figures 7.7 to 7.11. The alternation of grey and white backgrounds groups subsequent bricks which share the same degrees of freedom with different orientations relative to the cube face.

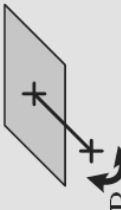
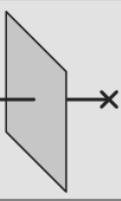
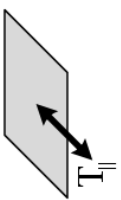
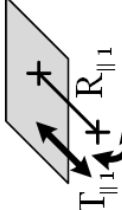
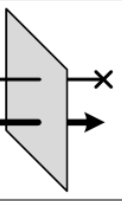
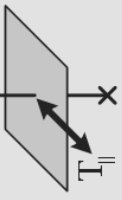
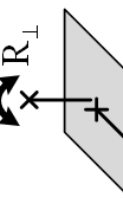
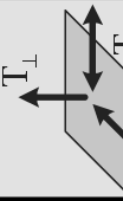
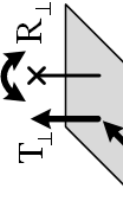
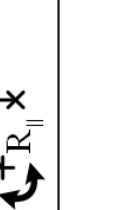





ACTIVE BRICKS					
R_{\parallel}		R_{\perp}		T_{\parallel}	
$T_{\parallel 1} R_{\parallel 1}$		$T_{\perp} R_{\perp}$		$T_{\perp} R_{\parallel}$	
R_{\perp}		$T_{\parallel 1} T_{\parallel 2} T_{\perp}$		$T_{\parallel} T_{\perp} R_{\perp}$	
$T_{\parallel 1} T_{\parallel 2}$		$T_{\parallel} T_{\perp} R_{\parallel 1}$		$T_{\parallel 1} T_{\parallel 2} R_{\parallel 1}$	
$T_{\parallel 1} T_{\perp}$		$T_{\parallel 1} T_{\parallel 2} R_{\parallel 2}$		$T_{\parallel 1} T_{\perp} R_{\parallel 2}$	

Figure 7.7 List of the conceptual active bricks (1/2). The bold line groups the bricks which share the same mobility.

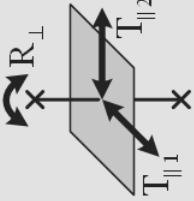
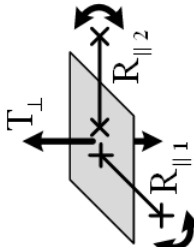
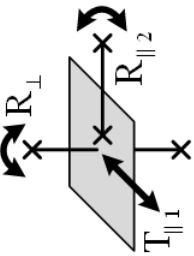
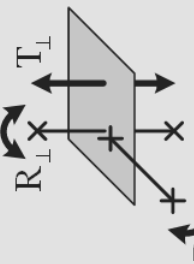
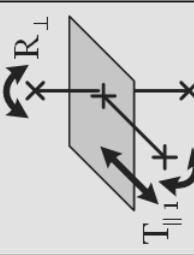
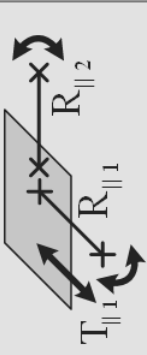
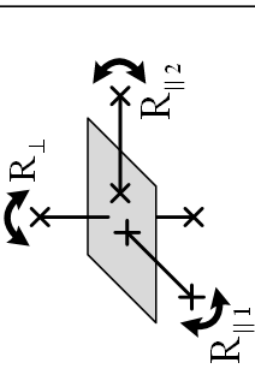
ACTIVE BRICKS, continued				
$T_{\parallel 1}T_{\parallel 2}R_{\perp}$	$T_{\perp}R_{\parallel 1}R_{\parallel 2}$	$T_{\parallel 1}R_{\parallel 2}R_{\perp}$	$T_{\perp}R_{\parallel 1}R_{\perp}$	$T_{\parallel 1}R_{\parallel 1}R_{\perp}$
				
$T_{\parallel 1}R_{\parallel 1}R_{\parallel 2}$		$R_{\parallel 1}R_{\parallel 2}R_{\perp}$		
				

Figure 7.8 List of the conceptual active bricks (2/2).

PASSIVE BRICKS					
$r_{ }$	r_{\perp}	$t_{ }$	t_{\perp}	$t_{ 1}t_{ 2}$	$t_{ }t_{\perp}$

Figure 7.9 List of the conceptual passive bricks (1/3).

PASSIVE BRICKS, continued					
$t_{\parallel 1} t_{\parallel 2} r_{\perp}$	$t_{\perp} r_{\parallel 1} r_{\parallel 2}$	$t_{\parallel 1} r_{\parallel 2} r_{\perp}$	$t_{\perp} r_{\parallel 1} r_{\perp}$	$t_{\parallel 1} r_{\parallel 1} r_{\perp}$	$t_{\parallel 1} r_{\parallel 1} r_{\perp}$
$t_{\parallel 1} r_{\parallel 1} r_{\parallel 2}$	$r_{\parallel 1} r_{\parallel 2} r_{\perp}$	$t_{\parallel 1} t_{\parallel 2} r_{\perp}$	$t_{\perp} t_{\parallel 1} r_{\parallel 1}$	$t_{\perp} t_{\parallel 1} r_{\parallel 2}$	$t_{\perp} t_{\parallel 1} r_{\perp}$
$t_{\parallel 1} r_{\parallel 1} r_{\parallel 2}$	$t_{\parallel 1} t_{\parallel 2} r_{\parallel 1} r_{\perp}$	$t_{\parallel 1} t_{\parallel 2} r_{\parallel 2} r_{\perp}$	$t_{\parallel 1} t_{\parallel 2} r_{\parallel 1} r_{\parallel 2}$	$t_{\parallel 1} t_{\parallel 2} r_{\parallel 1} r_{\parallel 2}$	$t_{\parallel 1} t_{\parallel 2} r_{\parallel 1} r_{\parallel 2}$

Figure 7.10 List of the conceptual passive bricks (2/3); the double line separates the passive version of the 25 active bricks, presenting one to three DOF, from the passive bricks performing four and five DOF.

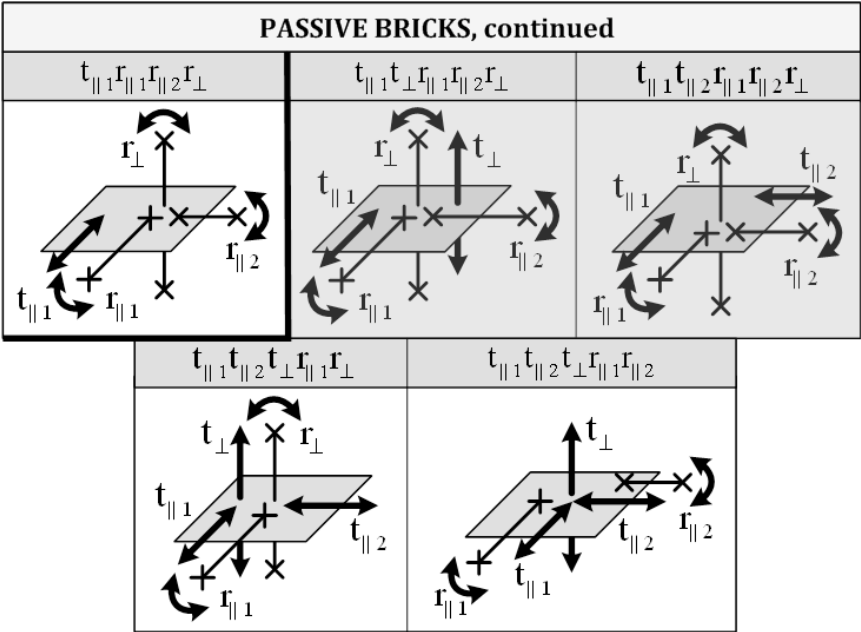


Figure 7.11 List of the conceptual passive bricks (3/3).

7.2.2 Exhaustive conceptual solution catalogue

The exhaustive conceptual solution catalogue is the core of the modular methodology, as it allows to significantly reduce the time necessary for synthesising the robot kinematics. All possible kinematics stemming from the concept are indeed listed in this catalogue, from which the robot designer can select the most suitable solution for his/her specific requirements.

This thorough catalogue needs to be generated only once. This process is entirely based on combinatory algorithms and includes two main steps: first, the exhaustive list of all active brick arrangements actuating the desired robot degrees of freedom is established for each of the 19 possible robot mobilities. Then, for each of these arrangements, all combinations of passive bricks performing the transmission of these motions without overconstraints are itemised. The complete procedure to generate the exhaustive conceptual solution catalogue can be found in (Richard, 2012).

In the end, the exhaustive conceptual solution catalogue features a total of 3175 kinematic solutions, including 547 different active bricks arrangements. All these possibilities are graphically represented in (Richard, 2012).

7.2.3 Conclusion

In conclusion, the objective of the methodology, which consists in decreasing the complexity of the kinematic design of parallel robots, is achieved: instead of having to synthesise a robot from scratch, the designer can select the most suitable kinematics for a specific application. At this point of the methodology, both the building bricks and the kinematic solutions are independent from any mechanical design; they thus allow a large variety of robots to be synthesised, from machine-tools to microscale robots. Figure 7.12 summarises the hypotheses which have led to the establishment of the exhaustive conceptual solution catalogue.

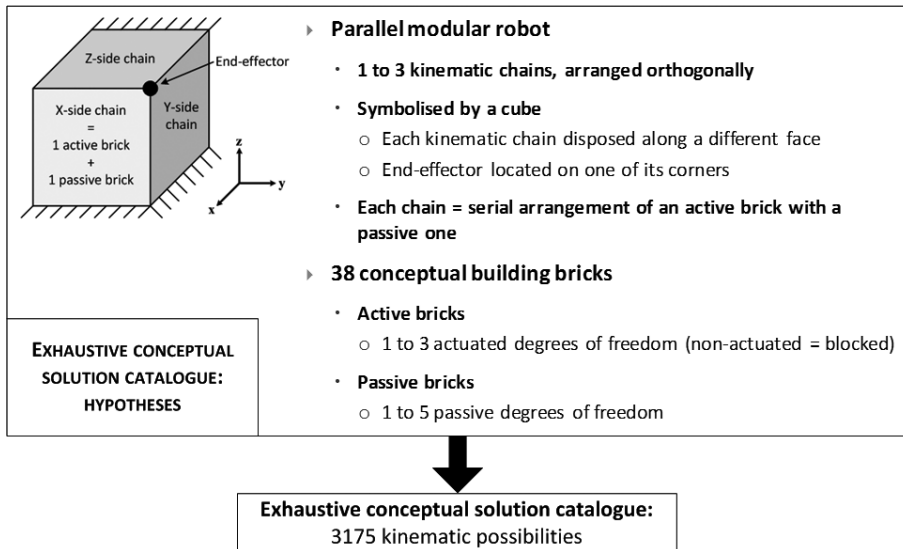


Figure 7.12 Summary of the hypotheses which have led to the establishment of the exhaustive conceptual solution catalogue.

Moreover, a reduction of the solution catalogue can be performed to improve the convenience of the methodology by diminishing the number of possible bricks arrangements. Although no building brick or kinematic solution from the list is *a priori* unsuitable regardless the purpose of the robot, selection criteria linked with the application domain can be formulated. As this work focuses on ultra-high precision, hypotheses linked with the mechanical design and the machining of flexure-based structures are presented in the following section: they will allow to establish a reduced and thus more functional conceptual solution catalogue.

7.3 Reduced solution catalogue for ultra-high precision

This section introduces the selection criteria linked with the design and machining of flexure-based mechanisms that have been used in this work to determine which building bricks can be smartly designed with flexure hinges. Consequently, only the kinematic solutions which are suited to ultra-high precision applications are retained to establish the reduced conceptual solution catalogue.

7.3.1 Hypotheses for ultra-high precision

High-performance flexure-based mechanisms can only be achieved if their design is shrewdly performed and if the machining of the structures is carefully examined at the beginning of the mechanical synthesis. By hypothesis, all flexure-based mechanisms which are designed in this work are *made of metals and intended for monolithical machining by Wire Electro-Discharge Machining (W-EDM)*. These considerations lead to two main criteria: only the building bricks that meet these requirements are retained for ultra-high precision applications.

- ***The building bricks for ultra-high precision are designed as planar mechanisms, or as structures presenting a rotational symmetry***: this criterion arises from the monolithic machining of flexure-based mechanisms by Wire Electro-Discharge Machining (W-EDM). Indeed, the relative configuration of the wire and the part only allows to machine-ruled surfaces. Moreover, the planarity hypothesis represents a crucial advantage for the design of these structures. The differentiation between a blocked and a free degree of freedom of a mechanism lies in its stiffness along the considered motion: the stiffness of the blocked displacement should be at least 100 times higher than that of a free motion (Henein, 2001). In practice, a factor of around 1000 is recommended to avoid low transverse eigenfrequencies. For a prismatic hinge or a leaf spring, the stiffnesses of the natural degrees of freedom are proportional to $I_y = \frac{bh^3}{12}$, whereas for the transverse blocked motions, they are proportional to $I_x = \frac{b^3h}{12}$, where b , h , and the x , y axes are defined in Figure 7.13 (Henein, 2001). If b is the thickness of the planar structure, increasing this parameter by a factor of 10 allows the transverse stiffness to be multiplied by 1000; while the natural stiffness is simultaneously increased by the same factor of 10, the admissible natural stroke is not influenced by this modification. This consideration is particularly significant for the active building bricks, as they are by definition located further from the robot end-effector than the passive bricks: the stiffnesses along their blocked degrees of freedom

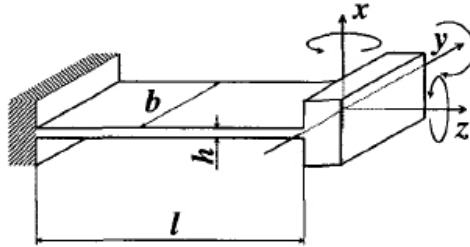


Figure 7.13 Prismatic hinge or leaf spring (Henein, 2001).

must be maximised to limit parasitic displacements resulting from the application of forces and moments on the robot end-effector.

- ***The active degrees of freedom are performed by linear actuators only:*** the lack of standard ultra-high precision rotary sensors and actuators on the market imposes the use of linear devices only. Consequently, rotations are achieved by differential actuation of two motors, or of one motor and the robot frame. By hypothesis, this differential motion takes place solely within the active bricks, i.e. no differential actuation is performed between two kinematic chains of the robot.

These hypotheses stem from design and machining considerations of flexure-based structures made of metals and machined with Wire Electro-Discharge Machining. Consequently, if these prerequisites are not fulfilled, these criteria must be revised.

7.3.2 Building bricks for ultra-high precision

Active bricks

Following the aforementioned hypotheses, an active building brick is suitable for ultra-high precision applications only if an efficient mechanical design fulfilling both the planarity and the linear actuation criteria exists. Figure 7.14 summarises the conceptual active bricks which are retained for ultra-high precision.

ACTIVE BRICKS FOR ULTRA-HIGH PRECISION											
R_{\parallel}	R_{\perp}	T_{\parallel}	T_{\perp}	$T_{\parallel 1}$	$T_{\parallel 2}$	$T_{\parallel \perp}$	$T_{\parallel R_{\perp}}$	$T_{\perp R_{\parallel}}$	$T_{\parallel 1} R_{\parallel 2}$	$T_{\parallel 1} T_{\perp R_{\parallel 2}}$	$T_{\parallel 1} T_{\parallel 2} R_{\perp}$

Figure 7.14 List of the active bricks retained for ultra-high precision.

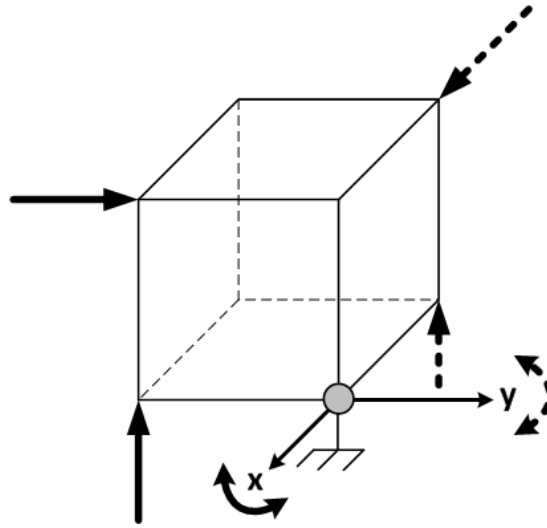


Figure 7.15 Sketch of a rigid body which can rotate around both x and y axes, with a common rotation centre. The arrows stand for the direction of the actuating forces (black to rotate around x and dashed to rotate around y).

Compared to the exhaustive list of building bricks, the following ones have been discarded:

- **Bricks which actuate more than one rotation:** Figure 7.15 illustrates a rigid body which is symbolised by a cube. This body is linked to a fixed frame with a ball joint, which is located on the desired centre of rotation (represented by the grey sphere); two rotations, around both x and y axes, have to be performed. The linear actuation hypothesis imposes that these rotations are created by the application of two forces: the black arrows represent the possible force directions to rotate around x , whereas the dashed arrows stand for the force directions to rotate around y . This graphical representation highlights the fact that the directions of both forces and the rotation centre cannot be included in the same plane. Consequently, the bricks actuating two or three rotations are discarded, as they cannot be designed as planar structures.
- **Bricks which include a cylindrical joint:** as no efficient design fulfilling both the planarity and the linear actuation criteria has been obtained, a kinematic chain including this joint is replaced by two kinematic chains including one brick performing the rotation and one performing the translation. Figure 7.16 illustrates the case of the cylindrical joint brick and one possible substitution.
- **Brick which actuates three translations,** which cannot be straightforwardly achieved by a purely planar structure.

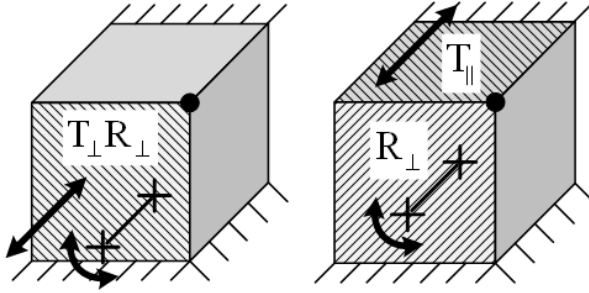


Figure 7.16 Example of the cylindrical joint brick, which can for instance be replaced by the 2-chain configuration on the right.

Passive bricks

The passive bricks which are relevant for ultra-high precision applications are selected on the basis of the hypotheses stated in Section 7.3.1: the bricks are thus retained only if one or more flexure-based designs fulfilling the planarity or the rotational symmetry criterion exist. Comparatively to the exhaustive list, only three types of bricks are discarded: these consist in the brick performing three translations ($t_{\parallel}t_{\perp}t_{\perp}$), the one presenting three rotations ($r_{\parallel}r_{\perp}r_{\perp}$), as well as both bricks performing three translations and one rotation ($t_{\parallel}t_{\perp}t_{\perp}r_{\perp}$ and $t_{\parallel}t_{\perp}t_{\perp}r_{\parallel}$). Nonetheless, these mobilities may be efficiently achieved by flexure-based structures which require other machining methods: Figure 7.17 shows two possible flexure-based designs performing a spherical joint, excerpted from (Henein, 2001). Figure 7.18 summarises the selected conceptual passive bricks for ultra-high precision.

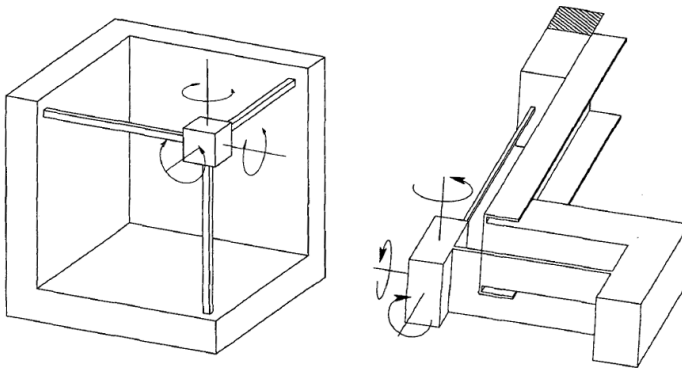


Figure 7.17 Sketch of two possible flexure-based structures performing a spherical joint. (Henein, 2001)

PASSIVE BRICKS FOR ULTRA-HIGH PRECISION										
$r_{ }$	r_{\perp}	$t_{ }$	t_{\perp}	$t_{ 1}t_{ 2}$	$t_{ }t_{\perp}$	$t_{ 1}r_{ 1}$	$t_{\perp}r_{\perp}$	$t_{ }r_{\perp}$	$t_{\perp}r_{ }$	$t_{ 1}r_{ 2}$
$r_{ 1}r_{ 2}$	$r_{ }r_{\perp}$	$t_{ }t_{\perp}r_{\perp}$	$t_{ 1}t_{\perp}r_{ 1}$	$t_{ 1}t_{ 2}r_{ 1}$	$t_{ 1}t_{\perp}r_{ 2}$	$t_{ 1}t_{ 2}r_{\perp}$				
$t_{\perp}r_{ 1}r_{ 2}$	$t_{ 1}r_{ 2}r_{\perp}$	$t_{\perp}r_{ }r_{\perp}$	$t_{ 1}r_{ 1}r_{\perp}$	$t_{ 1}r_{ 1}r_{ 2}$	$t_{ 1}t_{\perp}r_{ 2}r_{\perp}$	$t_{ 1}t_{\perp}r_{ 1}r_{ 2}$				
$t_{ 1}t_{ 2}r_{ 1}r_{\perp}$	$t_{ 1}t_{\perp}r_{ 1}r_{\perp}$	$t_{ 1}t_{ 2}r_{ 1}r_{ 2}$	$t_{\perp}r_{ 1}r_{ 2}r_{\perp}$	$t_{ 1}r_{ 1}r_{ 2}r_{\perp}$						
$t_{ 1}t_{\perp}r_{ 1}r_{ 2}r_{\perp}$	$t_{ 1}t_{ 2}r_{ 1}r_{ 2}r_{\perp}$	$t_{ 1}t_{ 2}t_{\perp}r_{ 1}r_{\perp}$	$t_{ 1}t_{ 2}t_{\perp}r_{ 1}r_{ 2}$							

Figure 7.18 List of the passive bricks retained for ultra-high precision.

7.3.3 Reduced conceptual solution catalogue

Finally, the reduced conceptual solution catalogue is obtained by retaining only the kinematic solutions which are exclusively composed of the bricks listed in Figures 7.14 and 7.18.

This catalogue includes 1429 possibilities, based on 193 active bricks arrangements, which thus a reduction of more than 55% of the amount of solutions. The graphical representation of the solutions can be found in (Richard, 2012).

Moreover, the hypotheses for ultra-high precision have considerably contributed to decrease the complexity of robot synthesis: they have indeed transformed this 3-D design problem into several 2-D ones. Whereas the flexure-based structures resulting from the 3-D synthesis are complex and scarcely flexible, the 2-D solutions are simpler, well-mastered and easier to machine monolithically. Figure 7.19 illustrates this observation, whereas Figure 7.20 summarises the hypotheses which have led to the establishment of the reduced conceptual solution catalogue.

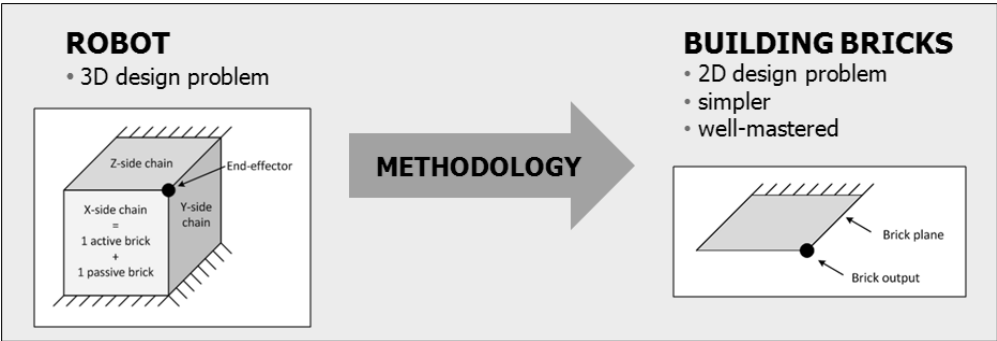


Figure 7.19 Graphical representation of the methodology.

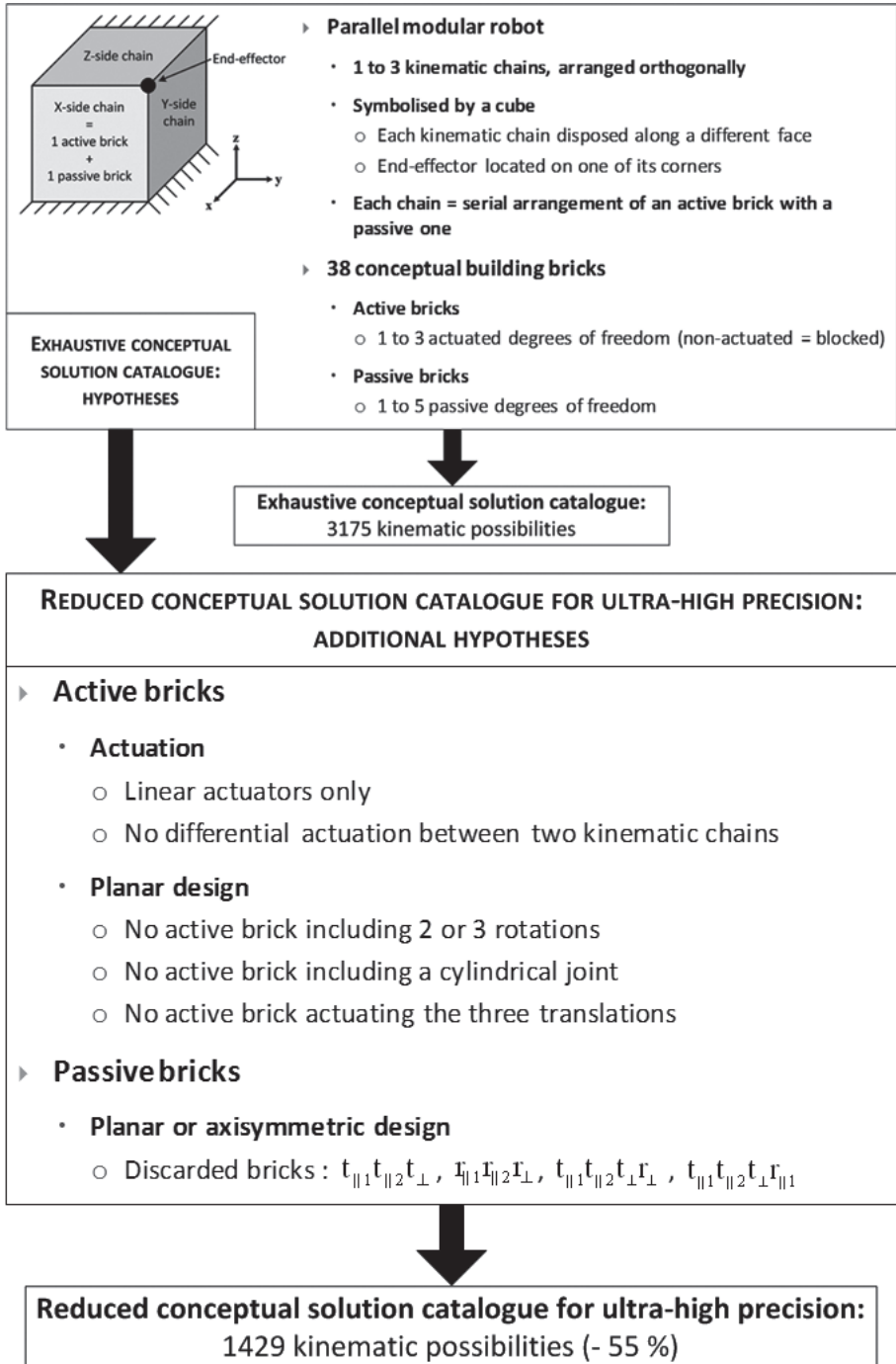


Figure 7.20 Summary of the successive hypotheses which have led to the establishment of the reduced conceptual solution catalogue for ultra-high precision.

Since the list of all conceptual building bricks suited for ultra-high precision has been established, the next step consists in examining their mechanical design. Consequently, the next section studies this aspect and proposes one or more efficient flexure-based structures fulfilling the aforescribed hypotheses for some interesting building bricks.

7.4 Mechanical design of the building bricks

The flexure-based design of the building bricks dedicated to ultra-high precision is detailed in this section. An efficient mechanical solution is proposed for each active brick, which includes a standardised actuation sub-brick, thus adding a new level of modularity to the concept. As for the passive bricks, only some examples are presented in this chapter, comprising original structures, as well as common and innovative uses of well-known mechanisms; the complete study is to be found in (Richard, 2012). Moreover, it is crucial to highlight the aim of this section, which is to group interesting brick designs as a tool for the robot designer rather than to propose a thorough catalogue of off-the shelf mechanical solutions.

7.4.1 Challenges in flexure-based brick design

As the trend to miniaturise industrial products goes hand in hand with the miniaturisation of the production lines, the main challenge of industrial high precision robots design consists in minimising their volume while maximising their workspace. Nonetheless, this is far from being straightforward, as the ratio between the strokes of flexure-based mechanisms and their volume are limited by the admissible stress in the material.

Moreover, numerous high-precision robots and mechanisms performing both rotational and translational motions *suffer from the same limitation: the maximum angle and the maximum translation cannot be achieved at the same time*. This situation is first caused by the strokes of the actuators, which are not sufficient to allow the combined motions. Then, the second cause of this phenomenon is illustrated in Figure 7.21: if the centre of rotation does not coincide with robot output, high translational compensatory motions are necessary to keep its position constant during the rotation. For instance, a distance of 10 mm between the system output and the rotation centre necessitates a compensatory displacement of 1.75 mm when a rotation of 10° is performed. A significant part of the robot translational range is thus necessary to compensate for this motion, which limits the functional translation which can be simultaneously achieved. The Sigma 6 robot (Helmer, 2006) epitomises

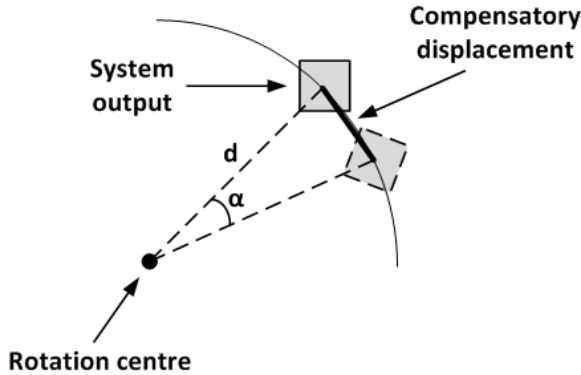


Figure 7.21 Sketch of the parasitic displacement generated by the rotation around a centre which does not coincide with the system output.

this observation: its maximal angle of 4° can indeed be obtained only with a translation inferior to 1 mm.

A smart design making use of a Remote Centre of Motion (RCM) can overcome this problem by virtually locating the rotation centre at the system output, without adding any mechanical parts at this point. All active bricks which perform rotational motions include this astute solution: detailed descriptions of its implementation with flexure hinges are found in Subsections pages 157, 161 and 162.

7.4.2 Mechanical design of the active bricks for ultra-high precision

This section introduces the standardised actuation sub-brick and possible flexure-based designs of each active brick for ultra-high precision.

Actuation sub-brick

As stated in Section 7.3, the actuation of the building bricks for ultra-high precision is performed by linear actuators only. Moreover, the guiding of the actuator moving part has to be performed without friction to fulfill the required submicrometric precision: a flexure-based structure is thus necessary to substitute for classical rolling or plain bearings. Consequently, each active brick comprises the same actuation system, which includes three components: a linear actuator, a guiding system for the actuator moving part and a position sensor. This subset forms the *actuation sub-brick*, which adds a new level of modularity to the methodology. Indeed, each active brick includes an actuation sub-brick for each of its degrees of freedom; the flexure-based mechanisms which transform the linear motions of the actuators into the desired mobility are then attached to them. The following subsections detail some efficient solutions for each component of the actuation sub-brick.

Linear flexure-based guiding mechanism

A simple and efficient flexure-based mechanism performing a translational motion consists in the **4-hinge table**, which is illustrated in Figure 7.22 as a reminder. Either elliptic, prismatic or truncated circular hinges are conceivable; however, the radii of both circular and elliptic joints necessary for achieving a high stroke in comparison with the space requirement of the mechanism are enormous, thus amounting to a nearly prismatic hinge. The chief disadvantage

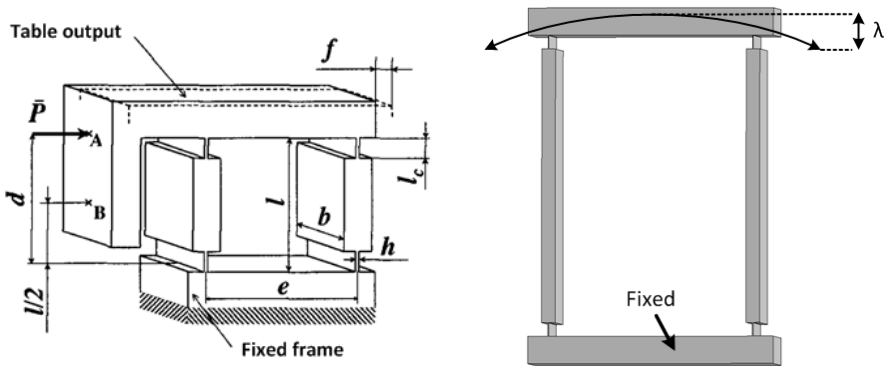


Figure 7.22 Sketch of the 4-prismatic hinge table with geometric parameters (left, (Henein, 2001)) and its quasi parabolic trajectory (right).

of the integration of the 4-hinge table in the actuation sub-brick is its parasitic displacement λ : this issue can be overcome by choosing an actuation principle which accepts a parasitic translation of its moving part.

Moreover, if the robot specifications impose a rectilinear motion, a **13-hinge compound table**, such as presented in Figure 6.7 can be used. Furthermore, the integration of this solution in the actuation sub-brick is only necessary when the robot includes a sole translation, or when the parasitic motions of the robot translations cannot be actively compensated for by the control algorithm.

Linear actuator

As the robots designed with this modular methodology are intended for industrial use, **electromagnetic actuators** are preferred over piezoelectric or ultrasonic actuators for their high repeatability. Two main types of actuators can thus be integrated in the actuation sub-brick, namely **voice coil** and **ironless EC (electronic commutation)** actuators. Their selection depends greatly on the availability of standard products on the market which fulfill the robot force and stroke requirements. As these are specific to each application, no preferred solution emerges at this point of the methodology.

Linear position sensor

The last component of the actuation sub-brick is the linear position sensor; at the present time, *optic incremental linear encoders* and *Linear Variable Differential Transformers (LVDT)* are the only standard products available on the market which allow the required submicrometric precision to be achieved. Furthermore, as the measurement of the actuation sub-brick guiding system determines the resolution of the whole robot and thus limits its repeatability and accuracy, the resolution of the sensor must be carefully chosen in regards to the specifications of the industrial application.

Active bricks mechanical design

The mechanical design of the active bricks including the aforementioned actuation sub-brick is now detailed. As stated in Section 7.3, the bricks must be designed as planar flexure-based mechanisms. Moreover, the physical plane including the flexure-based structure is not necessarily coincident with the plane of the brick on the conceptual cube (Fig. 7.23). Consequently, bricks which share the same mobility can be identically designed, regardless of the orientation of the motions relative to the cube face plane. In the following sections, the bricks are thus grouped according to their mobility: one efficient flexure-based design is proposed for each of them. Note that in this section, only sketches of the design principles are presented; the mechanical solutions of the T_{\parallel} and the $T_{\parallel}R_{\perp}$ active bricks will be thoroughly examined in Section 7.5.

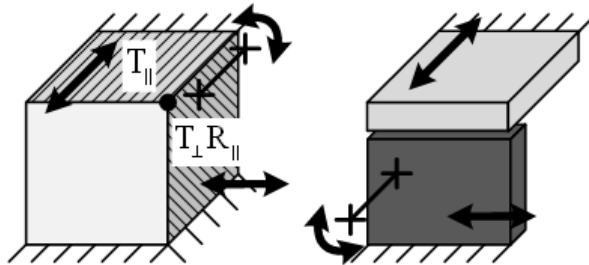


Figure 7.23 The conceptual kinematic arrangement (left) is built with two planar flexure-based mechanisms (right): for the brick performing the translation, the cube face plane is coincident with the plane of the mechanism, whereas for the second brick, the plane of the flexure-based structure is orthogonal to the face of the concept cube.

R_{\parallel} and R_{\perp} bricks

The mechanical flexure-based design of these bricks, which perform a single rotation, includes a Remote Centre of Motion (RCM) to ensure that the position of the robot end-effector is kept constant during the rotation without perform-

ing compensatory translations (Sect. 7.4.1). Figure 7.24 illustrates the design principle of these bricks, where two functional subsets can be highlighted:

- **The position of the rotation centre is defined by the virtual intersection of both hinges which link the brick output to the fixed frame.** The optimal angle between these two hinges is 90° , which maximises the transverse stiffness of the mechanism.
- **The linear motion of the actuation sub-brick performs the rotation:** through the vertical hinge, the force produced by the actuator is transformed into a moment, which causes the output to rotate. Moreover, the classical lever law $M = F \cdot d$ can be applied, where M is the moment, F is the actuation force and d is the orthogonal distance between the force and the rotation centre (Fig. 7.24).

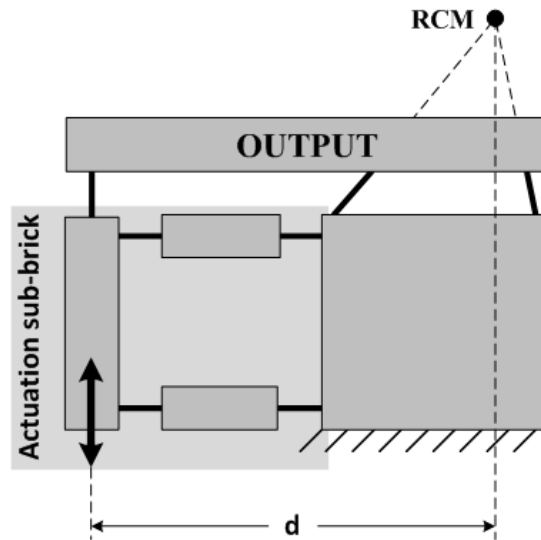


Figure 7.24 Sketch of the R_{\parallel} and R_{\perp} bricks design principle, including the actuation sub-brick and a Remote Centre of Motion. The proposed solution actuates a rotation which is orthogonal to the mechanism plane, and must be reoriented relative to the concept cube to perform a R_{\parallel} brick.

This flexure-based mechanism notably allows to freely choose the position of the rotation axis: the latter must be located on the end-effector of the robot, which is in most cases not coincident with the brick output, as in Figure 7.24. Its position must thus be carefully chosen regarding the robot kinematics and specifications.

Moreover, the choice of the distance between the actuator and the rotation centre (d in Fig. 7.24) influences the performances of the structure:

- The angular resolution is improved as this distance is increased.

- The actuation force which is necessary to rotate the output of a given angle decreases as the distance increases.
- The actuator linear stroke which is needed to perform this same angle conversely increases as the distance increases.

Consequently, the distance between the actuator and the Remote Centre of Motion should be optimised with respect to the robot specifications, as well as to the actuator performances.

Lastly, the actuation sub-brick consisting in a simple 4-hinge table is highly efficient within these bricks, as its role is only to apply a force to the flexure-based structure; the parasitic translation described in Subsection *Linear flexure-based guiding mechanism* (p. 156) does not influence the behaviour of the brick output.

T_{\parallel} and T_{\perp} bricks

As for the bricks which only perform a translation, their mechanical design simply consists in the actuation sub-brick described in Section 7.4.2 (Fig. 7.25).

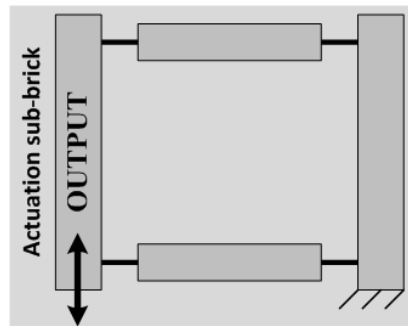


Figure 7.25 Mechanical design of the T_{\parallel} and T_{\perp} bricks; the proposed solution actuates a translation which is parallel to the mechanism plane, and must be reoriented relative to the concept cube to perform a T_{\perp} brick.

$T_{\parallel 1} T_{\parallel 2}$ and $T_{\parallel} T_{\perp}$ bricks

These active bricks, which perform two translations, admit two efficient designs, illustrated in Figures 7.26 and 7.27. The first solution, excerpted from (Hodac, 1999), includes two actuators which are oriented along the same direction. An inclined lever transforms these collinear motions into two orthogonal translations (Fig. 7.26).

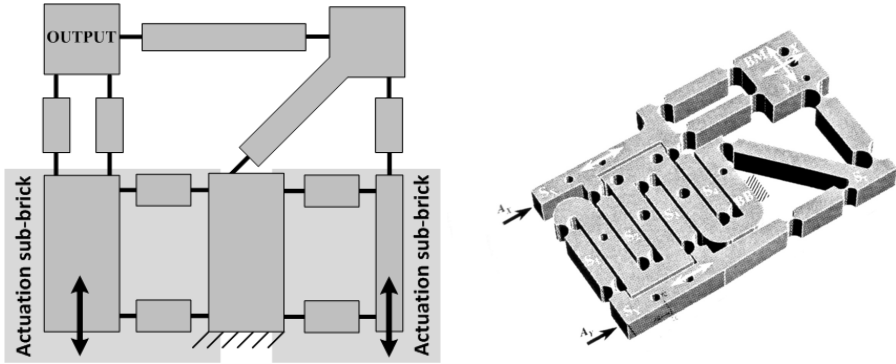


Figure 7.26 Sketch of the $T_{\parallel 1} T_{\parallel 2}$ and $T_{\parallel} T_{\perp}$ bricks first design principle, including two actuators oriented in the same direction (left) and illustration of the flexure-based mechanism developed in (Hodac, 1999) (right). The proposed solution actuates two translations which are parallel to the mechanism plane, and must be reoriented relative to the concept cube to perform a $T_{\parallel} T_{\perp}$ brick.

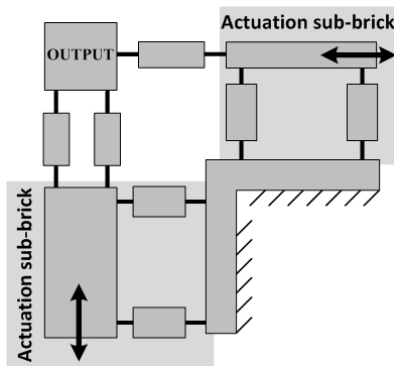


Figure 7.27 Sketch of the $T_{\parallel 1} T_{\parallel 2}$ and $T_{\parallel} T_{\perp}$ bricks second design principle.

This configuration presents the significant advantages of allowing a compact integration, as well as simplified electrical connexions. However, the output working range is limited by the admissible stroke of the sole hinge achieving the lever function.

Consequently, if the robot specifications impose high translational strokes, the second solution, which includes two actuators oriented along orthogonal directions, is an advantageous alternative (Fig. 7.27). Furthermore, both designs allow for an active compensation of the parasitic translations of the 4-hinge tables. Note that the solution proposed by (Koster, 2000), which also makes use of two collinear actuators and a lever system to transform the direction of the motion (Fig. 7.28), could also be adapted to alternatively perform this active brick.

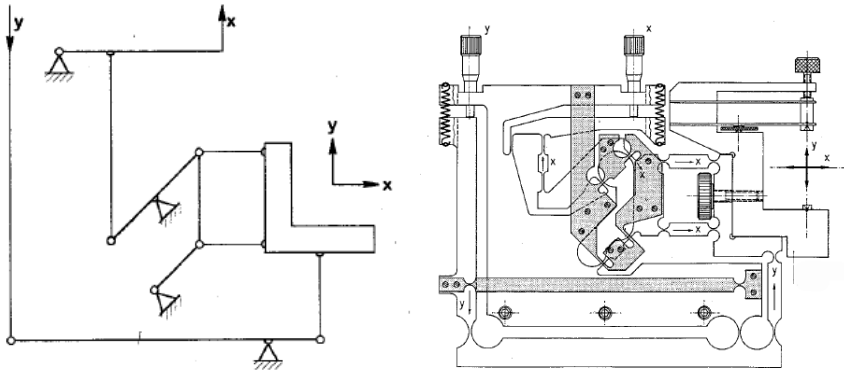


Figure 7.28 Kinematics (left) and design (right) of a Tx, Ty table with colinear actuators (Koster, 2000).

$T_{\parallel}R_{\perp}$, $T_{\perp}R_{\parallel}$ and $T_{\parallel 1}R_{\parallel 2}$ bricks

Performing a translation and a rotation which are oriented along two different directions, these three active bricks include a Remote Centre of Motion and a differential actuation. Figure 7.29 illustrates their design principle, as well as a mock-up with assembled leaf springs proving the soundness of this solution. In this mechanism, the translation is achieved by the synchronous motion of both actuators. As for the rotation, the position of the actuator linked with the hinges defining the rotation centre is kept constant, whereas the movement of

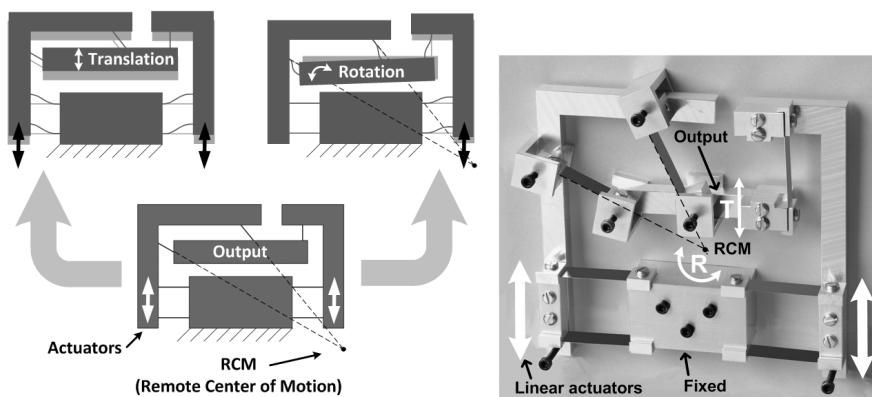


Figure 7.29 Sketch of the $T_{\parallel}R_{\perp}$, $T_{\perp}R_{\parallel}$ and $T_{\parallel 1}R_{\parallel 2}$ bricks design principle, including a RCM (left), and mock-up of the flexure-based structure (right).

the second linear actuator performs the rotation. As described in Subsection R_{\parallel} and T_{\perp} bricks (p. 157), the distance between this last actuator and the rotation centre must be carefully chosen.

$T_{\parallel 1} T_{\parallel 2} R_{\perp}$ and $T_{\parallel 1} T_{\perp} R_{\parallel 2}$ bricks

Finally, these two bricks performing a planar joint mobility include the design principles of all aforementioned active bricks: to simplify the understanding of the mechanism, Figure 7.30, top, first shows a solution without the Remote Centre of Motion. The first translation (along the vertical axis on Figure 7.30, top) is achieved by the synchronous motion of the two actuators on the right. Then, the movement of the far left actuator performs the second translation. Last, solely displacing the actuator on the far right allows for the rotation along an axis which is orthogonal to the structure. Including a Remote Centre of Motion is now straightforward, as it only consists in inclining two arms of the structure (Fig. 7.30, bottom).

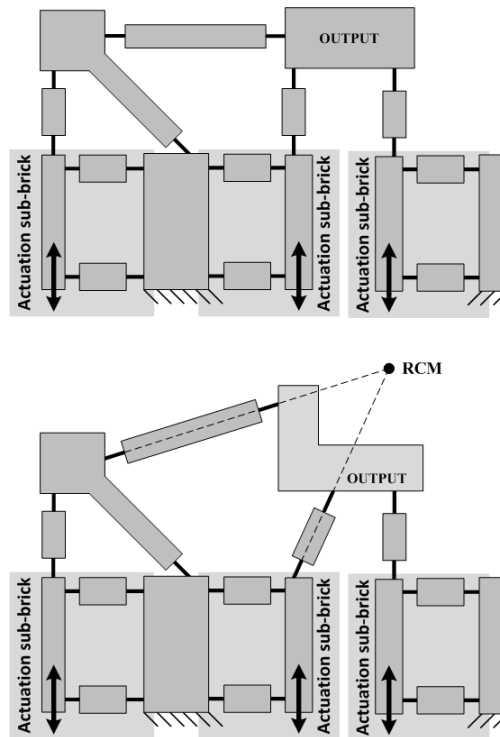


Figure 7.30 Sketch of the $T_{\parallel 1} T_{\parallel 2} R_{\perp}$ and $T_{\parallel 1} T_{\perp} R_{\parallel 2}$ bricks design principle: without RCM (top) and with RCM (bottom). The proposed solution actuates two translations which are parallel to the mechanism plane, and a rotation which is orthogonal to this plane. Consequently, it must be reoriented relative to the concept cube to perform a $T_{\parallel 1} T_{\perp} R_{\parallel 2}$ brick.

7.4.3 Mechanical design of the passive bricks for ultra-high precision

This section details the design principles of some of the passive bricks for ultra-high precision (see (Richard, 2012) for the complete study). As stated in Section 7.3, these must be planar flexure-based structures, or flexure-based mechanisms presenting a rotational symmetry to fulfill the synthesis and machining criteria. Consequently, one or several possible designs are presented, comprising original structures, as well as common and innovative uses of well-known mechanisms. Moreover, it is crucial to highlight that the aim of this section is to group interesting brick designs as a tool for the robot designer rather than to propose a thorough catalogue of off-the shelf mechanical solutions. Note that only sketches of the solution principles are presented; the $t_{||}t_{\perp}r_{||}r_{\perp}$ passive brick design will be comprehensively studied in Section 7.5.

$r_{||}$ and r_{\perp} bricks

These passive bricks, which perform a revolute joint, admit five flexure-based designs, which are the following:

- **The crossed-blades pivot** is illustrated as a reminder in Figure 7.31. It can include either unseparated or separated blades: whereas the unseparated cylindrical joint is easier to machine, the separated solution allows to achieve a higher rotation angle with a lower joint stiffness. Moreover, this option can also be performed with necked-down hinges rather than with leaf springs (Fig. 7.31, right): this structure, although not straightforward to manufacture, is more adapted to Wire Electro-Discharge Machining. More details about the stroke, stiffness and parasitic shift of the rotation centre of these cylindrical joints can be found in Chapter 5.

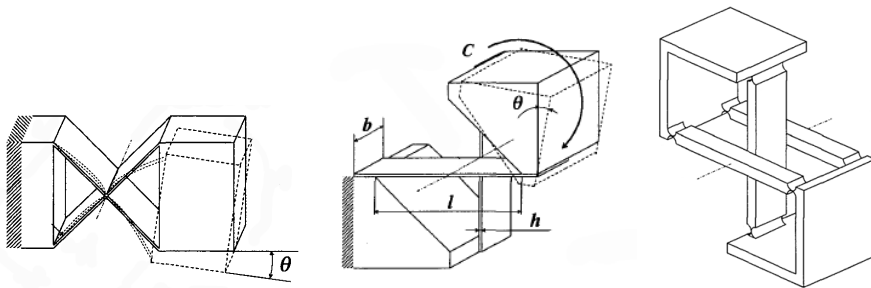


Figure 7.31 Sketches of the unseparated cross spring pivot (left) and of the separated cross pivot, with leaf springs (middle) and with flexure hinges (right) (Henein, 2001).

- **Planar high-stroke revolute joints**, which notably include the Butterfly pivot (Henein et al., 2003) and the redundant high-stroke pivot. (see Fig. 6.10). The advantages of these designs include the high achievable strokes ($\pm 15^\circ$), as well as the significant decrease in the parasitic shift of the rotation centre compared to other flexure-based revolute joints.
- **Torsion pivots**, which can admit several designs, as described in (Helmer, 2006). Nonetheless, significant drawbacks of the torsion pivots consist in the low angular strokes and in the parasitic shift of the rotation centre, which is caused by the shortening of the leaf springs during their combined torsion and bending.
- Furthermore, **a design combining the concepts of the torsion pivots and of the 13-hinge compound table (Fig. 6.7) has been developed** in the frame of this research: its principle consists in serially arranging two torsion pivots linked with a slaving mechanism which suppresses the internal degree of freedom. The crucial advantages of this design are first the increase of the stroke, which is equal to twice the rotation angle of a single torsion pivot. Then, the stress concentration in the leaf springs has been optimised by modifying the shape of the spring itself. Last, the compound design allows the parasitic shift of the rotation centre to be suppressed. Figure 7.32 shows the cylindrical joint principle, the optimal shape of the leaf springs, as well as a scaled W-EDM machined prototype of a single pivot stage. More details on this joint design can be found in (Richard and Clavel, 2010).

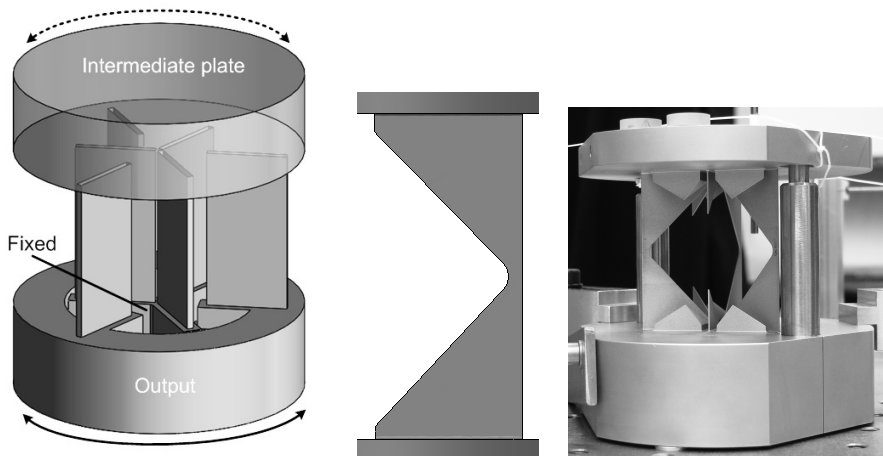


Figure 7.32 Sketch of the compound torsion pivot principle without its slaving mechanism (left), optimised leaf spring shape (middle) and scaled W-EDM machined prototype of a single pivot stage (right).

- Lastly, the *same flexure-based design as the active brick* performing a cylindrical joint can be used (see Fig. 7.24).

$t_{\perp}r_{\parallel 1}r_{\parallel 2}$ and $t_{\parallel 1}r_{\parallel 2}r_{\perp}$ bricks

A well-known flexure-based mechanism can efficiently perform the $t_{\perp}r_{\parallel 1}r_{\parallel 2}$ and $t_{\parallel 1}r_{\parallel 2}r_{\perp}$ bricks: it simply consists in a leaf spring, which can be designed with or without reinforcements, depending on the stroke and stiffness specifications (Fig. 7.33).

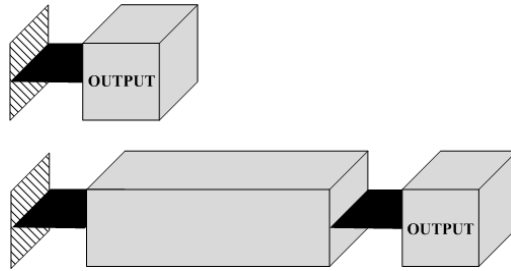


Figure 7.33 Sketch of the $t_{\perp}r_{\parallel 1}r_{\parallel 2}$ and $t_{\parallel 1}r_{\parallel 2}r_{\perp}$ bricks design principle, which simply consists of a leaf spring.

$t_{\parallel 1}t_{\perp}r_{\parallel 2}r_{\perp}$, $t_{\parallel 1}t_{\perp}r_{\parallel 1}r_{\parallel 2}$ and $t_{\parallel 1}t_{\parallel 2}r_{\parallel 1}r_{\perp}$ bricks

The design of the $t_{\parallel 1}t_{\perp}r_{\parallel 2}r_{\perp}$, $t_{\parallel 1}t_{\perp}r_{\parallel 1}r_{\parallel 2}$ and $t_{\parallel 1}t_{\parallel 2}r_{\parallel 1}r_{\perp}$ bricks admits two solutions: the first one is the well known space parallelogram mechanism (Fig. 7.34), which is featured in all flexure-based versions of the Delta kinematics. A second

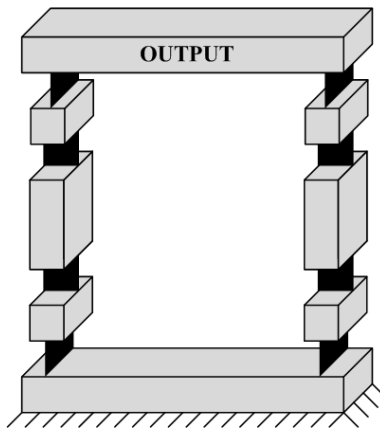


Figure 7.34 Sketch of the $t_{\parallel 1}t_{\perp}r_{\parallel 2}r_{\perp}$, $t_{\parallel 1}t_{\perp}r_{\parallel 1}r_{\parallel 2}$ and $t_{\parallel 1}t_{\parallel 2}r_{\parallel 1}r_{\perp}$ bricks design called space parallelogram, which is featured in the flexure-based versions of the Delta kinematics (see (Henein, 2001)).

design, which consists of the serial arrangement of a 4-hinge table and a leaf spring, is illustrated in Figure 7.35: although the machining of the final structure (Fig. 7.35, right) is not straightforward, this solution allows the traction and compression stresses in the hinges to be minimised by applying the translation force at mid-length of the arms (Fig. 7.22).

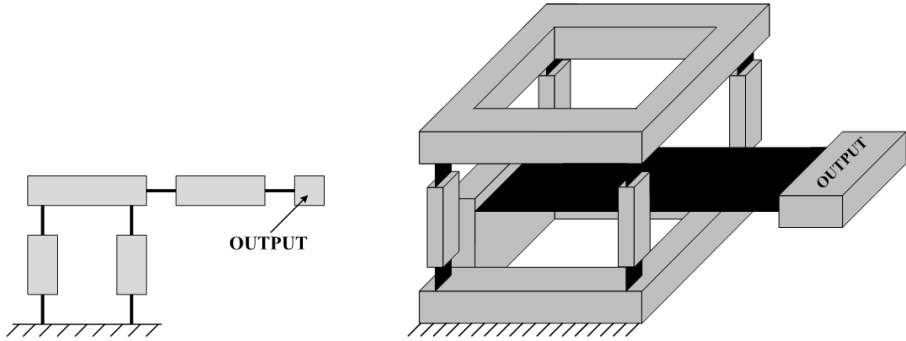


Figure 7.35 Sketches of the second $t_{||1}t_{\perp}r_{||2}r_{\perp}$, $t_{||1}t_{\perp}r_{||1}r_{||2}$ and $t_{||1}t_{||2}r_{||1}r_{\perp}$ bricks design: principle (left) and final structure (right).

$t_{||1}t_{\perp}r_{||1}r_{||2}r_{\perp}$ and $t_{||1}t_{||2}r_{||1}r_{||2}r_{\perp}$ bricks

This mobility, which only blocks one translation, can be efficiently achieved by an L-shaped leaf spring, or corner-blade, which is illustrated in Figure 7.36. Furthermore, the Sigma 6 arms design which is illustrated in Figure 7.37, can

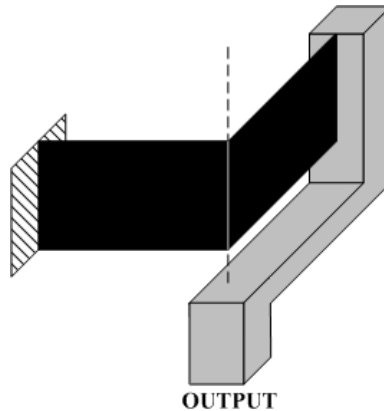


Figure 7.36 Use of a corner-blade as passive $t_{||1}t_{\perp}r_{||1}r_{||2}r_{\perp}$ and $t_{||1}t_{||2}r_{||1}r_{||2}r_{\perp}$ bricks. The output of the brick must be aligned with the blade corner to correctly block the translation along the vertical axis. Note that the illustrated solution facilitates the understanding of the design principle and can easily be adapted to strictly fulfill the planarity hypothesis.

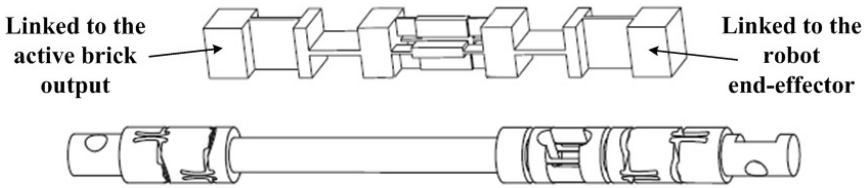


Figure 7.37 Use of the Sigma 6 robot arms (Helmer, 2006) as passive $t_{||1}t_{\perp}r_{||1}r_{||2}r_{\perp}$ and $t_{||1}t_{||2}r_{||1}r_{||2}r_{\perp}$ bricks.

also be used to perform this passive brick. The squirrel cage torsion pivot, although optional, allows to increase the angle of the arm torsion. This design is equivalent to a classical rod and only precludes the translation along the arm axis.

7.4.4 Discussion

The active and passive bricks designs which have been introduced in this section have been developed to fulfill the ultra-high precision criteria stated in Section 7.3: *the active bricks must be planar and linearly actuated mechanisms, whereas the passive bricks are planar structures or mechanisms presenting a rotational symmetry*. These hypotheses have been specified on the basis of the chosen manufacturing method, namely Wire Electro-Discharge Machining, and of the standard actuation solutions available on the market. Nonetheless, efficient flexure-based structures which do not satisfy these criteria can be achieved, for example making use of other machining means, such as the spherical joints presented in Figure 7.17.

Furthermore, the aim of this section has explicitly been to provide and group interesting brick designs as a tool for the engineer rather than to propose a thorough catalogue of off-the-shelf mechanical solutions. Two simple considerations highlight the crucial role of the designer who will use this methodology and mechanical solution catalogue:

- First, *two functions can be performed by the passive bricks degrees of freedom: they can either fulfill a functional need, which is to allow an end-effector motion, or to avoid overconstraints. The first role requires that the passive displacement presents the same high stroke as the end-effector degree of freedom, whereas the second demands a much lower motion range*. The robot designer has thus to carefully determine the role of each degree of freedom of the considered passive brick in order to set its stroke specifications: this may lead the engineer to design his/her own brick to fulfill the specific requirements of the application.

- Then, *the conceptual frame of the methodology necessitates the serial arrangement of the active and passive bricks of a kinematic chain. However, this does not imply that both bricks should be separately designed and assembled afterwards: a more global approach can be highly advantageous.* Indeed, at this stage of the methodology, one or several robot kinematics have already been selected in the conceptual solution catalogue: the active and passive bricks composing each kinematic chain are thus known. Consequently, the choice of the mechanical solutions to perform these bricks can and must take into account their combination within the kinematic chain and the arrangement of the chains within the robot. This global approach may, for example, lead to the design of a single monolithic mechanism performing the function of both active and passive bricks.

Consequently, the role of the robot designer is crucial when the modular methodology presented in this work is practically applied to an industrial robot synthesis. The next section, which details the case study of a 5-degree of freedom robot, will illustrate the complementarity of the methodology potentialities and the added value of the creative designer's work to achieve a high-performance ultra-high precision robot.

7.5 Case study: 5-DOF ultra-high precision robot

The application of the modular methodology is now illustrated with the study of a 5-degree of freedom ultra-high precision industrial robot. This section consequently presents the kinematic synthesis and the mechanical design which have led to the manufacturing of the Legolas 5 prototype. First, a kinematic solution is selected in the reduced solution catalogue for ultra-high precision, on the basis of the robot specifications. Then, the mechanical design of the necessary active and passive bricks is thoroughly examined, as well as some crucial aspects of the prototype finalisation, such as assembly and gravity compensation. Finally, a summary of the Legolas 5 characteristics is presented, and a discussion concludes this section.

7.5.1 Robot specifications

The choice of the 5-degree of freedom mobility to illustrate the use of the methodology has been motivated by a typical task an ultra-high precision industrial robot has to perform, namely micromanipulation. This often requires three translations (T_x , T_y and T_z) and two tip-tilt rotations (R_x and R_y). This kinematics is complex to design and manufacture, which explains the scarcity

of prototypes, especially in the industrial context. The specifications for this 5-DOF robot are the following:

- **Strokes:** ± 5 mm and $\pm 10^\circ$, maximum translation and angle simultaneously achievable
- **Resolution and repeatability:** 50 nm for the translations and $2 \mu\text{rad}$ [$0.4''$] for the rotations
- **Total robot volume:** minimised
- **Easily modifiable** into a 4-DOF or a 6-DOF robot
- **Minimal number of different bricks**

7.5.2 Kinematics synthesis

The first step of the methodology consists in the synthesis of the robot kinematics, which is selected in the reduced solution catalogue for ultra-high precision on the basis of the previously stated robot requirements.

Active bricks arrangements

The reduced solution catalogue for ultra-high precision lists 27 possible active bricks arrangements for the considered Tx, Ty, Tz, Rx, Ry mobility, which can be grouped in four categories (see appendix C of (Richard, 2012) for the solution catalogue including graphical representations of each kinematic) :

- *2 kinematic chains*, including a planar joint brick and a brick actuating a translation and a rotation along different axes
- *3 kinematic chains*, including a planar joint brick, a rotation brick and a brick actuating a translation
- *3 kinematic chains*, including a brick actuating two translations, a rotation brick and a brick actuating a translation and a rotation along different axes
- *3 kinematic chains*, including two bricks actuating a translation and a rotation along different axes, and a translation brick

The conceptual active bricks are now replaced by sketches of their mechanical design, whose planes are oriented to perform the required mobility. As stated in Section 7.4, although the bricks are designed as planar mechanisms, the physical plane including the flexure-based structure is not necessarily coincident with the plane of the brick on the conceptual cube (Fig. 7.23). Bricks which share the same mobility are thus identically designed, regardless the orientation of the motions relative to the cube face plane. Figure 7.38 illustrates the replacement of the conceptual bricks by their mechanical design principles for the first kinematic category: the resulting arrangements are notably reorientations of the same mechanical solution. This observation is the direct consequence of the hypothesis stated in Section 7.4: if bricks which share the same mobility are

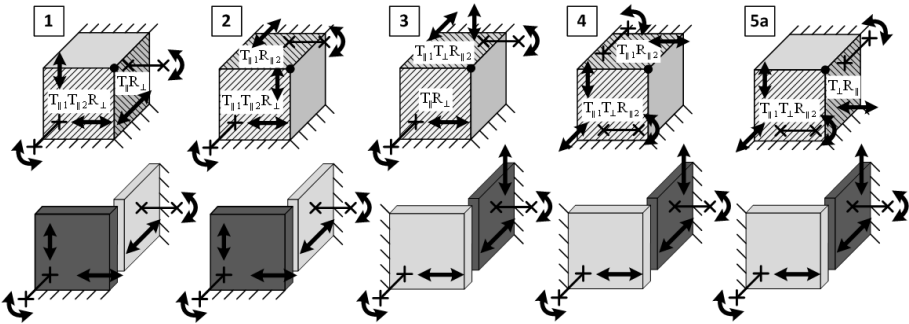


Figure 7.38 Conceptual active bricks solutions from the first category (top) and corresponding arrangements of their bricks mechanical designs (dark grey stands for the planar joint brick, whereas light gray stands for the 2-DOF brick).

designed differently depending on the orientation of their degrees of freedom relative to the conceptual cube face, this observation becomes irrelevant.

Once the conceptual active bricks have been replaced by their flexure-based planar designs, as in Figure 7.38, the possibilities from each kinematic category eventually amount to the same mechanical solution. Consequently, the corresponding passive bricks are also equivalent: only one active brick arrangement for each family can thus be retained for the next step of the methodology. This solution can be arbitrarily selected: in this example, the chosen active bricks possibility only includes bricks whose conceptual and physical planes are coincident. For instance, the selected active bricks arrangement of the first family is the first solution (far left in Fig. 7.38). Figure 7.39 illustrates the four remaining active bricks solutions for the considered 5-DOF robot.

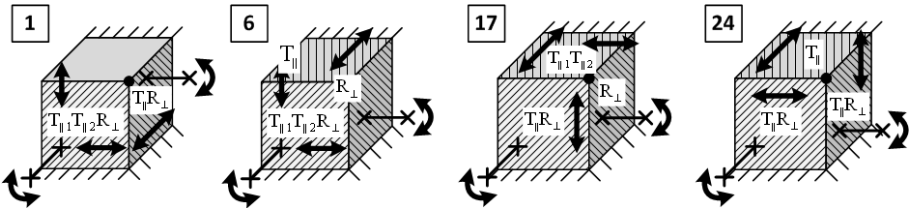


Figure 7.39 Sketches of the four remaining active brick arrangements for the Tx, Ty, Tz, Rx, Ry mobility.

Arrangements of passive bricks

The next step of the methodology consists in examining the possible passive bricks for each of the four remaining active bricks arrangements: these are excerpted from the reduced solution catalogue for ultra-high precision and illustrated in Figure 7.40. The aim of this step is to first discard the solutions which

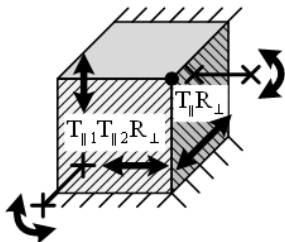
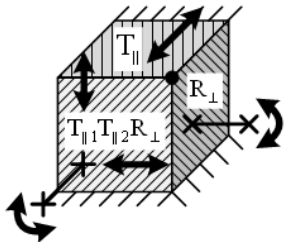
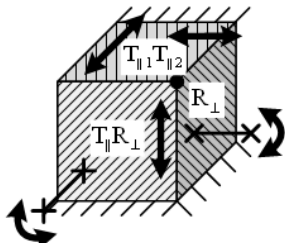
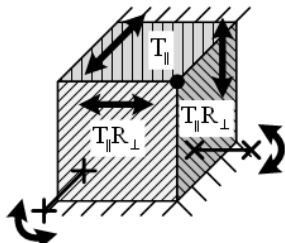
<div><div>1</div></div>	<div><div>6</div></div>																					
<table><tr><td>X-chain</td><td>Y-chain</td><td>Z-chain</td></tr><tr><td>$t_{\perp} r_{\parallel 1} r_{\parallel 2}$</td><td>$t_{\parallel 1} t_{\perp} r_{\parallel 2}$</td><td></td></tr><tr><td>$t_{\perp} r_{\parallel}$</td><td>$t_{\parallel 1} t_{\perp} r_{\parallel 1} r_{\parallel 2}$</td><td></td></tr></table>	X-chain	Y-chain	Z-chain	$t_{\perp} r_{\parallel 1} r_{\parallel 2}$	$t_{\parallel 1} t_{\perp} r_{\parallel 2}$		$t_{\perp} r_{\parallel}$	$t_{\parallel 1} t_{\perp} r_{\parallel 1} r_{\parallel 2}$		<table><tr><td>X-chain</td><td>Y-chain</td><td>Z-chain</td></tr><tr><td>$t_{\perp} r_{\parallel 1} r_{\parallel 2}$</td><td>$t_{\parallel 1} t_{\perp} t_{\perp} r_{\parallel 1} r_{\parallel 2}$</td><td>$t_{\parallel 1} t_{\perp} r_{\parallel 1} r_{\parallel 2}$</td></tr><tr><td>$t_{\perp} r_{\parallel}$</td><td>$t_{\parallel 1} t_{\perp} t_{\perp} r_{\parallel 1} r_{\parallel 2}$</td><td>$t_{\parallel 1} t_{\perp} r_{\parallel 1} r_{\parallel 2} r_{\perp}$</td></tr></table>	X-chain	Y-chain	Z-chain	$t_{\perp} r_{\parallel 1} r_{\parallel 2}$	$t_{\parallel 1} t_{\perp} t_{\perp} r_{\parallel 1} r_{\parallel 2}$	$t_{\parallel 1} t_{\perp} r_{\parallel 1} r_{\parallel 2}$	$t_{\perp} r_{\parallel}$	$t_{\parallel 1} t_{\perp} t_{\perp} r_{\parallel 1} r_{\parallel 2}$	$t_{\parallel 1} t_{\perp} r_{\parallel 1} r_{\parallel 2} r_{\perp}$			
X-chain	Y-chain	Z-chain																				
$t_{\perp} r_{\parallel 1} r_{\parallel 2}$	$t_{\parallel 1} t_{\perp} r_{\parallel 2}$																					
$t_{\perp} r_{\parallel}$	$t_{\parallel 1} t_{\perp} r_{\parallel 1} r_{\parallel 2}$																					
X-chain	Y-chain	Z-chain																				
$t_{\perp} r_{\parallel 1} r_{\parallel 2}$	$t_{\parallel 1} t_{\perp} t_{\perp} r_{\parallel 1} r_{\parallel 2}$	$t_{\parallel 1} t_{\perp} r_{\parallel 1} r_{\parallel 2}$																				
$t_{\perp} r_{\parallel}$	$t_{\parallel 1} t_{\perp} t_{\perp} r_{\parallel 1} r_{\parallel 2}$	$t_{\parallel 1} t_{\perp} r_{\parallel 1} r_{\parallel 2} r_{\perp}$																				
<div><div>17</div></div>	<div><div>24</div></div>																					
<table><tr><td>X-chain</td><td>Y-chain</td><td>Z-chain</td></tr><tr><td>$t_{\parallel 1} t_{\perp} r_{\parallel 1}$</td><td>$t_{\parallel 1} t_{\perp} t_{\perp} r_{\parallel 1} r_{\parallel 2}$</td><td>$t_{\perp} r_{\parallel 1} r_{\parallel 2} r_{\perp}$</td></tr><tr><td>$t_{\parallel 1} t_{\perp} r_{\parallel 1} r_{\parallel 2}$</td><td>$t_{\parallel 1} t_{\perp} t_{\perp} r_{\parallel 1} r_{\parallel 2}$</td><td>$t_{\perp} r_{\parallel 1} r_{\parallel 2}$</td></tr></table>	X-chain	Y-chain	Z-chain	$t_{\parallel 1} t_{\perp} r_{\parallel 1}$	$t_{\parallel 1} t_{\perp} t_{\perp} r_{\parallel 1} r_{\parallel 2}$	$t_{\perp} r_{\parallel 1} r_{\parallel 2} r_{\perp}$	$t_{\parallel 1} t_{\perp} r_{\parallel 1} r_{\parallel 2}$	$t_{\parallel 1} t_{\perp} t_{\perp} r_{\parallel 1} r_{\parallel 2}$	$t_{\perp} r_{\parallel 1} r_{\parallel 2}$	<table><tr><td>X-chain</td><td>Y-chain</td><td>Z-chain</td></tr><tr><td>$t_{\parallel 1} t_{\perp} r_{\parallel 1} r_{\parallel 2}$</td><td>$t_{\parallel 1} t_{\perp} r_{\parallel 1} r_{\parallel 2}$</td><td>$t_{\parallel 1} t_{\perp} r_{\parallel 1} r_{\parallel 2}$</td></tr><tr><td>$t_{\parallel 1} t_{\perp} r_{\parallel 1} r_{\parallel 2}$</td><td>$t_{\parallel 1} t_{\perp} r_{\parallel 1}$</td><td>$t_{\parallel 1} t_{\perp} r_{\parallel 1} r_{\parallel 2} r_{\perp}$</td></tr><tr><td>$t_{\parallel 1} t_{\perp} r_{\parallel 2}$</td><td>$t_{\parallel 1} t_{\perp} r_{\parallel 1} r_{\parallel 2}$</td><td>$t_{\parallel 1} t_{\perp} r_{\parallel 1} r_{\parallel 2} r_{\perp}$</td></tr></table>	X-chain	Y-chain	Z-chain	$t_{\parallel 1} t_{\perp} r_{\parallel 1} r_{\parallel 2}$	$t_{\parallel 1} t_{\perp} r_{\parallel 1} r_{\parallel 2}$	$t_{\parallel 1} t_{\perp} r_{\parallel 1} r_{\parallel 2}$	$t_{\parallel 1} t_{\perp} r_{\parallel 1} r_{\parallel 2}$	$t_{\parallel 1} t_{\perp} r_{\parallel 1}$	$t_{\parallel 1} t_{\perp} r_{\parallel 1} r_{\parallel 2} r_{\perp}$	$t_{\parallel 1} t_{\perp} r_{\parallel 2}$	$t_{\parallel 1} t_{\perp} r_{\parallel 1} r_{\parallel 2}$	$t_{\parallel 1} t_{\perp} r_{\parallel 1} r_{\parallel 2} r_{\perp}$
X-chain	Y-chain	Z-chain																				
$t_{\parallel 1} t_{\perp} r_{\parallel 1}$	$t_{\parallel 1} t_{\perp} t_{\perp} r_{\parallel 1} r_{\parallel 2}$	$t_{\perp} r_{\parallel 1} r_{\parallel 2} r_{\perp}$																				
$t_{\parallel 1} t_{\perp} r_{\parallel 1} r_{\parallel 2}$	$t_{\parallel 1} t_{\perp} t_{\perp} r_{\parallel 1} r_{\parallel 2}$	$t_{\perp} r_{\parallel 1} r_{\parallel 2}$																				
X-chain	Y-chain	Z-chain																				
$t_{\parallel 1} t_{\perp} r_{\parallel 1} r_{\parallel 2}$	$t_{\parallel 1} t_{\perp} r_{\parallel 1} r_{\parallel 2}$	$t_{\parallel 1} t_{\perp} r_{\parallel 1} r_{\parallel 2}$																				
$t_{\parallel 1} t_{\perp} r_{\parallel 1} r_{\parallel 2}$	$t_{\parallel 1} t_{\perp} r_{\parallel 1}$	$t_{\parallel 1} t_{\perp} r_{\parallel 1} r_{\parallel 2} r_{\perp}$																				
$t_{\parallel 1} t_{\perp} r_{\parallel 2}$	$t_{\parallel 1} t_{\perp} r_{\parallel 1} r_{\parallel 2}$	$t_{\parallel 1} t_{\perp} r_{\parallel 1} r_{\parallel 2} r_{\perp}$																				

Figure 7.40 Passive brick solutions for the four remaining active brick arrangements. The grey backgrounds indicate the solutions which are retained after selection of the passive brick arrangements.

do not lead to an efficient and compact robot kinematics: the two following criteria are thus valid regardless the specific requirements of the machine and can be applied on the synthesis of any ultra-high precision robot.

The *first dismissing criterion, based on force alignment observations*, aims at limiting parasitic displacements along the blocked degrees of the bricks, which result from the application of forces and moments on the robot end-effector. This is achieved by minimising the orthogonal distance between the robot output and the brick, which should ideally be aligned. In other words, the active and passive bricks of a kinematic chain must fulfill the following criterion: if the passive brick is planar, its plane must be parallel (ideally coincident) to the active brick plane, whereas if the passive brick presents a rotational symmetry, its axis must belong to a plane which is parallel to the

active brick. In the case of the 5-DOF mobility, this assumption allows the first passive bricks arrangement of solution 1 to be dismissed, as well as the third arrangement of solution 24 (Fig. 7.40): in both cases, the $t_{\parallel 1}t_{\perp}r_{\parallel 2}$ brick is inevitably orthogonal to the active brick plane.

Then, *the possibilities which include passive bricks which are excessively complex to machine must be examined*: the solution is retained only if the active and passive bricks of the considered kinematic chain can be designed as one efficient flexure-based mechanism. The involved passive bricks are the following (see (Richard, 2012): $t_{\parallel 1}r_{\parallel 1}$ and $t_{\perp}r_{\perp}$, $t_{\parallel}t_{\perp}r_{\perp}$, $t_{\parallel 1}t_{\perp}r_{\parallel 1}$ and $t_{\parallel 1}t_{\parallel 2}r_{\parallel 1}$, as well as $t_{\parallel 1}t_{\perp}r_{\parallel 1}r_{\perp}$ and $t_{\parallel 1}t_{\parallel 2}r_{\parallel 1}r_{\parallel 2}$. In the case of the 5-DOF mobility, the $t_{\parallel 1}t_{\perp}r_{\parallel 1}$ brick is included in solutions 17 and 24 (Fig. 7.40) and serially arranged with a $T_{\parallel}R_{\perp}$ active brick. Performing these two bricks with a single mechanism is nonetheless not straightforward. Consequently, both passive bricks solutions which include this configuration are dismissed.

The kinematic solutions which remain after the application of these two criteria are highlighted with grey backgrounds in Figure 7.40. Then, the specific robot requirements are used to select the most suitable kinematics for the application. In the case considered here, two kinematic specifications have not been exploited yet, namely the minimal number of different building bricks and the simple transformation into another mobility. The number of different building bricks of the remaining solutions is thus computed:

- *Active bricks arrangement #1* (Fig. 7.40): 4 building bricks
- *Active bricks arrangement #6*: 6 bricks for both solutions
- *Active bricks arrangement #17*: 6 bricks
- *Active bricks arrangement #24*: 3 bricks

The active brick arrangement #24 and the remaining passive brick solution thus consists in the optimal solution for the minimal number of building bricks criterion: this kinematic is recalled in Figure 7.41. Furthermore, the transformation into another mobility is straightforwardly performed: a 6-DOF robot is obtained by replacing the T_{\parallel} by a third $T_{\parallel}R_{\perp}$ brick, thus presenting only two different building bricks. Moreover, a 4-DOF robot is simply achieved by replacing one of the $T_{\parallel}R_{\perp}$ bricks by a T_{\parallel} or a R_{\perp} one, depending on the degrees of freedom which are required (three translations and one rotation, or two translations and two rotations).

Figure 7.42 presents the kinematic solution with sketches of the design principles, whereas Figure 7.43 illustrates a scaled mock-up including assembled leaf springs and hand-actuation.

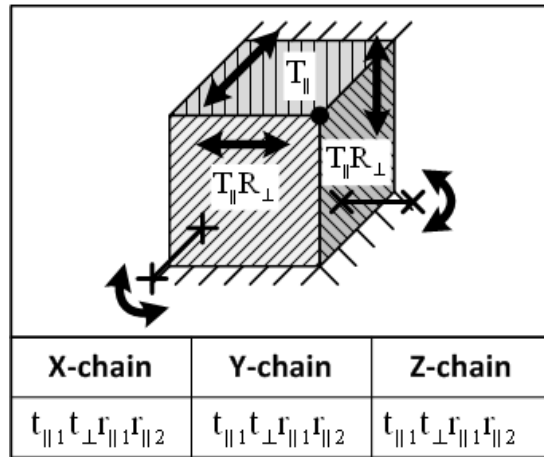


Figure 7.41 Final kinematic solution of the 5-DOF ultra-high precision robot.

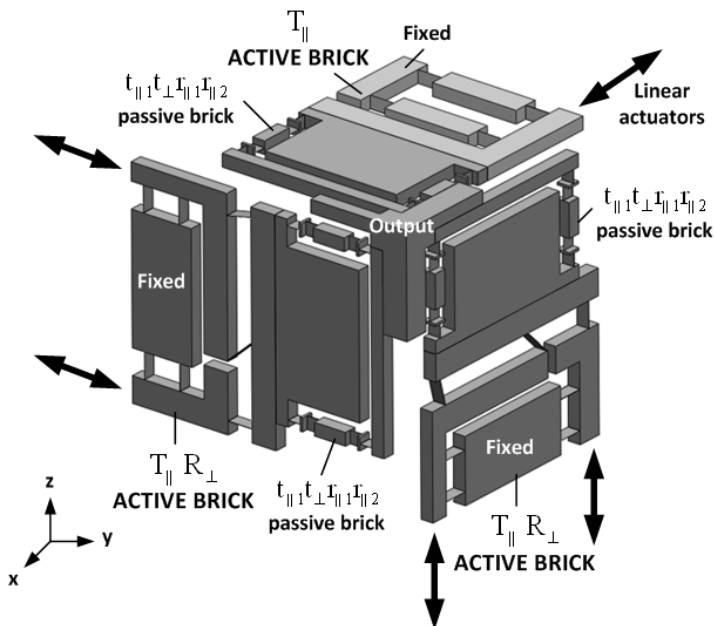


Figure 7.42 Sketch of the kinematic solution with the brick design principles.

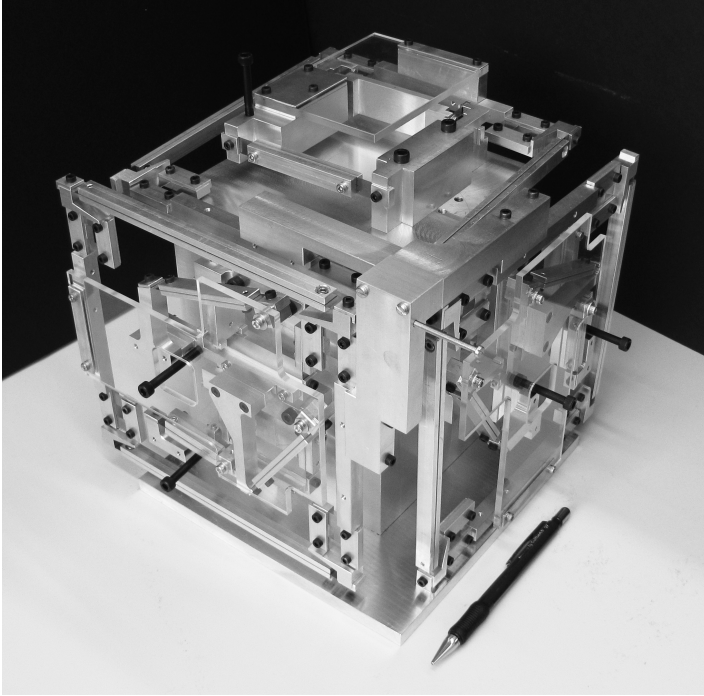


Figure 7.43 Scaled mock-up with assembled leaf springs and hand-actuation.

7.5.3 Mechanical design

This section is dedicated to the mechanical design of the Legolas 5 prototype: first, the selected solutions to perform the three necessary building bricks are detailed, including the actuation sub-brick development.

Active brick design

The development of the actuation sub-brick, which is featured in both robot active bricks, is the first step of the design process: it includes the choice of the sensors and actuators, as well as the dimensioning of the 4-prismatic hinge table, whose role is to guide the actuator moving part (see *Actuation sub-brick* below). The mechanical design of both T_{\parallel} and $T_{\parallel}R_{\perp}$ bricks is then presented.

Actuation sub-brick

As the Legolas 5 robot includes the $T_{\parallel}R_{\perp}$ active brick, two versions of the actuation sub-brick must be developed: the first actuates only the translation, while the second performs both the translation and the rotation. The latter must then present a higher stroke in order to simultaneously achieve the maximal displacement and angle (see Subsection $T_{\parallel}R_{\perp}$, $T_{\perp}R_{\parallel}$ and $T_{\parallel}R_{\perp 2}$ bricks, p. 161). The components which have been selected for the sub-brick are the following :

- **Sensor:** optical incremental linear encoder LIK-41 from Numerik Jena (Numerik Jena GmbH, 2015), which presents a resolution of 50 nm and a customer set measuring length
- **Actuator:** cylindrical voice coil LA15-26-000A from BEI Kimco (BEI Kimco Magnetics, 2015)
- **Linear flexure-based guiding mechanisms:** two 4-prismatic hinge tables; the first, presenting a ± 5 mm stroke, actuates only the translation, while the second, presenting a ± 10 mm stroke, actuates both the translation and the rotation. The selected hinges are 200 μm thick and 5 mm long, while the total length of the table arms is 80 and 100 mm.

However, the moving mass of the whole actuation sub-brick which performs the simultaneous translation and rotation reaches 0.6 kg when including a monolithic steel 4-hinge table, which highly limits its dynamical performances. Consequently, it must be drastically decreased, which is achieved by designing the *Legolas 5 prototype with aluminum parts and assembled steel leaf springs*. The total moving mass of the aforementioned actuation sub-brick is thus decreased by a factor of 3.7, which multiplies the theoretical maximum acceleration by the same value.

The development of the Legolas 5 prototype *will thus additionally prove that robots which are composed of assembled leaf springs can achieve precisions below 0.1 μm , and present high dynamic performances thanks to their lower moving mass*. Indeed, to the knowledge of the author, all ultra-high precision robots of the literature present monolithic structures, while assembly of flexures has only been performed for high precision machines (precision $> 0.1 \mu\text{m}$).

The following paragraphs present the design of the active and passive bricks with assembled leaf springs, whereas Section 7.5.5 will detail flexure alignment and mounting method. Note that the mechanical solutions have still been selected from Section 7.4, although the planarity and rotational symmetry criteria are less significant when the flexures are assembled.

T_{||} active brick

The mechanical design of the T_{||} active brick simply consists in the low-stroke actuation sub-brick, which only motorises the translation. Figure 7.44, left, presents the sub-brick 4-hinge table, including an integrated mechanical stop; the assembly of the leaf springs will be detailed in Section 7.5.5. Furthermore, Figure 7.44, right, shows the complete T_{||} active brick, where a key feature can be highlighted: the leaf springs present a non-constant breadth, which allows the transverse stiffness and eigenfrequency of the guiding system to be increased (Bacher, 2003).

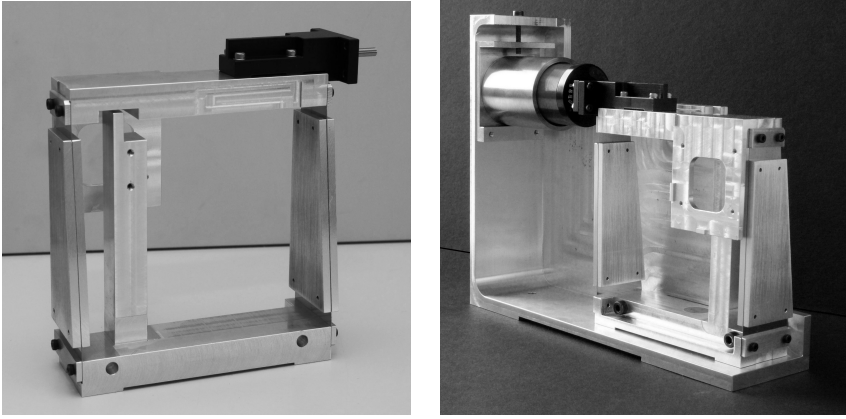


Figure 7.44 Assembled leaf springs 4-prismatic hinge table actuating the translation (left) and complete T_{\parallel} active brick (right).

$T_{\parallel}R_{\perp}$ active brick

The detailed mechanical design of the $T_{\parallel}R_{\perp}$ active brick, which is based on the principle described in Subsection $T_{\parallel}R_{\perp}$, $T_{\perp}R_{\parallel}$ and $T_{\parallel 1}R_{\perp 2}$ bricks, p. 161, is illustrated in Figure 7.45, left: the synchronous actuation of both sub-bricks perform the translation, whereas the rotation is obtained by the sole motion of the high-stroke sub-brick, thus allowing to simultaneously achieve the maximal translational stroke and angle. As in the case of the T_{\parallel} active brick, the 4-hinge tables leaf springs present a non-constant breadth to increase the transverse stiffness. Furthermore, Figure 7.46, left, shows both actuation sub-bricks, without the mechanism transforming the linear motion into a rotation. The latter is composed of two parts (see R_{\parallel} and R_{\perp} bricks, p. 157): first, two leaf springs, illustrated in Figure 7.46, right, define the position of the Remote Centre of Motion; they are assembled to the sub-brick which only actuates the translation (Fig. 7.45, right). Then, a single leaf spring, whose role is to transform the actuator force into a moment, is linked to the high-stroke sub-brick (Fig. 7.45, left). The orthogonal distance between this leaf spring and the rotation centre, d , is determined by the maximal rotation angle and the actuator stroke, as discussed in Subsection *Actuation sub-brick* (p. 174).

Note that the design of this active brick is not strictly planar, but rather consists of three planes which are arranged in parallel (Fig. 7.45, left): two of them include the actuation sub-bricks, whereas the third encompasses both parts of the RCM mechanism. This configuration leads to a more compact design, and also allows to align the RCM mechanism with the robot end-effector, thus limiting the effect of parasitic forces and moments. Furthermore, as illustrated in Figure 7.45, left, all three RCM leaf springs will be assembled

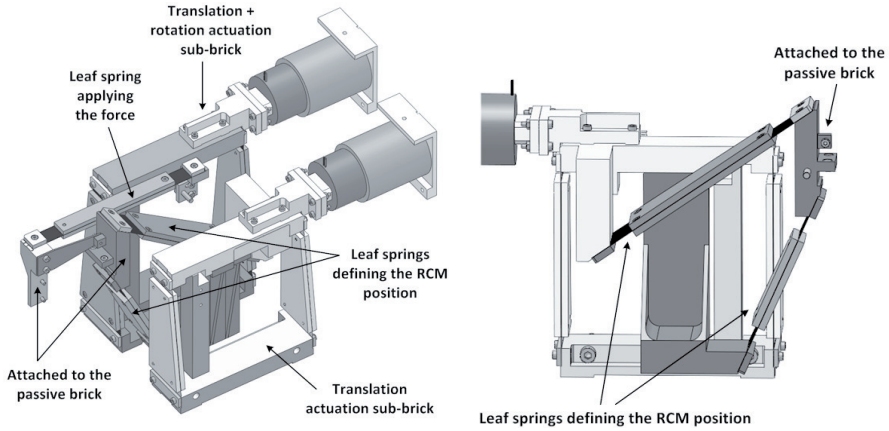


Figure 7.45 Detailed design principle of the $T_{\parallel}R_{\perp}$ active brick (left) and detail of the translation actuation sub-brick including the leaf springs defining the RCM position (right).

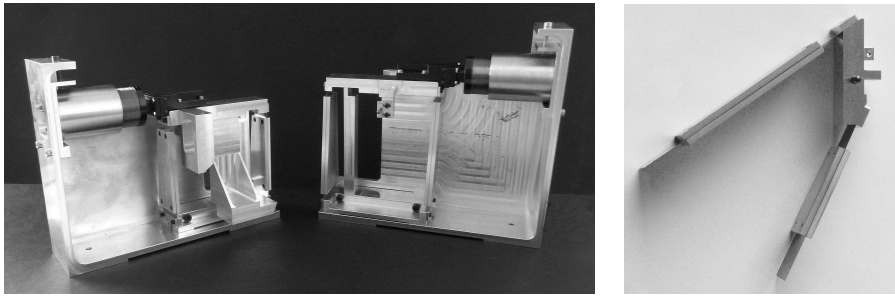


Figure 7.46 Picture of both actuation sub-bricks, without the RCM mechanism (left) and sub-assembly of the leaf springs defining the RCM position (right).

to the passive brick, which intrinsically causes overconstraints; to limit their effect, the position of the passive brick is set by both broad leaf springs defining the rotation centre, whereas the narrow leaf spring applying the force can easily adapt to this position by deforming itself. If necessary, an additional necked-down hinge can be performed in the latter to suppress the overconstraint.

7.5.4 $t_{\parallel 1}t_{\perp 1}r_{\parallel 1}r_{\parallel 2}$ passive brick design

The mechanical solution which has been retained for the three $t_{\parallel 1}t_{\perp 1}r_{\parallel 1}r_{\parallel 2}$ passive bricks of the Legolas 5 is composed of a 4-hinge table and of a 3-DOF serially arranged leaf spring (Fig. 7.35 and $t_{\parallel 1}t_{\perp 1}r_{\parallel 2}r_{\perp}$, $t_{\parallel 1}t_{\perp 1}r_{\parallel 1}r_{\parallel 2}$ and $t_{\parallel 1}t_{\parallel 2}r_{\parallel 1}r_{\perp}$ bricks, p. 165). This design notably presents the advantage of allowing the forces of both the table and the leaf spring to be aligned with the

end-effector, thus limiting parasitic deformations of the mechanical structure. The main criterion for the design of the 4-hinge table is the minimisation of the volume requirement. As for the leaf spring, its torsion axis must be aligned with the rotation axis of the robot, whereas its shape must allow for high-stroke combined torsion and flexion motions. Figure 7.47 illustrates the three passive bricks of the Legolas 5 robot: the first one, which corresponds to the X-side kinematic chain, features a broad leaf spring with a central hole, allowing both the compactness of the design and the limitation of the intrinsic overconstraints in a broad plate subject to torsion. On the other hand, the Y-side and Z-side bricks present a tensile specimen-like shape, which is also efficient at reducing stresses in the leaf spring during simultaneous torsion and flexion. Note that the parasitic deformations of the 4-hinge table are expected to be higher in the case of the Z-side design, as the leaf spring position does not coincide with the middle of the table arms.

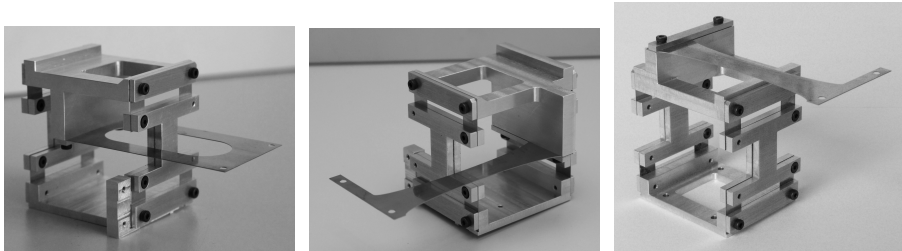


Figure 7.47 Detailed design of the X-side (left), Y-side (middle) and Z-side (right) passive bricks.

7.5.5 Design and assembly subtleties

Leaf spring assembly

The alignment and assembly of the leaf springs must be carefully performed in order to limit the parasitic deformations of the flexure mechanisms; in the Legolas 5 prototype, each leaf spring is assembled with screws and clamped between a support and a prismatic washer. The precise relative positioning of these three parts is achieved as illustrated in Figure 7.48, top: the vertical alignment, as well as the parallelism between the parts, are set by two protrusions on the support. Furthermore, the use of a precision gauge block during the assembly process allows the support, the leaf spring and the washer to be laterally aligned. Figure 7.48, bottom, presents a detail of a resulting leaf spring mounting. Note that in the case of 4-hinge tables, only three of the four clampings must present the alignment protrusions to avoid overconstraining the mechanism during assembly. Lastly, the machining geometric tolerances, which are presented in Figure 7.48, top, allow parasitic displacements of the 4-hinge tables to be minimised.

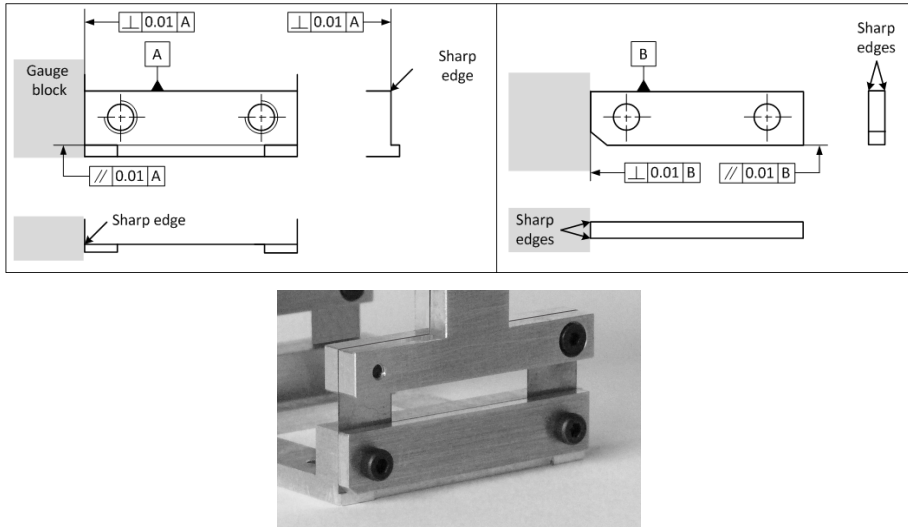


Figure 7.48 Assembly principle and geometric tolerances of the clamping parts: support (top left) and prismatic washer (top right); the chamfered edge of the washer only consists in an assembly point of reference. Bottom: detail of a 4-hinge table leaf spring assembly.

Gravity compensation

The compensation of gravity, or static balancing, is mandatory to avoid that the weight of the robot mobile parts does not plastically deform the leaf springs; in the Legolas 5 prototype, the solution which has been retained to counterbalance the gravity effects acts at two levels:

- *at the level of the actuation sub-bricks which present a vertical translation:* the gravitational force acting on the sub-brick mobile parts is counterbalanced by adding a traction spring in parallel with the 4-hinge table (Fig. 7.49, left). The equilibrium point of the system corresponds to the middle of the table stroke. In the Legolas 5 prototype, this solution is included in both actuation sub-bricks of the Y-side kinematic chain.
- *at the end-effector level:* the moment generated by gravity acting on the passive brick and RCM mechanism mobile parts is counterbalanced by adding a traction spring which links the output of the actuation sub-brick to the passive brick (Fig. 7.49, right). As previously, the equilibrium point of the system corresponds to the zero-stroke of the output. Moreover, the stiffness of the spring should be minimised to limit the effect of the force variation due to the end-effector displacements. Lastly, as the spring must withstand a rotation of $\pm 10^\circ$ between its extremities, increasing its length brings a noteworthy advantage. Both X-side and Y-side kinematic chains of the Legolas 5 include this solution.

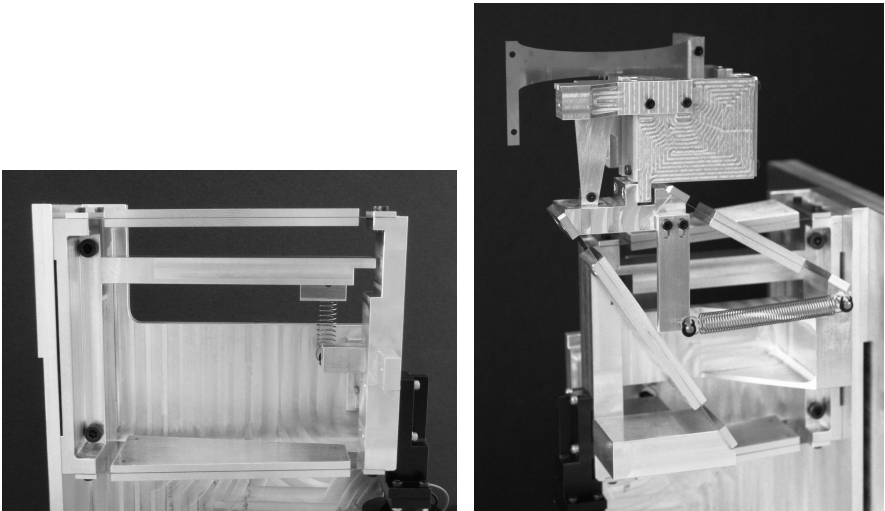


Figure 7.49 Left: Gravity compensation of an actuation sub-brick presenting a vertical translation. Right: Gravity compensation at the level of the end-effector.

7.5.6 Legolas 5 prototype

Figures 7.50 and 7.51 illustrate the resulting Legolas 5 prototype, presenting a general view, as well as a detail of the end-effector and passive bricks.

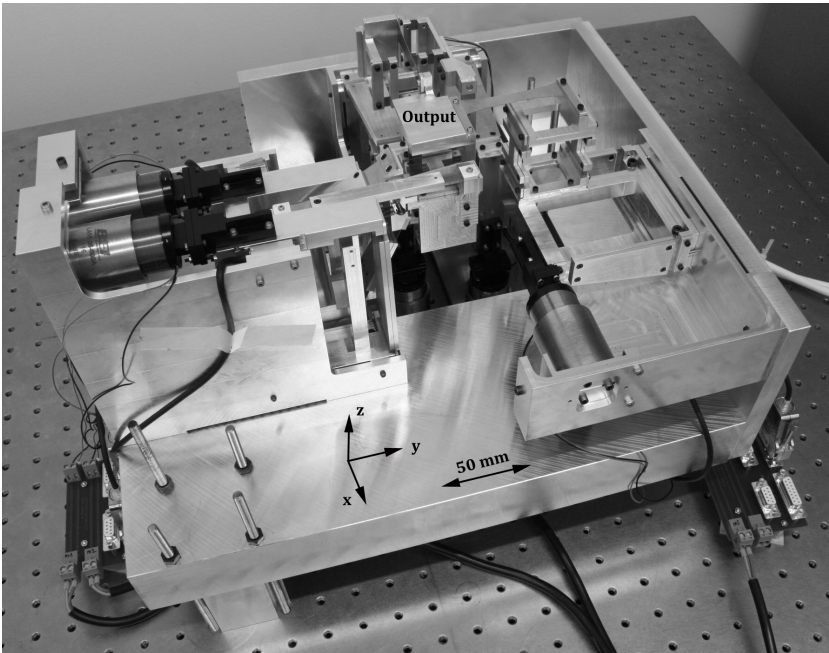


Figure 7.50 Legolas 5 prototype.

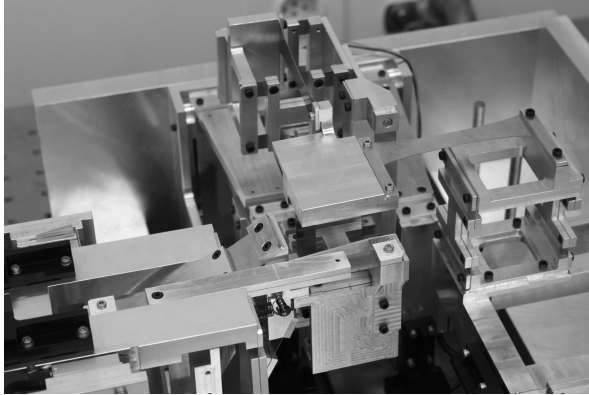


Figure 7.51 Detailed view of the Legolas 5 end-effector and passive bricks.

- Volume of the prism enclosing the robot mechanical parts: $339 \times 397 \times 269 \text{ mm}^3$
- Total linear stroke: 10 mm

The workspace characterisation of the Legolas 5 prototype has shown that the requirements are fulfilled, as combined strokes of $\pm 5 \text{ mm}$ for the translations and $\pm 10^\circ$ for the rotations can be achieved (see (Richard, 2012) for measurements). Furthermore, the real maximal strokes values simultaneously reach $\pm 15^\circ$ and $\pm 5 \text{ mm}$ without mechanical interference; nonetheless, these positions cause high stresses in the leaf springs, which have not been designed to achieve such high angles, and will not be allowed in this Legolas 5 prototype.

The resolution is evaluated by applying steps of 50 nm around a central position to the actuation system; varying the latter allows to verify that the degree of freedom resolution is constant on its whole stroke. The control algorithm ensures that the position of the actuation sub-brick oscillates between $\pm 50 \text{ nm}$ (with punctual higher peaks), with a mean value which is always lower than the sensor resolution. As for the repeatability, its evaluation consists in alternating between two actuation sub-brick positions distant of 2 mm, which corresponds to an end-effector displacement of around 2 mm and 4° (Fig. 7.52, middle). As in the case of the resolution, the central position can be changed to check the constancy of the repeatability over the whole motion stroke.

Figure 7.52 illustrates the obtained results for the Tx translation: the resolution graph (top) shows that steps of 50 nm can clearly be distinguished at the level of the robot end-effector, whereas the repeatability graph (centre and bottom) presents values which are below the sensor resolution. Note that the oscillations on the constant position areas, which represent the mean position error, present values which are below the sensor resolution and similar to the mean position error evaluated at the level of the actuation.

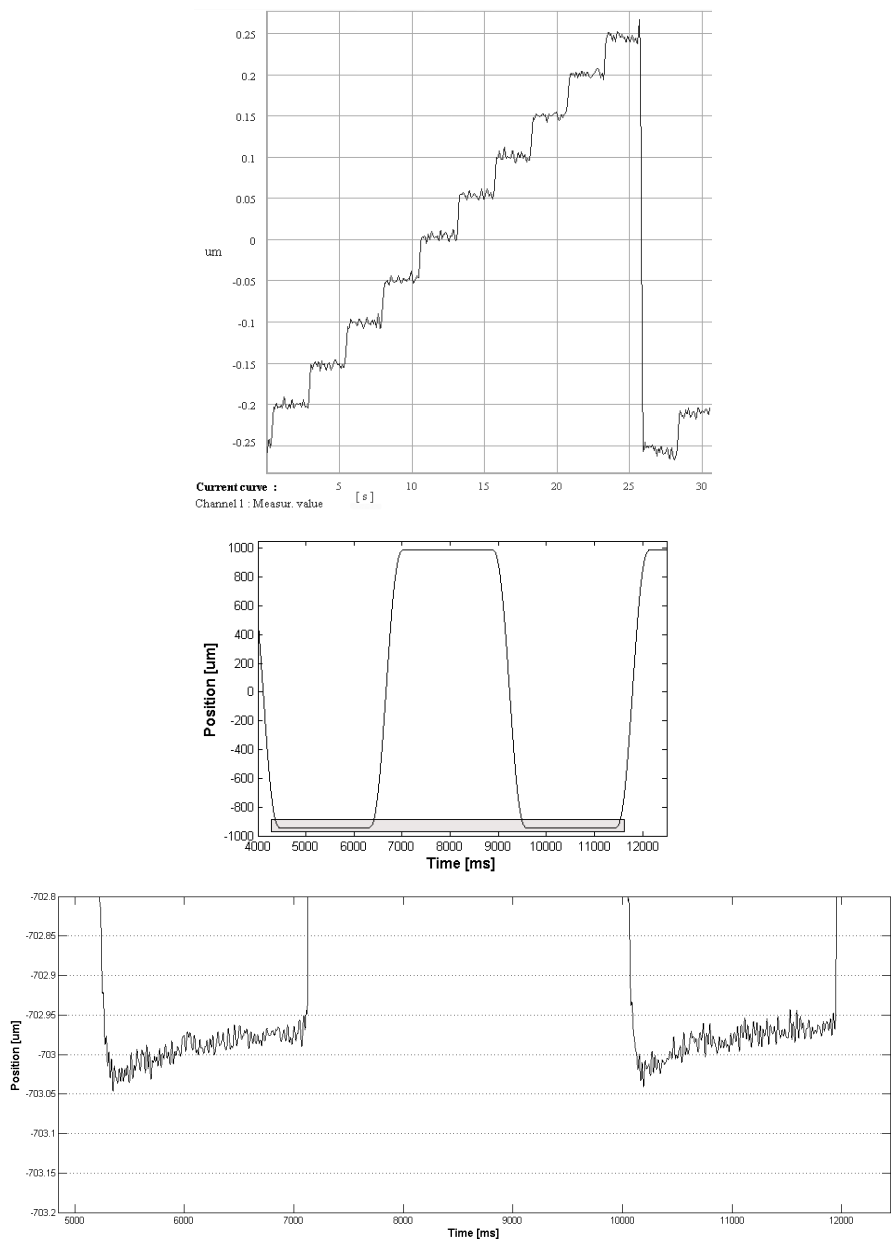


Figure 7.52 Top: resolution evaluation of the Tx translation; middle: position profile of the repeatability measurement; bottom: detailed view of two consecutive steps, allowing the repeatability of the Tx translation to be evaluated. Note that the position drift mainly results from the increase of the air temperature on the laser beam path, which is caused by the Tx actuation.

Finally, these measurements have been performed at five different positions of the Tx translation motion and exhibit similar results, thus proving that both the resolution and the repeatability are constant over the whole stroke.

The resolution and repeatability of the Legolas 5 rotations achieve 0.35'' (1.7 μ rad) for the Rx rotation, and 0.39'' (1.9 μ rad) the Ry rotation. Note that the thorough characterisation of the Legolas 5 robot can be found in (Richard, 2012).

7.5.7 Discussion

This section has detailed the application of the modular design methodology to a practical example, consisting in an ultra-high precision 5-degree of freedom robot. ***This case study has notably highlighted the creative design process which has to be accomplished to transform a kinematics and mechanical principle into a real and efficient robot:*** first, although the modular concept symbolises the robot with a cube, the final arrangement of the Legolas 5 only retains the orthogonal arrangement of the kinematic chains. Then, the detailed design of the Legolas 5 building bricks has illustrated the evolution of the flexure-based mechanisms, from the principles proposed in the mechanical solution catalogue to the final arrangement of the bricks. Finally, the shrewd assembly of the building bricks in the Legolas 5 prototype has underlined some design subtleties.

Subsequently, *the characterisation of the Legolas 5 prototype proves that the requirements of the robot are fulfilled*: the workspace estimation has first highlighted that simultaneous translations of 5 mm and rotations of 10° are achieved; Then, further measurements have shown that the resolution and repeatability of the motions attain 50 nm and 1.9 μ rad and are limited by the selected sensor resolution only. *These noteworthy results verify that the Legolas 5 prototype, and more generally robots which are synthesised with the modular design methodology and composed of assembled leaf springs, can achieve ultra-high precision.*

7.6 Ultra-high precision parallel robot family

The application of the methodology on the synthesis of robots presenting the same specifications as this 5-DOF case but different degrees of freedom has generated a new kinematic family, called the Legolas family. It presents a kinematic solution for each of the 19 possible end-effector mobilities, making use of only 6 different building bricks, which are the following:

- *Active bricks*: $T_{\parallel}, R_{\perp}, T_{\parallel}R_{\perp}$
- *Passive bricks*: $t_{\parallel}r_{\perp}, t_{\perp}r_{\parallel}, t_{\parallel}t_{\perp}r_{\parallel}r_{\perp}$

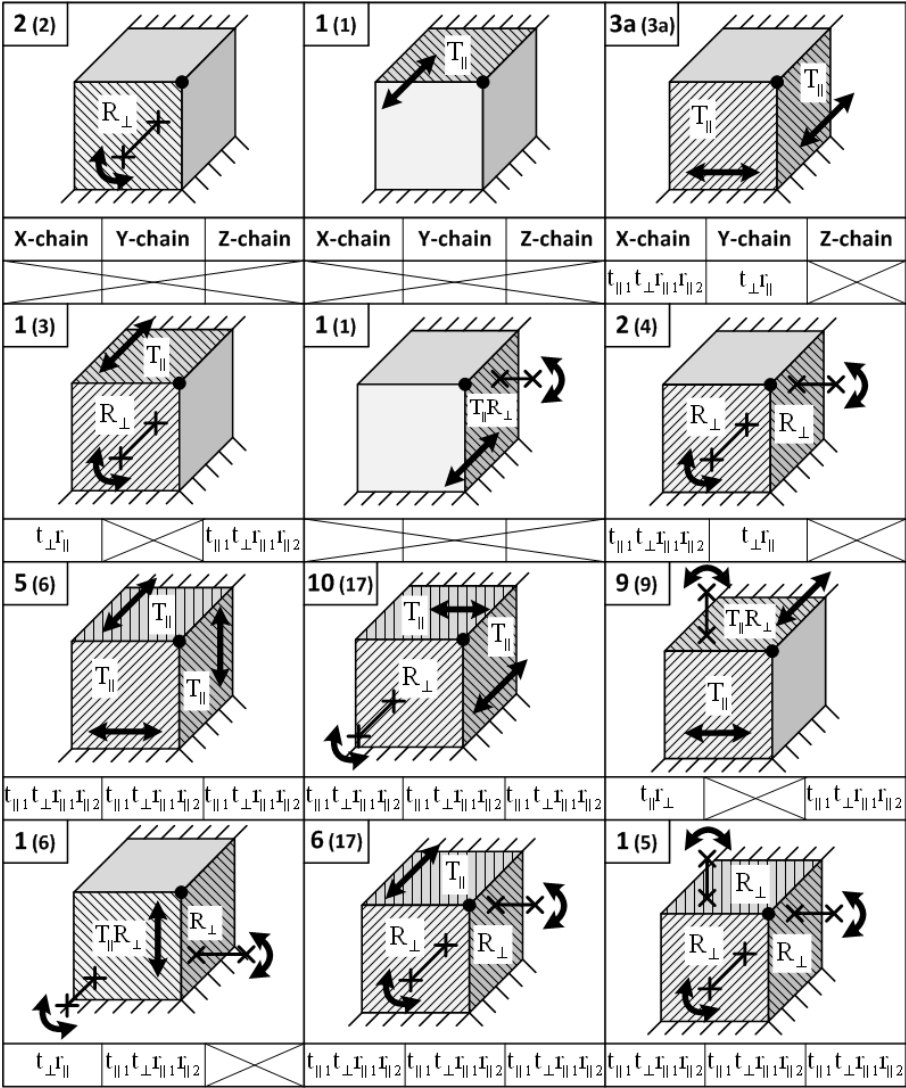


Figure 7.53 Active and passive bricks arrangements for each of the 19 possible mobilities of the Legolas family (1/2); the numbers refer to the position of the solutions in the reduced (plain) and exhaustive (in parentheses) solution catalogues.

Figures 7.53 and 7.54 illustrate the active and passive brick solutions for each robot mobility. Then, the arrangement and mechanical design of each robot of this family has been developed on the basis of the mechanical solutions and assembly considerations which have been presented in the previous section. The illustration of each resulting robot are to be found in (Richard, 2012).

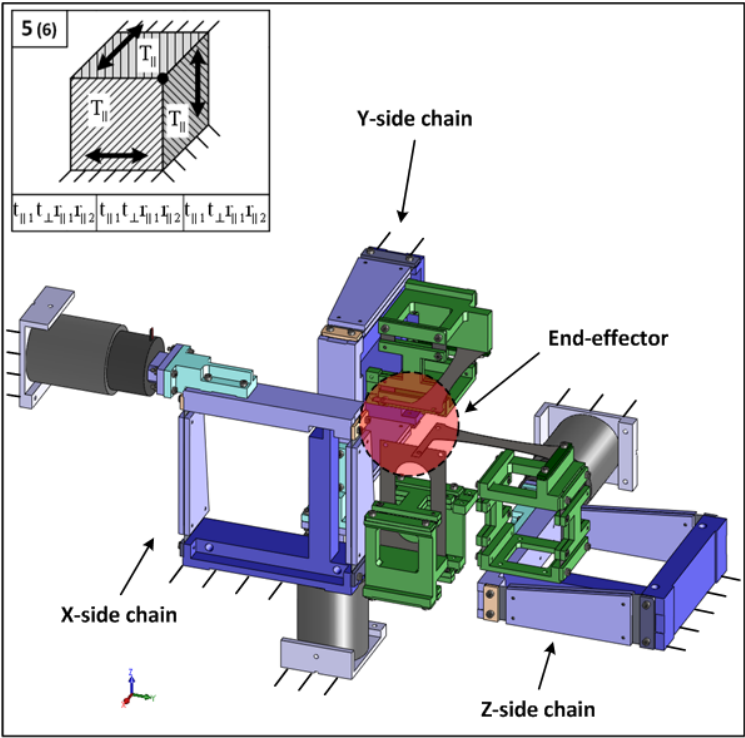


Figure 7.55 3-DOF (Tx, Ty, Tz) Legolas robot, including three times the same kinematic chain.

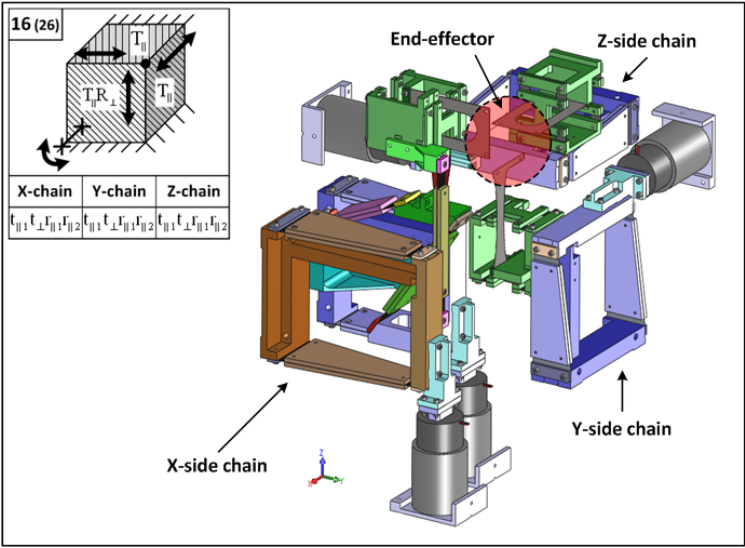


Figure 7.56 4-DOF (Tx, Ty, Tz, Rx) Legolas robot.

Furthermore, as the development of each Legolas robot stems from the same mechanical considerations which have led to the Legolas 5 prototype, the performances of each family member are expected to be as satisfactory as the results of the Legolas 5 characterisation. Consequently, the case study presented in the previous section has not only generated one ultra-high precision 5-DOF robot, but a whole family of 19 high-performance machines.

7.7 Conclusion

The research which has been presented in this chapter responds to the growing need for industrial production tools capable of manipulating and assembling devices with submicrometric precision: the current miniaturisation trend indeed tends to decrease the size of both the products and the production lines, thus demanding compact ultra-high precision robots to perform these tasks. However, their development is still highly costly, both in time and money, and results in machines that are barely flexible: if the customer specifications change during the design process, the latter has to be restarted, often from the very beginning, thus resulting in a significant waste of resources. This highlights the need for a global and modular approach which examines and proposes solutions for both the parallel kinematics synthesis and the flexure-based mechanical design of these robots – two crucial and interdependent aspects.

Consequently, this research has overcome these issues by proposing a modular design methodology, which can be paralleled to a robotic Lego: a finite number of conceptual building bricks allow to quickly design and modify parallel robots. The core of this concept lies in the exhaustive conceptual solution catalogue which, for each possible end-effector mobility, lists all combinations of building bricks performing the desired motions. Furthermore, this work focuses on ultra-high precision machines: it thus proposes a reduced conceptual solution catalogue, which is based on design and machining considerations, along with original flexure-based solutions for the mechanical design of the building bricks. Lastly, the case of an ultra-high precision 5-DOF robot has been studied to illustrate the practical use of the methodology. This has enhanced the creative process, which has led to the achievement of not only one 5-DOF robot, but a whole family of high-performance machines.

7.8 Final note

Finally, the flexibility and creativity allowed by the modular design methodology proposed in this work deserve to be highlighted: the concept can indeed be considered as a *design tree*, as the explicit statement of hypotheses at each

step of the methodology permits the user to enter at any level and to adapt it to his/her specific needs (Fig. 7.57). Whereas the ultra-high precision Legolas family provides fully designed robots, which only necessitate the adaptation of the mechanisms to the application requirements (strokes, position of the rotation centres), a more creative user may decide to modify the mechanical design criteria, thus defining a new reduced conceptual solution catalogue. Moreover, the chapter which proposes mechanical designs for the building bricks aims at gathering interesting flexure-based principles as a tool for the engineer, rather than at proposing a thorough catalogue of off-the-shelf solutions. Lastly, this methodology allows the expert in robot kinematics synthesis to start directly from the conceptual building bricks and the thorough solution catalogue to reinterpret the procedure according to his/her specific needs.

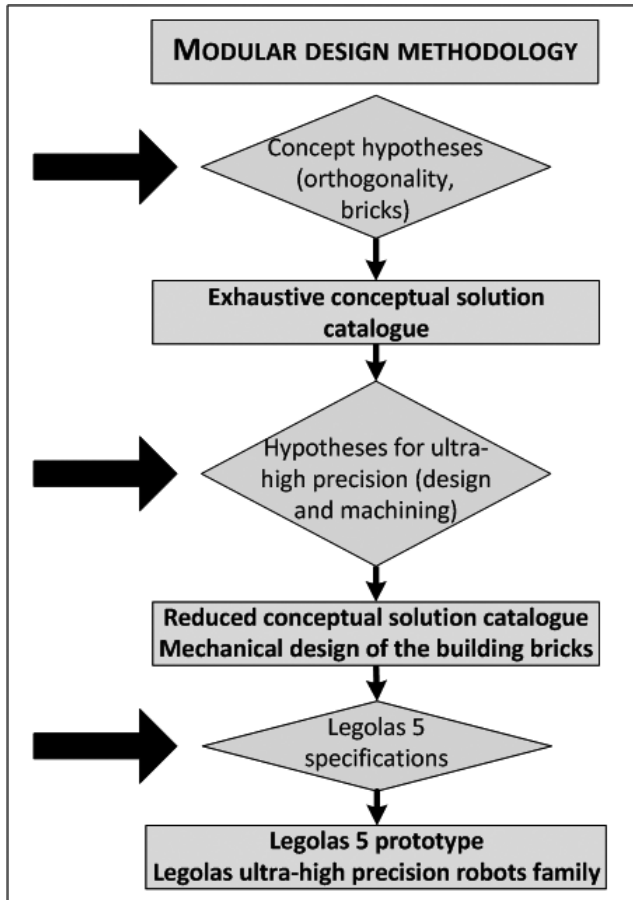


Figure 7.57 Illustration of the modular methodology as a design tree; the lateral arrows symbolise the different levels of hypotheses which the user can review to fulfill the specific needs of his/her application.

Moreover, neither this methodology nor solution catalogues are expected to optimally solve the challenging robot synthesis problem. No generic method is indeed capable of responding to the wide range of applications of parallel industrial robots as efficiently as an engineer, whose creativity and experience are essential and irreplaceable. Consequently, the concept proposed here provides kinematics and mechanical design suggestions, which help preventing the engineer from encountering the ‘writer’s block’. To conclude and further develop the analogy with the artistic world, Isaac Asimov’s following quote from one of his scientific essays (Asimov, 1997) completely illustrates the spirit of this work:

‘How often people speak of art and science as though they were two entirely different things, with no interconnection. An artist is emotional, they think, and uses only his intuition; he sees all at once and has no need of reason. A scientist is cold, they think, and uses only his reason; he argues carefully step by step, and needs no imagination. That is all wrong. The true artist is quite rational as well as imaginative and knows what he is doing; if he does not, his art suffers. The true scientist is quite imaginative as well as rational, and sometimes leaps to solutions where reason can follow only slowly; if he does not, his science suffers.’

Rectilinear flexure mechanisms

8.1 Introduction

8.1.1 Framework

Flexure-based rectilinear bearings are frequently required in high precision applications, such as space, metrology or microelectronics. The objective of the development presented here is to design precision linear bearings using flexure joints to meet the needs of a scientific experiment called the *watt balance*. This experiment is intended to provide a new definition of the unit of mass, the kilogram, which is a major issue in modern fundamental metrology.

The results presented here are part of the new Swiss watt balance project, the design work being in collaboration with METAS (Swiss Federal Institute of Metrology), which entrusted CERN (European Organization for Nuclear Research) with the realisation of a magnetic circuit, Mettler-Toledo (a Swiss world leader in high precision balances) with supplying a mass comparator and EPFL (École polytechnique fédérale de Lausanne) with providing a rectilinear translation system. Special acknowledgement is also given to CSEM (Swiss Center for Electronics and Microtechnology) for sponsoring the writing of this current chapter.

A catalogue of kinematic solutions for rectilinear motion is presented. Desired criteria for the target application are defined. Following this, two mechanisms are selected to create prototypes capable of delivering at their terminal output a linear translation of nearly 40 mm with a straightness error in the order of submicrons. The two selected mechanisms are the *Sarrus linkage* and the *13-hinge stage*. Characterisation reveals not only that it is possible to achieve this high linearity but that thanks to the flexure joints, which do not induce friction and provide high positioning precision, we obtain a deviation of only about two tenths of a micron on a translation of almost 40 mm.

8.1.2 Need for an ultrastraight bearing

As described below in Section 8.6.1, a major component of the watt balance project is an electromagnetic coil that is moved vertically in a magnetic field.

The vertical translation of the coil enables its electromagnetic characterisation to be carried out with high precision. As well as the various variables in the experiment, the characteristics of the coil must be known with a relative uncertainty of 10^{-8} . Any transverse motion of the coil during its vertical travel induces an error in the characterisation of the coil. It is therefore essential that the guidance mechanism be highly linear and display high transverse rigidities, while having a low natural stiffness.

8.1.3 Linear motion based on rotating joints

The demanding conditions of the experiment, including a high vacuum environment, the exclusion of any magnetic materials and the high precision required, lead naturally to the use of flexure joints, such as hinges and leaf springs. Hinges have the property of giving, in a first approximation, pure rotation. A kinematic issue that arises is how to obtain a straight path motion from an elementary rotary motion. When it comes to drawing a straight line, the traditional method is to use an object that is itself considered straight, such as a ruler or guide, but when we draw a circle with a compass, we use a fundamental property of the circle, i.e., that all points on the circle are equidistant from the center. We will see that similar tools exist for drawing a straight line, but they are not as simple as with the circle. Some lead to a purely linear guide and others produce a pseudolinear motion. We introduce the term *orthogyre* to designate kinematics that produces a translation from combined rotary motions (*ortho* straight and *gyre* based on rotation). In cases where the output motion is pseudolinear, we propose the term *pseudo-orthogyre*.

8.2 Rectilinear kinematics

8.2.1 Rectilinear and pseudorectilinear mechanisms based on rotation

It is possible to classify the mechanisms mentioned here according to several criteria. We first differentiate between *orthogyre* and *pseudo-orthogyre* mechanisms. Both, it must be remembered, combine rotary motions to create linear motions. However, the former result in a perfectly straight movement, while the latter give rise to a path that is approximately straight. In many applications, the path of the mechanism's output is linear enough to meet the required needs. In addition, the magnitude of the deviation varies greatly from one mechanism to another. The following section provides several examples, probably the most typical, of *orthogyre* and *pseudo-orthogyre* mechanisms. However, it must be noted that a large variety of *orthogyre* and *pseudo-orthogyre* mechanisms exist.

An additional criterion for classification of these mechanisms is their spatial arrangement. Many are planar; thus all their pivots are parallel to one other. One

nonplanar case is also considered. This mechanism is called the *Sarrus* linkage. Some of its joints are perpendicular to the others. It has three-dimensional kinematics.

A third criterion is given by the output structure. This can consist either of a single point whose trajectory is straight or it may be a solid shape. Depending on the specified application, a point may be sufficient. However, in many cases a guide is required to firmly displace a solid body, thus its whole output should not be just a point.

Only two of the mechanisms presented in this study have their output consisting of a solid that travels along a straight trajectory. These are the *Sarrus* linkage and the *13-hinge stage*, and they will be studied here in more depth. Note that in the case of a single point output, the mechanism can be constructed twice with each output connected to a common solid, thus meeting the above requirement. However, due regard should be given to the resulting overconstraint that arises when two mechanisms, each with five degrees of constraint, are linked. A partial decoupling can be achieved by mounting the connecting solid in two stiff gimbals.

Examples of orthogyres mechanisms

Sarrus

The Sarrus linkage (Fig. 8.1a) is the first orthogyre mechanism, having been described in 1853 (Bryant and Sangwin, 2008). This is the only mechanism described in this section that is not planar, since its kinematics is three-dimensional and some of its pivots are arranged perpendicular to the others.

Its principle is that two – or more – kinematic chains connect the fixed part to the output. Each chain or arm is composed of at least three coplanar pivots that constrain the output to a plane. The junction of the two arms restricts the output of the mechanism to the intersection of two generally perpendicular planes, namely a straight line. The arms cannot be arranged at 180° to each other. When they are at right angles to each other, the force of one arm on the other is optimally counteracted. An overconstraint is present in this mechanism, the orientation of the output around the axis of motion being dictated by both arms. The output retains its orientation along the stroke. The stroke-to-space ratio is good and the maximum angle variations are moderate.

Peaucellier-Lipkin

The Peaucellier-Lipkin invensor is historically the leading mechanism for transforming rotary motion into a perfectly straight line (Lemoine, 1873). It was independently invented by a French engineer named Peaucellier and a Russian mathematician named Lipkin. We call it an invensor because it uses the fact that the geometric inverse transform of a circle is a straight line. It consists

(Fig. 8.1b) of a diamond (convex quadrilateral ADEF) and an arrow (concave quadrilateral ADCF). It has a total of seven rods and ten pivots. The fixed points are the two lower pivots A and B. E follows a straight line. Two large rods (AD and AF) are designed with a length of about three times the length of the short rods (CD, DE, EF, FC). The large rods must be of the same size, as must the four small rods. The length AB must be the same as BC. The number of out-of-plane overconstraints is nine.

This mechanism has the advantage of creating a completely linear motion, but it is complex and not rigid enough. It is thus used more as a generator of movement than as a straight guide. However, the ratio of stroke to outer dimensions is interesting because it is 40% for a maximum angular displacement of 10° . It is available in both a standard and alternative configuration.

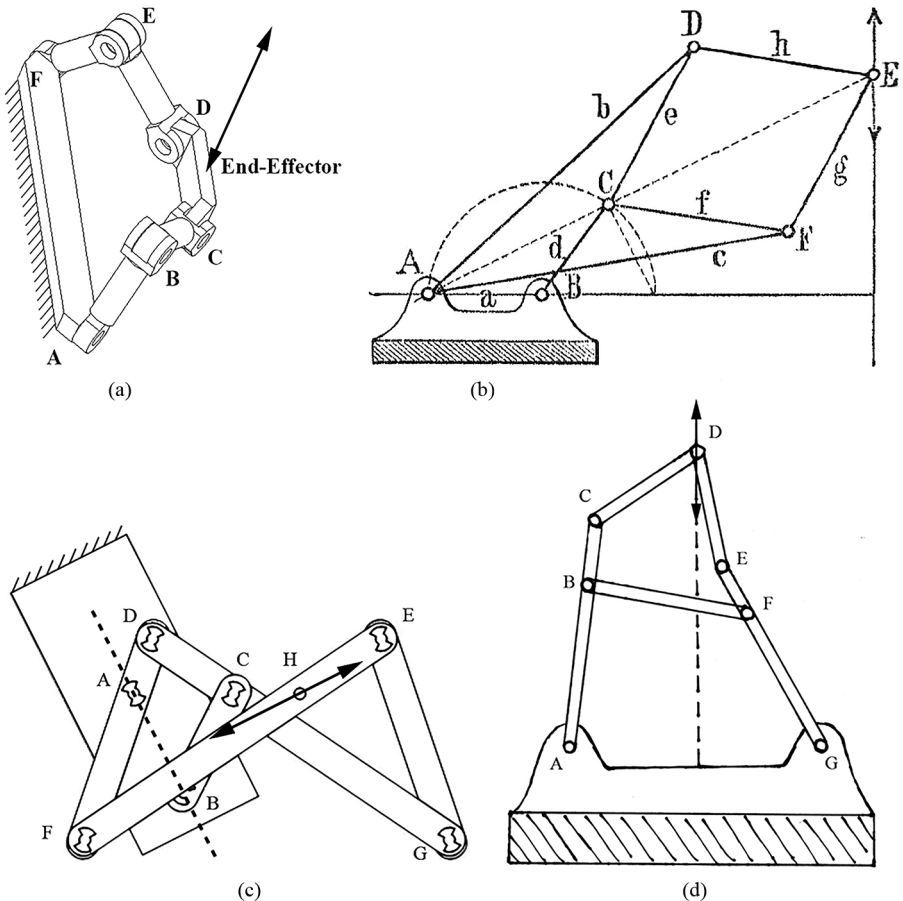


Figure 8.1 (a) Sarrus linkage (b) Peaucellier-Lipkin linkage (c) Hart's linkage (d) Hart's 'A' linkage.

Hart

In 1875, Hart proposed a model of a linear mechanism (Fig. 8.1c), which is also an invensor like the Peaucellier-Lipkin linkage (Koetsier, 1983), but with a smaller number of rods: five instead of seven. It has seven pivots. A and B are fixed and the point H moves along a straight path perpendicular to the line AB. Hart also describes a version in the form of an 'A' (Fig. 8.1d), in which the two fixed points are A and G. In this configuration, the two pairs of arms form congruent triangles (ACD and DEG). AD and DG have the same length, so D is always located on a line equidistant between A and G and thus follows a straight path. Let a be the length of CD and ED, b the length of AC and GE, and c the distance BC (equal to the distance EF). To obtain a linear mechanism, it is necessary to select the lengths that satisfy $b^2 = ac$. In both Hart's mechanisms, the ratio of stroke to size is poor for limited angular strokes. The stroke is 5% of the size for an angular deflection of 10° in the 'A' version of the Hart linkage and only 4% in the traditional version. Hart's mechanisms both contain 6 out-of-plane overconstraints.

Examples of pseudo-orthogyre mechanisms

We present here the mechanisms whose behaviors are pseudolinear, i.e., their linearity is not theoretically perfect. We introduce the straightness ratio, defined by $R_{rect} = s_r / \epsilon_{rect}$, where s_r is the length of the pseudostraight stroke and ϵ_{rect} the straightness error over the stroke considered. This ratio provides an indicator of the linearity of the motion of a mechanism. It quantifies the quality of the straightness and should be as large as possible.

Watt's linkage and Watt's parallelogram

James Watt patented both mechanisms in 1784. The principle of the linkage (Fig. 8.2a) is based on the combination of three links: two horizontal rods (AB and CD) are pivoted at their ends and are connected at the center by a third link BC. Its center (point E) approximately follows a straight line. A more compact version of this construction is Watt's parallelogram (Fig. 8.2b). The number of segments is increased to five, but the principle is substantially the same. The point following a straight line has been relocated from P to Q and the stroke thus doubled compared to the three-bar Watt linkage, as the dashed line through D, P and Q indicates. Figure 8.3a shows the general profile of the straightness error of the Watt linkage. It is a polynomial of the sixth degree. Wunderlich (Wunderlich, 1978) made an approximation of the fifth degree.

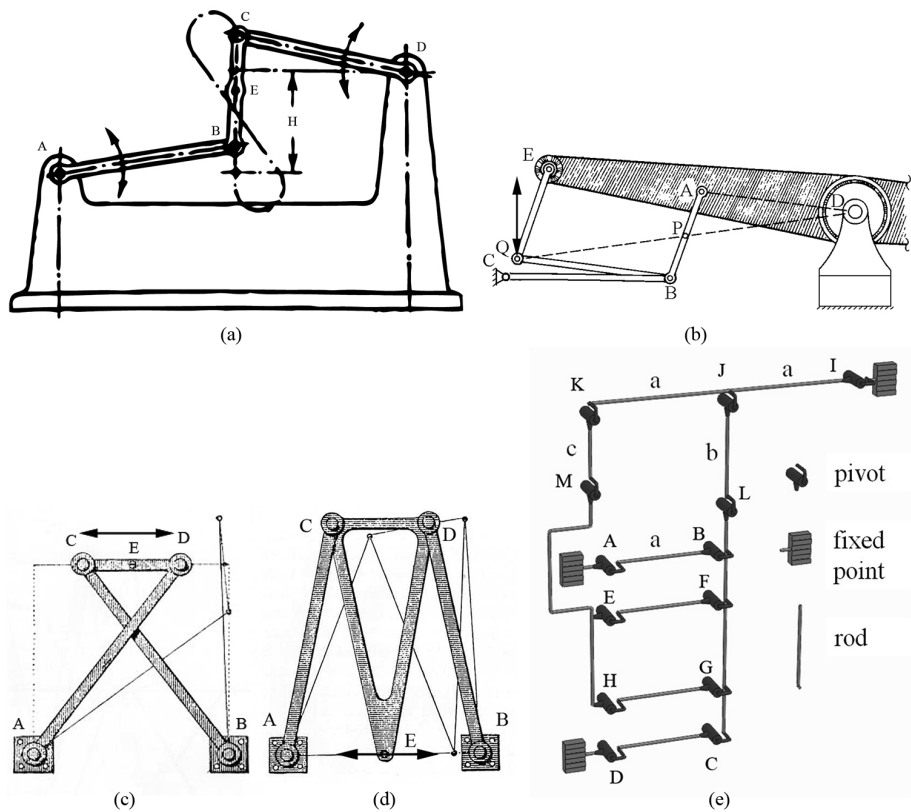


Figure 8.2 (a) Watt linkage (b) Watt parallelogram linkage (c) Chebyshev linkage (d) Robert linkage (e) 13-Hinge linkage.

For parameters chosen optimally, we obtain this formula for ϵ_{rect} , the straightness error:

$$\epsilon_{rect} \approx \frac{s^5}{256a^3b} \tag{8.1}$$

where a is the length of the long rods, b the half-length of the short rod and s the stroke over which the approximation is considered. An example with $a = 150 \text{ mm}$ $b = 30 \text{ mm}$ and $s = 58.6 \text{ mm}$ gives a straightness error of $h = 0.027 \text{ mm}$, corresponding to a straightness ratio $R_{rect} = 1085$. For a maximum pivot rotation of 10° , we obtain a displacement of 25% of the outer dimension in the case of the Watt parallelogram and 12% in the case of the Watt three-bar linkage. The orientation of the output is not maintained, but its variation is low in comparison with other mechanisms: less than 3° for a 10° rotation of the pivots.

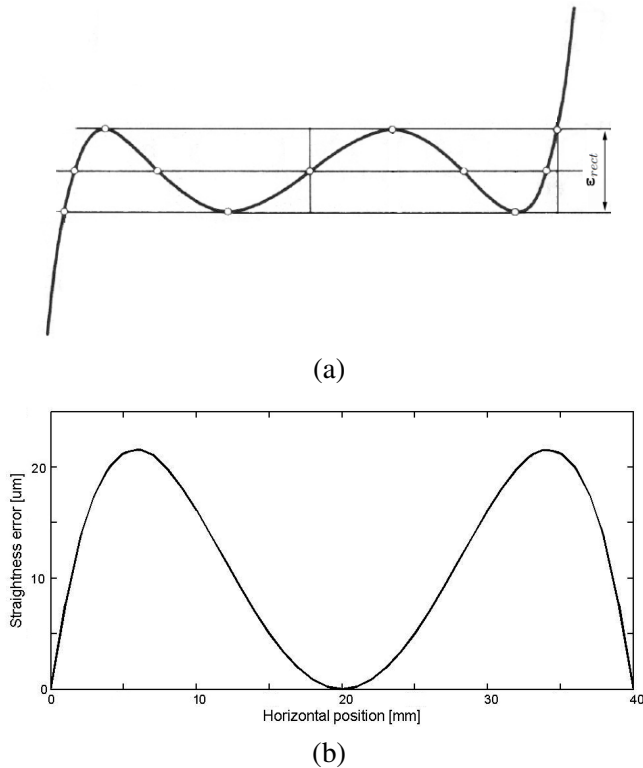


Figure 8.3 (a) Watt's linkage straightness error (b) Robert's linkage straightness error.

Chebyshev

Chebyshev invented a mechanism (Fig. 8.2c) fairly similar to the linkage of James Watt. It differs mainly in that the two main rods rotate on the same side of the middle bar. A further difference is that one must be precise when selecting the lengths of the links and the positions of the rotary pivots. The distance AB has to be twice the distance CD and the distance AD (equal to the distance CB) must be 2.5 times the distance CD. The point E following a pseudorectilinear trajectory is then in the middle of the upper rod. The mechanism comprises one single kinematic chain.

Roberts

The Roberts linkage (Fig. 8.2d) is equivalent to Watt's and Chebyshev's linkages in terms of kinematic quantities (pivots, fixed pivots, kinematic chain, links). However, it does not require such a strict placing of the pivots. In fact, it is only necessary to arrange the four pivots and the output point so that three nested isosceles triangles result with the distance between the two top pivots (distance

CD) being half the distance separating the two lower fixed pivots (distance AB). For a mechanism with a width of 40 mm (distance AB), a straightness error simulation shows a maximum value of 22 μm , as shown in Figure 8.3b. That corresponds to a straightness ratio of $R_{rect} = 1818$. For a maximum rotation of 10° on the pivots, we have a displacement of 34.5% of the outer dimension of the mechanism and an angle of inclination of the output of less than 5° .

13-hinge stage

The 13-hinge stage (Fig. 8.2e) consists of two parallelograms arranged head-to-toe and connected in series. The first is defined by points A, B, C and D and the second is defined by the points E, F, G and H. A coupling lever (IK) is connected to the two parallelograms by two links (KM of length c and JL of length b). This coupling lever ensures that the relative movement of the two parallelograms is the same. That is to say, the absolute motion of the inner parallelogram is twice that of the outer or intermediate parallelogram.

R. V. Jones first studied this mechanism in 1962 (Jones, 1962). It has also been analysed without the coupling lever (Smith et al., 1987). We count ten moving pivots, three fixed pivots, nine links and five kinematic chains in the 13-hinge stage. The mechanism is advantageous in terms of angular displacements. A maximum 10° rotation of the pivots produces a stroke equal to 20% of the maximum dimension of the mechanism. Moreover, the output of the mechanism has a constant orientation, because it does not rotate at all during the actuation of the mechanism. In Section 8.4 it is shown that there is an optimum ratio of the lengths b and c . The straightness then becomes excellent with a straightness ratio of $R_{rect} > 10^9$ for a displacement of 10% of the mechanism's outer dimension.

8.2.2 Kinematic analysis of orthogyres and pseudo-orthogyres

Table 8.1 summarises the kinematic parameters of the mechanisms presented above, using the following notation:

- p : number of pivots
- p_f : number of fixed pivots
- l : number of kinematic loops
- l_i : number of internal kinematic loops (i.e., that do not include any fixed pivot)
- c : number of kinematic chains
- H_{op} : number of out-of-plane hyperstatics
- M_o : mobility of the mechanism
- s : number of moving solid bodies
- s_b : number of solid bodies including the fixed base

Table 8.1 Kinematic features of two-dimensional orthogyre and pseudo-orthogyre mechanisms.

Mechanism	p	p_f	l	l_i	c	H_{op}	M_o	s	s_b
Watt	4	2	1	0	2	3	1	3	4
Chebyshev	4	2	1	0	2	3	1	3	4
Roberts	4	2	1	0	2	3	1	3	4
Watt parallelogram	7	2	2	1	3	6	1	5	6
Hart	7	2	2	1	3	6	1	5	6
Hart's 'A'	7	2	2	1	3	6	1	5	6
Peaucellier	10	3	3	1	4	9	1	7	8
13-Hinge stage	13	3	4	2	5	12	1	9	10

Note that the Sarrus linkage is not included in this table, because the analysis made here only applies to planar mechanisms. Also, the mobility of the system is one for every mechanism, simply because all have one degree of freedom in translation. It should be noted that the following relation exists for all planar linkages composed of pivots only:

$$l = p - s. \quad (8.2)$$

Moreover, the mobility of such mechanisms is given by:

$$M_o = 3s - 2p. \quad (8.3)$$

In addition, the number of out-of-plane overconstraints is easily known:

$$H_{op} = 3b, \quad (8.4)$$

as every time a kinematic loop is closed, two orientations and one translation (out-of-plane) are imposed twice.

8.2.3 Choice of two mechanisms

In the framework of this project, two mechanisms have been chosen to be developed into prototypes: the Sarrus linkage and the 13-hinge stage. The reason for this choice is that both mechanisms have an output as a solid part. That is to say, there is no need to double the linkage to achieve the desired output with a constant orientation. Also, they are of the parallel type and therefore have generally interesting features, such as high stiffness and stress resistance. Moreover, the Sarrus is three-dimensional and orthogyre while the 13-hinge stage is planar and pseudo-orthogyre but with a good straightness. It is interesting in the framework of this project to realise and analyse two mechanisms with different characteristics and to compare their pros, cons and performance.

8.3 Sarrus guiding mechanism

8.3.1 Sarrus linkage kinematics

General considerations

The Sarrus kinematics comprises two or more kinematic chains connected in parallel to an output stage. The kinematic chains are often arranged orthogonally and include at least three pivots. Each chain forces the output stage to travel along a plane perpendicular to the pivots in that chain. Once the endpoints of the kinematic chains are linked, the output is constrained at the intersection of the two planes, that is to say, a theoretically perfect line.

As shown in Figure 8.4, a variety of arrangements are possible. Four are presented here: closed (a), open with simple arms (b), with parallelograms (c) and open with overconstrained simple arms (d). We will study the second and third variants (b and c) in more detail. The reason is that (b) is more generic and can be used by designers to provide a kinematic analysis of the construction, and (c) has been chosen for the implementation of the prototype.

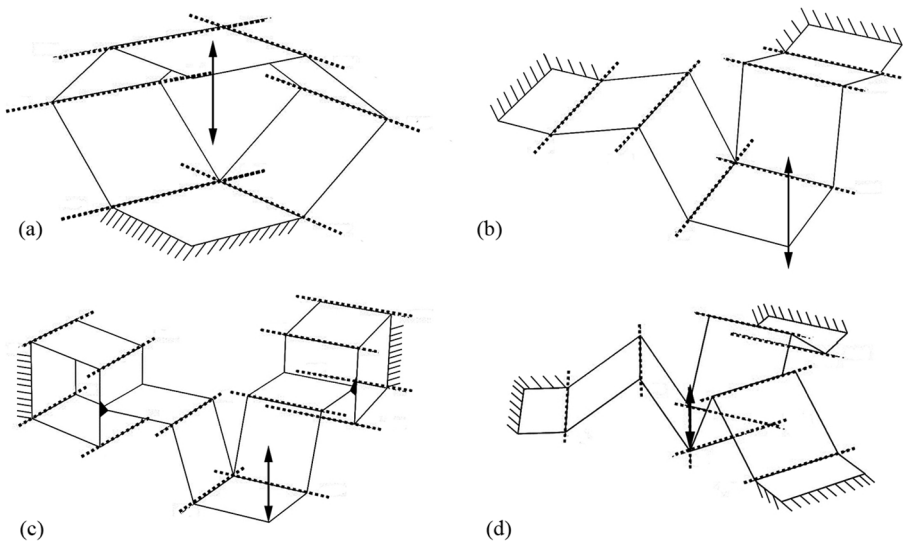


Figure 8.4 The Sarrus linkage can take many possible configurations. (a) and (b) have two arms, each with three pivots, (c) has two arms, each with six pivots and a parallelogram and (d) has three arms, each with three pivots.

Generally, the parameters determining the configuration of a Sarrus linkage are: the number of arms (two or more), the number of pivots per arm (three or more), the angle between the arms (any angle except 180° and 0°) and the

possible presence of a parallelogram along a section of an arm. Also, there can be one arm coming from the top and one from the bottom.

The first and second configurations are equivalent from a kinematic point of view, (b) being the opened-up version of (a). The base is located below in (a) and at the rear in (b). Version (c) is kinematically different from the others because the first segment is replaced by a parallelogram. The advantage of this variant is to maintain the orientation at the second pivot. Forces are also transmitted better as the parallelogram provides significant transverse stiffness. Each kinematic chain consists effectively of four pivots, not three as is the case in other examples. The fourth version is an overconstrained form of (b). It has a ternary geometry, with three arms arranged at 120° from one another. Both (a) and (b) have one overconstraint around the vertical axis, the orientation being imposed by the two kinematic chains. Similarly, (d) has two overconstraints, because any vertical rotation of the output is constrained by three arms. In (c) there are three overconstraints per parallelogram plus one at the output (as in b), so seven in total.

Sarrus kinematic modelling

A kinematic model that gives the angles is developed here. It is based on the lengths of the arms and the initial position of the output. The configuration discussed is (b), it being the most general. In addition, apart from the overconstraints, it is equivalent to (d). Only one of the arms is considered, because all arms behave identically. A vectorial approach is used to establish the model. Figure 8.5a uses the following notation:

- l_1 : length of rod OA
- l_2 : length of rod AP
- d : distance between the base (O) and the path of the output (P)
- s : vertical position of P
- α_1 : angle between the horizontal axis and OA
- α_2 : angle between AP and the perpendicular to OA
- α_3 : angle between the vertical axis and AP

First, we define the position of P:

$$P = \begin{pmatrix} d \\ s \end{pmatrix}. \quad (8.5)$$

As O and P are known, we obtain the position of A by intersecting two circles. We then use formulas (8.6) to (8.8), Figure 8.6 illustrating the notations

used. These formulas give the general expression for the intersection point of two circles C_1 and C_2 centered at (x_1, y_1) and (x_2, y_2) and radii $(r_1$ and $r_2)$:

$$Ix_{12} = \frac{x_1 + x_2}{2} + \frac{(x_1 - x_2)(r_1^2 - r_2^2)}{2d^2} \pm \frac{y_2 - y_1}{2d^2} \sqrt{((r_1 + r_2)^2 - d^2)(d^2 - (r_1 - r_2)^2)} \quad (8.6)$$

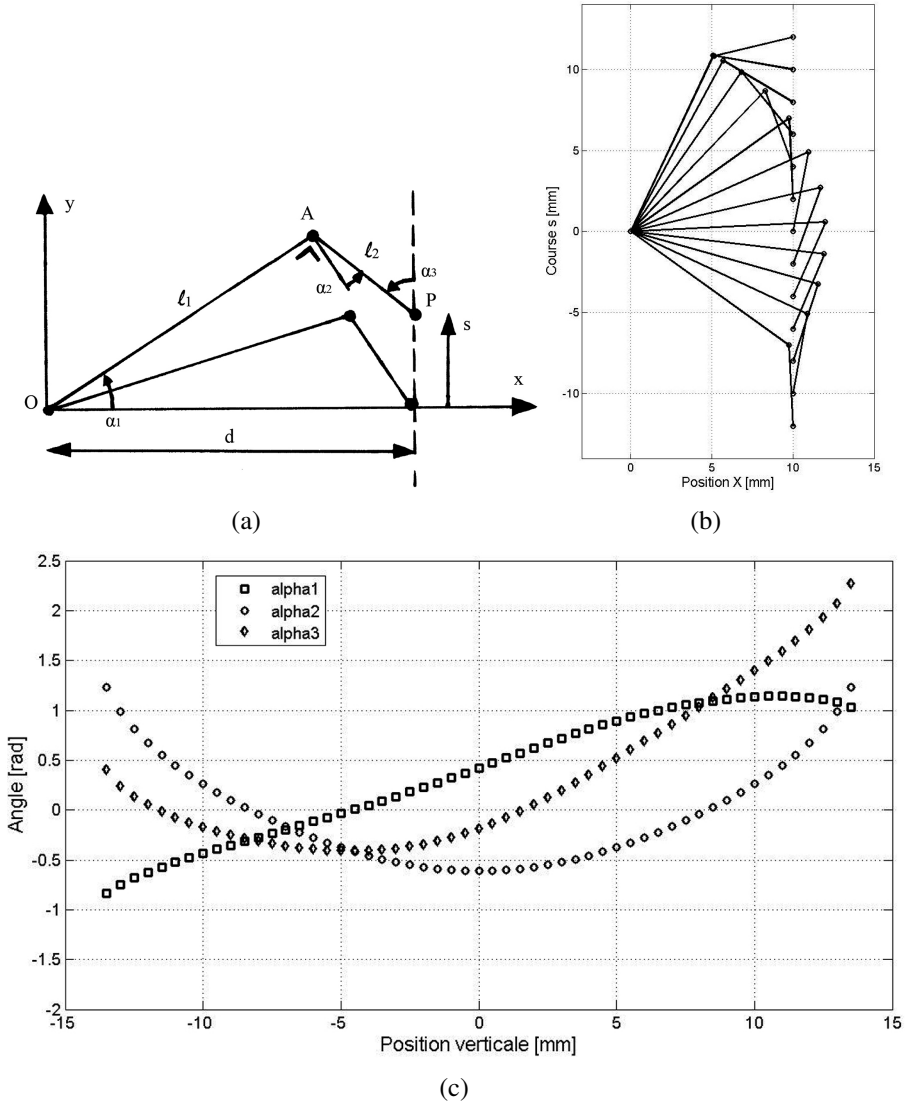


Figure 8.5 Kinematic modelling of the Sarrus linkage. (a) Notation and references used in the model, (b) Positions of Sarrus segments shown for various positions of the vertical output, (c) Angles between the Sarrus segments. The parameters used are $d = 10$ mm, $l_1 = 11$ mm, $l_2 = 5$ mm and the vertical position varies from -12 mm to $+12$ mm.

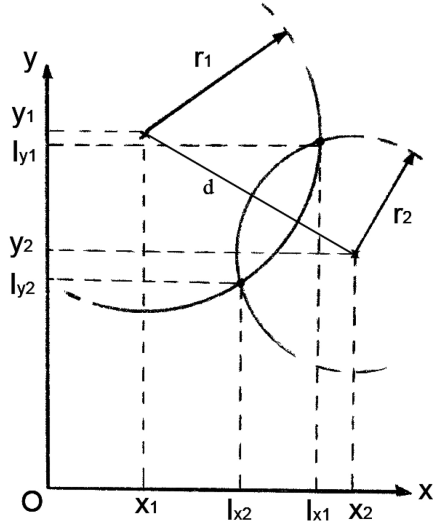


Figure 8.6 Notation used in formulas (8.6)-(8.8). These give the general analytical expression of the intersection of two circles.

$$I_{y12} = \frac{y_1 + y_2}{2} + \frac{(y_1 - y_2)(r_1^2 - r_2^2)}{2d^2} \pm \frac{x_2 - x_1}{2d^2} \sqrt{((r_1 + r_2)^2 - d^2)(d^2 - (r_1 - r_2)^2)} \quad (8.7)$$

where d is the distance between the two circle centers given by:

$$d = \sqrt{(x_2 - x_1)^2 + (y_2 - y_1)^2} \quad (8.8)$$

Finally, the three angles are given by:

$$\alpha_1 = \text{sgn}(A_y) \arccos\left(\frac{A_x}{\|\vec{OA}\|}\right) \quad (8.9)$$

$$\alpha_2 = \frac{\pi}{2} - \arccos\left(\frac{\vec{OA} \cdot \vec{AP}}{\|\vec{OA}\| \|\vec{AP}\|}\right) \quad (8.10)$$

$$\alpha_3 = \text{sgn}(A_x - d) \arccos\left(\frac{P_y - A_y}{\|\vec{AP}\|}\right) + \pi \quad (8.11)$$

Use of parallelograms and preloading of the output

The use of the parallelogram configuration (Fig. 8.4c) reduces the deflection angle at the pivot A. This effect is illustrated in Figures 8.7a and 8.7b. In the case of the Sarrus variants with *simple arms* (Fig. 8.4a, 8.4b and 8.4d), the

angles of the first and second segments are cumulative. On the other hand, the output of the parallelogram remains vertical along the stroke of the mechanism and the angle made with the terminal part is not added to the angle of the *parallelogram arm*. The force exerted on the output by the flexure of this pivot remains small. Furthermore, the torque generated at the pivot O is not transmitted to the output in the variant with parallelograms. These factors mean that the output straightness is better when a mechanism with parallelograms is used. The situation can be summarise, using the symbols I and II for the *simple arm* and the *parallelogram arm* Sarrus linkages respectively, together with the notation of Figures 8.7a and 8.7b:

$$\Delta\alpha^I > \Delta\alpha^{II} \quad (8.12)$$

$$\alpha_d^I + \alpha_u^I > \alpha_0^{II} + \alpha_u^{II}. \quad (8.13)$$

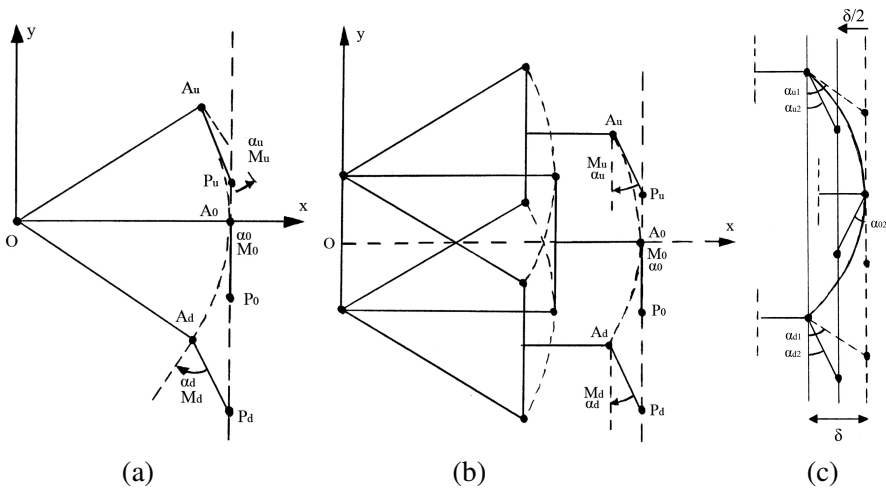


Figure 8.7 (a) Schematic of the simple arms Sarrus. (b) Schematic of the parallelogram arms Sarrus. On the parallelogram Sarrus, the angle variation of the pivot A is much lower than on the simple arms Sarrus. The efforts transmitted on the output are also reduced. (c) Pretension of the output lead also to a reduction of the maximal angle of deflection over pivot A.

Another factor helps to reduce the angular deflection at the pivot A. As the parallelogram output displays a pseudocircular movement (δ), a shift of the point P of magnitude $\delta/2$ toward the rear of the parallelogram preloads the output and limits the maximum amplitude of flexure. Figure 8.7c illustrates this effect. The figure does not represent the parallelogram; only its output is shown. The angles of rotation are thus reduced. Instead of transmitting a major

force at the ends and none at the center of the stroke, the effect of preloading the output is to halve the parasitic displacement. This also results in forces of the same magnitude being transmitted in the middle and at the end of the stroke. Somewhere in-between, no force is transmitted, because the angle is null. The maximum deflection angle is divided approximately by a factor of two, as is the flexure torque. We can describe this by:

$$\max(|\alpha_{u1}|, |\alpha_{d1}|) \simeq \frac{1}{2} \max(|\alpha_{u2}|, |\alpha_{o2}|, |\alpha_{d2}|). \quad (8.14)$$

8.3.2 Realisation of a Sarrus prototype

The kinematics chosen here is the Sarrus linkage with parallelograms as introduced above. The output is connected to a first parallelogram by a part with cross leaf springs and to a second parallelogram by a part with single leaf springs. Thus only one of the two connecting parts has cross leaf springs. The reason of doing so is to block rotation of the output around the vertical axis. If both outputs had cross leaf springs, it would introduce an additional overconstraint. In Figure 8.8, a CAD view shows the parallelograms and the output parts. One has single leaf springs and is fixed to the cross leaf springs part. This way of connecting the outputs together enables the force to be taken up efficiently and the torque effect limited.

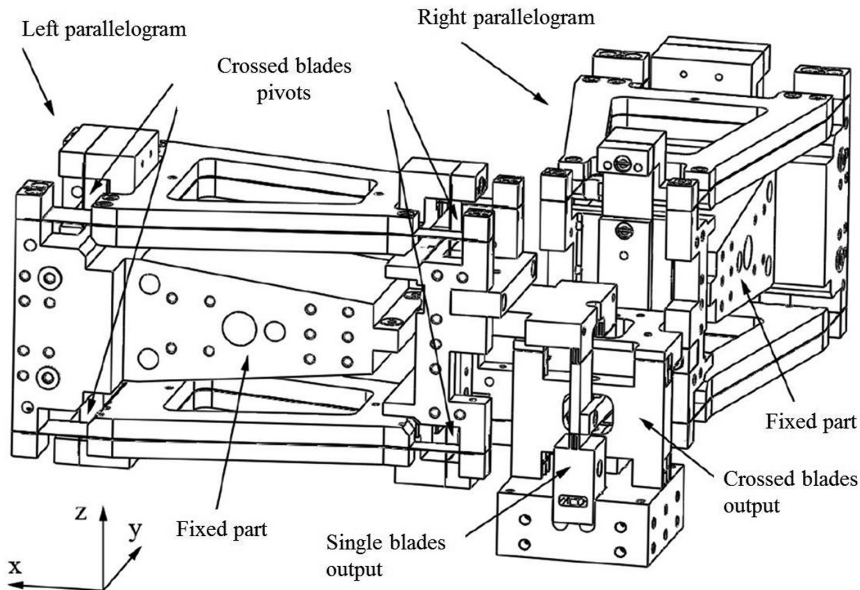


Figure 8.8 CAD view of the Sarrus prototype. The overall dimensions are 290 mm × 290 mm × 150 mm. Two parallelograms are linked to the output parts, one with cross leaf springs, one with single leaf springs.

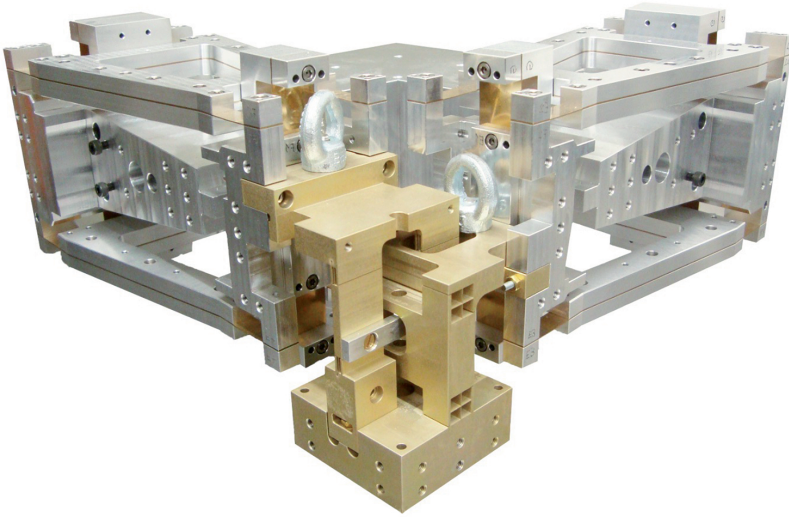


Figure 8.9 Photograph of the Sarrus prototype. The parallelograms are assembled with CuBe2 leaf springs sandwiched between aluminium plates and the output parts are electroeroded in solid aluminium.

The two parallelogram arms are identical, but one of them is upside down. The leaf springs of the parallelograms are made of CuBe2 with a thickness of $350\text{ }\mu\text{m}$, while the leaf springs are eroded in the output part in aluminium 7022 and have a thickness of $160\text{ }\mu\text{m}$. It can be seen that for a better alignment of the pivots, the leaf springs of the parallelograms run all the way through the aluminium segments. The actuation is at the upper part of the output, as shown in the photograph (Fig. 8.9).

8.3.3 Straightness measurement

Straightness measurement is performed by moving the linkage vertically and measuring the lateral positions of the output part by laser interferometry. The measurement is repeated 10 times for both lateral axes. Each measurement is for both the advance and retract movements. A point is recorded every 1 mm along the z -axis, over a length of more than 30 mm. The curves in Figure 8.10 show the straightness errors averaged over the ten measurements. It should be noted that the beam of the interferometer is reflected by a mirror, which must be aligned with the translational movement.

On the x -axis, a straightness error was measured with an amplitude of $\pm 102\text{ nm}$ over a stroke of 35 mm. The difference in measurement readings between the advance and retract movements display a standard deviation of 1.4 nm, while over the 10 measurements there is an average standard deviation of 3.9 nm.

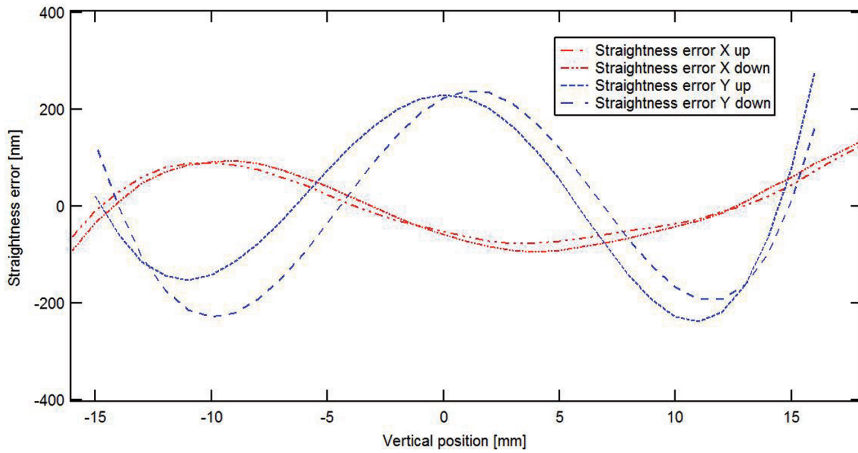


Figure 8.10 Straightness error of the Sarrus linkage. The measurement is averaged over ten advance and retract movements.

On the y-axis, the error amplitude is ± 257 nm, measured over 31 mm. The difference between advance and retract has a standard deviation of 72 nm, which is mainly due to a relatively large hysteresis. Over the 10 measurements there is an average standard deviation of 3.1 nm.

8.4 13-hinge stage mechanism

8.4.1 13-hinge stage kinematics

General considerations

The mechanism of the 13-hinge stage was proposed by Jones in 1962 (Jones, 1962) and then developed by Katoh in 1984 (Katoh et al., 1984). It is also referred to in the literature as the *slaved compound rectilinear spring* (Smith, 2003). It is composed of two parallelograms (OBFO' and JEGH in Fig. 8.11a) arranged in series head-to-toe. A lever (CD) is used to ensure that the movement of the first parallelogram is half that of the second. Thus, the parasitic movements of the two parallelograms cancel each other out and the resulting lateral movement of the output is theoretically zero. Two connecting rods (DP and AB) attach the lever to the parallelograms. Traditionally, these two rods have been considered as having dimensions such that the front rod (length c) has twice the length b of the rear rod, so that $c/b = 2$. In this section, it is shown that on the contrary a length ratio of $c/b = 1/2$ is optimum and leads to a decrease in the straightness error of 3 to 4 orders of magnitude.

This mechanism has some advantages, such as high straightness and a conserved orientation of the output. It can also be constructed to ensure a

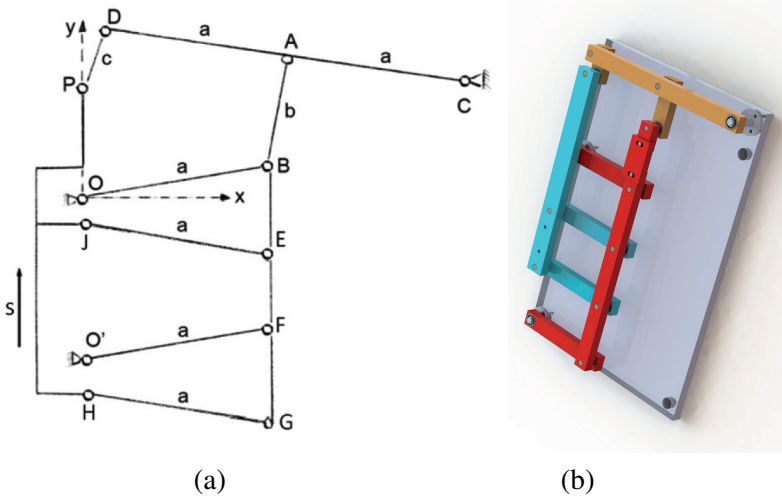


Figure 8.11 (a) Schematic of the 13-hinge stage kinematic linkage in the upper position. Only twelve pivots appear because the point B is a double pivot linked to three rods, (b) CAD view of a 13-hinge stage demonstrator. The movements of the two parallelograms (red and blue) are synchronised by the lever (yellow).

high lateral stiffness and can be produced almost entirely by wire EDM, thus achieving good dimensional tolerances.

13-Hinge kinematic modelling

The following analysis is based on the notation of Figure 8.11a. Lowercase letters indicate the lengths of geometric segments and capital letters refer to geometric points. We set the length of the lever ($2a$) at twice the length of the parallelogram arms (a). The rod (AB) connecting the lever and the intermediate stage has a length b . The link (DP) between the lever and the output has a length c . We introduce the ratio of these two lengths as $R_{slav} = \frac{c}{b}$ (slaving ratio). The fixed parts are the points O, O' and C. The reference point is centred at O and the vertical position of the output is s .

The method used to determine the straightness error of the mechanism is as follows: as the vertical position of point B affects the straightness error, we begin with the position P to determine the position of D by the intersection of two circles. The first circle is centred at P, of radius c , and the second is centred at C, of radius $2a$. Point A is then easily found, as it is the middle position between C and D. Position B is then determined by the intersection of two circles again. These are now centred at A, of radius b , and at O, of radius a . The last step is then to find the relationship between the vertical component of point B and the lateral straightness error. The positions of points C and P are

given as follows:

$$\vec{C} = \begin{pmatrix} 2a \\ b \end{pmatrix} \quad (8.15)$$

$$\vec{P} = \begin{pmatrix} 0 \\ b - c + s \end{pmatrix}. \quad (8.16)$$

It is assumed that the point P is located on the y -axis. In reality, the straightness error should be introduced here as a horizontal component of the point P. The straightness error function would be recursive. However, as it is small, we consider it as zero, at this point. In addition, a numerical study shows that this assumption does not affect the quality of the analysis. Now we refer to the formulas (8.6)-(8.8) introduced above and using the notation of Figure 8.6. These equations provide the general expression for the intersection of two circles C_1 and C_2 centred at point (x_1, y_1) and (x_2, y_2) and having radii r_1 and r_2 . The point D is found using the parameters:

$$\vec{x}_1 = \vec{OP} \quad (8.17)$$

$$r_1 = c \quad (8.18)$$

$$\vec{x}_2 = \vec{OC} \quad (8.19)$$

$$r_2 = 2a. \quad (8.20)$$

Then, the position of the point A, the middle point of the lever, is calculated from:

$$\vec{OA} = \frac{\vec{OC} + \vec{OD}}{2}. \quad (8.21)$$

The critical position that determines the output straightness error is the vertical component of the point B, namely B_y . The position of B is given again by the formulas (8.6) to (8.8), using the parameters:

$$\vec{x}_1 = \vec{OA} \quad (8.22)$$

$$r_1 = b \quad (8.23)$$

$$\vec{x}_2 = \vec{OD} = \begin{pmatrix} 0 \\ 0 \end{pmatrix} \quad (8.24)$$

$$r_2 = a. \quad (8.25)$$

B_y determines the slaving ratio, thus the displacement between the intermediate stage and the output stage, which should ideally be the half of s . At this point, we want to know how the slaving ratio influences the output straightness

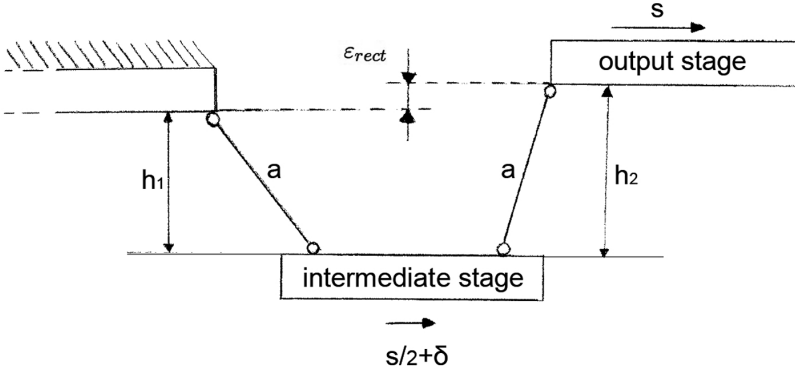


Figure 8.12 Impact of the *slaving ratio* error δ on the straightness error ϵ_{rect} .

error. Figure 8.12 shows the lengths to consider to highlight this impact. The straightness error is expressed as:

$$\epsilon_{rect} = h_2 - h_1 = \sqrt{a^2 - \left(\frac{s}{2} - \delta\right)^2} - \sqrt{a^2 - \left(\frac{s}{2} + \delta\right)^2}. \quad (8.26)$$

The following assumption is made:

$$\delta^2 \approx 0. \quad (8.27)$$

Doing so, we obtain the simplified formula:

$$\epsilon_{rect} = \sqrt{a^2 - \frac{s^2}{4} - s\delta} - \sqrt{a^2 - \frac{s^2}{4} + s\delta} \quad (8.28)$$

with the slaving ratio error being:

$$\delta = B_y - \frac{s}{2}. \quad (8.29)$$

Expression for straightness

In this section, we show the graphical representation of the error function and interpret it to understand how the 13-hinge mechanism behaves as a function of the lengths of the rods. Figure 8.13 presents the function computed with the following parameters:

$$a = 200 \text{ mm} \quad (8.30)$$

$$b = 70 \text{ mm} \quad (8.31)$$

The graph shows that the straightness error as an ‘S’ shape along the axis of displacement. When $R_{slav} < 1/2$, a negative stroke results in a negative error and

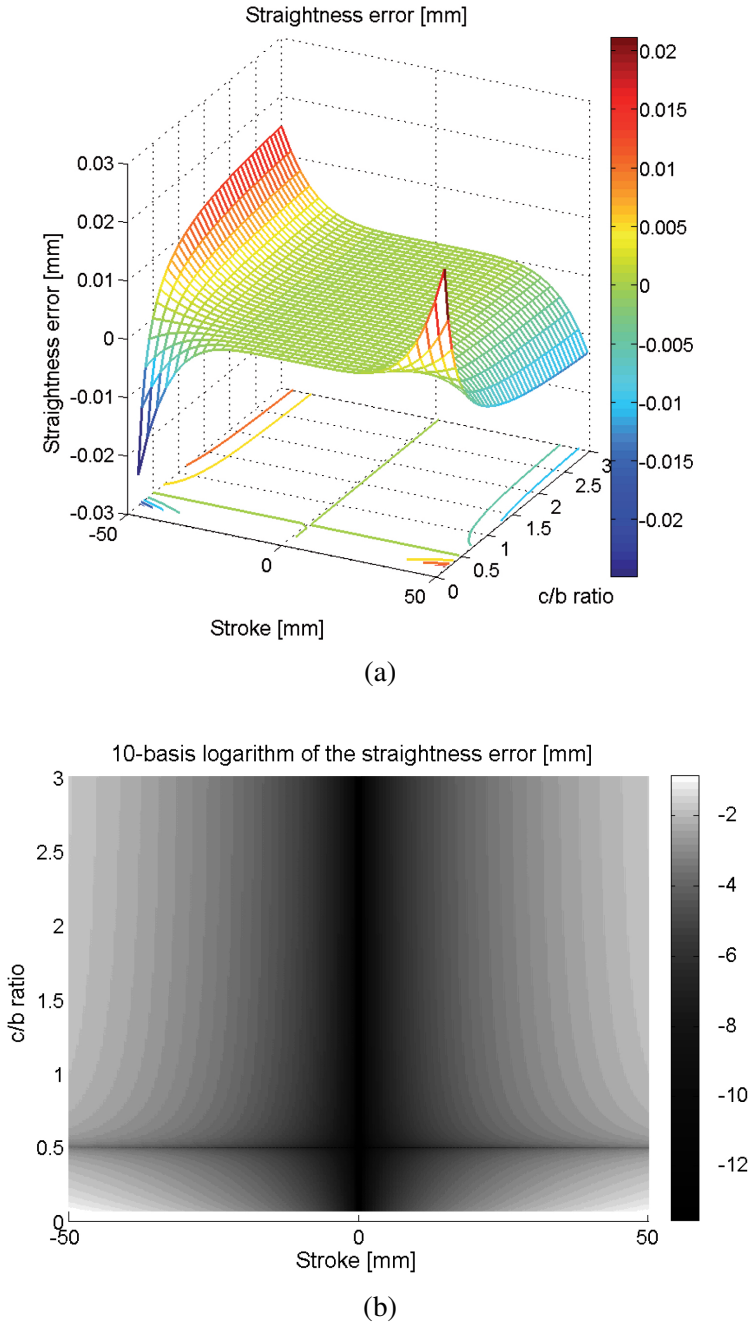


Figure 8.13 (a) Straightness error of the 13-hinge stage with the parameters $a = 200$ mm and $b = 70$ mm. The straightness error has an ‘S’-shaped profile along the stroke. (b) Logarithmic value of the straightness error. It reveals a horizontal dark line corresponding to the optimal ratio of the length b and c . Along this line, the theoretical straightness error is 10^3 to 10^4 times lower compared to other ratios values.

a positive stroke results in a positive error, but when $R_{slav} > 1/2$, the situation is reversed. For $R_{slav} = 1/2$, the straightness error is very low and remains positive for both positive and negative displacements, see Figure 8.13. This illustration gives a clear idea of the situation with the logarithmic value of the straightness error. The horizontal black line around $R_{slav} = c/b = 1/2$ indicates a straightness error of 3 to 4 orders of magnitude smaller than the errors in the other areas ($R_{slav} \neq 1/2$). The vertical black line indicates a zero straightness error at a zero stroke, whatever is the slaving ratio, which is to be understood as a trivial condition.

Figure 8.14 is a graph of straightness error for a mechanism with a maximum outer dimension of 400 mm and lengths b and c in the optimum ratio $R_{slav} = 1/2$. The straightness error remains smaller than 100 pm over the whole stroke.

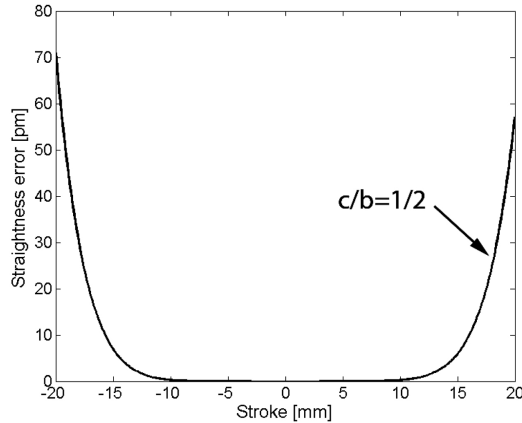
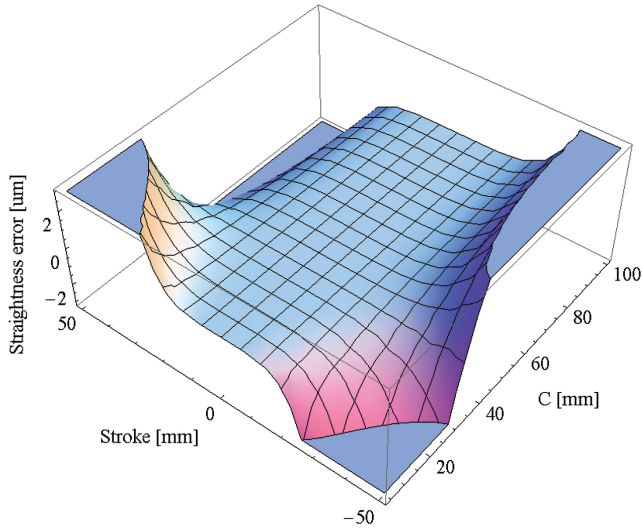


Figure 8.14 Theoretical straightness error function computed for a 400 mm mechanism. The lever linkages lengths used here are optimum ($c/b = 1/2$).

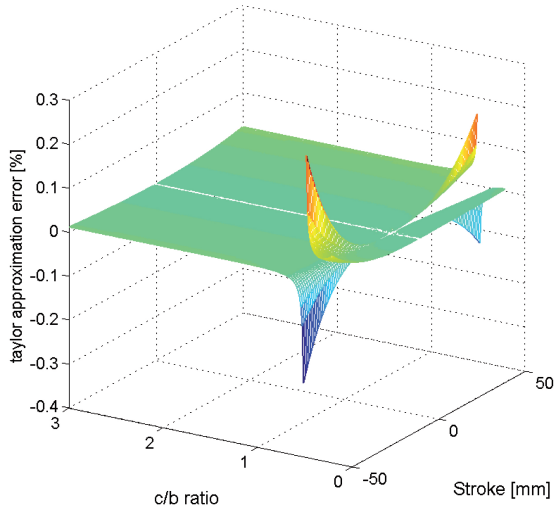
The model developed in this chapter assumes that the rods OB, DA and AC all have the same length a . A possible improvement of the model is the introduction of a different length for each segment and thus the establishment of a more general expression for the straightness error. Another optimisation criterion could be the space required for construction of the mechanism. However, from a practical point of view, further optimising the theoretical correctness would not really make sense, because the most significant part of the straightness error does not come from the kinematics, but from other effects such as thermal expansion, gravity, pivots not being punctiform and manufacturing aspects. The expression of straightness error calculated as a mathematical function has a long and complex formulation, so it is not given here, only its graphical representation being shown. A Taylor series is calculated for the four variables

a , b , c and s to the fifth order around zero, for each variable:

$$\epsilon_{rect}(a, b, c, s) \approx \frac{(b - 2c)s^5}{64a^3bc}. \quad (8.32)$$



(b)



(b)

Figure 8.15 (a) Taylor approximation of the exact function of the straightness error. (b) Relative error of the approximate function compared to the exact expression. The maximum error is 0.3 %.

As shown in Figure 8.15b, the difference between the approximate function and the exact function does not exceed 0.3%. However, asymptotes can be seen around the line where $c/b = 1/2$, because both the dividend and divisor are close to zero. In fact, one of them is exactly zero. The simplified function calculated by the Taylor approximation to the 5th order for the four variables can also be formulated in that way:

$$\epsilon_{rect}(a, b, c, s) \approx \frac{s^5}{64a^3} \left(\frac{1}{c} - \frac{2}{b} \right). \quad (8.33)$$

The formulation of equation (8.33) gives a good understanding of how the function behaves. It is axisymmetric along the axis defined by $s = 0$. This expression is doubly helpful. First, it is easy to use it practically, thanks to its simple formulation, and its sufficient exactness ensures its reliable use. Second, it is now very easy to demonstrate that the slaving ratio is optimum for the value $R_{slav} = 1/2$. When this value is used, the error function is effectively zero:

$$\frac{c}{b} = \frac{1}{2} \Rightarrow \epsilon_{rect}(a, b, c, s) \approx 0. \quad (8.34)$$

8.4.2 Realisation of a 13-Hinge stage prototype

The structure that has been developed is made from a monolithic block of aluminium whose initial size was 450 mm × 350 mm × 140 mm. It was first machined, then the flexure hinges were cut out by wire EDM. The parallelogram

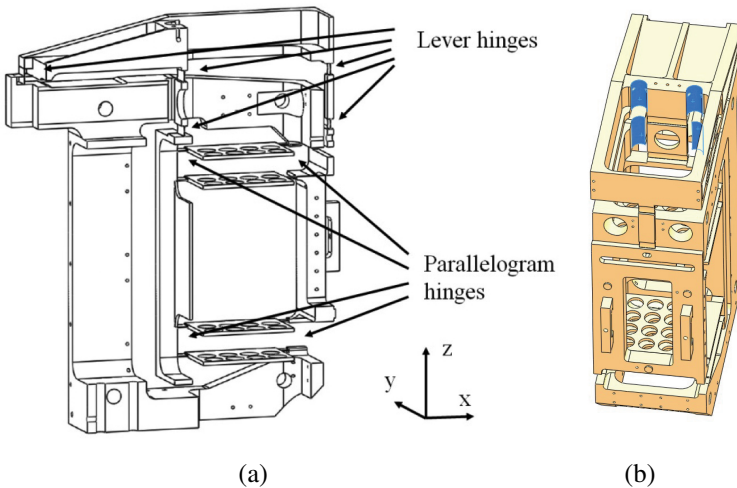


Figure 8.16 (a) Cutaway view of the 13-hinge stage, (b) The two circular notches milled from the top to ‘liberate’ the central connecting rod are shown in blue.

hinges (cutaway view of Fig. 8.16a) are $155\text{ }\mu\text{m}$ thick and the lever hinges are $180\text{ }\mu\text{m}$ thick. The left lever hinge is a cross leaf springs pivot, to avoid an internal degree of freedom that would have resulted in a horizontal advance and retract movement of the lever.

One of the difficulties lay in machining the central slaving hinges, as they are confined within the top of the chassis. An opening was milled from the rear and two circular notches were milled from the top (Fig. 8.16b) to liberate the central connecting rod from the solid aluminium.

The main rear release of the intermediate stage was performed to reduce its central thickness to 3 mm, while maintaining a thickness of 20 mm on its periphery. This reduces the weight, but retains some rigidity. The upper opening was machined to access the parallelogram arms in order to drill the weight-reducing holes.

The slaving lever is also hollow to reduce its weight. After machining, this part was chemically treated by immersion in an electroplating bath to improve its structural stability and resistance to cracking and corrosion. This process gave the yellowish color to the piece. A photograph of the final part is shown in Figure 8.17.

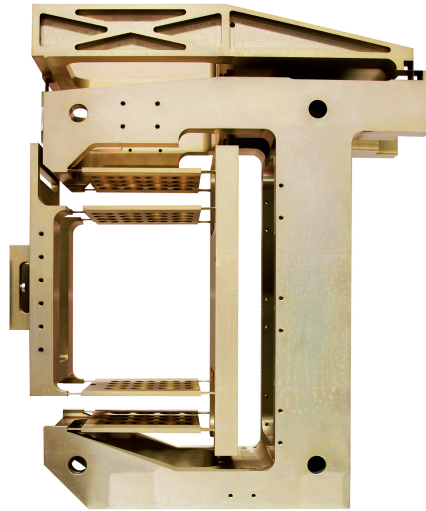


Figure 8.17 Photograph of the 13-hinge stage prototype. The outer dimensions are $450\text{ mm} \times 350\text{ mm} \times 140\text{ mm}$. The piece was machined and then electroeroded.

8.4.3 Straightness measurement

The lateral straightness error is measured by vertical displacement of the stage, while a 0.1 nm resolution laser interferometer records the lateral position of the output. Figure 8.18 shows the head of the interferometer used for the

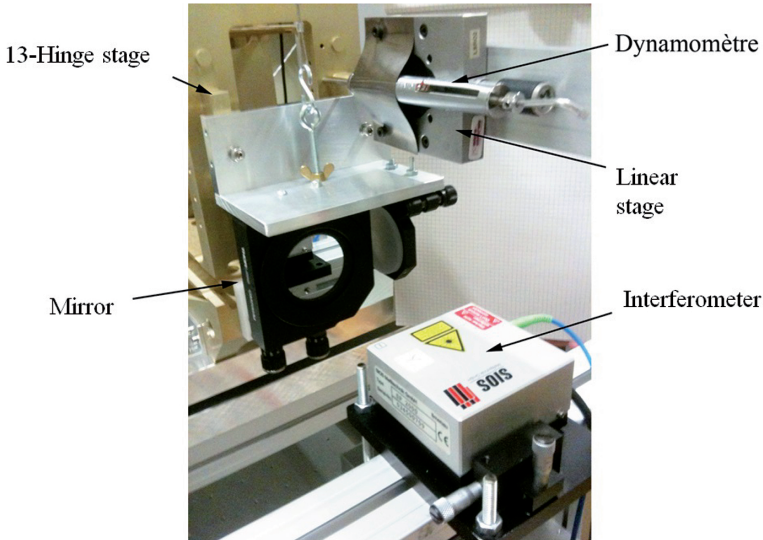


Figure 8.18 Set-up used to characterise the straightness and the stiffness of the 13-hinge stage.

measurement and the mirror mounted on the moving part of the stage. The mirror has a diameter of 2 inches. It is large enough to measure the stroke of 40 mm and its flatness is specified to be less than 30 nm over the entire surface. The x -axis is measured on the image. A dynamometer is used to measure the stiffness of the guide. It is removed when measuring straightness. The measurement is repeated 20 times on each of the two axes. Each measurement represents an advance and retract movement. A point is recorded every 200 microns along the z -axis, over a little less than 40 mm.

The two curves of Figure 8.19 show the straightness error measured on the two axes perpendicular to the direction of motion, averaged over all the measurements. Along the x -axis, a peak-to-peak amplitude of the straightness error ± 93 nm is measured over a stroke of 35 mm. The standard deviation between the advance and retract positions is 8.3 nm. Over the 20 measurements there is an average standard deviation of 40.2 nm.

Along the y -axis, the maximum straightness error is ± 19.6 nm, measured over a stroke of 38 mm. The difference between advance and retract has a standard deviation of 4.8 nm. Over all the measurements there is an average standard deviation of 18.0 nm.

To improve measurement quality, it is preferable to perform it at night to avoid any daytime disturbances. It is also advisable to have a tube around the laser beam of the interferometer to preclude air movements that disturb

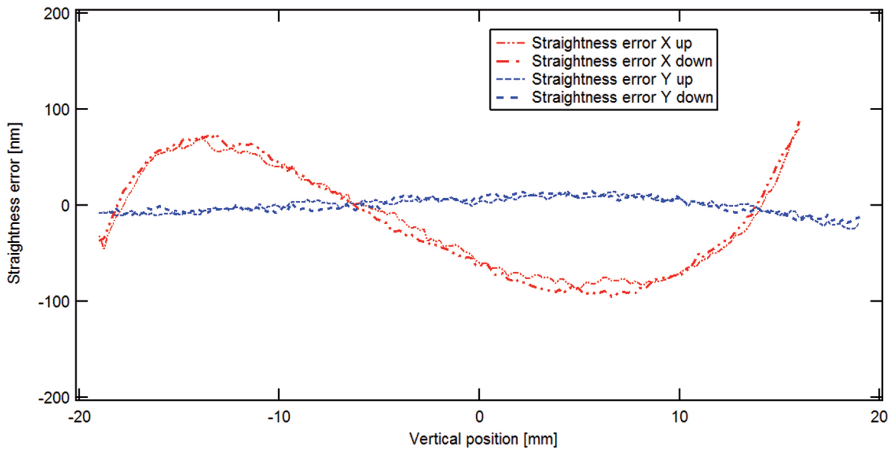


Figure 8.19 Straightness error measured on the 13-hinge stage. The measurement is averaged over 20 advance and retract movements. A hysteresis of less than 10 nm is measured on both axes.

the measurement. The head of the interferometer should therefore be as close as possible to the mirror, in order to minimise the distance traveled by the laser beam in air. It is also important to minimise the length of the structure connecting the interferometer head and the mirror, in order to minimise the effects of thermal expansion and vibration. This structure also has to be rigid, to reduce vibration problems. In addition, when the stiffness of the stage is measured, it is necessary to fasten the measuring device to a structure other than that which holds the dynamometer. Otherwise, the compliance of the holding structure will be added to that of the stage.

8.5 Analysis and comparison

A comparison has been made between the two mechanisms developed. The criteria applied for this comparison are listed and explained. They relate to kinematics, manufacture and measurement.

8.5.1 Comparison criteria

Criteria related to the kinematics:

Theoretical straightness: This is an essential characteristic for our application.

In the case of the Sarrus linkage, the straightness is perfect, while in the case of the 13-hinge stage, it is pseudolinear. However the straightness ratio is excellent.

Conservative orientation: We want a solid body – not just a point – moving without any coupled rotation. On a kinematic level, both guides have zero theoretical rotation of the mechanism output.

Angular stroke: This determines whether the mechanism is suitable for manufacture by EDM. Both guides are relatively well adapted. They reach the desired stroke with reasonable angles ($< 8^\circ$) at the flexure joints.

Stroke-to-size ratio: This relates to the compactness of the mechanism. It is 10% for the 13-hinge stage and 15% for the Sarrus linkage, for a 6° maximum rotation of the pivots.

Overconstraints: Risk of introducing stiff points or bistable behaviour with associated hysteresis. The Sarrus linkage has 7 overconstraints and the 13-hinge stage has 12 overconstraints.

Ease of modeling: This is not a very important factor, except for optimising the guide. The Sarrus linkage is easier to model than the 13-hinge stage, due to its symmetry and perfectly straight output motion. Only one arm needs to be modelled, as both arms behave in the same way.

Criteria related to the manufacture of prototypes:

Ease of implementation: The ease of implementation depends on the complexity of the mechanism. As the kinematics of the 13-hinge stage is planar, it is easier to machine. The use of the EDM process also gives a wider choice of possible designs for the joints.

Compactness: The Sarrus linkage design is more compact than the 13-hinge stage. This is partly due to the machining method. Hinges produced by EDM have angular strokes that are generally lower than those of leaf springs used in mechanisms that are assembled. The outer dimensions of the Sarrus linkage are $270\text{ mm} \times 270\text{ mm} \times 150\text{ mm}$ and the 13-hinge stage has outer dimensions of $140\text{ mm} \times 350\text{ mm} \times 450\text{ mm}$.

Cost: The cost of the conventional machining used to produce the Sarrus linkage is lower than that of the EDM process. The 13-hinge stage therefore costs more due to the expense of EDM.

Perfectibility: By this we mean two things. The performance of the Sarrus linkage can be improved, because its parts are assembled. We are able to disassemble it and change some parts. On the other hand, the 13-hinge stage was not manufactured in accordance with the optimum design presented in the previous section. Improved kinematics can be adopted for a possible future version.

Stiff points: The presence of stiff points can greatly affect the straightness of the guide. Neither of the guides displays stiff points. The Sarrus linkage has a bar connecting the two arms of the single leaf springs

output (Fig. 8.8, connecting bar). When this bar is removed, the guide has a stiff point with bistable behaviour.

FEA simulations: FEA simulations of the two guides are quite complex during the meshing part of the process. Thin flexure pivots require a high number of elements, even more if the joints are leaf springs rather than hinges, as these have a more slender profile.

Suitability for the EDM process: As seen above, EDM offers undeniable advantages. The kinematics of the 13-hinge stage is planar in nature. It is therefore well suited to EDM. The flexure joints of the Sarrus linkage can be produced entirely by EDM but a monolithic approach is hardly possible. However, conventional premachining is required in all cases.

Accessibility: An important aspect for the integration of the guide in the dedicated application. The 13-hinge stage offers good accessibility. The Sarrus linkage also has fairly good accessibility, although the overconstrained configuration of this linkage (introduced in Sect. 8.3) offers less accessibility.

Criteria related to the measurements:

Straightness: This is the characteristic most desired for the prototypes. The assessment of the straightness is good for both guides. However, the 13-hinge stage is best by a factor of about 3. The magnitude of the error reaches 180 nm and 40 nm on the two lateral axes. It is 500 nm and 200 nm in the case of the Sarrus linkage. The stroke in both cases is about 35 mm.

Angular attitude: We want this to remain constant. The Sarrus linkage has a variation in attitude of $270 \mu\text{rad}$ and $230 \mu\text{rad}$ on its two lateral axes, while the angular error is only 9 and $5 \mu\text{rad}$ for the 13-hinge stage.

Stiffness: This is an attribute desired for any precision mechanism. A high rigidity enables it to withstand the influence of external disturbances, such as a lateral component of the driving force. The eigenfrequency increases with the stiffness for a given moving mass. The transverse stiffnesses measured on both guides are of the same order of magnitude. We have for the Sarrus linkage $K_{mesx} = 0.17 \text{ N}/\mu\text{m}$ and $K_{mesy} = 0.25 \text{ N}/\mu\text{m}$ and for the 13-hinge stage $K_{mesx} = 0.26 \text{ N}/\mu\text{m}$ and $K_{mesy} = 0.4 \text{ N}/\mu\text{m}$. The natural stiffness of the Sarrus linkage is $K_{mesz} = 551.2 \text{ N/m}$, while that of the 13-hinge stage is lower : $K_{mesy} = 43 \text{ N/m}$.

Eigenfrequencies: The eigenfrequencies measured on the prototypes are higher on the Sarrus linkage. The lowest transverse frequency of the 13-hinge stage is 72.5 Hz and that of the Sarrus linkage 160 Hz.

Hysteresis: Mainly detected on the y-axis of the Sarrus linkage. Its amplitude is about 70 nm.

Repeatability: This is important in positioning accuracy. It depends largely on the quality of measurement. It can be influenced by changes in temperature. In addition, the length of the mechanical loop between the measurement device and the output guide affects the accuracy of the measurement. The average repeatability is about 16 nm for the 13-hinge stage and 12 nm for the Sarrus linkage.

8.5.2 Comparison chart

Table 8.2 shows the scores obtained by the two mechanisms for the previously defined criteria.

8.5.3 Performances table

Table 8.3 (p. 222) summarises the performances and measured values for both guiding systems.

8.6 Application to the watt balance

8.6.1 Description of the project

The two guiding systems are part of the watt balance project. The purpose of this experiment is to realise a measurement of the kilogram by an alternative approach and provide a new definition for the unit mass of the International System of Units. Currently, several approaches are being considered in the field of metrology to achieve this goal. The International Committee for Weights and Measures (CIPM) plans to respond in 2016 to the question of what new approach should be considered to define the kilogram. The watt balance experiment has the goal of linking the kilogram to a fundamental physical constant, the Planck constant h . This relationship involves the comparison of a mechanical power (product of the weight of a mass and a speed) and an electrical power (product of a voltage and of an induced current).

The experiment is conducted in two phases: the static phase and the dynamic phase (Fig. 8.20). During the static phase, the weight of a test mass is compensated by the Lorentz force produced by an electric coil of length l , situated in a magnetic field of induction B carrying a current I . The characteristic equation of this phase is:

$$I \int \vec{B} dl = mg. \quad (8.35)$$

During the dynamic phase, the value of the integral parameter $\int \vec{B} dl$ is measured. It is characteristic of the coil and magnetic field couple. The measurement is made by means of the voltage induced across the coil while

Table 8.2 Comparison of the two guiding systems. Criteria regarding kinematics, manufacture and measured performances are assessed and weighted. For every criterion a rating between 1 and 3 is given. The total number of points gives an indication of the overall performance of the guides.

Sarrus linkage				13-hinge stage	
Criterion	Weighting	Rating	Value	Rating	Value
Kinematic					
Theoretical straightness	10	***	30	**	20
Conservation of orientation	9	***	27	***	27
Angular stroke	5	**	10	**	10
Stroke-to-size ratio	5	***	15	**	10
Overconstraints	6	**	12	*	6
Ease of modeling	3	**	6	*	3
Manufacture					
Ease of manufacture	6	*	6	**	12
Compactness	6	***	18	**	12
Cost	5	**	10	*	5
Perfectibility	5	**	10	*	5
Stiff points	8	**	16	***	24
Simulations	6	*	6	*	6
Suitability for EDM process	6	**	12	***	18
Accessibility	8	**	16	***	24
Measurements					
Straightness	10	**	20	***	30
Angular attitude	9	*	9	***	27
Stiffness	7	*	7	**	14
Eigenfrequencies	7	***	21	**	14
Hysteresis	9	**	18	***	27
Repeatability	8	**	16	**	16
Total			285	310	

Table 8.3 Summary of the measured values for both guiding systems.

Sarrus guide									
13-hinge stage									
Translation			Rotation			Translation			Rotation
Axis	X	Y	Z	θ_x	θ_y	X	Y	Z	θ_x θ_y
Measured length	35 mm	31 mm	-	36 mm	36 mm	35 mm	38 mm	-	32 mm 32 mm
Measurement step	1 mm	1 mm	-	1 mm	1 mm	200 μm	200 μm	-	200 μm 200 μm
Advance and retract	yes	yes	-	yes	yes	yes	yes	-	yes yes
Number of measurements	10	10	-	5	5	20	20	-	12 12
Error amplitude	205 nm	514 nm	-	268 μrad	228 μrad	183.4 nm	39.2 nm	-	8.76 μrad 5.29 μrad
Straightness ratio	$1.71 \cdot 10^5$	$6.03 \cdot 10^4$	-	-	-	$1.91 \cdot 10^5$	$9.74 \cdot 10^5$	-	-
Hysteresis	1.4 nm	72 nm	-	0.38 μrad	0.19 μrad	8.3 nm	4.8 nm	-	0.37 μrad 0.39 μrad
Reproducibility	3.9 nm	3.1 nm	-	0.71 μrad	0.29 μrad	40.2 nm	18.0 nm	-	3.18 μrad 0.46 μrad
Simulated stiffness	0.56	0.59	625 N/m	-	-	2.86	1.5 N/ μm	53.4 N/m	-
	N/ μm	N/ μm				N/ μm			
Measured stiffness	0.17	0.25	551 N/m	-	-	1.73	0.67	43 N/m	-
	N/ μm	N/ μm				N/ μm	N/ μm		
Ratio K_{sim}/K_{meas}	3.29	2.36	1.13	-	-	1.65	2.24	1.24	-
Simulated eigenfrequencies	137 Hz	137 Hz	2 Hz	-	-	332 Hz	87 Hz	0.61 Hz	-
Measured eigenfrequencies	160 Hz	170 Hz	3.42 Hz	-	-	342 Hz	72 Hz	0.6 Hz	-
Ratio f_{sim}/f_{meas}	0.86	0.81	1.71	-	-	0.97	1.21	1.02	-

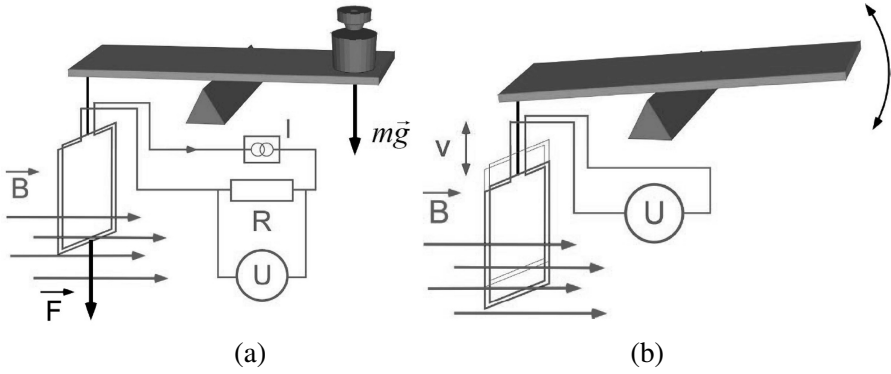


Figure 8.20 Schematic of a watt balance, (a) The weight of a test mass is counterbalanced by the electromagnetic force produced by a current flowing through a coil situated in a magnetic field (static mode). (b) An induced voltage is measured across the coil when it is moved vertically through the magnetic field (dynamic mode) (Eichenberger et al., 2011).

the latter is moved vertically at velocity v in the magnetic field. The induced voltage has the following expression

$$U = v \int \vec{B} dl. \quad (8.36)$$

This approach is necessary to know the value of $\int \vec{B} dl$ with a relative accuracy of 10^{-8} . Characterisation by direct measurement of the magnetic field and the length of the coil would not provide a relative accuracy better than 10^{-4} , which is insufficient. When equations (8.35) and (8.36) are combined by eliminating the electromagnetic parameter $\int \vec{B} dl$, we obtain the following relationship:

$$mgv = UI. \quad (8.37)$$

The equality of the electrical and mechanical power appears then clear. We talk about virtual power, because the terms of the products are not measured during the same phase of the experiment. In addition, a precise measurement of the electrical resistance is done using the quantum Hall effect (Von Klitzing, 1986):

$$R_h = \frac{h}{ie^2} \quad (8.38)$$

where i is an integer, e the electrical elementary charge and h the Planck constant. The induced voltage is also measured accurately with a Josephson network using the effect of the same name (Kajastie et al., 2009):

$$U_j = \frac{nf_j h}{2e} \quad (8.39)$$

where n is an integer, f_j the Josephson frequency. In practice, the current measurement is done using the two effects simultaneously, and a binary Josephson junction network is used to provide a very precise voltage, selected for example between ± 1.18 V in steps of $144 \mu\text{V}$ (Genevès et al., 2007). Thus, using the standard voltage and electrical resistance through the quantum Hall effect and the Josephson effect respectively, it is possible to connect the two physical quantities h and m . By substituting (8.38) and (8.39) into (8.37), we obtain the equation connecting the kilogram and the Planck constant:

$$m = C \frac{f_j f'_j}{g v} h \quad (8.40)$$

where C is a calibration constant and f_j and f'_j are the Josephson frequencies of the static and dynamic phases respectively. The watt balance experiment therefore relates the unit of mass to the meter, the second and the Planck constant. The parameters g and v must both be known with an uncertainty of about 10^{-8} .

8.6.2 Problems related to the watt balance experiment

The main issues raised by the needs of the experiment are (Eichenberger et al., 2009):

Calibrated test mass: A mass is needed for the experiment. It must be calibrated with a relative uncertainty of 10^{-8} , or better. For a mass of 1 kg, this corresponds to an absolute uncertainty of $10 \mu\text{g}$. The mass does not need to be 1 kilogram itself; it can be chosen freely. The choice of material for the test mass is important. It must not be porous, and the density must be high in order to minimise its surface, which must be polished.

Magnetic field: A magnetic circuit uses permanent magnets to generate a magnetic field. Superconducting electromagnets may also be used, but they are bulky. It is desirable that the magnetic field be homogeneous in space and that the dependence of the field on temperature is minimised. A magnetic field with a radial geometry is generally used. Moving ferromagnetic components in close proximity to the experimental apparatus must be absolutely avoided. This would result in a change of the spatial distribution of the magnetic field. It is desirable to have a strong magnetic field to reduce the current needed in the coil. Joule heating is then also reduced.

Electrical standards: The induced voltage in the dynamic phase and the current flowing during the static phase must be measured with an uncertainty of 10^{-8} . This is possible thanks to programmable Josephson junction

arrays (PJVS) and a standard resistance obtained by the quantum Hall effect.

Gravitational acceleration: An absolute gravimeter is used in the vicinity of the device to determine g (Van Camp et al., 2003). The variation of g with altitude is high: $-300 \mu\text{Gal/m}$. A relative gravimeter is therefore used to calibrate the variation in situ. Interpolation is finally made to obtain g at the site of the measurement with maximum accuracy. Ideally, the masses of the biggest components in the device should themselves be taken into account.

Speed of the coil: One or more interferometers are used to measure the vertical velocity of the coil. It must be known with a relative uncertainty better than 10^{-8} . The movement of the coil is regulated so that the relative stability of its speed is about 10^{-5} .

Trajectory of the coil: The path of the coil is measured in terms of position and angle. A bad orientation of the coil induces parasitic forces and distorts the outcome of the experiment. At the weighing position (vertical position where the static phase takes place), the horizontal velocity of the coil must be zero. Rectilinear movement of the coil throughout its trajectory allows weighing at different vertical positions.

Measuring the residual force: The Lorentz force generated by the current in the coil and the gravitational force acting on the test mass should be compared and equalised. A system called a mass comparator performs this comparison. It ensures two equal forces by regulating the current supplied to the coil.

Alignments: Several components of the balance must be aligned with the vertical. The guide should be aligned vertically to avoid inducing horizontal displacements of the coil. The mass comparator must also be aligned with the vertical, in order to offer its maximum sensitivity. The magnetic circuit must be aligned and positioned so that the electrical center of the coil coincides with its own center. If this alignment is not done correctly, it results in a horizontal component of the Lorentz force. Additionally, the optical center (point of the vertical speed measurement) must be known and must as far as possible be coincident with the electrical center and the center of gravity of the coil.

8.6.3 Context of the watt balance experiment

Five prototypes of the watt balance have been built (some are still under development) by national metrology institutes in England, USA, France, and Switzerland, as well as by the BIPM (Bureau International des Poids et Mesures). The NPL (National Physical Laboratory, the British National Measurement Institute) recently ceased operations on the watt balance after transferring its device to the

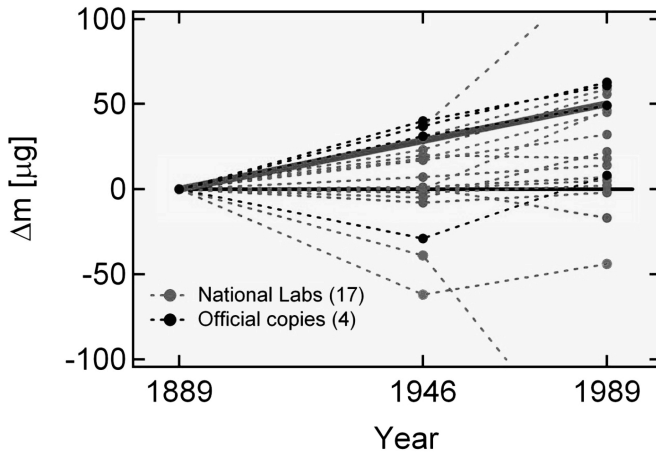


Figure 8.21 Relative drift between the International Prototype of the Kilogram and the official copies. A comparative measurement is done approximately every 50 years.

Canadian National Research Council (NRC). The Chinese National Institute of Metrology is also developing an alternative watt balance (Han et al., 2010; Li et al., 2010, 2012; Zhang et al., 2010, 2011), in which the magnetic characterisation is done by measuring mutual inductance. This experiment is called the *joule balance*. The national metrology institutes in Germany and New Zealand also plan to produce versions of the watt balance (Sutton, 2009).

The desire to define the kilogram through the watt balance has several origins. First, the current definition, based on the conservation of a unique standard, formerly known as the *grave*, has some disadvantages, including its uniqueness and its vulnerability. Second, since its adoption in 1889 as a mass reference, a relative fluctuation of the masses of the official and national copies (Fig. 8.21) compared to the primary standard has been observed. The magnitude of the average fluctuation is about 50 μg in a hundred years. This corresponds approximately to the mass of a grain of sand 0.4 mm in diameter. This variation is small, but the stability of the international SI system of units is potentially compromised, especially as other SI units are dependent on the kilogram. The mole, ampere and candela are by definition related to the unit of mass. Moreover, mass is the last SI unit still referred to a material artifact and not connected to a universal constant, as is the case for other units. Whether it is the meter, second or kelvin, all are referenced to a physical constant through an experiment theoretically repeatable at any time and in any place.

The definition of the kilogram is at present as follows: ‘*The kilogram is the unit of mass; it is equal to the mass of the international prototype of the kilogram (IPK)*’. This definition dates from 1889. The standard is a cylinder 39 mm in

diameter and 39 mm high, made of platinum-iridium. The concentration of iridium in the alloy is 10%. It is kept in Sèvres, near Paris, at the BIPM, where it is stored under three bell jars in a high security vault. The new definition would be as follows: ‘*The kilogram is such that the Planck constant is exactly $6.6260693 \times 10^{-34}$ joule-seconds*’.

8.6.4 METAS watt balance mark II

One of the guiding systems, the 13-hinge stage, has been integrated in the watt balance experiment, as shown in Figure 8.22. A CAD view of the apparatus shows the different units of the system.

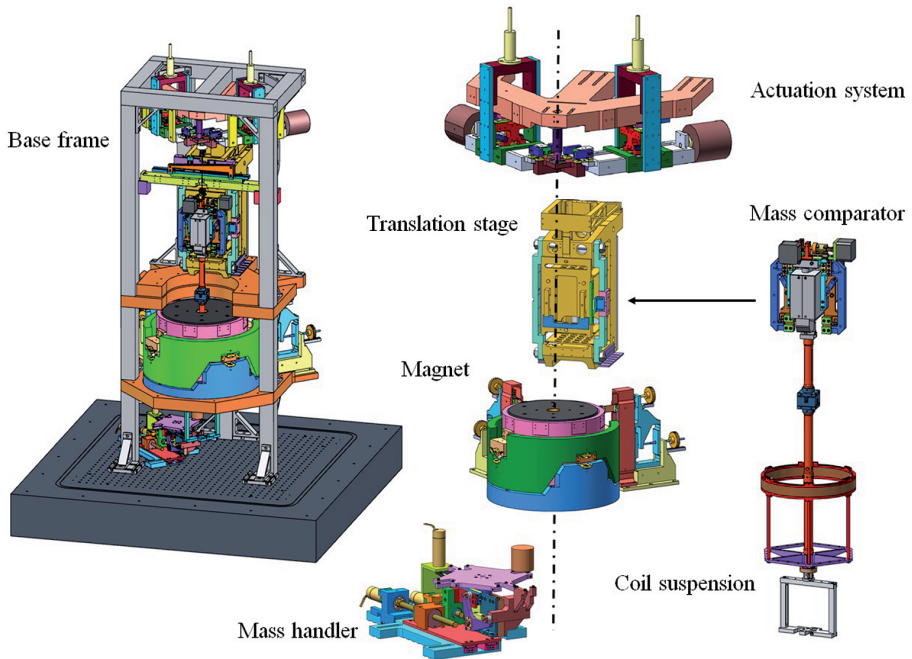


Figure 8.22 Computer view of the BWMII experiment. On the left, the apparatus is assembled. The main modules are represented on the right. They are all arranged around a vertical axis.

The translation stage, coupled to a linear position encoder, is mounted in the base frame and connected to the actuation system by a titanium wire. The actuation system has Sarrus kinematics and combines three functions: balancing the dead weight of the moving system, reducing the rigidity of the vertical translation by adding masses above the pivot point of the Sarrus arms and guiding the moving part of the motor. The mass comparator is inserted in the 13-hinge stage with a tip-tilt system. The coil suspension is hung under the mass comparator, passing through the magnet and supporting the coil in the gap

of the magnet. The magnet is placed in a tilting and translation system. A mass pan is located at the bottom of the suspension. Three electronically commutated vacuum-compatible motors are used in the mass handler. The whole system has been designed to be modular.

8.7 Conclusions

8.7.1 General conclusions

At the kinematic level, we note three main points. First, we found and showed that the 13-hinge stage has an optimum ratio of the length of the connecting rods to the slaving lever. In fact, the judicious choice of the relative lengths of the two connections between the lever and the stage leads to a straightness error up to 3000 times lower than what is seen in the literature.

Then, choosing a planar mechanism has many advantages, including the fact that the off-plane straightness does not depend on the kinematics. Finally, we see that perfect kinematics does not necessarily lead to a better performance of the mechanism, compared to pseudolinear kinematics.

Regarding manufacturing, we conclude that a monolithic machine has many advantages, especially in relation to the use of vacuum and nonmagnetic materials. Indeed, joining and fixing parts are sources of magnetic impurities. Consistency in the quality of materials can cause problems that are avoided by using a monolithic workpiece.

8.7.2 Potential applications

Various sectors are likely to benefit from the performance of the systems described in this chapter. Whether for their nonmagnetic characteristics, compatibility with a vacuum, ultra-high straightness or extremely small angular deviations, the potential applications are numerous. The guides can be used in ultra-high precision robotics, as linear modules. Alignments of etching masks in micro- and nanoelectronics are to ever higher levels of accuracy. Thus, the use of an ultralinear guide has every reason to be considered. In optics, elements (lenses, beam splitters, corner cubes, mirrors, etc.) are moved and measured with extreme accuracy. So we can easily imagine using a Sarrus linkage or a 13-hinge stage to make these movements, as well as for a profilometer or for measurements of very high precision. Space applications require the use of precision-guided systems with very high lifetimes, a total lack of maintenance and vacuum compatibility. The guides described here have all of these characteristics. One can also envisage a use for accurate microdrilling or microstereolithography, in fast prototyping for example.

Out-of-plane flexure mechanisms¹

9.1 Introduction

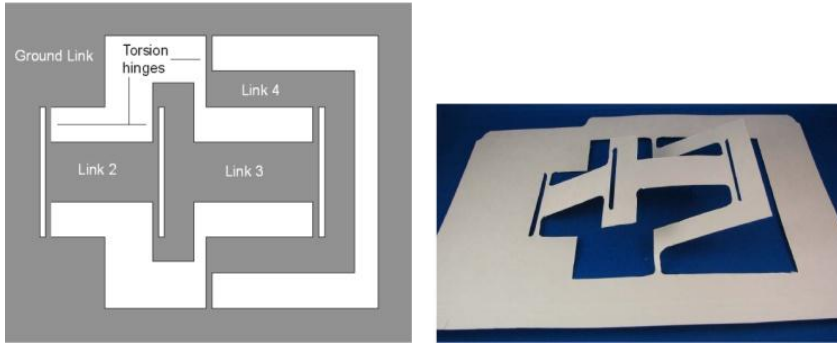
Flexure mechanisms are monolithic structures taking advantage of elasticity to produce movement. The absence of backlash and friction allows for the production of very accurate movements making them suitable for medical devices (Kota et al., 2005; Choi and Riviere, 2005; Savall et al., 2006), micropositioning (Tian et al., 2010; Richard and Clavel, 2011) and space applications (Fowler et al., 2011). In order to fulfill design criteria such as compactness, it is interesting to consider flexure mechanisms with planar configurations. One challenge is to design them with multiple degrees of freedom and out-of-plane motions while having adequate stiffness performances, i.e., demonstrating low stiffnesses along the desired degrees of freedom (DOF) and high stiffnesses in the other directions. For the design of flexure mechanisms there are three common synthesis approaches, described in (Gallego and Herder, 2009): the kinematic-based approaches, the building blocks approaches and the structural optimisation-based approaches. Among the kinematic-based approaches, we can distinguish two categories. The first one is the freedom and constraint topology (FACT) method which does not require knowledge of existing rigid-body mechanisms, the synthesis being performed using screw theory (Hopkins and Culpepper, 2011; DiBiasio and Culpepper, 2012). The second one, mostly used, and used in this book is the rigid-body replacement approach which is very interesting as it takes advantage of the large number of existing rigid-body mechanisms and their modelling tools (Olsen et al., 2010). With this approach, a rigid-body mechanism is first designed, or selected in the literature, then converted into a flexure mechanism, followed by pseudo-rigid body modelling (PRBM) (Howell, 2001) and optimisation. Complex flexure mechanisms with multiple DOF can thus be obtained (Bachta et al., 2011; Ouyang, 2011; Richard and Clavel, 2011; Xu and Li, 2011). The present chapter follows on from the rigid-body replacement approach and develops it further.

¹This chapter builds on material published previously in (Rubbert et al., 2012b, 2014a,b). Selected text segments and figures have been adapted and integrated to provide a coherent and updated synthesis of the research conducted during that period.

The design or selection of the rigid-body mechanism architecture is critical. In fact, for identical mobilities, the mechanism architecture can be, for instance, serial or parallel. For a mechanism with serial architecture, a direct conversion into a flexure mechanism may lead to insufficient stiffness performances, whatever the geometry of the flexure joints is. In such a situation, it is interesting to provide the designer with alternative solutions. Olsen et al. proposed a classification scheme to identify subgroups in a mechanism which can be independently converted into flexure elements (Olsen, 2010; Olsen et al., 2010). The main idea is that some subchains from an initial architecture can be efficiently replaced by alternative architectures to improve the final performances of the flexure mechanism. The use of parallel architectures has been proposed for this purpose because of their interesting intrinsic stiffness properties. Selecting or proposing a parallel mechanism is however a delicate task. First, even though many parallel architectures exist (Merlet, 2000), the choice of a parallel mechanism with particular mobilities is generally not obvious. Second, each parallel mechanism has its own workspace and its kinematic properties that are strongly dependent on the mechanism configuration (Mattson et al., 2004). Therefore, selecting a parallel mechanism also requires an expertise in the definition of the configuration used for the flexure mechanism. In addition, the manufacturing of spatial parallel compliant architectures remains complex. This is even more true at the microscale where the manufacturing becomes even more complex due to the fabrication process limitations.

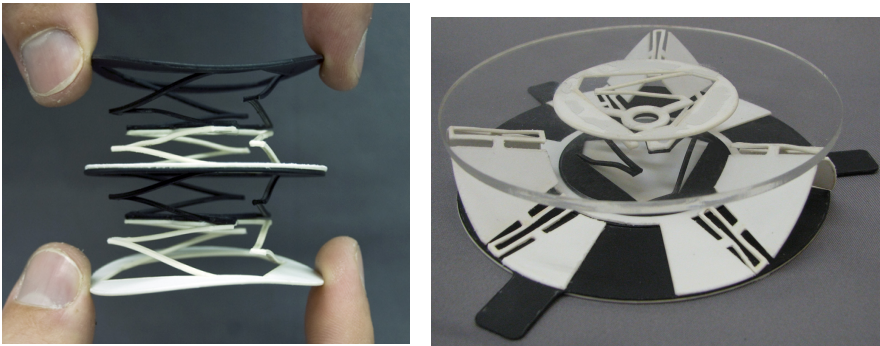
An approach for designing three dimensional micromechanisms consists in designing first the mechanism in an in-plane configuration before extracting it to an out-of-plane configuration (Choueifati et al., 2007; Lusk and Howell, 2008). This design strategy can be applied at the macroscale as it offers more simple manufacturing of the compliant structures and therefore reduce fabrication costs. Lamina Emergent Mechanisms (LEM) are based on this principle (Jacobsen et al., 2007; Andersen et al., 2009; Jacobsen et al., 2009; Ferrell et al., 2011; Wilding et al., 2012b) which is illustrated in Figure 9.1. LEMs aim to be manufactured from layers where material can only be completely removed or leaved as they are thought to be designed at microscale. The joints of the LEMs are therefore not obtained by changing the thickness of the layer but by designing specific joint geometry, here torsion hinges (Fig. 9.1a). The LEMs can be arranged in parallel or serially, i.e., combining multiple layers, in order to extend their kinematical capabilities (Gollnick et al., 2011) (Fig. 9.2).

LEM describes the current requirement for microfabrication: the possibility to manufacture in a layer, i.e., on a wafer, a flexure mechanisms with out-of-plane motions. At the macroscale, an in-plane manufacturing of flexure mechanisms is also interesting as the machined structure can be redundantly fixed to the ground and therefore helps to reduce the effects of milling vibrations. As a consequence it allows to machine more accurate thin hinges or blades.



(a) In-plane compliant four bar mechanism. (b) Out-of-plane compliant four bar mechanism.

Figure 9.1 Principle of lamina emergent mechanisms (Andersen et al., 2009).



(a) Serial arrangement of lamina emergent mechanisms. (b) Parallel arrangement of lamina emergent mechanisms.

Figure 9.2 Combination of lamina emergent mechanisms (Gollnick et al., 2011).

At this stage, LEMs are a trial to design out-of-plane flexure mechanisms at microscale but this approach has limitations. There is no methodology for the design of such mechanisms, there is no consideration for plastic deformations due to the out-of-plane extraction, and the lack of transverse stiffness is considered only through the study of particular LEM joints geometries (Jacobsen et al., 2009; Ferrell et al., 2011; Wilding et al., 2012a).

In this chapter we present the design and benefits of planar flexure mechanisms with out-of-plane motions. We mainly focus on the design of two parallel flexure mechanisms: the 3-RRR spherical mechanism (**3** legs, each composed of three **R**evolute joints) and the 3-US mechanism (**3** legs, each composed of a **U**niversal joint and a **S**pherical joint). Parallel architectures are chosen for

the design of the compliant structures for their intrinsic stiffness properties. Within planar configurations, kinematic singularities may occur (Gosselin and Angeles, 1990), which is the main thread of the two design approaches. In fact, one approach consists in exploiting the vicinity of singular configuration, while the second one consists in exploiting the mechanical properties offered by singularities. These two design approaches applied respectively to the 3-RRR and 3-US mechanisms are the first two contributions of this chapter. In order to illustrate more specifically the benefits of the 3-RRR and 3-US mechanisms as flexure mechanisms, we consider the example of the design of a compact surgical robotic tool. This study case is the third contribution: it shows how stacking multiple planar compliant structures can solve the problem of 2D micro-manufacturing constraints and increase the compactness of flexure mechanisms. The device is a flat planar 2-DOF mechanism with out-of-plane rotational motions. This mechanism has a generic function: it could be used for mirror tilting in MEMS for optical applications or any other application where the same mobilities are required at the micrometer scale.

In this chapter we first introduce the design context with our case study: the design of a compact active cardiac stabiliser. We then formulate the need for different planar compliant elements which leads to the design of the planar 3-RRR flexure mechanism and the planar 3-US flexure mechanism. The actuation mechanism and the integration of the different elements of the new active stabiliser is then addressed.

9.2 Example: design of an active cardiac stabiliser

Surgical robotics helps increase surgeon hand accuracy and limits the invasiveness of the operations. The complexity of an operation room implies designing surgical devices that are as compact as possible and that can be easily sterilised. One interesting design approach is to combine flexure mechanisms, which have a monolithic structure, and piezoelectric actuators (Kota et al., 2005; Choi and Riviere, 2005). Based on this approach, a robotic device for minimally invasive coronary artery bypass grafting has been proposed in (Bachta et al., 2011). The latest prototype, the *Cardiolock II*, is illustrated in Figure 9.3. This device successfully helps to increase the stabilisation of the beating heart surface during surgery, but its compactness needs to be increased for an optimal integration in the operation room.

The design approach proposed in this chapter in order to reduce the size of the compensation mechanism is to consider an assembly of planar manufactured structures. This helps to simplify the manufacturing process, allows microfabrication processes to be considered and generally may increase compactness.

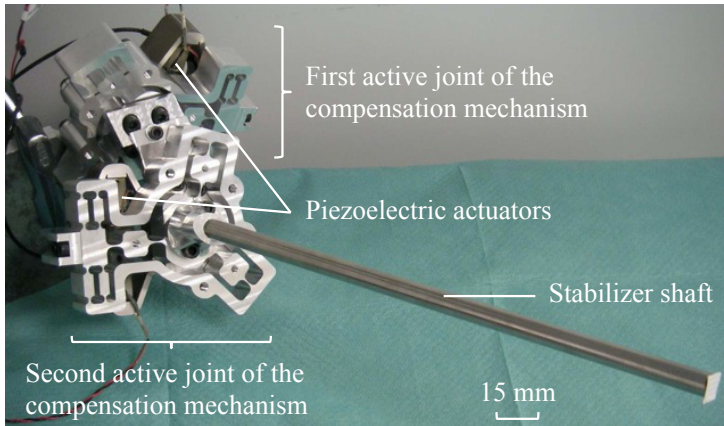


Figure 9.3 The *Cardiolock II*.

Similarly to the *Cardiolock II* device, the new stabiliser must be able to produce displacements along the directions normal to the shaft axis to compensate for the flexibilities of the device and its mounting system. It is therefore a two degrees of freedom (DOF) mechanism, that will be actuated by piezoelectric actuators which have a wide bandwidth but exhibit small displacements. The stroke of these actuators must be therefore amplified. A solution is to take advantage of the oblong geometry of the shaft and to decompose the compensation mechanism by distributing the mobilities into two planes, P_1 and P_2 placed close enough in order to provide a high displacement amplification ratio. Thus, we propose to use the kinematic architecture represented in Figure 9.4. The shaft is oriented with a spherical joint in O_2 and actuated in the two required directions in O_1 with two prismatic joints lying in P_1 . In order to kinematically link the spherical joint and the two prismatic joints between O_1 and O_2 , a RRP coupling mechanism composed of a universal joint (RR) in O_1 and a prismatic joint (P) along the shaft axis is required. Given the application requirements, the distance O_1O_2 must be less than or equal to 12 mm. This constrains the design of the device components presented further in this section.

9.3 In the vicinity of singularities

In this section we first consider the design of the spherical joint in O_1 . Several classes of spherical mechanisms have been identified in the literature (Gosselin and Angeles, 1989; Gregorio, 2004; Carricato and Parenti-Castelli, 2004). For the design of the passive compliant spherical joint in the plane P_1 (Fig. 9.4), we chose the architecture of the 3-RRR parallel spherical manipulator proposed by

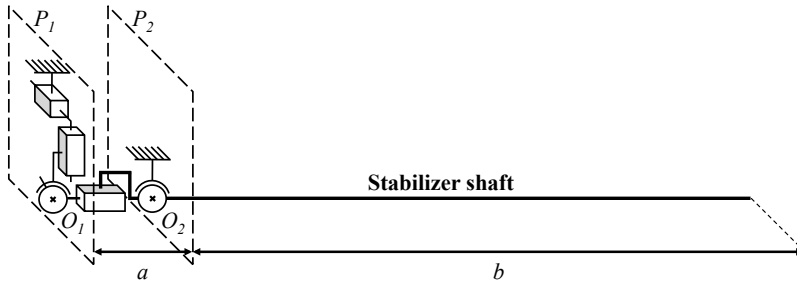


Figure 9.4 Planar decomposition and kinematical scheme.

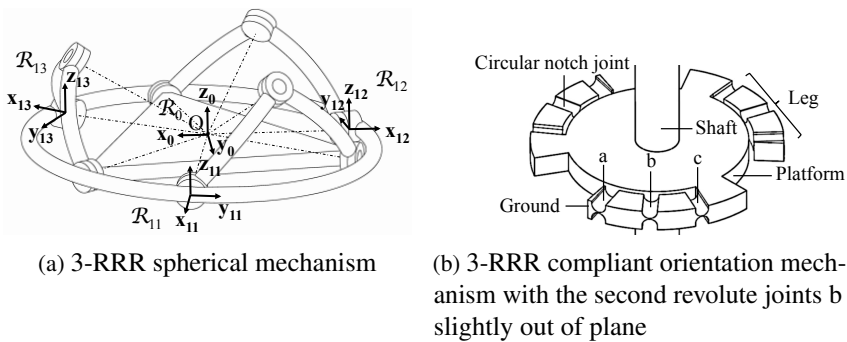


Figure 9.5 Planar compliant orientation mechanism obtained from a 3-RRR spherical mechanism.

(Gosselin and Hamel, 1994; Gosselin and St-Pierre, 1997) composed only of revolute joints which can be easily manufactured as notch joints. The spherical kinematical properties are guaranteed by the existence of a single intersection point (Fig. 9.5a) for all the revolute joint axes.

The 3-RRR flexure mechanism could be easily manufactured in the planar configuration which is also a compact configuration. But if all the revolute joints of the mechanism are located in a plane, the 3-RRR mechanism is in a singular configuration of type 1 and type 2 (Gosselin and Angeles, 1990; Bonev and Gosselin, 2006), with an increase of the stresses in the joints when moments are applied on the end-effector. To avoid this singular configuration, the mechanism must be out of the planar configuration. We therefore propose to design a passive flexure mechanism in the configuration illustrated in Figure 9.5a but close to the singularity by initially manufacturing the second revolute joints (joints b) of each leg slightly out of the mid-plane as illustrated in Figure 9.5b. This is possible by introducing some asymmetries during the manufacturing of the mechanism. With this approach, it is possible to benefit from the quasi-

planar configuration and its compactness without the singularities and therefore a pseudo-rigid body modelling can be performed as in the following.

9.3.1 Modelling of the 3-RRR spherical parallel mechanism

For reasons of symmetry, the geometry of the three legs of the mechanism is identical. In our context, all the revolute joints will be passive joints. We only use the compliance of the joints to obtain the spherical movements of the end-effector. In order to describe the stiffness of the mechanism, and also to determine the stresses in the compliant joints, we need first to determine the joint angles for a given orientation of the end-effector.

The end-effector orientation is defined by three angles (σ, ϕ, ψ) around respectively \mathbf{z}_0 , \mathbf{y}_0 and \mathbf{x}_0 of the frame R_0 (Fig. 9.5a).

The angles θ_i , γ_i and ξ_i defining the angular position of the 3 joints of the leg i , $i \in [1, 3]$ (Fig. 9.6) depend on the relative position of points A_i , B_i and C_i . In order to determine these angles, a local frame R_{1i} is built. Its origin is at the center A_i of the joint on the base, \mathbf{x}_{1i} colinear to \mathbf{OA}_i , and \mathbf{y}_{1i} in the plane $A_1A_2A_3$.

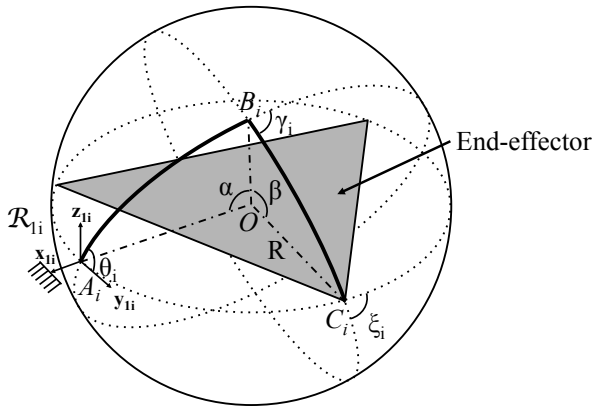


Figure 9.6 Parameterisation of one leg of the 3-RRR mechanism.

The cartesian coordinates of the point C_i can be computed from a given set of angles (σ, ϕ, ψ) in the frame R_0 and then in the local frame R_{1i} .

Because of the definition of R_{1i} , the coordinates of the points A_i are identical in the frames R_0 and R_{1i} .

The coordinate along \mathbf{x}_{1i} of point B_i is invariant with respect to the rotation θ_i . The coordinates y_{Bi} and z_{Bi} along \mathbf{y}_{1i} and \mathbf{z}_{1i} are determined by expressing the norm of vectors $\mathbf{A}_i\mathbf{B}_i$ and $\mathbf{B}_i\mathbf{C}_i$. Since these norms are also equal to the chords of the corresponding arcs, respectively αR and βR (Fig. 9.6), the two coordinates

can be computed. Four distinct sets of solutions exist. The coordinates y_{Bi} and z_{Bi} are chosen to be both positive in the configuration illustrated in Figure 9.6 when $z_{Ci} = 0$.

Once the coordinates of A_i , B_i and C_i are known in R_{1i} , the angle θ_i can be determined by

$$\theta_i = \arctan 2 \left(\frac{z_{Bi}}{y_{Bi}} \right). \quad (9.1)$$

The angle γ_i can be calculated using spherical trigonometry for an unitary sphere. The arc length of A_iC_i is equal to

$$\text{arc}_{A_iC_i} = 2 \cdot R \cdot \arcsin \left(\frac{A_iC_i}{2R} \right) \quad (9.2)$$

with A_iC_i the distance between the points A_i and C_i . The angle γ_i is obtained from

$$\gamma_i = \arccos \left(\frac{\cos \left(\frac{\text{arc}_{A_iC_i}}{R} \right) - \cos(\alpha) \cos(\beta)}{\sin(\alpha) \sin(\beta)} \right) - \pi. \quad (9.3)$$

Once the angles θ_i and γ_i are estimated, it is possible to compute the orientation of the last element of the leg i . Since the end-effector orientation is known, the angle ξ_i can then be computed.

9.3.2 Rotational stiffness of the 3-RRR flexure mechanism

Circular notches were successfully used for the design of the compliant joints in a previous prototype of cardiac stabiliser (Rubbert et al., 2011). The same geometry is therefore considered in this design (Fig. 9.7). A rotational stiffness model of circular joint is given in Section 3.5.2. The rotational stiffness describing each joint is here however based on the model derived in (Schotborgh et al., 2005), considered as the most accurate and with the widest range of validity in (Yong et al., 2008). The rotational stiffness K is therefore here modelled by

$$K = \frac{E \cdot w \cdot t^2}{12} \left(-0.0089 + 1.3556 \sqrt{\frac{t}{2 \cdot r}} - 0.5227 \frac{t}{2 \cdot r} \right) \quad (9.4)$$

with E the Young's modulus of the material, t , r and w respectively the minimum thickness, the notch radius and the width of the joint. Noting δ the angular deflection of the joint, the bending moment M in each joint is equal to

$$M = K \cdot \delta. \quad (9.5)$$

For a given end-effector orientation, it is now possible to express the angles θ_i , γ_i and ξ_i , $i \in [1, 3]$ describing the joint rotations in the mechanism. Considering the initial and current configurations of the mechanisms, the angular deflections δ that appear in Eq. (9.5) can therefore be computed for each joint.

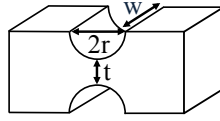


Figure 9.7 Parameterisation of a circular notch joint.

The 3-RRR mechanism is over-constrained. In order to compute the mechanism rotational stiffness from the joint stiffnesses, the end-effector is virtually split into three identical elements. Each element is connected on one end to a leg, and on the other end to the other two elements. For each resulting isostatic chain composed of three elements, it is possible to compute the rotational stiffness at the center O of the mechanism, to finally obtain the mechanism stiffness by superposition of the contributions of the three chains.

9.3.3 Analysis of the in-plane stiffness of the 3-RRR flexure mechanism

In the application we consider, the spherical joint will be submitted to large forces in the mechanism plane. In order to get an initial evaluation of the flexure mechanism behaviour under these forces, we assume in this section that the end-effector and the legs are in the plane of the base, to determine analytically the in-plane stiffnesses of the spherical joint. In fact the design approach assumes that the mechanism is so close to the planar configuration that this assumption can be made. During the optimisation, the in-plane stiffnesses will be maximised in order to limit the end-effector translations.

Deflection of a curved beam

The mechanism legs are composed of curved beams that are first modeled. The expression of the deflection of a simple curved beam located in a plane $(O, \mathbf{x}, \mathbf{y})$ (Fig. 9.8) can simply be obtained with the Bernoulli-Euler beam model. We consider a beam of constant rectangular cross-section of quadratic moment I_{Gz} submitted to a load described by the forces F_x , F_y respectively along \mathbf{x} and \mathbf{y} and a moment M_z along \mathbf{z} at point O .

The elementary rotation $d\zeta$ around G defined by the angle τ along a portion of the neutral axis $Rd\tau$ is equal to

$$d\zeta(\tau) = \frac{1}{EI_{Gz}} M_{fz} \cdot Rd\tau \quad (9.6)$$

therefore,

$$\zeta(\tau) = \frac{1}{EI_{Gz}} \int M_{fz} \cdot Rd\tau + A_\zeta \quad (9.7)$$

with $M_{fz} = R\cos(\tau)F_y - R\sin(\tau)F_x - M_z$ the bending moment in G around \mathbf{z} . The integration constant A_ζ is obtained with the condition $\zeta(0) = 0$.

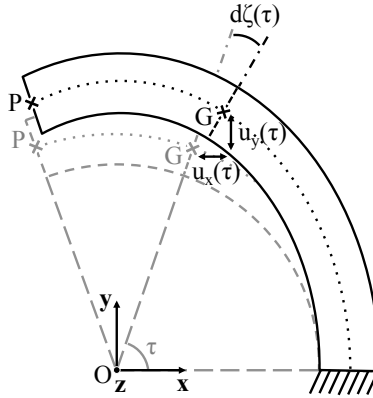


Figure 9.8 Curved beam submitted to a load in ϕ .

The variation of the position of the center G of the section defined by the angle τ is equal to

$$\begin{cases} u_x(\tau) = \int \zeta(\tau) \cdot R \cdot \cos(\tau) d\tau + A_x \\ u_y(\tau) = \int \zeta(\tau) \cdot R \cdot \sin(\tau) d\tau + A_y \end{cases} \quad (9.8)$$

with the integration constants A_x and A_y obtained using the conditions $u_x(0) = 0$ and $u_y(0) = 0$.

Curved beam with variable cross-sections

In the case of a curved beam with different rectangular cross-sections along the neutral axis, the same calculation can be performed, using, however, one integration per section. The integration constants A_ζ , A_x and A_y associated to a section of the beam are obtained using the angle and displacement values at the end of the previous section.

The calculation of the deflection of a circular notch joint cannot be easily performed as it is indeed not possible to perform the integration in Eq. (9.7) with the exact expression of the cross-section quadratic moment I_{Gz} , which is a function of the parameter τ . The geometry is thus simplified by considering the average thickness along the profile of the circular notch joint for preliminary in-plane stiffness evaluation.

Each leg of the 3-RRR mechanism can be described as a set of five curved beams with four different cross-section values: three for the compliant joints and one for the links connecting them. The computation of the deflection angle and displacements at the tip of the leg requires therefore five integrations with the corresponding quadratic moments.

Evaluation of the in-plane stiffness of the 3-RRR mechanism

The 3-RRR mechanism is hyperstatic. During the in-plane stiffness evaluation, it is therefore not possible to compute directly the forces applied at the tip of a leg i from the set of forces F_X , F_Y applied on the end-effector. In order to determine the mechanism deflection and then the in-plane stiffness, we first describe the load applied at the tip of the leg as composed of forces F_{x_i} , F_{y_i} and a moment M_{z_i} applied in O . The bending moment in the leg i is then equal to

$$M_{fz_i} = R \cos(\tau) F_{y_i} - R \sin(\tau) F_{x_i} - M_{z_i} \quad (9.9)$$

with τ defining the angular position around \mathbf{z}_0 of the center of the considered beam section and R the leg radius.

The resulting translations and the rotation of the leg i tip are therefore functions of F_{x_i} , F_{y_i} and M_{z_i} applied in O on the leg i . The new position of point O and the rotation of the platform can be expressed as

$$\begin{cases} x_i &= a_{xx_i} F_{x_i} + a_{xy_i} F_{y_i} + a_{xz_i} M_{z_i} \\ y_i &= a_{yx_i} F_{x_i} + a_{yy_i} F_{y_i} + a_{yz_i} M_{z_i} \\ \zeta_i &= b_{x_i} F_{x_i} + b_{y_i} F_{y_i} + b_{z_i} M_{z_i} \end{cases} \quad (9.10)$$

with a_{xx_i} , a_{xy_i} , a_{xz_i} , a_{yx_i} , a_{yy_i} , a_{yz_i} , b_{x_i} , b_{y_i} and b_{z_i} the nine terms determined by deriving the expression of the beam deflection.

The positions (x_i, y_i) of the point O and the rotation ζ_i obtained for each leg must be equal since they are connected to the end-effector which deformation is neglected. Eq. (9.10) therefore provides six conditions

$$\begin{cases} x_1 &= x_2 \\ x_1 &= x_3 \\ y_1 &= y_2 \\ y_1 &= y_3 \\ \zeta_1 &= \zeta_2 \\ \zeta_1 &= \zeta_3 \end{cases} \quad (9.11)$$

In addition, expressing the equilibrium of the end-effector provides three additional relationships for this in-plane study

$$\begin{cases} \sum_{i \in [1,3]} F_{x_i} &= F_X \\ \sum_{i \in [1,3]} F_{y_i} &= F_Y \\ \sum_{i \in [1,3]} M_{z_i} &= 0 \end{cases} \quad (9.12)$$

The three sets of forces and moments $(F_{x_i}, F_{y_i}, M_{z_i})$, $i \in [1, 3]$ can thus be estimated as a function of the forces F_X and F_Y from Eq. (9.11) & (9.12). Consequently, the end-effector movement can be determined from Eq. (9.10).

9.4 Optimisation of the spherical compliant joint

Performing a trial-and-error design process with finite element analysis tool to determine acceptable mechanism geometry is time consuming. As we now have the model of the planar spherical compliant joint, an optimisation is here performed to get a first evaluation of the behaviour of a 3-RRR compliant spherical mechanism.

9.4.1 Formulation of the optimisation problem

Performance criteria

In our case study, during the stabilisation, power is sent to the actuators to counterbalance the deflections induced by the forces applied by the heart on the device. In order to minimise the energy required for stabilisation, it is better to minimise the stiffness of the spherical joints which deformation requires some energy. In other words, the rotational stiffnesses of the 3-RRR mechanism must be minimised.

Because of the device kinematics, significant forces applied on the spherical joints come from the actuators. The in-plane stiffness of the mechanism evaluated earlier has therefore to be maximised.

The forces developed by the actuators will be much higher than the forces exerted by the heart on the device. Considering the force and moment equilibrium of the shaft, one can then notice that the two orientation joints in O_1 and O_2 will be submitted to forces of the same amplitude (Fig. 9.4). We thus can make a preliminary consideration that the stabiliser is only composed of two identical 3-RRR flexure mechanism in O_1 and O_2 . Thus the design problem can be simplified to the optimisation of one of the two spherical joints in order to evaluate the performance of a 3-RRR flexure mechanism as a compliant spherical joint.

Optimisation constraints

The modelling of the mechanism is performed using Euler-Bernoulli theory. The mechanism description may hence be expected to lack accuracy if short beams are considered. Therefore, for this first performance evaluation, we restrict the research space in the optimisation to consider only leg elements compatible with the Euler-Bernoulli hypotheses.

As mentioned earlier, the 3-RRR mechanism needs to be placed outside its singular configuration, when the legs are located in a single plane. In the optimisation, we consider that the mechanism configuration is modified by moving the end-effector around \mathbf{z}_0 (Fig. 9.5a) with an angle σ . The position

of the center of the compliant joints B_i is therefore modified in the thickness of the mechanism plane. It means that the legs and the end-effector of the equivalent mechanism do not lie in a common plane but tend to be in the configuration illustrated in Figure 9.5a, even though the manufacturing can be performed from a single element, without any additional out-of-plane movement. We here investigate if such configurations provide sufficient performances by constraining the positions of B_i thickness range of the mechanism.

The material must be able to withstand the stresses induced by the load on the mechanism. The circular notch joints are designed to constitute the revolute joints of the 3-RRR mechanism. Their cross-section is therefore significantly smaller than the cross section of their connecting elements, and maximal stresses will be encountered in these cross-sections. During the optimisation, a simple estimation of the stresses in the joints can be obtained by considering the sum of the stress induced by the rotation of the end-effector and the stress due to the force applied on the mechanism when this latter is in a planar configuration. This sum s must be lower than the yield stress of the material. Its value can be expressed analytically using a beam model and introducing stress concentration factors to refine the stress value (Pilkey and Pilkey, 2008):

$$s = k_T \cdot \frac{F}{t \cdot w} + k_B \cdot \frac{6 \cdot M}{t^2 \cdot w} + \frac{6 \cdot M_{fz}(\tau)}{w^2 \cdot t} \quad (9.13)$$

with k_T and k_B two stress concentration factors, M (Eq. (9.5)) the bending moment due to the rotation of the end-effector, $M_{fz}(\tau)$ (Eq. (9.9)) and F due to force developed by the actuators. These forces are computed using the geometry introduced in Figure 9.4, assuming that the stabiliser shaft is in equilibrium.

9.4.2 Optimisation method and performance evaluation

The 3-RRR flexure mechanism is now described by a discrete set of geometrical parameters. For a given architecture, the rotational stiffnesses, the in-plane stiffnesses and the stresses in the joints can be computed. Each geometrical parameter can take a value in a range defined by the limits of the manufacturing process or design requirements. Gradient-based optimisation algorithms usually have a low efficiency due to the presence of many local minima in the optimisation function. Metaheuristic optimisations, based on stochastic algorithms, can constitute interesting alternatives. We propose to use a modified Ant Colony Optimisation (ACO, (Dorigo et al., 1999)) algorithm for its ease of implementation. The method does not need a delicate tuning of many internal parameters to be efficient.

Ant colony optimisation of flexure mechanisms

Ant colony optimisation (ACO) mimics the behaviour of ants that are able to collectively optimise the path between their house and a source of food by using pheromone, a chemical marker, for local stigmergic communication (Dorigo and Gambardella, 1997). The colony evolves by sequences of local moves to find the shortest path, and the decision policy uses local information without lookahead.

Considered initially for combinatorial problems (Dorigo and Gambardella, 1997), an extension has been proposed for continuous domain in (Socha and Dorigo, 2008; Blum, 2005). We here use an adaptation of the ACO algorithm dedicated to mechanism optimisation introduced in (Rubbert et al., 2011). In such a situation, the optimisation problem is very constrained and the efficiency of cross-overs between solutions would be very low. Thus, instead of making cross-overs among parameters of different initial solutions as in (Socha and Dorigo, 2008), we prefer to explore sequentially one solution after another. As a consequence, the algorithm explores the neighborhoods of the initial solution as real ants would do. The algorithm uses two pheromone models. In the first model, the pheromone is simulated by the exploration of a restrained domain and its evaporation is simulated by the abandoning of the less efficient solutions. The exploration of a restrained domain is performed with a uniform distribution law around the best solution corresponding to 20 % of the range of the parameters. To avoid a blockage of the solution evolution, the size of the restricted domain grows incrementally by 4% until the search space reaches 40 % of the parameter space. The choice of these values does not strongly affect the optimisation success: dividing those values by two still allows us to obtain the same final performances. In the second model, when the search space of the first pheromone model reaches 40 %, ant collaboration is simulated to find the best solution locally. The solution generation is performed by switching to a gaussian distribution law for the look-around radius of each parameter. The mean value and standard deviation are computed using the sets of viable configurations determined in the previous generation of solutions. Gaussian law helps to increase the density of parameter sets around the best solution so that a smaller number of parameter sets is necessary.

The search space

A path chosen by an ant is a compliant 3-RRR leg architecture defined by a set Π of eleven geometrical parameters: σ the pre-orientation of the end-effector around \mathbf{z}_0 which modifies the height of the points B_i , the radius R of the neutral fiber, the two arc angles α and β , the three joint thicknesses t , the three radii r of the circular notches and the leg width w . The ranges of values of t and r are limited by the machining performances. The overall thickness is chosen to be

the half of the length l the distance between O_1 and O_2 , the centers of the two 3-RRR mechanisms (Fig. 9.4).

The set of constraints

The ants have to find the best path, i.e., the parameter set Π that minimises rotational stiffnesses, maximise the in-plane stiffnesses, while respecting a set of constraints:

- The width of a leg can not be wider than 30% of the radius R to use the Euler-Bernoulli theory.
- The arc angle of the leg can not be greater than 105 degrees to leave some space at the leg ends to connect the end-effector and the base.
- The maximum stress in each joint must be compatible with the material properties.
- The geometry of each joint must not interfere with the dimensions of the leg.
- The height of point B_i must be lower than the half of its joint thickness, to remain close to a planar configuration.
- The proportion between the thickness t and the radius r in each joint must respect the threshold given in (Schotborgh et al., 2005).

These constraints constitute a set of ten linear and three non-linear inequalities.

The evaluation function

As outlined in the design of Cardiolock 2 (Bachta et al., 2011), a displacement between 0.5 and 1 mm is required at the stabiliser tip to compensate for the deflections due to the interaction with the heart. The mechanism must be able to provide this displacement for any orientation of the mechanism with respect to the heart. Consequently, the corresponding rotation of the 250-mm long shaft is applied for different orientations of the spherical joint with respect to the displacement direction. Ten orientations with an increment of 12 degrees are used. For each of them, the rotational stiffness is computed. The orientation for which the stiffness is the highest is identified. We then associate this stiffness K_r to the mechanism, which is a worst-case estimator. In the same configuration, the in-plane stiffness K_p is also computed.

The maximal force applied by the heart at the stabiliser tip is equal to 5 N (Bachta et al., 2011). Considering the shaft equilibrium and the spherical joint stiffness, the force that must be developed by the actuator to get the shaft equilibrium can be computed. So, we can determine the stresses in the joints in that situation.

The size of the spherical joint is part of the performance of the mechanism. The size of the 3-RRR mechanism is characterised by the outer radius R_{\max} which is equal to $R + \frac{w}{2}$.

Finally, we propose the following evaluation evaluation function:

$$\text{Performance}(\Pi) = \frac{K_p}{K_r \cdot R_{\max}}. \quad (9.14)$$

In the ACO algorithm, each time a better solution is found, the best values of K_r , K_p and R_{\max} are introduced as thresholds in the selection constraints for the next generations of solutions in order to avoid a Pareto front.

9.4.3 Results

The set of parameters obtained after optimisation can be found in (Rubbert et al., 2012b). In order to assess the accuracy of the modelling, the mechanism is designed using Pro/Engineer and evaluated using finite element analysis (FEA) with Pro/Mechanica. The flexure mechanism is illustrated in Figure 9.9. The mechanism is 6 mm thick, with an outer radius of 34.5 mm, which will allow the two spherical joints to be stacked and to obtain a length a (Fig. 9.4) of only 6 mm.

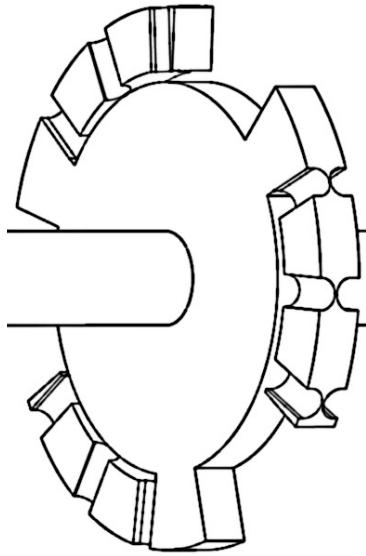


Figure 9.9 CAD view of the compliant 3-RRR.

In order to compute the mechanism rotational stiffness, a set of forces is applied on a beam linked to the end-effector and the rotation is computed using the displacement values (Fig. 9.10). The relative error between the stiffness obtained using PRBM and FEA is around 10 %, which is satisfactory.

With the knowledge of the stabiliser shaft length b , the length a and the rotational stiffnesses of the spherical joints, it is possible to compute the required

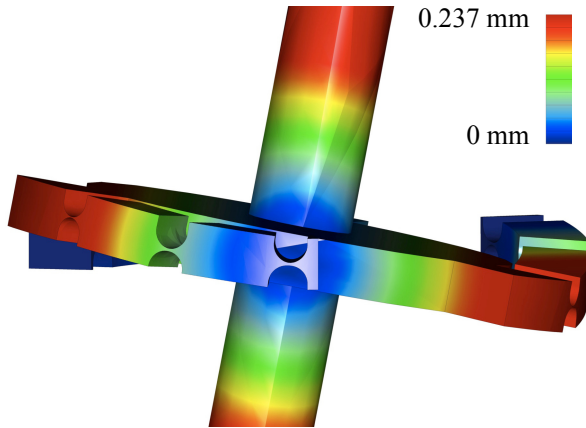


Figure 9.10 Displacement field during rotation stiffness evaluation.

forces applied by the active mechanism to get the equilibrium of the shaft. With a cardiac force equal to 5 N, the active mechanism must apply 217 N. In the absence of the rotational stiffnesses, the force is equal to 208 N. It means the minimisation of the rotation stiffness of the spherical joint is efficient: the actuator force required to rotate the joints is very limited.

During stabilisation, we now know the forces and torques applied on each spherical joint. A simulation is performed to compare the stresses in the joints to the estimator introduced during the optimisation. The maximum stress, according to the modelling used during the optimisation, was equal to 549 MPa. FEA shows a maximum stress equal to 525 MPa. The maximum in-plane displacement of the end-effector is then approximately equal to 0.05 mm, which is small enough compared to the 0.5 to 1 mm displacement required at the stabiliser tip.

These results lead to three main conclusions about the use of the 3-RRR mechanism for the design of a spherical joint for the active stabiliser. First, the modelling of the compliant spherical parallel mechanism is efficient enough to determine a structure adapted to our context. Prediction of the rotational stiffness and joint stresses is satisfactory. Second, placing the points B_i (Fig. 9.6) out of the plane containing the points A_i and C_i is sufficient to get a satisfactory behaviour of the spherical mechanism. No out-of-plane movement needs to be applied initially, and the stresses in the joints are in particular compatible with the considered material. Third, the interest of using a spherical parallel mechanism to design a compliant spherical joint based on a planar mechanism is clear: an interesting compromise between rotational stiffnesses, to be minimised, and in-plane stiffness, to be maximised, is obtained.

9.5 Exploiting the singularities of parallel mechanisms

In this section, we address the design of the flexure joint in O_2 laying in plane P_2 which takes advantage of the properties of the singularities of parallel mechanisms. Therefore, this section begins with the presentation of this particular rigid-body replacement design method.

One well-known feature of parallel mechanisms is the existence of so-called singular configurations. In those configurations, the parallel mechanism locally exhibits specific mobilities. Since flexure mechanisms usually work around a given position, it seems interesting to start their design with the architectures obtained from parallel mechanisms in singularity, for three reasons. First, the designer only has to focus on the selection of a parallel architecture with adequate singular configurations, instead of having to select a parallel mechanism and afterwards a configuration. Second, the designer can benefit from the knowledge of singularity analysis for many parallel manipulators (Merlet, 2000; Amine et al., 2012). It is then easy to obtain mechanisms that can achieve particular mobilities with parallel architectures for the sake of stiffness. Third, many spatial parallel manipulators reach a singular configuration in planar configurations. Planar configurations are of particular interest for the design of flexure mechanisms since their manufacturing is usually largely simplified (Choueifati et al., 2007; Lusk and Howell, 2008).

In this section, the singularity analysis of parallel manipulators is considered in the type-synthesis of flexure mechanisms based on the rigid-body replacement approach. Therefore, the singularities of parallel manipulators, that are generally avoided, are here at the center of a design approach.

As the proposed design approach for rigid-body mechanism selection is intrinsically related to the singularities of parallel manipulators they are first briefly outlined. Then details are given on how mechanism selection can be achieved by using them.

9.5.1 Singularities of parallel manipulators

For a given parallel manipulator, \mathbf{q}_a and \mathbf{q}_p denote the actuated joint angle vector and the passive joint angle vector, respectively. The full twist \mathbf{T} describes the velocities along the 6-DOF of the end-effector. It can be divided into \mathbf{T}_n , the velocities of the n -DOF of the end-effector of the manipulator, and $\mathbf{T}_{\bar{n}}$, the complementary velocities which should be zero in normal case. The relationship between the input velocities of the actuators $\dot{\mathbf{q}}_a$, the passive joint velocities $\dot{\mathbf{q}}_p$ and the full twist of the end-effector \mathbf{T} can be written as (Zlatanov et al., 1995; Merlet, 2000):

$$\mathbf{A}\dot{\mathbf{q}}_a + \mathbf{B}\mathbf{T} + \mathbf{C}\dot{\mathbf{q}}_p = \mathbf{0}. \quad (9.15)$$

This equation can be rewritten as:

$$L(\mathbf{q}_a, \dot{\mathbf{q}}_p, \mathbf{T})^T = 0 \quad (9.16)$$

where L is a $N \times (N + n)$ matrix, N being the number of equations and $N + n$ the number of unknowns.

If the end-effector does not move while the actuators have non-zero velocities, the manipulator is in a serial singularity, or redundant input singularity (Type 1 (Gosselin and Angeles, 1990)). Therefore it can be said that the end-effector loses one or more DOF. Inversely, if the end-effector of the manipulator can move locally even if the actuators are locked and $\|\mathbf{T}_n\| \neq 0$ the manipulator is in a parallel singularity, or redundant output singularity (Type 2 (Gosselin and Angeles, 1990)). It can be said that the end-effector gains one or more DOF. The manipulator is in a Type 3 singularity if the manipulator reaches both serial and parallel singularities. In case of a parallel singularity, if $\|\mathbf{T}_n\| = 0$ and $\|\mathbf{T}_{\bar{n}}\| \neq 0$, the manipulator reaches a constraint singularity that includes the case of architectural singularity where self-motions occur and the end-effector can move with finite amplitude (Zlatanov, 1998; Merlet, 2000). If the actuators are locked, $\|\mathbf{T}\| = 0$ and the passive joints can move, the manipulator is in a redundant passive motion singularity.

Here, the redundant output singularities where the end-effector moves while the actuators are locked are interesting for the design of flexure mechanisms. As a matter of fact, as a flexure mechanism only works around a given configuration, the motions of the moving platform can be used to produce the required displacements. At the same time, the actuated joints can be suppressed as they are considered locked, which simplifies the architecture of the flexure mechanism.

It is noteworthy that Type 2 singularities have already been considered for simple mechanisms, for instance in the case of orthoplanar mechanisms (Parise et al., 2001) or the development of 1-DOF structures such as torque sensors (Chapuis et al., 2004; Renaud and de Mathelin, 2009), but have never been applied in a more generic way to flexure mechanisms.

9.5.2 Principle of the design approach

The approach to select a rigid-body mechanism from parallel mechanisms in a singular configuration is introduced with the example of the design of a 1-DOF flexure mechanism equivalent to a revolute joint. The approach is broken down into four steps.

Step 1 – Selection of a mechanism: First, a parallel manipulator needs to be selected or identified. It needs to exhibit in singularity at least the desired

mobilities of the compliant linkage. Here, the 3-PRR planar parallel manipulator illustrated in Figure 9.11a is chosen. The singularity analysis of this manipulator was performed in (Bonev et al., 2003). The manipulator has a planar architecture and is composed of three identical limbs and has three degrees of freedom. Each limb contains a prismatic actuated joint and two passive revolute joints. The 3-PRR can reach some parallel singularities and the gained motions are instantaneous rotations about an axis normal to the plane of motion.

Step 2 – Singularity analysis: For a given architecture, the nature of the displacements in singularity depends on the actuated joints, i.e., the actuation mode. For parallel singularities, the end-effector motion is obtained while the actuated joints are locked. The choice of these actuated joints is crucial for the design of the compliant structure since this latter is obtained by their suppression. Consequently, Step 2 consists in analysing all possible actuation modes for the selected architecture, in order to identify the one that most simplifies the subsequent compliant structure.

In the case of the 3-PRR architectures, their singular configurations have been analysed with the screw theory (Bonev et al., 2003). Considering symmetrical actuation modes, i.e., the same joint in each leg is actuated, a singular configuration of Type 2 exists for the three possible actuation modes. Considering the 3-PRR parallel manipulator, the singular configuration occurs when the lines associated with the distal links intersect at a single point as illustrated in Figure 9.11b. Considering the 3-PRR parallel manipulator and the 3-PRR parallel manipulator, their singular configurations of Type 3 occur when the lines associated with the distal links intersect at one point and are normal to the axis of their prismatic joint as illustrated in Figures 9.11c and 9.11d.

Step 3 – Actuation mode selection: If different actuation modes allow the manipulator in singularity to have the desired mobilities, the one that most simplifies the flexure mechanism architecture and its manufacturing is selected. It is noteworthy that revolute joints are the simplest and easiest-to-manufacture joints (Lobontiu, 2003). A prismatic joint is more complex to manufacture as it requires at least two leaf-spring joints (Sect. 4.1) or four notch joints (Sect. 4.3). A flexure mechanism only composed of compliant revolute joints may therefore be preferred. If a parallel manipulator is composed of joints of the same kind, i.e., it is only composed of revolute joints or prismatic joints, the designer has to choose the actuation mode that mostly simplifies the conversion to a flexure mechanism: decision criteria will be based on the manufacturing process and on the global arrangement with respect to space requirements.

Here, the architecture illustrated in Figure 9.11e, obtained from the first actuation mode after suppression of the prismatic joints, has only revolute joints and is therefore preferred.

Step 4 – Design of the flexure mechanism: The simplified kinematic architecture can now be converted to a flexure mechanism by replacing each joint by a notch joint. Here, the 3-RR architecture of the final flexure mechanism is illustrated in Figure 9.11f.

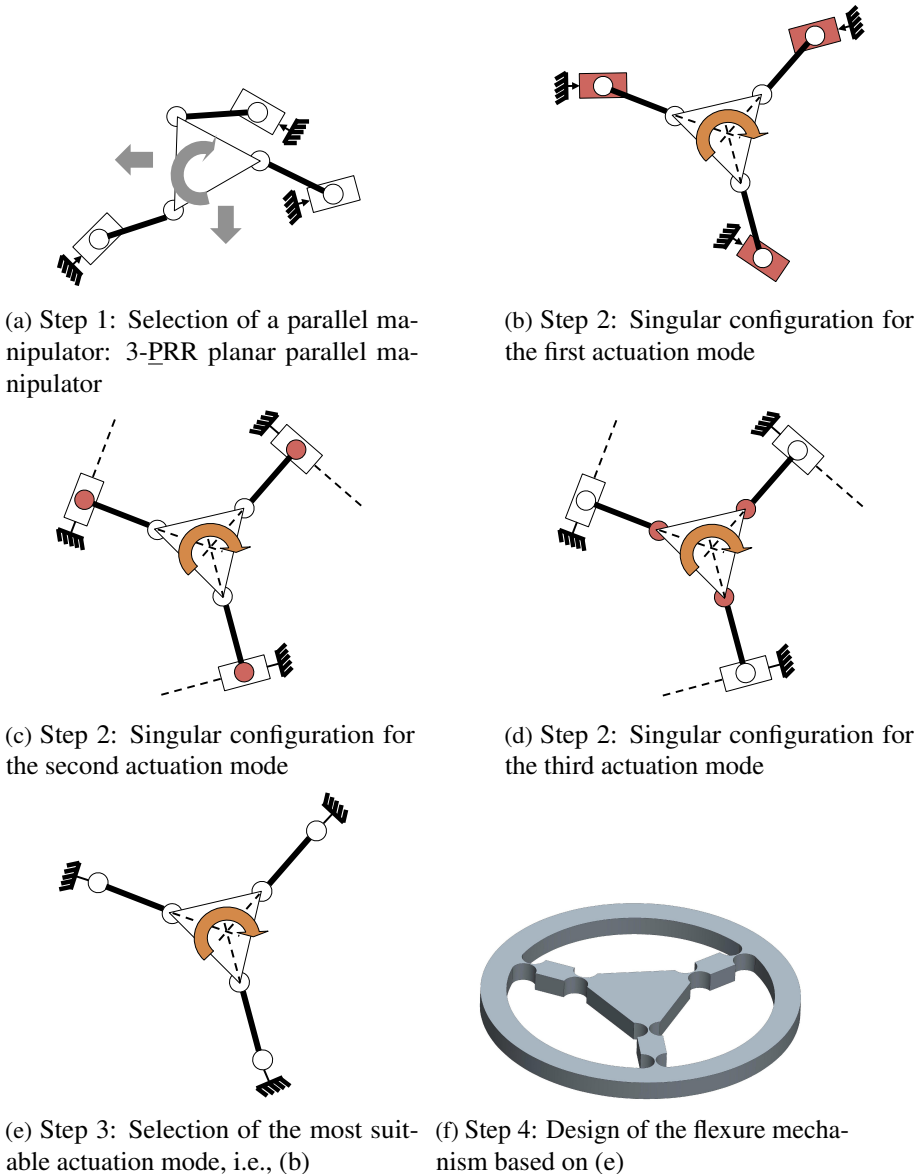


Figure 9.11 Principle of the design approach based on singularity analysis of parallel manipulators. Coloured joints represent the actuated joints considered locked, big arrows represent the possible instantaneous motions of the end-effector.

9.5.3 Design of a flexure mechanism for an active cardiac stabiliser

The design approach which was introduced in the previous subsection is now applied in our study case of a medical device design. The aim now is first to show the interest of the proposed approach during the design of a compliant device, and second to show its potential efficiency, with the introduction of a non-trivial 3-DOF mechanism.

We here now focus on the serial subgroup with RRP mobilities, i.e., the DOF of a universal joint (RR) serially connected to a prismatic joint (P), connects the spherical joint and the end of the shaft in O_1 . As mentioned previously, the piezoelectric stacks will deliver high forces to counterbalance the cardiac forces exerted on the shaft tip. The subgroup will therefore be subjected to high loads. Converting the RRP chain in three serially connected equivalent compliant joints may lead to a compliant structure with limited stiffness, which will exhibit significant deflections. Therefore, this section deals with the design of a planar flexure mechanism with RRP mobilities.

9.5.4 Step 1: selection of the 3-US parallel manipulator

An interesting parallel mechanism is the 3-DOF 3-US mechanism, considered for lamina emergent mechanisms and for foldable mechanisms (Andersen et al., 2009; Qin and Dai, 2012), illustrated in Figure 9.14.

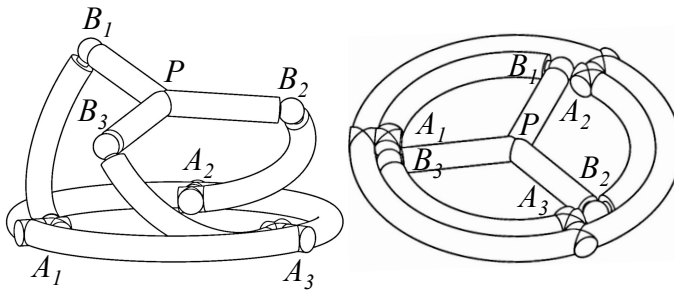
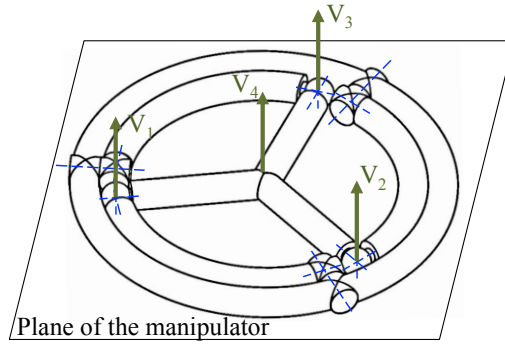


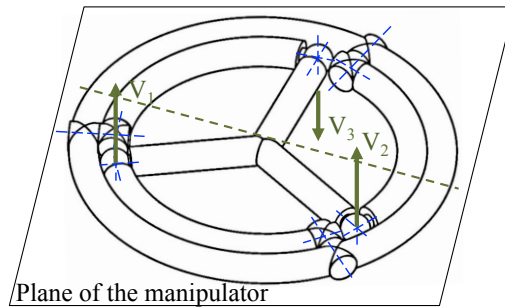
Figure 9.12 3-US parallel manipulator and its planar configuration.

The architecture of the 3-US mechanism is interesting since it has three identical legs only composed of a universal joint in A_i and a spherical joint in B_i that can be broken down into five revolute joints, which are easy to manufacture.

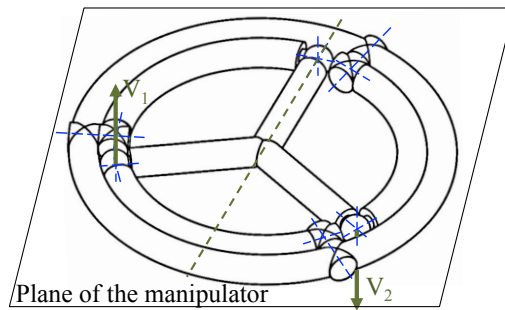
Here, the planar configuration is interesting as the possible motions of the end-effector are translations normal to the plane of the mechanism (Fig. 9.13a) and rotations around the axes in the plane of the mechanism (Fig. 9.13b and Fig. 9.13b). So, in the planar configuration, the end-effector of the 3-US mechanism has precisely the RRP mobilities.



(a) Translation velocity vector field



(b) First rotation velocity vector field



(c) Second rotation velocity vector field

Figure 9.13 Instantaneous motions of the 3-US manipulator in the planar configuration.

Moreover, in the planar configuration, at least one Type 2 singular configuration can be identified. In fact, if the first or the second revolute joints of the universal joints are locked, it is not possible to counterbalance the normal forces applied to the end-effector. In this case, the end-effector exhibits instantaneous motions corresponding to the desired RRP mobilities.

As for the design of the 1-DOF flexure mechanism illustrated in the previous section, the architecture of the 3-US may be simplified in a 3-RS mechanism. But another simplified architecture could be obtained in the planar configuration with another actuation mode that would finally ease the design and the manufacturing of the flexure mechanism. We therefore perform the singularity analysis of the 3-US in the planar configuration for the different possible actuation modes.

9.5.5 Step 2: singularity analysis for different actuation modes

Each leg of the 3-US parallel mechanism is composed of a universal joint and a spherical joint. The universal joint is similar to two revolute joints with perpendicular and intersecting axes. The spherical joint can be broken down into three revolute joints with perpendicular and intersecting axes as shown in Figure 9.14.

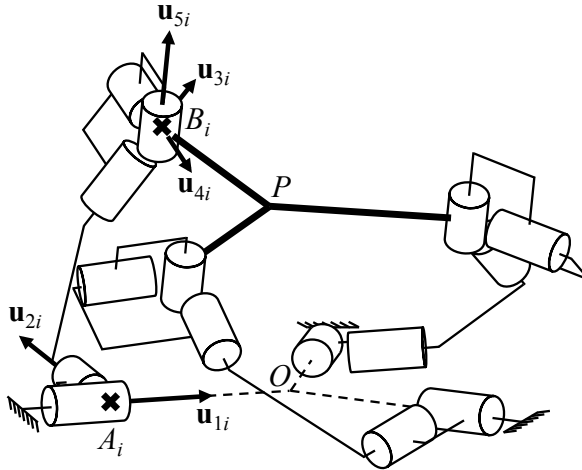


Figure 9.14 3-US manipulator broken down into rotational joints.

Hence, there are $\binom{15}{3} = 455$ possible actuation modes. Among these 455 modes, 5 of them are symmetric, i.e., the same rotational joint on each leg is actuated. If we consider that the manipulator has similar legs, there are also 150 unique asymmetric actuation modes. Among these 155 possible unique actuation modes there may be many singular configurations which could lead to different flexure mechanism architectures.

Analysing the five symmetric actuation modes of the 3-US parallel manipulator is indeed sufficient to analyse the 155 possible unique actuation modes. This will be shown later after detailing the singularity analysis of the symmetric actuation modes.

A direct analysis of the singularities of the extended forward Jacobian matrix involves the calculation of its determinant which may be a difficult task even with symbolic computation softwares (Merlet, 2000). Here, the singularities are analysed using screw theory (Kong and Gosselin, 2007), which allows us to obtain the global wrench system of the manipulator. In fact, the degeneration of the global wrench system of a parallel manipulator is directly related to the degeneration of its extended forward kinematic Jacobian matrix. The singularity analysis of the 3-US manipulator is therefore performed through the analysis of its global wrench system degeneration. In (Rubbert et al., 2012a) the singularity analysis of the mechanism was performed in the whole workspace for the five symmetric actuation modes. Screw theory and Grassmann-Cayley algebra were then used. Here, we perform the singularity analysis for all possible actuation modes of the 3-US manipulator but only in the planar configuration. In this situation, the use of the screw theory is sufficient.

The global wrench system of the 3-US is spanned by the constraint wrench system and its actuation wrench system. The constraint wrench system describes how the end-effector is constrained by the leg of the manipulator and the actuation wrench system describes how the actuators act on the end-effector. Therefore, in a non-singular pose, the global wrench system describes how the end-effector is mechanically fully constrained. If the global wrench system degenerates, the end-effector is no longer constrained and the manipulator reaches a parallel singularity.

Twist system of the 3-US

A *twist* is a screw representing the instantaneous motion of a rigid body. An infinite-pitch twist ϵ_∞ represents a pure translation, whereas a zero-pitch twist ϵ_0 represents a pure rotation. As the 3-US can be represented using only revolute joints, the twist system T^i associated with the i -th leg of the 3-US is spanned by five zero-pitch twists defined as (Kong and Gosselin, 2007):

$$\begin{aligned} \hat{\epsilon}_{01}^i &= \begin{bmatrix} \mathbf{u}_{1i} \\ \mathbf{a}_i \times \mathbf{u}_{1i} \end{bmatrix}, \hat{\epsilon}_{02}^i = \begin{bmatrix} \mathbf{u}_{2i} \\ \mathbf{a}_i \times \mathbf{u}_{2i} \end{bmatrix}, \hat{\epsilon}_{03}^i = \begin{bmatrix} \mathbf{u}_{3i} \\ \mathbf{b}_i \times \mathbf{u}_{3i} \end{bmatrix} \\ \hat{\epsilon}_{04}^i &= \begin{bmatrix} \mathbf{u}_{4i} \\ \mathbf{b}_i \times \mathbf{u}_{4i} \end{bmatrix}, \hat{\epsilon}_{05}^i = \begin{bmatrix} \mathbf{u}_{5i} \\ \mathbf{b}_i \times \mathbf{u}_{5i} \end{bmatrix}, \quad i = 1, 2, 3. \end{aligned} \quad (9.17)$$

\mathbf{u}_{1i} and \mathbf{u}_{2i} are the unit vectors of the first and second revolute joint axes of the universal joint of the i -th leg. \mathbf{u}_{3i} , \mathbf{u}_{4i} and \mathbf{u}_{5i} are the unit vectors of the revolute joints associated with the spherical joint of the i -th leg. \mathbf{a}_i and \mathbf{b}_i are the Cartesian coordinate vectors of points A_i and B_i shown in Figure 9.14. The

twist system T of the 3-US is the intersection of T^1 , T^2 and T^3 , namely,

$$T_{3US} = \bigcap_{i=1}^3 T^i. \quad (9.18)$$

Constraint wrench system

A *wrench* is a screw representing a system of forces and moments acting on a rigid body. The constraint wrench system describes how the legs constrain the end-effector of the 3-US parallel manipulator. Hence, for each leg, the constraint wrench associated to the leg must be reciprocal to the twist system T^i of the leg. In a non-singular configuration, the constraint wrench system W^c of the 3-US is a three-system spanned by the following three pure forces (Fig. 9.15):

$$\mathcal{F}_i^c = \begin{bmatrix} \mathbf{n}_i \\ \mathbf{b}_i \times \mathbf{n}_i \end{bmatrix}, \quad i = 1, 2, 3 \quad (9.19)$$

\mathbf{n}_i being the unit vector of $\overrightarrow{A_i B_i}$.

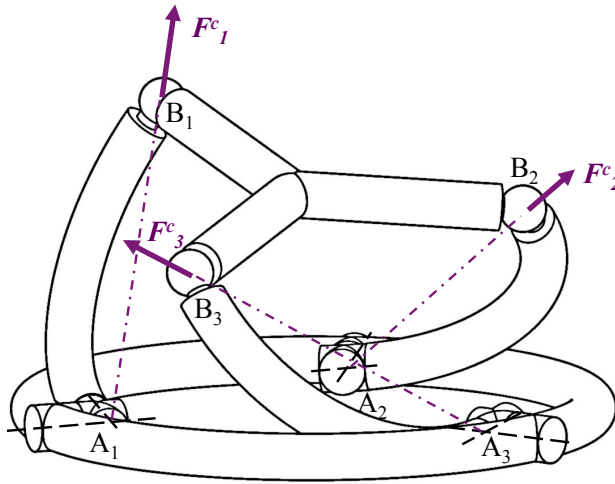


Figure 9.15 Constraint forces applied by the legs to the moving-platform.

Actuation wrench system

The actuation wrench system W^a of the 3-US manipulator depends on its actuation scheme and describes how the actuators act on the end-effector. Hence, for each leg, the actuation wrench should be reciprocal to the twists in the leg, except for the twist associated with the actuated joint. Moreover, it should lie in the constraint wrench system W^c . In case the first revolute joint of each leg

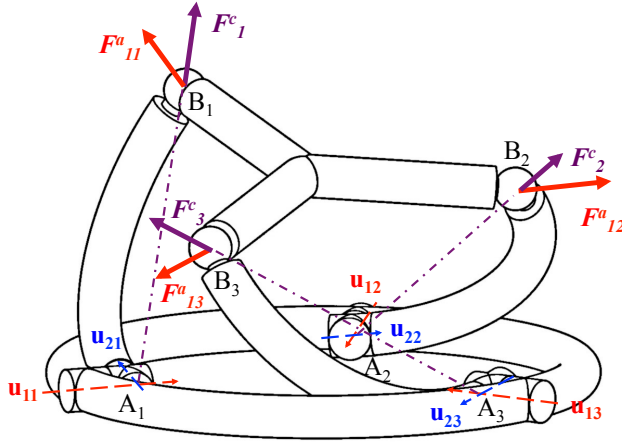


Figure 9.16 Constraint and actuation wrench system of the 3-US parallel manipulator for the first actuation mode.

is actuated, W^a is spanned by the following three pure forces, called actuation forces (Fig. 9.16):

$$\hat{\mathcal{F}}_{1i}^a = \begin{bmatrix} \mathbf{u}_{2i} \\ \mathbf{b}_i \times \mathbf{u}_{2i} \end{bmatrix}, \quad i = 1, 2, 3. \quad (9.20)$$

In case the second revolute joint of each leg is actuated, W^a is spanned by the following three pure forces:

$$\hat{\mathcal{F}}_{2i}^a = \begin{bmatrix} \mathbf{u}_{1i} \\ \mathbf{b}_i \times \mathbf{u}_{1i} \end{bmatrix}, \quad i = 1, 2, 3. \quad (9.21)$$

In case the j -th revolute joint of each leg is actuated, $j = 3, 4, 5$, W^a is spanned by the following three pure forces:

$$\hat{\mathcal{F}}_{ji}^a = \begin{bmatrix} \mathbf{v}_{ji} \\ \mathbf{c}_{ji} \times \mathbf{v}_{ji} \end{bmatrix}, \quad i = 1, 2, 3 \quad (9.22)$$

\mathbf{v}_{ji} being the unit vector of the intersection line \mathcal{L}_{ji} of planes \mathcal{P}_{1i} and \mathcal{P}_{ji} . \mathbf{c}_{ji} is the Cartesian coordinate vector of any point C_{ji} on line \mathcal{L}_{ji} . \mathcal{P}_{1i} is spanned by vectors \mathbf{u}_{1i} and \mathbf{u}_{2i} and passes through point A_i . \mathcal{P}_{3i} is spanned by vectors \mathbf{u}_{4i} and \mathbf{u}_{5i} and passes through point B_i . \mathcal{P}_{4i} is spanned by vectors \mathbf{u}_{3i} and \mathbf{u}_{5i} and passes through point B_i . \mathcal{P}_{5i} is spanned by vectors \mathbf{u}_{3i} and \mathbf{u}_{4i} and passes through point B_i (Fig. 9.17 for the fourth actuation mode).

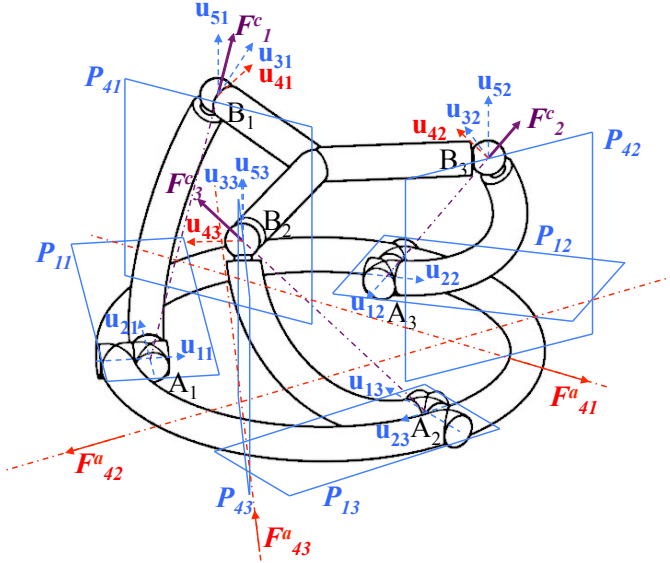


Figure 9.17 Constraint and actuation forces of the 3-US parallel manipulator for the fourth actuation mode.

Global wrench system

Let k be the number of the actuated joint in each leg for the k -th actuation mode of the mechanism, $k = 1, \dots, 5$. As a result, the global wrench system \mathcal{W}_{3US}^k of the 3-US associated with its k -th actuation scheme is spanned by \mathcal{W}^a and \mathcal{W}^c , namely,

$$\mathcal{W}_{3US}^k = \text{span}(\hat{\mathcal{F}}_1^c, \hat{\mathcal{F}}_2^c, \hat{\mathcal{F}}_3^c, \hat{\mathcal{F}}_{k1}^a, \hat{\mathcal{F}}_{k2}^a, \hat{\mathcal{F}}_{k3}^a), \quad k = 1, \dots, 5. \quad (9.23)$$

Instantaneous gained motions

For the manipulator in the planar configuration and for the five symmetrical actuation modes, the three actuation forces are in the plane of the manipulator (Fig. 9.18a). It means that the actuation wrench system degenerates and the 3-US manipulator reaches a parallel singularity in such a configuration. As the three actuation forces are coplanar, the actuators are not able to counterbalance the forces normal to the end-effector and the moments around the axes in the plane of the manipulator.

In Section *Actuation wrench system* (p. 254) we have seen that actuating any of the five revolute joints of a leg produces an actuation force in the plane of the planar configuration. In other words, there is no actuation mode that produces non-coplanar actuation forces. It means that for any of the 150 asymmetrical possible actuation modes, the actuation wrench system will always be composed

of coplanar pure forces in the planar configuration of the 3-US manipulator. As a consequence, the planar configuration of the 3-US parallel manipulator is, for the 155 possible actuation modes, a singular configuration of Type 2 where the end-effector exhibits the desired instantaneous RRP mobilities. 155 unique architectures can thus be considered when designing a compliant structure with adequate mobilities. Design and manufacturing considerations are used to make a selection.

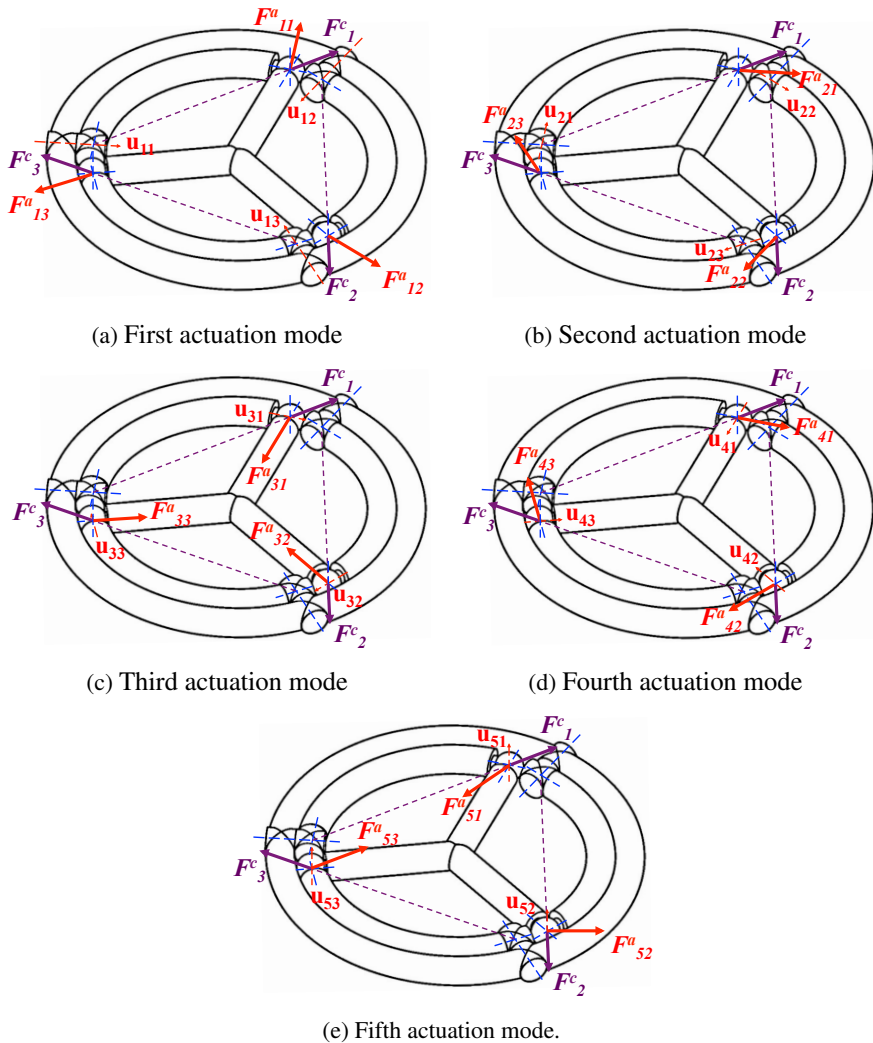


Figure 9.18 Constraint and actuation forces of the 3-US parallel manipulator for the five actuation modes.

9.5.6 Step 3: selection of an actuation mode

A first remark is that the design of a spherical flexure joint is complex. In fact, two design options can be considered. One solution consists in designing a single revolute notch (Xu and Li, 2006). With this solution, the ratio between the translational and the rotational stiffnesses along the revolution axis of this joint can be low. Thus, the kinematic behaviour would be different of that of a spherical joint. Moreover, the small cross-section can lead to high stresses. A second solution consists in designing a spherical flexure joint with three compliant revolute joints. Stiffness properties are improved, but since we would like to have a device composed of two planar mechanisms, the joint needs to be machined in a plate. Manufacturing three compliant revolute joints with orthogonal and intersecting axes as proposed by (Xu and Li, 2006) is then complex. Thus it is more interesting to choose an actuation mode which allows to suppress one revolute joint that composes the spherical joints and therefore to have a flexure mechanism only composed of universal joints.

In order to machine this planar structure, it is more convenient to machine flexure joints with revolute joint axes in the plane. Hence, it seems easier to consider the fifth symmetric actuation mode (\mathbf{u}_{5i} , Fig. 9.14), which suppresses the three revolute axes normal to the base and moving platform in the planar configuration of the 3-US manipulator. As a result, the 3-US architecture becomes a 3-UU architecture as illustrated in Figure 9.19.

To the best of our knowledge, such an architecture has never been considered to obtain this type of mobilities. Without the proposed approach, it would have been very difficult to identify this structure for the design of the active stabiliser.

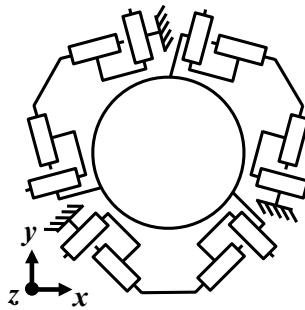


Figure 9.19 3-UU planar mechanism with RRP mobilities.

9.5.7 Step 4: design of the flexure mechanism

The 3-UU flexure mechanism is only composed of universal joints. Interesting designs of compliant universal joints have been proposed in (Xu and Li, 2006)

and (Tanik and Parlaktas, 2012), but they can not be manufactured in a planar structure or requires an assembly.

For the design of the compliant universal joints we therefore propose manufacturing two compliant revolute joints in the plane with intersecting axes in A_i or B_i depending on the considered universal joint. The 3-UU flexure mechanism is then designed by replacing each revolute joint by a circular flexure hinge. A computer-aided design (CAD) of the compliant 3-UU mechanism is shown in Figure 9.20.

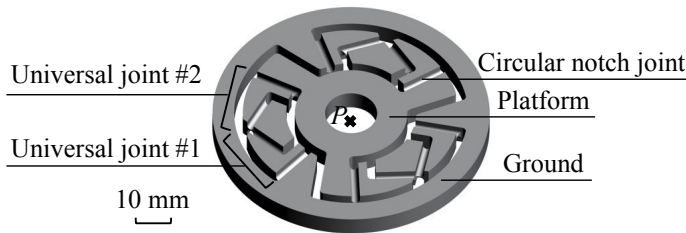


Figure 9.20 CAD view of the 3-UU flexure mechanism.

Considering our study case, the dimensional synthesis of the obtained flexure mechanism is performed by considering the other elements that compose the active stabiliser, i.e., the two prismatic joints and the spherical joint.

The length of the stabiliser shaft $b = 250$ mm is constrained by the medical context. The only way to modify the amplification ratio of the device is therefore to modify the distance a between planes P_1 and P_2 . The distance a cannot exceed 12 mm (Fig. 9.4) to get sufficient shaft displacements. In this situation, static analysis shows that the PZT stacks deliver forces above 100 N in O_1 .

Contrarily to the previous section, there is no kinematical model for the 3-UU mechanism. Thus, for a first dimensional synthesis of the 3-UU mechanism, a trial-and-error design is performed using finite element analysis (FEA). To limit the number of possibilities, we only tuned two design parameters: the radius and the thickness of the circular notches. As a matter of fact, the notch thicknesses mainly influence the global stiffness of the compliant structure and the circular notch radius mainly influences the level of the stress concentration. The goal is then to find a good compromise between output displacement amplitude of the whole mechanism and the maximal stress level. Finally, the thickness of the 3-UU mechanism and the outer radius of its legs have been chosen equal to 5 mm and 35 mm, respectively. The compliant joints have a thickness equal to 0.2 mm, a width equal to 15 mm and the radius of the circular notches is equal to 2 mm.

9.5.8 Performance of the flexure mechanism

With the considered design, PZT stacks should apply forces in the order of 300 N on the planar 3-UU flexure mechanism in order to counterbalance the cardiac forces during the stabilisation task. Stiffness of the mechanism must be high enough in order to limit the deflections that can lower the device performance. In Figure 9.21a and 9.21c, 300 N forces are applied in the plane XY . This produces an in-plane displacement of less than 20 μm which is small compared to the 0.7 mm that can be generated by the device. In comparison, in Figure 9.21e, applying 300 N along Z produces a displacement of 10 mm. The in-plane stiffnesses are therefore 200 times greater than along Z . In Figure 9.21b and 9.21d, a moment of 100 N·mm around X and Y is applied and produces a rotation of $1.3\text{e-}2$ rad. In comparison, in Figure 9.21f applying a moment of 100 N·mm around Z only produces a rotation of $1.0\text{e-}5$ rad. The torsional stiffness is 1300 times greater than the other rotational stiffnesses.

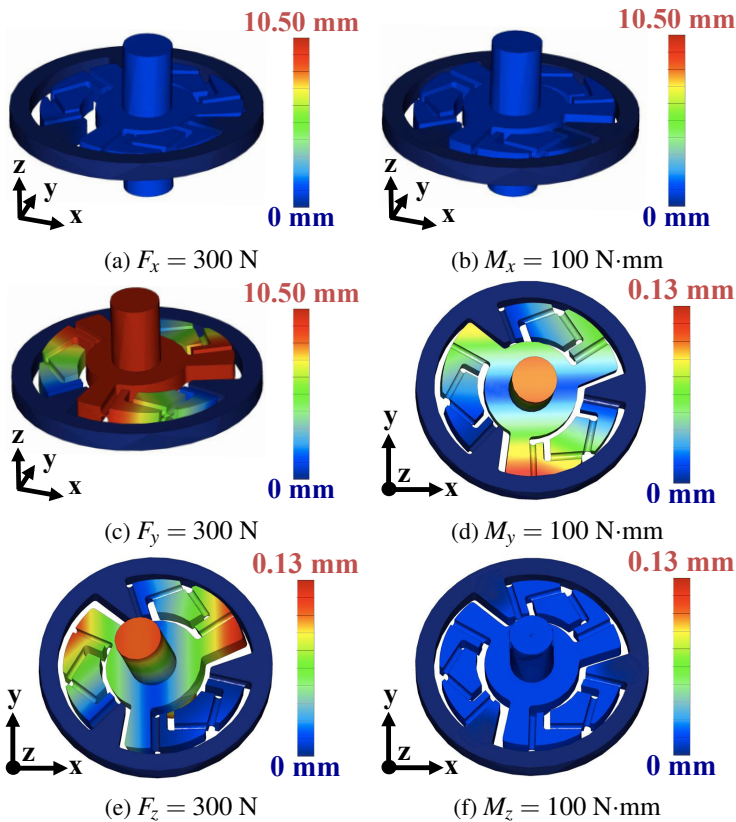


Figure 9.21 Finite element analysis of the 3-UU mechanism. Forces F and moments M are applied at the center of the mechanism.

The estimation of the compliance of the 3-UU structure is given by the compliance matrix, a 6×6 matrix, which relates the displacement $\mathbf{u} = [x; y; z; \theta_x; \theta_y; \theta_z]$, in millimeters and in radians, to the load $\mathbf{L} = [F_x; F_y; F_z; M_x; M_y; M_z]$, in newtons and newtons per millimeter, applied at the center of the end-effector:

$$\mathbf{u} = \mathbf{C} \cdot \mathbf{L} \quad (9.24)$$

The 6×6 compliance matrix \mathbf{C} is evaluated using a finite element analysis (PTC Pro/Mechanica):

$$\mathbf{C} = \begin{bmatrix} \mathbf{4.6e-5} & 1.0e-8 & 2.6e-8 & -4e-8 & -6.7e-6 & 3.5e-9 \\ 5.4e-8 & \mathbf{4.6e-5} & 1.6e-7 & -6.6e-6 & 8.0e-6 & 7e-10 \\ 1.4e-8 & 2.0e-8 & \mathbf{3.5e-2} & 2.3e-6 & 1.1e-6 & 2.9e-9 \\ -5.6e-9 & 0.0 & 4.6e-6 & \mathbf{1.3e-4} & -1.2e-7 & 9.3e-11 \\ 0.0 & 1.7e-9 & 6.8e-7 & 1.1e-8 & \mathbf{1.3e-4} & 2.5e-9 \\ 1.4e-9 & 0.0 & 0.0 & 0.0 & 0.0 & \mathbf{1e-7} \end{bmatrix} \quad (9.25)$$

When three forces are applied at the center of the mechanism, there is only a displacement along the vertical axis. When three moments are applied at the center of the mechanism, there are only two significant rotations about in-plane axes. Therefore, from a kinematic point-of-view, the behaviour of the mechanism is in accordance with the need for a RRP mechanism.

9.6 Selection of an actuation mechanism

The coupling mechanism must be integrated in one of the two planes. As the 3-RRR compliant orientation mechanism will be integrated in the first plane, the coupling mechanism will be integrated in the second one. Therefore, the coupling mechanism will be integrated in the actuation mechanism. Among the 2-DOF planar parallel mechanism proposed in the literature, the 2PRR-RR mechanism proposed by (Gosselin, 1996) is particularly relevant: it has a planar geometry and it can integrate the coupling mechanism in its platform. As it will be actuated by piezoelectric actuators, it will only work around a given configuration. Considering q_1 and q_2 the actuators positions and x and y the cartesian coordinates of the platform point O_2 , the configuration illustrated in figure 9.22 allows, locally for small displacements, a decoupling and a direct transmission of the actuators to O_2 as shown by the Jacobian matrix in equation 9.26. As the ratio between the actuators displacements δx , δy and the distance B_3O_2 is high, the induced rotation $\delta\theta$ of the platform remains of small amplitude, and is therefore not a concern for the application.

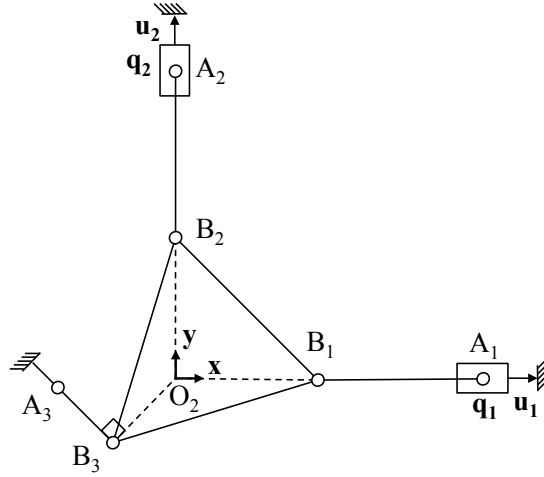
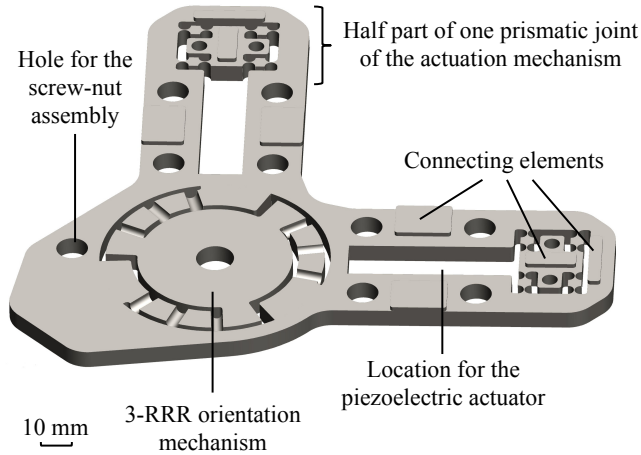


Figure 9.22 Chosen configuration for the 2-PRR 1-RR actuation mechanism.

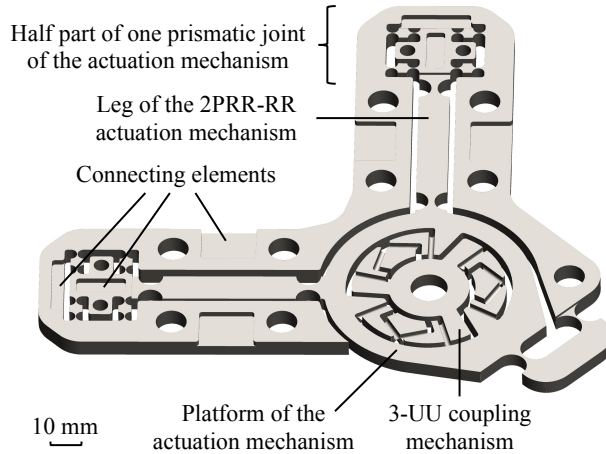
$$\begin{pmatrix} \delta x \\ \delta y \\ \delta \theta \end{pmatrix} = \begin{pmatrix} 1 & 0 \\ 0 & 1 \\ \frac{-\sqrt{2}}{2B_3O_2} & \frac{\sqrt{2}}{2B_3O_2} \end{pmatrix} \begin{pmatrix} \delta q_1 \\ \delta q_2 \end{pmatrix} \quad (9.26)$$

9.7 Integration of the three mechanisms in two planes

The different components of the compensation mechanism must be integrated in only two planes. In the first plane, only the orientation mechanism must be integrated in contrary to the second plane which contains the coupling mechanism and the actuation mechanism. Therefore, we propose, in addition to the 3-RRR flexure mechanism, to integrate the two piezoelectric actuators in the first plane. Since the piezoelectric actuators need obviously to be linked to the actuation mechanism, the two compliant prismatic joints of the actuation mechanism are decomposed in two parts designed in the two planes with connecting elements in order to transmit the actuator forces from the first plane to the second plane. This is illustrated in Figure 9.23a, with the first machined plane. It contains the 3-RRR flexure mechanism for the shaft orientation, the two locations for the piezoelectric actuators and the two half compliant prismatic joints for the force transmission with the second plane. In the second machined plane, illustrated in Figure 9.23b, we can find the actuation mechanism with the embedded 3-UU compliant coupling mechanism. The two planes are assembled and maintained in position with dedicated connecting elements, screws and



(a) First plane of the compensation mechanism



(b) Second plane of the compensation mechanism

Figure 9.23 Integration of the planar flexure mechanisms.

nuts. The assembled device with its piezoelectric actuators is illustrated in Figure 9.24a.

After a simple trial and error pre-dimensioning of the whole mechanism using FEA, we obtain interesting performances. The planar structures in P_1 and P_2 have thicknesses equal to 5 mm and 6 mm respectively. The presented design allows us to produce a displacement of 0.7 mm which is sufficient to compensate for the flexibilities of the device and the mounting system, according to (Bachta et al., 2011). With an optimisation process, this output displacement could still be increased as the maximal stress level reaches only 82% of the fatigue limit of the material, which is here alloy steel. Finally,

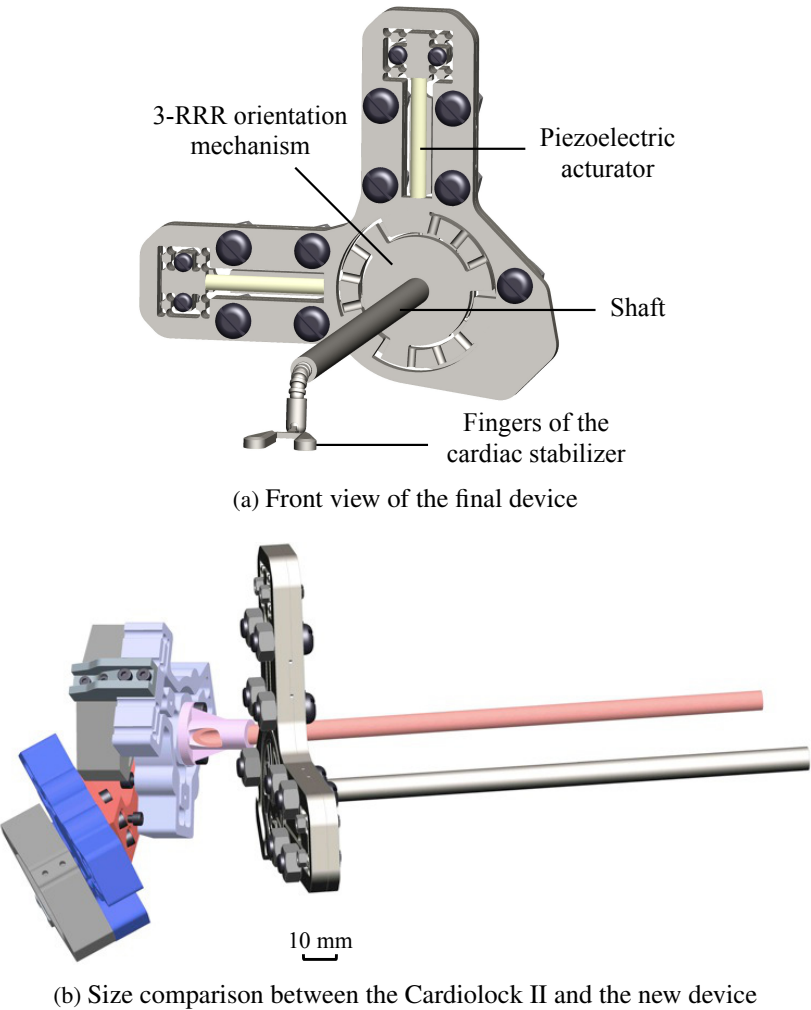


Figure 9.24 Compensation mechanism based on planar flexure mechanisms.

the size of the device is divided by four compared to the previous one, the *Cardiolock II* (Fig. 9.3). The device compactness is significantly improved by considering an assembly of planar structures.

9.8 Conclusion

In this chapter we have presented, through the example of the design of a 2-DOF compensation mechanism for an active cardiac stabiliser, different

design approaches for planar flexure mechanisms based on a 3-RRR and 3-US parallel mechanisms.

The first design approach consists in decomposing a complex compliant structure in an assembly of planar parallel compliant structures in order to consider microfabrication processes which is based on layer design but also simplify macrofabrication processes.

This approach implies of thinking in a plane while out-of-plane motions are still required. This leads to consider 3D parallel mechanisms in a planar configuration which is often a singular configuration. From this observation, two additional design approaches have been presented in this chapter.

The first consists of being close to the planar configuration in order to have the compactness and at the same time avoiding the singularities by introducing asymmetry in the manufacturing of the compliant structure. Thus it is still possible to apply the pseudo-rigid body modelling and perform classical geometry optimisation from the model of the mechanism.

The second, on the contrary, takes advantage of the singularities to design a passive parallel architecture with interesting stiffness properties. Here the designer benefits from knowledge of the singularity analysis of parallel manipulator in the literature in order to explore designs of non-trivial compliant structures. The configuration of the mechanism remains planar and the compliant structure can be simplified by removing superfluous joints.

Finally a new highly compact active cardiac stabiliser has been presented in this chapter. However this architecture can be used for any micromechanism requiring out of plane rotations, such as miroir tilting for MEMS, for example.

Afterword

It may seem surprising that a general methodology for conceiving flexible structure was first attempted only in the 21st Century, even though mechanisms have always required bearings and the theoretical tools for analysing them have been adequate since the 19th Century, as described in (Timoshenko, 1953). An explanation can be found in (Daumas, 1968):

Technological inventively can seldom be reduced to a single event or to a single person. It is a complex process which, before resulting in industrial innovation, benefits from centuries of experience, accumulated from one generation to the next by individuals most often separated by time and space. It takes its finalised form only when the era allows it. A number of concurrent factors are required to make it both possible and useful, and the social context has to be sufficiently mature. We observe that this process is continually accelerating as we approach the current age.

Flexure mechanisms illustrate this: they were made possible by the advent of wire electro-discharge machining as a widespread reliable machining technology. Moreover, they perfectly satisfy the requirement of very precise robot motion as well as particle free and lubrication free bearings in harsh environments, such as operating rooms in medicine and clean rooms for semiconductor manufacturing. This conjunction explains the rapid rise in the last twenty years of flexure mechanisms in a wide variety of applications fields: Micro-Electro-Mechanical-Systems (MEMS), Optomechanical mechanisms for aerospace, earth based telescopes and medical instruments. This book compiles the work of four Ph.D. theses published between 2000 and 2013, therefore covering a substantial span of flexure mechanism design history.

The text addresses flexure mechanism design by starting with the simplest and most well-known building blocks, the elastic leaf spring and the elastic rod. A higher level of design complexity is achieved by showing how these elementary elastic elements can be combined to constitute bearings with a limited number of degrees of freedom to design the common pivot joint, linear guide, universal joint, ball joint, etc. Flexure-based bearings in high precision robotics is addressed in more depth: advanced flexure-based modules are presented and combined to constitute multi-degrees-of-freedom articulated structures. Parallel kinematic design specific to robotics is combined with flexure bearing design.

A concrete example is the design of a five degree-of-freedom robot. A second example is the design of a long stroke rectilinear bearing used in a Watt scale at the Swiss Federal Institute of Metrology (METAS) to provide a new standard of the kilogram unit of mass. Two very different architectures satisfying the specifications are proposed with both architectures leading to outstanding kinematic performance with straightness error on the order of 200 nm for strokes on the order of 30 mm, i.e., straightness ratios of order 10^5 .

The book ends with novel kinematic design approaches exploiting the specificity of flexure mechanism. Indeed the latter are well suited for monolithic planar or '2.5 D' design and the realisation of planar mechanisms having out-of-plane functionality. This shows how 'design for manufacturability' can be integrated into the design process. The concrete example of an active beating heart stabiliser for heart surgery illustrates this approach.

Our conceptual approach as well as specific mathematical formulas, realised systems and detailed experimental data, will be useful to engineers facing concrete design issues. The authors are convinced that flexure mechanisms have yet to achieve their full potential and that they will become indispensable in the technology of tomorrow. This book is not just a design aid, but also a springboard for creativity in science and engineering.

Bibliography

- Ackerson, D. S. and Harry, D. R. (1985). Theory, experimental results, and recommended standards regarding the static positioning and orienting precision of industrial robots. *Robotics and Computer-Integrated Manufacturing*, 2, No. 3/4:247–59.
- Amine, S., Tale-Masouleh, M., Caro, S., Wenger, P., and Gosselin, C. (2012). Singularity analysis of 3T2R parallel mechanisms using Grassmann-Cayley algebra and Grassmann line geometry. *Mechanism and Machine Theory*, 52:326–340.
- Ananthasuresh, G. K. and Kota, S. (1995). Designing compliant mechanisms. *Mechanical Engineering*, 117(11):93–96.
- Andersen, C., Magleby, S., and Howell, L. (2009). Principles and preliminary concepts for compliant mechanically reactive armor. In *ASME/IFTOMM International Conference on Reconfigurable Mechanisms and Robots. ReMAR 2009*, pages 370–376.
- André, P., Kauffmann, J.-M., Lhote, F., and Taillard, J.-P. (1983). *Les robots*, volume 4. Hermes Publishing, France.
- Artobolevski, I. (1975). *Les mécanismes dans la technique moderne*, volume 1. Edition MIR, Moscou.
- Asimov, I. (1997). *The Roving Mind*. Prometheus Books, New York.
- Bacher, J.-P. (2003). *Conception de robots de très haute précision à articulations flexibles : interaction dynamique-commande*. PhD thesis, Ecole polytechnique fédérale de Lausanne (EPFL). No. 2907.
- Bachta, W., Renaud, P., Laroche, E., and Gangloff, J. (2011). The Cardiolock project: Design of an active cardiac stabilizer for cardiac surgery. *ASME Journal of Mechanical Design*, 133(7):071002–1–071002–10.
- Beams, J. W., Young, J. W., and Moore, J. W. (1946). The production of high centrifugal fields. *Journal of Applied Physics*, 17:886–890.
- BEI Kimco Magnetics (2015). Voice Coil Actuators and Brushless DC Motors for Industrial, Aerospace/Defense, and Transportation Applications, <http://www.beikimco.com>.
- Bellouard, Y. (2000). *Conception de dispositifs en alliage à mémoire de forme en microtechnique*. PhD thesis, Ecole polytechnique fédérale de Lausanne (EPFL). No. 2308.

- Bleuler, H. (1984). *Decentralized Control of Magnetic Rotor Bearing Systems*. Ph D. thesis, Swiss Federal Institute of Technology Zürich (ETHZ).
- Blum, C. (2005). Ant colony optimization: Introduction and recent trends. *Physics of Life Reviews*, 2(4):353–373.
- Boillat, P. (1997). Compteur d'énergie pour vélo. *Travail pratique de diplôme, IPM-DMT-EPFL*.
- Bonev, I. and Gosselin, C. (2006). Analytical Determination of the Workspace of Symmetrical Spherical Parallel Mechanisms. *Robotics, IEEE Transactions on*, 22(5):1011–1017.
- Bonev, I. A., Zlatanov, D., and Gosselin, C. M. (2003). Singularity Analysis of 3-DOF Planar Parallel Mechanisms via Screw Theory. *Journal of Mechanical Design*, 125(3):573–581.
- Boresi, A. P., Schmidt, R. J., and Sidebottom, O. M. (1993). *Advanced Mechanics of Materials*. John Wiley and Sons, Inc., USA, 5th edition.
- Brand, A. (1984). Fatigue des alliages ferreux: approche classique. *Techniques de l'Ingénieur*, B5 I:B5050.
- Bryant, J. and Sangwin, C. (2008). *How round is you circle, where engineering and mathematics meet*. Princeton University Press.
- Carricato, M. and Parenti-Castelli, V. (2004). A novel fully decoupled two-degrees-of-freedom parallel wrist. *The International Journal of Robotics Research*, 23(6):661–667.
- Chapuis, D., Gassert, R., Sache, L., Burdet, E., and Bleuler, H. (2004). Design of a simple MRI/fMRI compatible force/torque sensor. In *IEEE/RSJ International Conference on Intelligent Robots and Systems*, volume 3, pages 2593–2599.
- Choi, D. and Riviere, C. (2005). Flexure-based manipulator for active handled microsurgical instrument. In *27th Annual International Conference of the IEEE Engineering in Medicine and Biology Society*, pages 2325–2328.
- Choueifati, J., Lusk, C., Pang, X., and Volinsky, A. A. (2007). Compliant MEMS Motion Characterization by Nanoindentation. In *MRS Proceedings*, volume 1052.
- Clavel, R. (1991). *Conception d'un robot parallèle rapide à 4 degrés de liberté*. PhD thesis, Ecole polytechnique fédérale de Lausanne (EPFL). No. 925.
- Clavel, R. (1994). Robots parallèles. *Techniques de l'Ingénieur*, R7710:1–8.
- Coiffet, P. (1992). *La robotique*. Paris: Hermes, 3rd edition.
- Collins, J. A. (1993). *Failure of materials in mechanical design*. John Wiley and Sons, New York, 2nd edition.

- Danescu, G. (1995). *Une méthode algébrique de synthèse et conception des mécanismes articulés*. PhD thesis, U.F.R. des Sciences et Techniques de l'Université de Franche-Comté. No. 460.
- Daumas, M. (1968). *Histoire générale des techniques, Tome III : L'expansion du machinisme*, pages VII–XXIV. Presses universitaires de France.
- Del Pedro, M. (1985). *Cours de résistance de matériaux*, volume 1 and 2. Ecole polytechnique fédérale de Lausanne, Département de mécanique, Laboratoire de mécanique appliquée.
- Del Pedro, M. and Gmür, T. (2001). *Eléments de mécanique des structures*. Presses polytechniques et universitaires romandes, Lausanne.
- Del Pedro, M. and Pahud, P. (1989). *Mécanique vibratoire*. Presses polytechniques et universitaires romandes, Lausanne.
- DiBiasio, C. M. and Culpepper, M. L. (2012). A building block synthesis approach for precision flexure systems with integrated, strain-based position sensing. *Precision Engineering*, 36(4):673–679.
- Domininghaus, H. (1993). *Plastics for Engineers*. Hanser Publishers, Munich.
- Dorigo, M., Di Caro, G., and Gambardella, L. M. (1999). Ant algorithms for discrete optimization. *Artificial Life*, 5:137–172.
- Dorigo, M. and Gambardella, L. M. (1997). Ant colonies for the travelling salesman problem. *Biosystems*, 43(2):73–81.
- Dowson, D. (1998). *History of Tribology*. Professional Engineering Publishing Limited, London and Bury St Edmunds, 2nd edition.
- Duchemin, M. (1984). Ressorts: considérations générales. *Techniques de l'Ingénieur*, B5 II:B5430.1–B5430.18.
- Duprat, D. (1997). Fatigue et mécanique de la rupture des pièces en alliage léger. *Techniques de l'Ingénieur*, B5 I:B5052.
- Eichenberger, A., Baumann, H., Jeanneret, B., Jeckelmann, B., Richard, P., and Beer, W. (2011). Determination of the Planck constant with the METAS watt balance. *Metrologia*, 48(3):133–141.
- Eichenberger, A., Genevès, G., and Gournay, P. (2009). Determination of the Planck constant by means of a Watt balance. *European Physical Journal Special Topics*, 172(1):363–383.
- Erdman, A. G., editor (1993). *Modern Kinematics. Developments in the last forty years*. John Wiley and Sons, Inc.
- Fazenda, N. (2007). *Calibration of high-precision flexure parallel robots*. PhD thesis, Ecole polytechnique fédérale de Lausanne (EPFL). No. 3712.

- Ferrell, D. B., Isaac, Y. F., Magleby, S. P., and Howell, L. L. (2011). Development of criteria for lamina emergent mechanism flexures with specific application to metals. *Journal of Mechanical Design*, 133(3):031009.
- Flückiger, L. (1998). *Interface pour le pilotage et l'analyse des robots basée sur un générateur de cinématiques*. PhD thesis, Ecole polytechnique fédérale de Lausanne (EPFL). No. 1897.
- Fowler, R. M., Howell, L. L., and Magleby, S. P. (2011). Compliant space mechanisms: A new frontier for compliant mechanisms. *Mechanical Sciences*, 2(2):205–215.
- Gallego, J. A. and Herder, J. (2009). Synthesis methods in compliant mechanisms: An overview. In *ASME 2009 International Design Engineering Technical Conferences and Computers and Information in Engineering Conference*, pages 193–214.
- Genequand, P.-M. (1996). Dispositif de liaison unidirectionnelle entre deux objets. *Demande de Brevet Européen EP 0 770 813 A1*.
- Genevès, G., Gournay, P., Villar, F., Pinot, P., Juncar, P., Lecollinet, M., Chassagne, L., Clairon, A., Landragin, A., Holleville, D., Pereira Dos Santos, F., David, J., Besbes, M., Alves, F., Topcu, S., Haddad, D., Gosset, A., Silvestri, Z., Meury, P.-A., Madec, T., and Mace, S. (2007). La balance du Watt : vers une nouvelle définition de l'unité de masse ? *Revue française de métrologie*, 9(1):3–34.
- Genoud, D. (2000). Capteur de puissance pour vélo. *Travail pratique de diplôme, IPM-DMT-EPFL*.
- Gere, J. M. and Timoshenko, S. P. (1990). *Mechanics of Materials*. PWS-KENT, Boston, 3rd edition.
- Girard, L. D. (1865). Hydraulique appliquée: note sur le chemin de fer glissant. (*Gauthier-Villars, Paris*), (8p).
- Gogu, G. (2008-2010). *Structural Synthesis of Parallel Robots, Part I - Methodology, Part II - Translational Topologies with Two and Three Degrees of Freedom, Part III - Topologies with planar motion of the moving platform*. Springer, Berlin.
- Gollnick, P. S., Magleby, S. P., and Howell, L. L. (2011). An introduction to multilayer lamina emergent mechanisms. *Journal of Mechanical Design*, 133(8):081006.
- Gosselin, C. and Angeles, J. (1989). The optimum kinematic design of a spherical three-degree-of-freedom parallel manipulator. *Journal of Mechanisms, Transmissions, and Automation in Design*, 111:202–207.
- Gosselin, C. and Angeles, J. (1990). Singularity analysis of closed-loop kinematic chains. *IEEE Transactions on Robotics and Automation*, 6(3):281–290.
- Gosselin, C. and Hamel, J.-F. (1994). The agile eye: A high-performance three-degree-of-freedom camera-orienting device. In *IEEE International Conference on Robotics and Automation*, pages 781–786.

- Gosselin, C. M. (1996). Kinematische und statische analyse eines ebenen parallelen manipulators mit dem freiheitsgrad zwei: Kinematic and static analysis of a planar two-degree-of-freedom parallel manipulator. *Mechanism and Machine Theory*, 31(2):149–160.
- Gosselin, C. M. and St-Pierre, E. (1997). Development and experimentation of a fast 3-dof camera-orienting device. *The International Journal of Robotics Research*, 16(5):619–630.
- Gregorio, R. D. (2004). Kinematics of the 3-RSR wrist. *IEEE Transactions on Robotics and Automation*, 20:750–754.
- Grübler (1917). *Getriebelehre*. Springer, Berlin.
- Han, B., He, Q., Zhang, Z., Li, Z., and Li, C. (2010). The Magnetic System of Joule Balance in NIM. In *Conference on Precision Electromagnetic Measurements*, pages 526–527, Daejeon Convention Center, Daejeon, Korea.
- Haringx, J. A. (1949). The cross-spring pivot as a constructional element. *Applied Science Research*, A1:313–332.
- Helmer, P. (2006). *Conception systématique de structures cinématiques orthogonales pour la micro-robotique*. PhD thesis, Ecole polytechnique fédérale de Lausanne (EPFL). No. 3365.
- Henein, S. (2001). *Conception des guidages flexibles*. Presses Polytechniques et Universitaires Romandes, Collection Meta, Lausanne.
- Henein, S., Boillat, P., and Jacot, J. (2000). Power sensing device. *Demande de brevet EP 00109196.6*. Titulaire : Sensile Technologies SA.
- Henein, S., Bottinelli, S., and Aymon, C. (1998). Pivot flexible à grande course angulaire et à rigidité élevée. *Brevet Europe No. 98123953.6*. Titulaire: Sysmelec S.A. CH-2002 Neuchâtel.
- Henein, S., Spanoudakis, P., Droz, S., Myklebust, L. I., and Onillon, E. (2003). Flexure pivot for aerospace mechanisms. In *Proceedings of the 10th European Space Mechanisms and Tribology Symposium*, Spain.
- Hirn, G. (1854). Sur les principaux phénomènes qui présentent les frottements médiats. *Bulletin de la Société Industrielle de Mulhouse*, 26:188–277.
- Hodac, A. (1999). *A macro/micro-manipulator for high speed and accurate pick and place operations*. PhD thesis, Swiss Federal Institute of Technology Zurich (ETHZ). ETH No. 13148.
- Hopkins, J. B. and Culpepper, M. L. (2011). Synthesis of precision serial flexure systems using freedom and constraint topologies (FACT). *Precision Engineering*, 35(4):638 – 649.

- Howell, L. (2001). *Compliant mechanisms*. Wiley-IEEE.
- Hull, D. and Clyne, T. W. (1996). *An Introduction to Composite Materials*. Cambridge Solid State Science Series. Cambridge University Press, 2nd edition.
- Hunt, K. H. (1978). *Kinematic Geometry of Mechanisms*. Oxford University Press, Oxford.
- Jacobsen, J. O., Chen, G., Howell, L. L., and Magleby, S. P. (2009). Lamina Emergent Torsional (LET) Joint. *Mechanism and Machine Theory*, 44(11):2098–2109.
- Jacobsen, J. O., Howell, L. L., and Magleby, S. P. (2007). Components for the Design of Lamina Emergent Mechanisms. *ASME Conference Proceedings*, 2007(43041):165–174.
- Jones, R. (1962). Some Uses of Elasticity in Instrument Design. *Journal of Scientific Instrumentation*, 39(5):193–203.
- Kajastie, H., Riski, K., and Satrapinski, A. (2009). Mass determination with the magnetic levitation method proposal for a new design of electromechanical system. *Metrologia*, (46):298–304.
- Katoh, T., Tsuda, N., and Sawabe, M. (1984). One Piece Compound Parallel Spring with Reduction Flexure Levers. *Bulletin of Japan Society of Precision Engineering*, 18(4):329–334.
- Kemper, H. (1937). Overhead suspension railway with wheelless vehicles employing magnetic suspension from iron rails. *German Patent Nr 643316 and 644302*.
- Kobel, P. and Clavel, R. (2011). Miniaturization Challenges and Their Impact on the Micro-factory Concept and Manipulators. *Japan of the Japan Society of Precision Engineering*, 77(3):263–268.
- Koetsier, T. (1983). A Contribution to the History of Kinematics II: the Work of English Mathematicians on Linkages during the Period 1869 to 1878. *Mechanism and Machine Theory*, 18(1):43–48.
- Kong, X. and Gosselin, C. (2007). *Type Synthesis of Parallel Mechanisms*. Springer.
- Koster, M. P. (2000). *Constructieprincipes voor het nauwkeurig bewegen en positioneren*. Twente University Press, Twente.
- Kota, A., Li, Z., and Saggere, L. (1999). Tailoring unconventional actuators using compliant transmissions: Design methods and applications. *IEEE/ASME Transactions on Mechatronics*, 4(4):396–408.
- Kota, S., Lu, K.-J., Kreiner, Z., Trease, B., Arenas, J., and Geiger, J. (2005). Design and application of compliant mechanisms for surgical tools. *Journal of Biomechanical Engineering*, 127(6):981–989.

- Kutzbach, K. (1929). Mechanische leitungsverzweigung. *Maschinenbau, Der Betrieb*, 8:710–716.
- Lemoine, E. (1873). Note sur le losange articulé du commandant du génie peaucellier, destiné à remplacer le parallélogramme de Watt. *Journal of Theoretical and Applied Physics*, 2(1):130–134.
- Lender, T., Delavault, R., and Moigne, A. (1992). *Dictionnaire de biologie*. Presses Universitaires de France, 2nd edition.
- Letonje, J. and Janezic, I. (1999). Determination of the equation of bending stiffness of a hyperbolic notch with finite element analysis. In *Tenth World Congress of the Theory of Machine and Mechanisms*, volume 2, pages 610–615, Oulu, Finland.
- Li, C., He, Q., Zhang, Z., Li, Z., and Han, B. (2010). The Balance System Of Joule Balance In NIM. In *2010 Conference on Precision Electromagnetic Measurements*, pages 281–282, Daejeon Convention Center, Daejeon, Korea.
- Li, S., Han, B., Li, Z., and Lan, J. (2012). Precisely measuring the Planck constant by electromechanical balances. *Measurement*, 45(1):1–13.
- Lobontiu, N. (2003). *Compliant Mechanisms - design of flexure hinges*. CRC Press.
- Lu, J. and Lieurade, H.-P. (1998). Concentration de contraintes. *Techniques de l'Ingénieur*, B5 I:BM 5040–1–BM 5040–24.
- Lubrano, E. (2011). *Calibration of Ultra-High-Precision Robots Operating in an Unsteady Environment*. PhD thesis, Ecole polytechnique fédérale de Lausanne (EPFL). No. 5098.
- Lusk, C. P. and Howell, L. L. (2008). Components, building blocks, and demonstrations of spherical mechanisms in microelectromechanical systems. *Journal of Mechanical Design*, 130(3):034503.
- Massonnet, C. and Cescotto, S. (1994). *Mécanique des matériaux*. De Boeck University, Brussels.
- Mattson, C. A., Howell, L. L., and Magleby, S. P. (2004). Development of commercially viable compliant mechanisms using the pseudo-rigid-body model: Case studies of parallel mechanisms. *Journal of Intelligent Material Systems and Structures*, 15(3):195–202.
- Merlet, J.-P. (1997). *Les robots parallèles*. Hermes, Paris, 2nd edition.
- Merlet, J.-P. (2000). *Parallel robots*. Kluwer Academic Publishers, London.
- Mesnager, A. (1903). *Comptes Rendus de l'Académie des Sciences, Paris*, (137):908.
- Moore, D. F. (1975). *Principles and Applications of Tribology*, volume 14 of *International Series on Materials Science and Technology*. Pergamon Press, Oxford.

- Niaritsiry, T. (2006). *Optimisation de la conception du robot parallèle Delta Cube de très haute précision*. PhD thesis, Ecole polytechnique fédérale de Lausanne (EPFL). No. 3567.
- Numerik Jena GmbH (2015). <http://numerik.cycro-project.de>. online: accessed 2015.
- Olsen, B. M. (2010). *A Design Framework that Employs a Classification Scheme and Library for Compliant Mechanism Design*. Master's thesis, Brigham Young University.
- Olsen, B. M., Issac, Y., Howell, L. L., and Magleby, S. P. (2010). Utilizing a Classification Scheme to Facilitate Rigid-Body Replacement for Compliant Mechanism Design. In *ASME 2010 International Design Engineering Technical Conferences and Computers and Information in Engineering Conference*, pages 475–489.
- Ouyang, P. (2011). A spatial hybrid motion compliant mechanism: Design and optimization. *Mechatronics*, 21(3):479 – 489.
- Parise, J. J., Howell, L. L., and Magleby, S. P. (2001). Ortho-planar linear-motion springs. *Mechanism and Machine Theory*, 36(11-12):1281–1299.
- Paros, J. M. and Weisbord, L. (1965). How to design flexure hinges. *Machine Design*, 25:151–156.
- Pilkey, W. D. and Pilkey, D. F. (2008). *Peterson's Stress Concentration Factors (3rd Edition)*. John Wiley & Sons.
- Pomey, G. and Lieurade, H.-P. (1982). Essais de fatigue. *Techniques de l'Ingénieur*, M1 II:M130.
- Pozna, C. (2007). Modular robots design concepts and research directions. In *Proceedings of the 5th International Symposium on Intelligent Systems and Informatics*, pages 113–118, 24-25 August, Subotica (Serbia).
- Qin, Y. and Dai, J. S. (2012). Forward Displacement Analysis of Two Foldable 3US Parallel Mechanisms. In Dai, J. S., Zoppi, M., and Kong, X., editors, *Advances in Reconfigurable Mechanisms and Robots I*, pages 805–814. Springer, London.
- Renaud, P. and de Mathelin, M. (2009). Kinematic analysis for a novel design of MRI-compatible torque sensor. In *IEEE/RSJ International Conference on Intelligent Robots and Systems*, pages 2640–2646.
- Reuleaux, F. (1875). *Theoretische Kinematik: Grundzüge einer Theorie des Maschinenwesens*. Braunschweig, Druck und Verlag von Friedrich Vieweg un Sohn.
- Richard, M. (2012). *Concept of Modular Kinematics to Design Ultra-high Precision Parallel Robots*. PhD thesis, Ecole polytechnique fédérale de Lausanne (EPFL). No. 5377.

- Richard, M. and Clavel, R. (2010). A new concept of modular kinematics to design ultra-high precision flexure-based robots. In *Proceedings for the Joint Conference of the 41st International Symposium of Robotics and the 6th German Conference on Robotics*, pages 940–947, Munich, 7-9 June 2010, Germany.
- Richard, M. and Clavel, R. (2011). Concept of modular flexure-based mechanisms for ultra-high precision robot design. *Mechanical Sciences*, 2(2):99–107.
- Rubbert, L., Caro, S., Gangloff, J., and Renaud, P. (2014a). Using singularities of parallel manipulators to enhance the rigid-body replacement design method of compliant mechanisms. *Journal of Mechanical Design*, 136(5):51010.
- Rubbert, L., Caro, S., Renaud, P., and Gangloff, J. (2012a). A Planar RRP Compliant Mechanism based on the Singularity Analysis of a 3-US Parallel Mechanism. In *Advances in Robot Kinematics*.
- Rubbert, L., Renaud, P., Bachta, W., and Gangloff, J. (2011). Compliant mechanisms for an active cardiac stabilizer: Lessons and new requirements in the design of a novel surgical tool. *Mechanical Sciences*, 2(1):119–127.
- Rubbert, L., Renaud, P., Caro, S., and Gangloff, J. (2014b). Design of a compensation mechanism for an active cardiac stabilizer based on an assembly of planar compliant mechanisms. *Mechanics & Industry*, 2(15):147–151.
- Rubbert, L., Renaud, P., and Gangloff, J. (2012b). Design and optimization for a cardiac active stabilizer based on planar parallel compliant mechanism. In *Proceedings of the ASME 2012 11th Biennial Conference on Engineering Systems Design and Analysis*, 2-4 July 2012, Nantes.
- Sabnis, A. V., Dendy, J. B., and M., S. F. (1975). A magnetically suspended large momentum wheel. *Journal on Spacecraft*, 12(7):420–427.
- Savall, J., Manrique, M., Echeverria, M., and Ares, M. (2006). Micromanipulator for enhancing surgeon's dexterity in cochlear atraumatic surgery. In *Proceedings of the IEEE Engineering in Medicine and Biology Society*. 31 Aug.-3 Sep. 2006, New York. Annual International Conference.
- Schaller, R. and Benoit, W. (1979). Effets du frottement intérieur sur le facteur de qualité des résonateurs mécaniques. In *Proceedings of the 10th International Congress of Chronometry*, pages 377–383, Genève. Edited by the Swiss Society of Chronometry.
- Schoenflies, A. and Grübler, M. (1908). Kinematik. *Encyklopaedie der Mathematischen Wissenschaften*, 4, Mechanik (eds. Klein, F. and Müller, C.), Leipzig, Teubner:190–278.
- Schotborgh, W. O., Kokkeler, F. G. M., Tragter, H., and van Houten, F. J. A. M. (2005). Dimensionless design graphs for flexure elements and a comparison between three flexure elements. *Precision Engineering*, 29(1):41–47.

- Schweitzer, G., Bleuler, H., and Traxler, A. (1994). *Active Magnetic Bearings*. vdf Hochschulverlag AG an der ETH Zürich.
- Smith, S. T. (2003). *Foundations of Ultra-Precision Mechanism Design*. CRC Press, Boca Raton, Florida.
- Smith, S. T., Chetwynd, D. G., and Bowen, D. K. (1987). Design and assessment of monolithic high precision translation mechanisms. *Journal of Physics E: Scientific Instruments*, 20(8):977–983.
- Socha, K. and Dorigo, M. (2008). Ant colony optimization for continuous domains. *European Journal of Operational Research*, 185(3):1155–1173.
- Spinnler, G. (1997a). *Conception des machines. Principes et application. Dimensionnement.*, volume 3. Presses polytechniques et universitaires romandes, Lausanne.
- Spinnler, G. (1997b). *Conception des machines. Principes et applications. Statique.*, volume 1. Presses polytechniques et universitaires romandes, Lausanne.
- Sutton, C. M. (2009). An oscillatory dynamic mode for a Watt balance. *Metrologia*, 46(5):467–472.
- Tanik, E. and Parlaktas, V. (2012). Compliant cardan universal joint. *Journal of Mechanical Design*, 134(2):021011.
- Thurston, R. H. (1885). *A treatise on Friction and Lost Work on Machinery and Millwork*. Wiley, New York, 7th edition. 1903.
- Tian, Y., Shirinzadeh, B., and Zhang, D. (2010). Design and dynamics of a 3-dof flexure-based parallel mechanism for micro/nano manipulation. *Microelectronic Engineering*, 87(2):230–241.
- Timoshenko, S. P. (1953). *History of Strength of Materials*. McGraw-Hill Book Company, York, PA.
- Tolfree, D. (2006). Commercialising nanotechnology, concepts - products - markets. *International Journal of Nanomanufacturing*, 1(1):117–133.
- Van Camp, M., Camelbeeck, T., and Richard, P. (2003). Le kilogramme, la constante de planck et le soulèvement de l’ardenne. *Physicalia Magazine*, pages 161–174.
- Verettas, I. (2006). *Microfabrique: méthodologie de conception de systèmes de production miniaturisés et modulaires, disposant d’un environnement salles blanches*. PhD thesis, Ecole polytechnique fédérale de Lausanne (EPFL). No. 3549.
- Von Klitzing, K. (1986). The quantized Hall effect. *Reviews of Modern Physics*, 58(3):519–531.
- Waldron, K. J. and Kinzel, G. L. (1999). *Kinematics, Dynamics and Design of Machinery*. John Wiley and Sons, Inc., The Ohio State University.

- Wilding, S. E., Howell, L. L., and Magleby, S. P. (2012a). Introduction of planar compliant joints designed for combined bending and axial loading conditions in lamina emergent mechanisms. *Mechanism and Machine Theory*, 56(0):1–15.
- Wilding, S. E., Howell, L. L., and Magleby, S. P. (2012b). Spherical lamina emergent mechanisms. *Mechanism and Machine Theory*, 49(0):187–197.
- Willis, R. R. (1828). On the pressure produced on a flat surface when opposed to a stream of air issuing from an orifice in a plane surface. *Transactions of the Cambridge Philosophical Society*, 3(1):121–140.
- Wittrick, W. H. (1951). The properties of crossed flexure pivots, and the influence of the point at which the strips cross. *The Aeronautical Quarterly*, II(4):272–292.
- Wunderlich, W. (1978). Approximate Optimization of Watt's Straight-Line Mechanism. *Mechanism and Machine Theory*, 13(2):155–160.
- Xu, Q. and Li, Y. (2006). Mechanical design of compliant parallel micromanipulators for nano scale manipulation. In *1st IEEE International Conference on Nano/Micro Engineered and Molecular Systems*, pages 653–657. 18–21 January 2006.
- Xu, Q. and Li, Y. (2011). Analytical modeling, optimization and testing of a compound bridge-type compliant displacement amplifier. *Mechanism and Machine Theory*, 46(2):183–200.
- Yong, Y. K., Lu, T.-F., and Handley, D. C. (2008). Review of circular flexure hinge design equations and derivation of empirical formulations. *Precision Engineering*, 32(2):63 – 70.
- Zhang, Z., He, Q., Li, Z., Lu, Y., Zhao, J., Han, B., Fu, Y., Li, C., and Li, S. (2011). Recent Development on the Joule Balance at NIM. *IEEE Transactions on Instrumentation and Measurement*, 60(7):2533–2538.
- Zhang, Z., He, Q., Li, Z., Lu, Y., Zhao, J., Han, B., Li, C., Li, S., and Fu, Y. (2010). The Progress Of Joule Balance in NIM. In *2010 Conference on Precision Electromagnetic Measurements*, pages 516–517, 13–18 June 2006, Daejeon Convention Center, Daejeon, Korea.
- Zlatanov, D., Fenton, R. G., and Benhabib, B. (1995). A unifying framework for classification and interpretation of mechanism singularities. *Journal of Mechanical Design*, 117(4):566–572.
- Zlatanov, D. S. (1998). Classification and interpretation of the singularities of redundant mechanisms. In *Proceeding of DETC98*, 13–16 September 1998, Atlanta.

Index

13-hinge stage, 207
2PRR-RR mechanism, 261
3-RRR sperical mechanism, 231
3-US mechanism, 231
3-UU flexure mechanism, 258

active cardiac stabiliser, 232
actuation
 mode, 248
 sub-brick, 155, 174
 wrench, 254
air bearings, 6
allowable stress, 15, 19, 21
analogous bearings, 110
angular stiffness, 23
Ant Colony Optimisation (ACO),
 241
architectural singularity, 247
articulated structure, 8, 109
assembled leaf spring, 175, 178,
 183
asymmetries, 234
axis of torsion, 35

base, 109
bellows, 27
bending, 15
buckling, 52, 53, 72
building brick, 139, 149

Cardiolock, 232
circular notch hinge, 36, 43
circular notches, 236
clamping, 33
compactness, 229, 264

conceptual solution, 146
constraint wrench system, 254
corrected fatigue limit, 18, 19
correction factor, 17, 21
critical
 load, 52
 stress, 16, 18, 19
cross pivot, 98, 101
cross spring pivot, 101
curved beam, 237

degrees of constraint, 193
Delta, 165, 185
 robot, 136, 141
demonstrator, 208
design, 167, 183, 187
displacement amplification, 233
dynamic behaviour, 8

elastic restoring force, 124
electrical discharge machining, 37
elementary flexible articulations, 7
end effector, 109
endurance limit, 16
estimation of the stresses, 241
external DOFs, 112

fabrication, 9
fatigue
 damage, 14, 16
 limit, 16, 20, 21
fillet, 44
flexure
 bearings, 7
 joint elements, 25

force alignment, 171, 177
 four prismatic notch hinge, 70
 fretting, 3
 friction, 2

 generalised stiffness, 24
 generalised stiffnesses, 27, 28
 global wrench system, 253, 256
 Grassmann-Cayley algebra, 253
 gravity compensation, 179

 homologous bearings, 110
 hydrodynamic bearings, 6
 hydrostatic bearings, 6

 ideal bearings, 111
 in-plane
 manufacturing, 230
 stiffness, 239
 instantaneous center of rotation, 96,
 101
 interferometer, 206
 internal
 degrees, 114
 degrees of freedom, 112, 114
 DOF, 118
 DOFs, 114
 material friction, 3
 intersection, 202

 Jacobian matrix, 253
 joined cross spring pivot, 91

 kilogram, 226
 kinematic
 -based approaches, 229
 analogy, 110
 analysis, 111
 chains, 198
 loops, 198
 modelling, 202, 208
 singularities, 232

Lamina Emergent Mechanisms
 (LEM), 230
 leaf, 30
 leaf spring, 28
 Legolas, 168, 174, 180, 183
 Legolas family, 183
 lever, 207
 load cell, 129
 lubrication, 3

 magnetic bearings, 5
 mass reference, 226
 materials, 8
 maximum allowable moment, 15
 measurement, 216
 mechanical
 design, 174, 187, 189
 stops, 123
 mechanical design, 154, 168
 mechanics of structures, 13
 medical devices, 229
 membranes, 27
 MEMS, 232, 265
 metal alloys, 8
 microfabrication, 265
 micropositioning, 229
 mirror, 206
 tilting, 232
 mobility, 198
 modular, 134, 138
 modularity, 137
 monolithic components, 4
 motoric segments, 110

 natural
 angular stiffness, 23
 forces, 23
 moments, 23
 rigidity, 4
 stiffness, 23
 translational stiffness, 23
 notch, 18

- effect, 18
- hinges, 96, 101
- optimisation, 240
- orthogyre, 192
- parallel
 - mechanisms, 246
 - robot, 115, 136, 138
 - singularity, 247
- parasitic
 - movements, 207
 - translation, 90, 96, 101, 119
- piezoelectric actuators, 232
- planar configurations, 229
- plastic deformation, 14
- play, 4
- Poisson's ratio, 29
- primary standard, 226
- prismatic notch hinge, 70
- prototype, 205, 214
- pseudo-orthogyre, 192
- pseudo-rigid body modelling, 229
- quality factor, 3
- quasi-planar configuration, 235
- range of motion, 4
- RCC pivot, 93, 96
- redundant
 - DOFs, 117
 - input singularity, 247
 - output singularity, 247
 - passive motion singularity, 247
 - rotational bearing, 121
 - translational bearing, 118
- Remote Center Compliance (RCC), 93
- Remote Centre of Motion (RCM), 155, 157, 161, 162, 176
- restoring force, 4
- rigid-body replacement approach, 229
- robot
 - designer, 168
 - synthesis, 134, 152, 189
- robotic Lego, 134
- rod, 30, 32
- safety factor, 19, 20
- Sarrus
 - kinematics, 227
 - linkage, 200
- scale effect, 17, 18
- scaling laws, 38
- secant stiffness, 126, 128
- segment, 109
- seizing, 3
- self-motions, 247
- separate cross spring pivot, 89
- serial
 - arrangement, 117
 - singularity, 247
- shear center, 35
- shear force, 14
- SI units, 226
- singularities, 246
- singularity analysis, 248, 252
- small deformation hypothesis, 8
- solution catalogue, 152, 167
- space applications, 229
- static behaviour, 8
- statically indeterminate, 113
- stiffness ratio, 26, 29
- stiffnesses, 22
- stochastic algorithms, 241
- straightness
 - error, 195, 208, 216
 - measurement, 206
 - ratio, 195
- strain, 117
- stress concentration, 85
 - factors, 241
- stresses, 241

- estimation of the –, 241
- surface roughness, 21
- surgical robotics, 232
- synthesis, 168, 169, 187
 - of robots, 183
- tangent stiffness, 126, 128
- Taylor series, 212
- theoretical straightness, 212
- thermal expansion, 212
- tip-tilt, 227
- torsion, 16, 19
 - bar, 33
 - pivots, 164
- translational stiffness, 22
- transverse
 - rigidity, 3
 - stiffness, 23

- stiffnesses, 25
- travel, 14
- twist, 246, 253
- ultra-high precision, 136, 148, 149,
168, 183
- uniform bending strength, 129
- utilisation coefficient, 129
- velocities, 246
- vicinity of singularities, 233
- warping, 33, 40
- watt balance, 220
- wear, 3
- wire-cut electrical discharge ma-
chining, 9
- Wöhler curve, 20, 21
- wrench, 254